

# UC Berkeley

## UC Berkeley Electronic Theses and Dissertations

### Title

Characterizing and Modeling Spin Polarization from Optically Pumped Nitrogen-Vacancy Centers in Diamond at High Magnetic Fields

### Permalink

<https://escholarship.org/uc/item/3hg0d1zm>

### Author

Drake, Melanie

### Publication Date

2016

Peer reviewed|Thesis/dissertation

Characterizing and Modeling Spin Polarization from Optically Pumped Nitrogen-Vacancy Centers  
in Diamond at High Magnetic Fields

By

Melanie Elizabeth Drake

A dissertation submitted in partial satisfaction of the

requirements for the degree of

Doctor of Philosophy

in

Chemical Engineering

in the

Graduate Division

of the

University of California, Berkeley

Committee in charge:

Professor Jeffrey A. Reimer, Chair  
Professor Markita Landry  
Professor Alexander Pines

Fall 2016



Characterizing and Modeling Spin Polarization from Optically Pumped Nitrogen-Vacancy Centers  
in Diamond at High Magnetic Fields

Copyright 2016  
By  
Melanie Elizabeth Drake

## Abstract

### Characterizing and Modeling Spin Polarization from Optically Pumped Nitrogen-Vacancy Centers in Diamond at High Magnetic Fields

by

Melanie Elizabeth Drake

Doctor of Philosophy in Chemical Engineering

University of California, Berkeley

Professor Jeffrey Reimer, Chair

The small thermal polarization of nuclear spins currently limits the capabilities of nuclear spin based technologies such as nuclear magnetic resonance spectroscopy (NMR) and magnetic resonance imaging (MRI). Existing techniques for polarizing nuclear spins beyond their thermal equilibrium, called dynamic nuclear polarization (DNP), utilize cryogenic temperatures and expensive microwave technologies to transfer the larger thermal polarization of electron spins to targeted nuclei. Ubiquitous access to polarized nuclei through a room temperature, microwave-free alternative to DNP would revolutionize the capabilities of NMR and MRI.

Optically pumping nitrogen-vacancy (NV) defects in diamond can generate room temperature, microwave-free  $^{13}\text{C}$  nuclear polarization at the high magnetic fields used in NMR (7.05T, 9.4T). The mechanism of NV center electronic polarization is well understood, and  $^{13}\text{C}$  polarization has been observed, but the mechanism for polarization transfer from NV to  $^{13}\text{C}$  remains unknown. Here we present NMR and EPR results characterizing the polarization dependence of  $^{13}\text{C}$  and NV in diamond, as well as a quantum mechanical model describing a possible polarization transfer mechanism.

The sign and magnitude of the  $^{13}\text{C}$  polarization sensitively depends on the orientation of the diamond with respect to the directions of the applied magnetic field and laser polarization. The polarization magnitude further depends on the defect concentrations, magnitude of the applied magnetic field, temperature, and the illumination conditions: wavelength, power, and exposure time.

To better understand the source of polarization, the NV defects were characterized with EPR to determine relaxation times, concentrations, and homogeneity. EPR was also used to determine the orientation dependence of NV polarization. The NV polarization is constant in the defect frame, which, when rotated into the laboratory frame, results in highest polarization when aligned with the field, zero polarization at 54 degrees, and inverted polarization at higher angles. These EPR insights into the NV physics were incorporated into models for  $^{13}\text{C}$  polarization mechanisms.

Dipolar coupled pairs of NV centers are proposed as the source for  $^{13}\text{C}$  polarization in NV- diamonds at high magnetic fields. Our model shows these dipolar-coupled manifolds have transitions matching the frequency of the  $^{13}\text{C}$  nuclei, making them a feasible source of spontaneous polarization transfer. The model also qualitatively captures the observed polarization sign changes as a function of crystal orientation.

Dedicated to my parents

# Table of Contents

---

<b>1 Introduction</b>	<b>1</b>
1.1 Nuclear Magnetic Resonance and the Motivation for Signal Enhancement	1
1.2 Electron Paramagnetic Resonance	2
1.3 Hyperpolarization Methods	3
1.4 Nitrogen-Vacancy Centers in Diamond	4
<b>2 Equipment and Samples</b>	<b>9</b>
2.1 NMR Setup	9
2.2 Tuneless Probe	10
2.3 Temperature Control	14
2.4 Lasers and Optics	14
2.5 EPR Systems	16
2.6 Diamond Samples	17
2.7 Acknowledgements	18
<b>3 <math>^{13}\text{C}</math> Polarization from Nitrogen Vacancy Centers at 9.4T</b>	<b>19</b>
3.1 Abstract	19
3.2 Introduction	19
3.3 Methods	20
3.4 Orientation Dependence	21
3.5 Time Dependence	22
3.6 Laser Wavelength Dependence	28
3.7 Temperature Dependence	29
3.8 Conclusion	29
3.9 Acknowledgements	30
<b>4 Orientation-Dependent Two-Spin Cross Relaxation Model of NV-Mediated <math>^{13}\text{C}</math> Polarization in Diamond at High Magnetic Fields</b>	<b>31</b>
4.1 Abstract	31
4.2 Introduction	31
4.3 Dipolar Coupled NV-NV Polarization Model	31
4.4 Model Results	39
4.5 Additional Model Refinements	43
4.6 Conclusions	45

<b>5 Double Electron-Electron Resonance Measurements</b>	<b>46</b>
5.1 Abstract	46
5.2 Introduction	46
5.3 Methods	46
5.4 Double Electron-Electron Resonance (DEER)	48
5.5 Conclusion	56
5.6 Acknowledgements	57
<b>6 Nitrogen Vacancy and Substitutional Nitrogen Relaxation in Diamond</b>	<b>58</b>
6.1 Abstract	58
6.2 Introduction	58
6.3 Methods	58
6.4 NV and P1 Relaxation Time Constants	60
6.5 Conclusion	79
6.6 Acknowledgements	80
<b>7 NV- Spin Polarization: Dependence on Orientation and P1 Concentration</b>	<b>81</b>
7.1 Abstract	81
7.2 Introduction	81
7.3 Methods	81
7.4 Polarization of NV as a function of Field Alignment and P1 Concentration	84
7.5 Conclusion	88
7.6 Acknowledgements	89
<b>8 Conclusions and Suggested Future Work</b>	<b>90</b>
8.1 Conclusions	90
8.2 Future Work	90

<b>References</b>	<b>97</b>
<b>Appendix A: Calculating NV Orientation Relative to Magnetic Field</b>	<b>107</b>
<b>Appendix B: Modeling NV Light Absorption</b>	<b>110</b>
<b>Appendix C: Derivation of NV Ensemble Density Matrix from that of Individual Defects</b>	<b>117</b>
<b>Appendix D: Simulating NV EPR Spectra</b>	<b>120</b>
<b>Appendix E: Mathematica Code of Orientation-Dependent Model of Dipolar Coupled NV Polarization</b>	<b>125</b>

# 1 Introduction

## 1.1 Nuclear Magnetic Resonance and the Motivation for Signal Enhancement

Despite its ubiquity in the broad fields of science and medicine, magnetic resonance applications are still limited by low sensitivity. Detecting a nuclear magnetic resonance (NMR) signal requires a sufficient difference in the number of spins populating two energy levels between which the spins can transition. This requires not only a sufficient total number of spins in the sample, but also a sufficient distribution of spin population among energy levels <sup>1</sup>. The thermal equilibrium distribution can be improved through lowering sample temperature or increasing the magnetic field strength, but the spins will still be in a thermal Boltzmann distribution among the energy levels. In order to make a significant improvement in NMR sensitivity, the system must be put in a non-equilibrium state, also called a polarized or hyperpolarized state, with a non-Boltzmann distribution of spins.

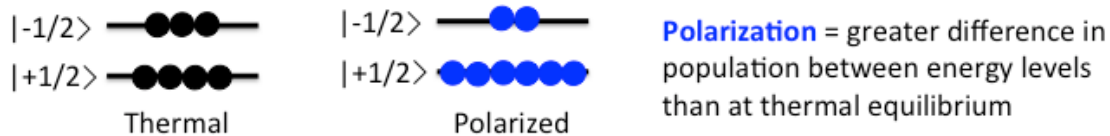


Figure 1 Simplified depiction of thermal (Boltzmann) versus polarized distribution of spins between the two energy levels of a spin-1/2 system. Polarized systems can also be made to invert populations between the upper and lower energy levels. In the case that more population is in the higher energy level, we call this 'negative' polarization.

Figure 1 visually depicts the difference in spin populations for a spin-1/2 system in a thermal equilibrium state and a polarized state. Each circle represents spin-1/2 nuclei, and its position represents which energy level it occupies. Equation 1 defines the percent of polarization between two energy levels for a spin-1/2 nuclei, where  $N_i$  is the number of spins in level  $i$ .

$$\%P = \frac{N_{1/2} - N_{-1/2}}{N_{1/2} + N_{-1/2}} 100\% \quad (1)$$

If the system is in thermal equilibrium,  $N_i$  are set by a Boltzmann distribution. Equation 2 describes the Boltzmann distribution of spins in a spin-1/2 system, where  $N_i$  is the number of spins in level  $i$ ,  $k$  is the Boltzmann constant,  $\Delta E$  is the energy difference between each level, and  $T$  is the temperature <sup>1</sup>.

$$\frac{N_{-1/2}}{N_{+1/2}} = e^{\frac{-\Delta E}{kT}} \quad (2)$$

Equation 3 describes the resulting percent polarization at thermal equilibrium.



$$\%P_{Eq} = \tanh\left(\frac{\gamma_n \hbar B_0}{2kT}\right) 100\% \quad (3)$$

Equation 3 is derived by inserting the expression for energy, given in Equation 4, into Equation 2. As seen in Equation 4 and Figure 2, the energy levels are determined by the applied magnetic field <sup>1</sup>. In equation 4,  $\hbar$  is the reduced Planck's constant,  $\gamma$  is the gyromagnetic ratio of the nuclei, and  $m_s$  is the secondary spin quantum number of the nuclei.

$$E = -\hbar\gamma B_0 m_s \quad (4)$$

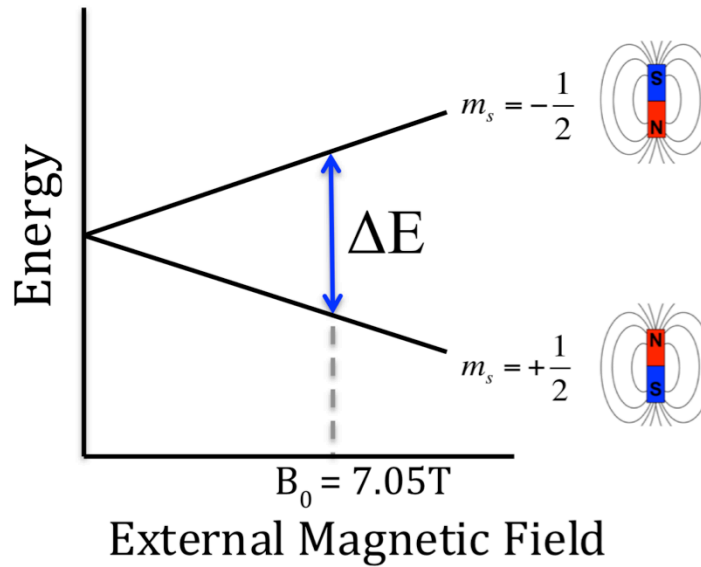


Figure 2 Spin-1/2 energy level structure as a function of magnetic field. NMR experiments observe transitions between the two levels

## 1.2 Electron Paramagnetic Resonance

Electron paramagnetic resonance (EPR) is the application of magnetic resonance to observe spin transitions of unpaired electrons. Electron spin transitions occur on the microwave energy scale (GHz). The hardware associated with microwaves involves waveguides and resonant cavities as opposed to the transmission lines and coils used in handling RF signals in NMR. EPR is typically implemented using continuous wave (CW) systems in which the magnetic field (or less often the microwave frequency) is continuously swept across the spectrum while applying a constant frequency (or field). When the field is swept through a transition matching the applied microwave frequency, the sample absorbs some of the microwave power, slightly rotating the magnetization and resulting in a peak in the EPR spectrum. Detailed explanations of EPR can be found elsewhere <sup>2,3</sup>. The description here is limited to a cursory overview of important experimental considerations.

Experimental parameters unique to EPR include microwave power, field sweep rate, field modulation frequency, field modulation amplitude, and sample geometry relative to the microwave profile in the cavity.

### **1.2.1 Microwave power and field sweep rate**

If the microwave power is too strong or the field sweep rate too fast, the spins can be saturated (unable to return to their initial state within the measurement time) and the spectrum double integral loses quantitative meaning. Saturation regimes are determined by plotting a power saturation curve - a plot of the EPR signal amplitude as a function of the square root of the applied microwave power. EPR spectra taken at microwave powers in the linear regime of the power saturation curve can be used for quantitative analysis.

### **1.2.2 Field modulation frequency and amplitude**

The swept magnetic field is modulated on the order of kHz. This generates the same modulation in the detected signal, enabling it to be separated from noise using a lock-in amplifier, significantly increasing the signal to noise of the resulting spectrum. This field modulation also leads to CW spectra with dispersive line shapes. These can be integrated to attain the absorption line shapes. Only spectral features larger than the field modulation amplitude can be resolved. Peaks are distorted if the field modulation is larger than the feature width. Optimal field modulation is determined by trial-and-error to find a field modulation that does not change the width of spectral features when lowered further. Choice of modulation frequency only becomes a concern when sample relaxation times are on the same order of magnitude.

### **1.2.3 Sample geometry in the cavity**

Applied microwaves will generate a profile across the sample cavity, leading to spatially dependent absorption by the sample. This becomes an important consideration when trying to draw quantitative comparisons between spectra from samples of different geometries.

## **1.3 Hyperpolarization Methods**

It is becoming increasingly common to overcome the sensitivity limitations of magnetic resonance by putting systems into a hyperpolarized state. There are a growing number of methods for accomplishing this, most of which are limited by the nature of the polarization agent. There are generally two-steps: 1) generating a large difference in population across electron spin transition levels (thermal or polarized), and then 2) transferring that polarization to the nuclei of interest. Table 1 summarizes common methods for nuclear spin polarization with a select, but in no way comprehensive, set of references for learning more.

**Table 1 Summary of Nuclear Polarization Methods with Example References**

Technique	Electron Spin Source	Electron Polarization Manipulator	Electron Polarization Mechanism	Nuclear Polarization Mechanism	Ref.
<b>OPNMR - Alkali Metals and Noble Gases</b>	Alkali metal valence electrons	Helicity of light	Spin-dependent excitation	Hyperfine-mediated cross relaxation while gas is complexed with alkali atom	4
<b>OPNMR - Semiconductors</b>	Unpaired electrons in semiconductors	Helicity of light	Spin-dependent excitation	Hyperfine-mediated cross relaxation with defect or conduction band electrons	5-7
<b>ISC-OPNMR</b>	NV- (diamond) or $V_{Si}V_C$ (SiC)	light	Spin-dependent ISC decay from triplet to singlet	Hyperfine-mediated cross relaxation with single defect at GSLAC or ESLAC fields, or with paired defects at high fields	8-13
<b>ISC-OPNMR + DNP</b>	NV- (diamond)	light	Spin-dependent ISC decay from triplet to singlet	Microwave-induced SE or CE transfer	12,14-16
<b>CIDNP</b>	Photosensitizer molecules	n/a	n/a	Nuclear spin-dependent ISC of spin-correlated radical pair	17
<b>Photoexcitation + DNP</b>	Organic molecules with photo-excited triplet states	Light	Spin-dependent ISC decay from photo-excited singlet to triplet	Microwave irradiation	18-20
<b>DNP – Solid Effect (SE)</b>	Radicals in solution or unpaired electrons in solids	Low temperature	Low temperature thermal	Microwave irradiation at ZQ or DQ transition at $\omega_{MW} = \omega_e \pm \omega_n$	21-27
<b>DNP – Cross Effect (CE)</b>	Radicals in solution or unpaired electrons in solids	Low temperature	Low temperature thermal	Microwave irradiation at SQ transition in e-e-n system where $\Delta\omega_e = \omega_n$	25,26,28,29
<b>DNP – Overhauser Effect (OE)</b>	Radicals in solution or unpaired electrons in solids	Low temperature	Low temperature thermal	Time-dependent hyperfine interactions after microwaves saturate electronic transition	30,31
<b>DNP – Thermal Mixing (TM)</b>	Radicals in solution or unpaired electrons in solids	Low temperature	Low temperature thermal	Multi-electron version of CE	32
<b>Parahydrogen Induced Polarization (PHIP) – PASADENA or ALTADENA</b>	n/a	n/a	n/a	pH2 enriched through catalysis at low T. pH2 reacts across a bond, transferring spin order to bonded nuclei	33-36
<b>Signal Amplification by Reversible Exchange (SABRE)</b>	n/a	n/a	n/a	pH2 enriched through catalysis at low T. pH2 transfers spin order by chemical exchange with target molecule over a catalyst.	37,38

## 1.4 Nitrogen-Vacancy Centers in Diamond

This work studies the nitrogen-vacancy center in diamond due to its ability to generation large room temperature nuclear polarization without the use of microwaves<sup>39</sup>. The nitrogen-vacancy center in diamond is the first system in which a coupled optical pumping and intersystem crossing and decay mechanism was used

to polarize nuclear spins <sup>8</sup>. This section discusses the structure, formation, and polarization physics of the NV<sup>-</sup> center, as well as a brief overview of the literature pertaining to NV-mediated nuclear polarization.

### 1.4.1 Structure

The nitrogen-vacancy (NV) center in diamond is an electronic defect composed of a substitutional nitrogen and adjacent vacancy (Figure 3). The neutral form (NV<sup>0</sup>) is a spin 1/2 defect composed of 5 electrons: one from each carbon dangling bond about the vacancy, and two from the nitrogen dangling bond. The negative form (NV<sup>-</sup>) is a spin-1 defect, composed of the same 5 electrons as the neutral defect with an additional electron taken from other defects in the diamond lattice <sup>40</sup>. Substitutional nitrogen defects, also called P1 centers, are typically present in much larger quantities than NV centers and are often attributed as the donors of the sixth electron to the NV<sup>-</sup> centers <sup>41</sup>. These six electrons fill the NV<sup>-</sup> molecular energy levels as seen in Figure 5a <sup>42,43</sup>. Two electrons are left unpaired in both the ground and excited state configurations, giving the defect its spin-1 ground and excited states. See reference <sup>43</sup> for a full description of the molecular orbitals of the NV-defect.

NV<sup>-</sup> centers have C<sub>3v</sub> symmetry, with a primary axis running through the nitrogen and vacancy. In diamonds where NV<sup>-</sup> centers are generated homogeneously throughout in the bulk, the NV<sup>-</sup> centers will exist in four orientations with respect to the crystal surface normal. These orientations can be thought of as the four ways in which the primary axis can point along different bond directions of a tetrahedral subunit, as seen in Figure 3b.

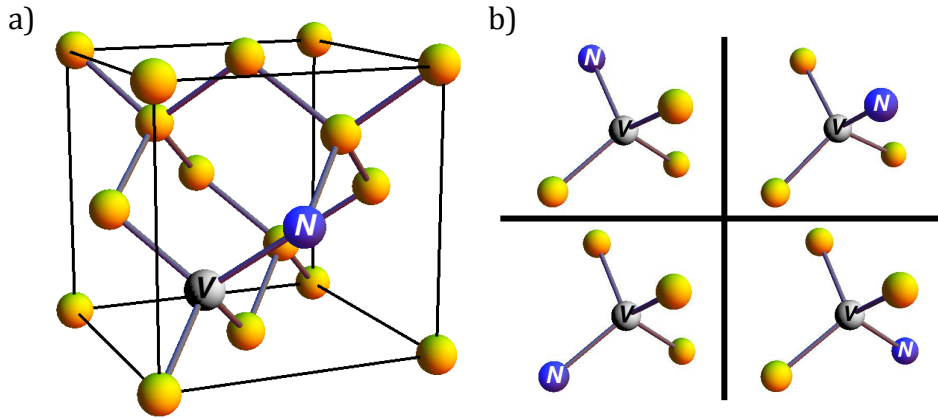


Figure 3: a) Unit cell of nitrogen-vacancy center in diamond. Yellow balls represent carbon, purple 'N' represents a nitrogen atom, and grey 'V' represents a vacancy. b) Tetrahedral subunits illustrating the four NV orientations present within the sample.

### 1.4.2 Formation

Small quantities of NV centers will form during diamond synthesis, often enough for single-defect studies. For high NV concentration applications, substitutional

nitrogen and vacancies are introduced separately and then annealed to form NV centers. Substitutional nitrogen can be introduced during chemical vapor deposition (CVD) or high-pressure high temperature (HPHT) diamond synthesis, or introduced post-synthesis through high-energy ion implantation. Vacancies can be generated through ion or electron irradiation, processes in which high energy particles knock carbon atoms from their lattice positions. After irradiation, the diamond is annealed at high temperatures (850°C for 2 hours in the case of the samples used in this work), allowing vacancies to diffuse through the diamond lattice and form NV centers by combining with substitutional nitrogen.<sup>44-51</sup> Figure 4 shows the diamond color at each treatment step.

While there has been some success generating low concentration NV doped diamonds with a single defect orientation<sup>52</sup>, typical high concentration (“purple”) samples have NV centers equally present in four orientations (Figure 3b).

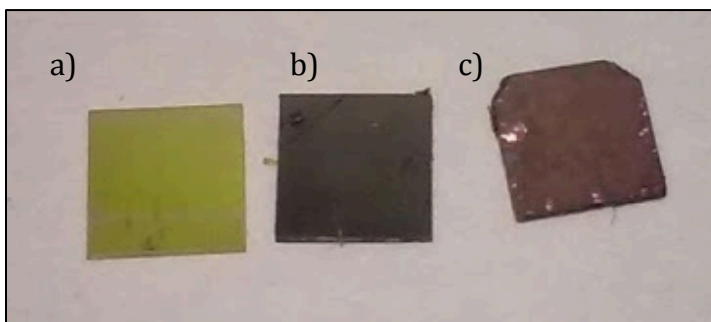


Figure 4 Photo of Type 1b HPHT synthetic diamonds a) upon purchase (P1 centers) b) post-electron-irradiation (P1 centers and vacancies) c) post-irradiation and annealing (P1 centers and NV centers)

### 1.4.3 NV- Polarization Physics

The NV- center has a triplet ground state, triplet excited state, and two singlet states (Figure 5)<sup>53</sup>. The ground state can be excited by optical illumination through a spin-conserving transition. There are two decay pathways from the excited state back to the ground state: the reverse spin-conserving radiative transition directly back to the ground state (emitting 637 nm light), or a non-radiative decay through an intersystem crossing (ISC) into the singlet states which does not conserve spin. The ISC pathway rates are faster for the  $m_s = \pm 1$  excited states than the  $m_s = 0$  excited state, and this asymmetry leads to an accumulation into the  $m_s = 0$  ground state<sup>54</sup>.

### 1.4.4 Photoionization

Laser excitation can not only move the NV- and NV<sup>0</sup> into their excited states, but can also photo-ionize them by pushing electrons from the defect states into the conduction band or bringing them up from the valence band<sup>55</sup>. Photoionization moves electrons between NV and P<sub>1</sub> centers via the conduction band. Positively charged P<sub>0</sub> centers charge balance the negative NV defect<sup>41</sup>. Figure 6 shows this photoionization process, recreated from a figure in the literature<sup>55</sup>. The same study was able to observe individual photoionization events for a single NV defect through observing a time trace of the NV defect fluorescence.

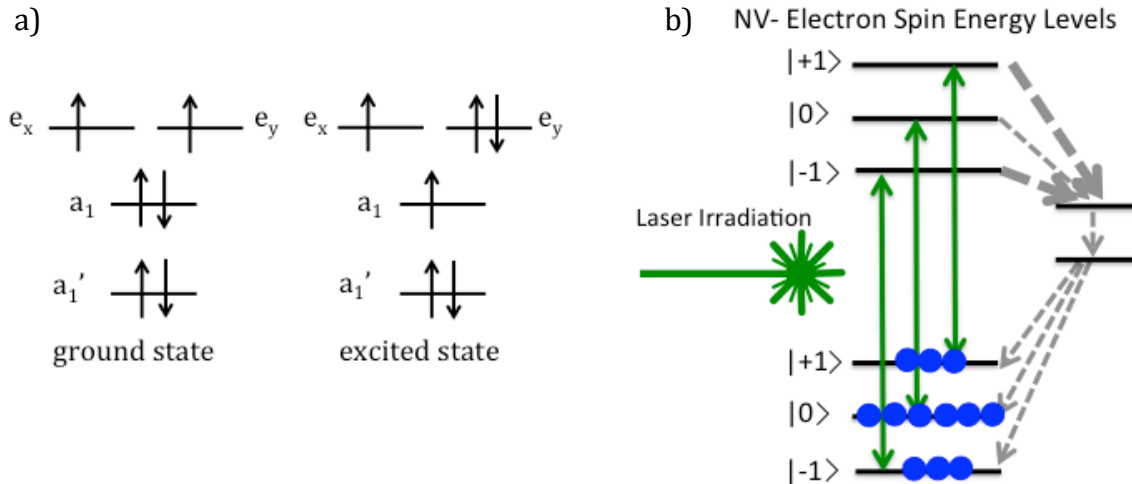


Figure 5: a) Molecular energy level structure leading to the spin-1 nature of the ground and excited states of the NV- center. b) Spin energy level structure of the NV- center at high magnetic field (level separations not-to-scale), showing the radiative (green) and non-radiative (gray) excitation and decay pathways (arrows). Blue circles qualitatively illustrate the relative population distribution upon laser irradiation for a defect aligned with a magnetic field. This polarized distribution is the result of an increased ISC rate for the  $\pm 1$  excited state levels, indicated as thicker arrows in the figure.

Photoionization leads to different steady-state NV<sup>-</sup>:NV<sup>0</sup> ratios at different illumination conditions. These ratios have been studied by comparing the relative NV<sup>-</sup> and NV<sup>0</sup> zero phonon line (ZPL) photoluminescence as a function of laser power at cryogenic temperatures<sup>56</sup>. The steady-state NV<sup>-</sup>:NV<sup>0</sup> ratio decreases with increasing laser intensity<sup>56</sup> and is reached on a microsecond timescale<sup>57</sup>. This ratio has also been studied as a function of laser wavelength, and is highest over the range of 480 – 560nm illumination<sup>55</sup>.

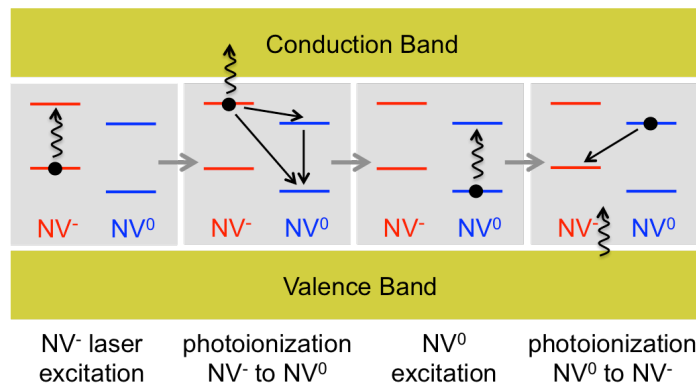


Figure 6: Four-step process illustrating the photoionization, which interconverts an NV center between its NV<sup>-</sup> and NV<sup>0</sup> forms. Sinusoidal black arrows indicate laser-induced excitation pathways, and straight black arrows indicate decay pathways. In the first step, laser illumination excites the NV<sup>-</sup>. In the second step, laser illumination excites an excited-state NV<sup>-</sup> electron into the conduction band, turning the NV<sup>-</sup> into a neutral charge NV<sup>0</sup>, which is either created in the excited or ground state, but eventually ends up as a ground-state NV<sup>0</sup>. In the third step, the ground state NV<sup>0</sup> is excited by laser illumination. In the final step, laser illumination excites an electron from the valence band, and the excited NV<sup>0</sup> becomes an NV<sup>-</sup>.<sup>55</sup>

### 1.4.5 NV- Polarization Transfer to Nuclei in the Diamond

NV- electron polarization has been transferred both with and without the use of microwaves to both  $^{14}\text{N}$  and  $^{15}\text{N}$  nuclei of the NV- defect and to  $^{13}\text{C}$  nuclei in the diamond lattice. Table 2 outlines the NV-mediated nuclear polarization literature.

Table 2 Literature Overview of Nuclear Polarization from NV Centers

Polarized Nuclei	Maximum Polarization	Magnetic Field	Temp.	Year	Reference
<b><i>Laser-only Polarization Transfer from NV- to Nuclei in Diamond</i></b>					
$^{15}\text{N}$ (of NV)	98%	500G (ESLAC)	RT	2009	8
$^{13}\text{C}$ (proximal)	90%	500G (ESLAC)	RT		
$^{13}\text{C}$ (bulk)	5%	9.4T	5K	2010	9
$^{13}\text{C}$ (proximal)	~100%	1000G (GSLAC)	RT	2013	10
$^{14}\text{N}$ (of NV)	90%	0 – 500G (ESLAC)	4K - RT	2013	13
$^{13}\text{C}$ (proximal)	70%	500G (ESLAC)	RT		
$^{13}\text{C}$ (bulk)	0.5%	500G (ESLAC)	RT	2013	11
$^{13}\text{C}$ (bulk)	0.125%	7T	RT	2016	58
$^{13}\text{C}$ (bulk)	1-3%	7T	20K		
<b><i>Laser + Microwave Polarization Transfer from NV- to Nuclei in Diamond</i></b>					
$^{13}\text{C}$ (3 <sup>rd</sup> shell)	91%	ESLAC	RT	2009	15
$^{15}\text{N}$ (of NV)	95%	ESLAC, 10s of Gauss	RT		
$^{14}\text{N}$ (of NV)	95%	ESLAC, 10s of Gauss	RT		
$^{14}\text{N}$ (of NV)	80%	57, 302, 777G	RT	2014	16
$^{13}\text{C}$ (bulk)	250x enhancement	ESLAC, 0-900G	RT	2015	12
$^{13}\text{C}$ (1st shell)	Not quantified	ESLAC, 0-900G	RT		
$^{13}\text{C}$ (bulk)	6%	4200G	RT	2015	14

## 2 Equipment and Samples

### 2.1 NMR Setup

The NMR experiments of this work were performed on a 9.4 T Oxford superconducting magnet with a Tecmag spectrometer and homebuilt tuneless NMR probe. Low temperature experiments were performed in an Oxford cryostat.

#### 2.1.1 Single Channel Mode

Figure 1 is a flow diagram of the equipment used and signals transmitted among them in a single frequency NMR experiment. The crossed diodes, crossed diodes to ground, quarter wave cable, and probe are all homebuilt in these experiments.

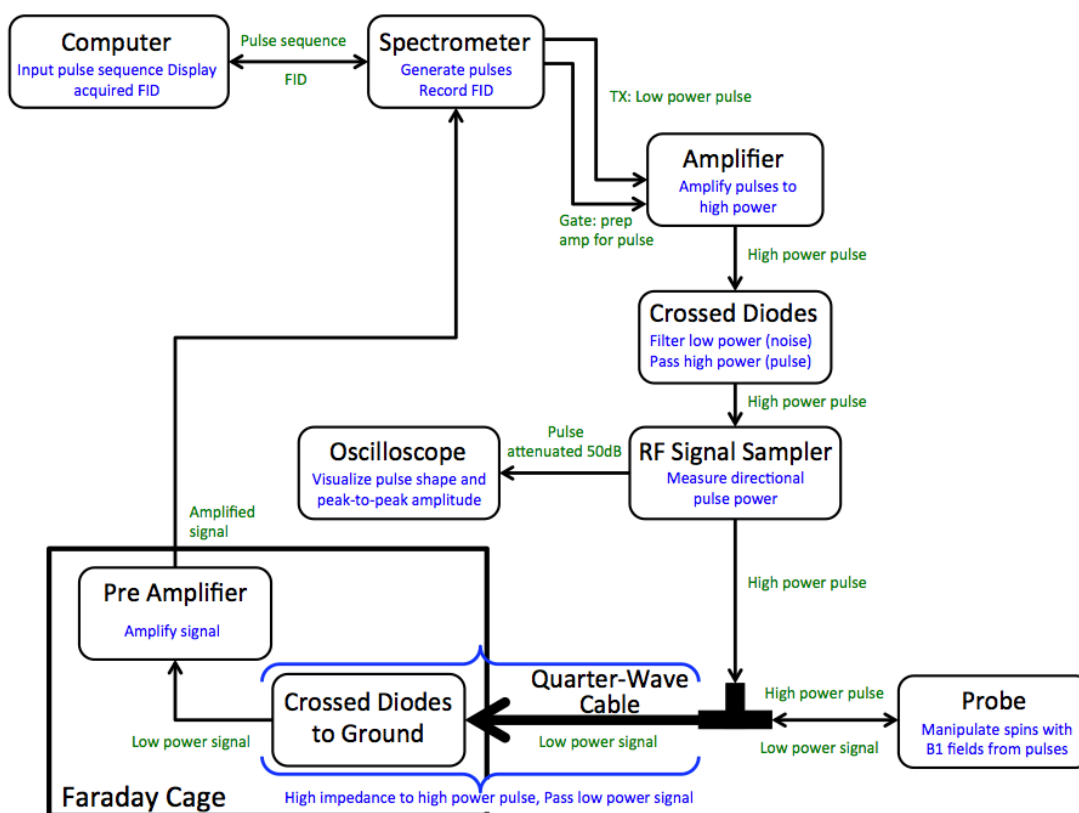


Figure 1: Schematic of NMR experimental setup, including equipment (black text), equipment purpose (blue text), and transmitted signals (green text).

#### 2.1.2 Double Channel Mode

Figure 2 is a flow diagram of the equipment used and signals transmitted among them in a double frequency NMR experiment. High power filters are needed to prevent the high power pulses being sent into the opposite frequency amplifiers.



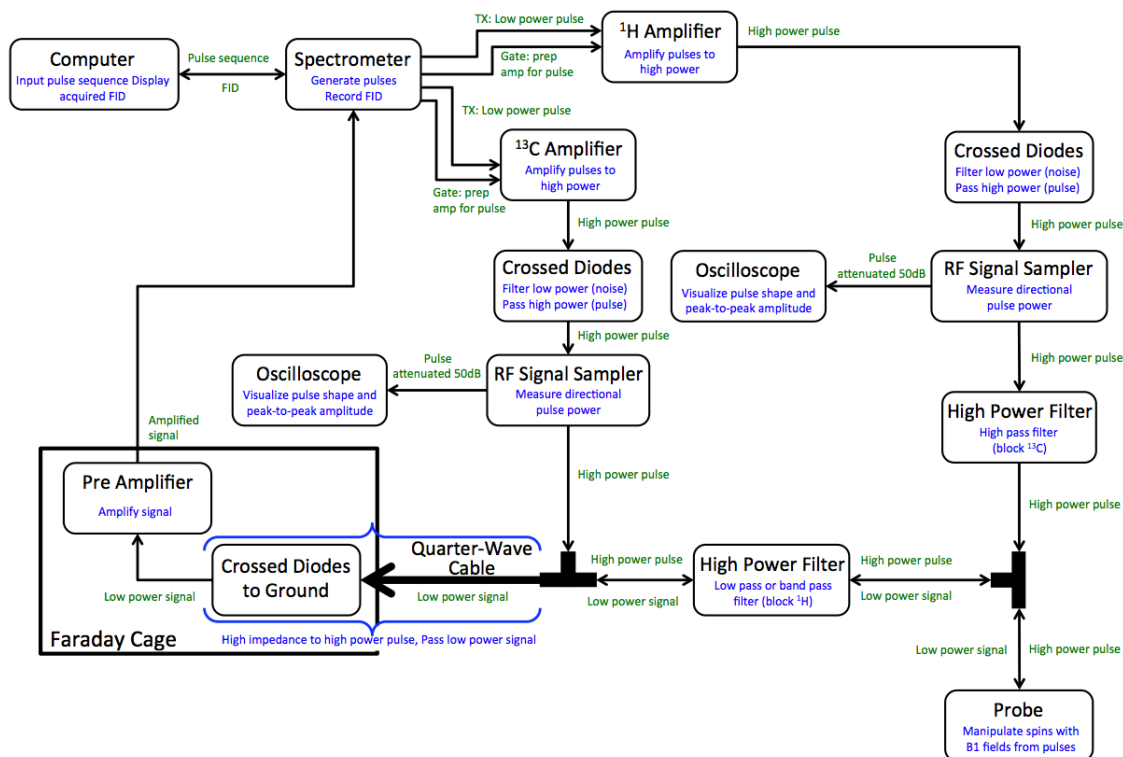


Figure 2 Schematic of NMR cross polarization experimental setup, including equipment (black text), equipment purpose (blue text), and transmitted signals (green text).

## 2.2 Tuneless Probe

Tuneless NMR probes were used for all NMR experiments in this work. This section reviews tuned probes, transmission line electronics, and tuneless probes.

### 2.2.1 Tuned Probe Theory

A typical tuned NMR LC circuit (Figure 3) has a characteristic frequency that depends on the inductance and capacitance of the circuit according to Equation 1. This characteristic frequency is tuned to the Larmor frequency of the nuclei being probed with NMR by adjusting the capacitance of the ‘tuning’ capacitor shown in Figure 3.

$$\nu_0 = \frac{1}{2\pi\sqrt{LC}} \quad (1)$$

The ‘matching’ capacitor shown in Figure 3 is used to match the impedance of the probe to that of the transmission line, which is 50 Ohms. Impedance matching maximizes power transfer to the probe, minimizing reflected power.

Tuned circuits are evaluated by their quality factor, or Q factor, which is a measure of how under-damped an oscillator is (Equation 2). Higher Q factor circuits resonate

longer. The Q factor also describes the bandwidth of the resonator with respect to the center frequency (Equation 3).

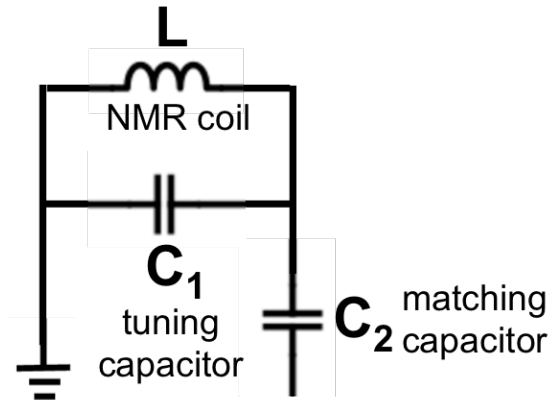
$$Q = \frac{2\pi (\text{energy stored})}{(\text{energy dissipated})} \quad (2)$$

$$Q = \frac{\nu_0}{\Delta\nu} \quad (3)$$

Ideal probe parameters have conflicting dependencies on the Q factor, necessitating tradeoffs in probe design. Table 1 outlines these dependencies.

**Table 1 Probe parameter considerations and their dependence on Q factor**

Probe Parameter	Q-Dependence	Desired Value
Pulse Length	$Q^{-1/2}$	Short
Dead time	Q	Short
Max RF Voltage in Probe	Q	Low
Bandwidth	$Q^{-1/2}$	High
Sensitivity	$Q^{1/2}$	High



**Figure 3 Schematic of tuned NMR circuit**

### 2.2.2 Transmission Line Theory

A transmission line is composed of concentric center conductor, dielectric layer, and outer conductor. Transmission lines have a characteristic impedance,  $Z_0$ , determined by the diameters of the inner ( $d_1$ ) and outer ( $d_2$ ) conductors and the relative permittivity of the dielectric ( $k_r$ ).

$$Z_0 = \frac{138}{\sqrt{k_r}} \log \frac{d_1}{d_2} \quad (4)$$

This characteristic impedance can also be described by the inductance and capacitance of a lossless line (Equation 5), or of a line incorporating resistances

(Equation 6). The red outline in Figure 4 encompasses the circuit diagram for a transmission line.

$$Z_0 = \sqrt{\frac{L}{C}} \quad (5)$$

$$Z_0 = \sqrt{\frac{R_1 + i2\pi\nu_0 L}{1/R_2 + i2\pi\nu_0 C}} \quad (6)$$

RF signals are transmitted in 50 Ohm impedance transmission lines. To maximize power transfer, the impedance of the source ( $Z_s$ , spectrometer) and load ( $Z_L$ , NMR probe) must match this 50 Ohm impedance of the transmission line ( $Z_0$ ). Unmatched lines will have standing waves.

### 2.2.3 Tuneless Probe Theory

A tuneless probe is constructed to mimic a 50 Ohm transmission line terminated with a 50 Ohm resistor. Figure 4 shows the circuit diagram for the transmission line and probe, highlighting the region of the probe circuit made to mimic that of the transmission line. There is no characteristic frequency in a tuneless probe.

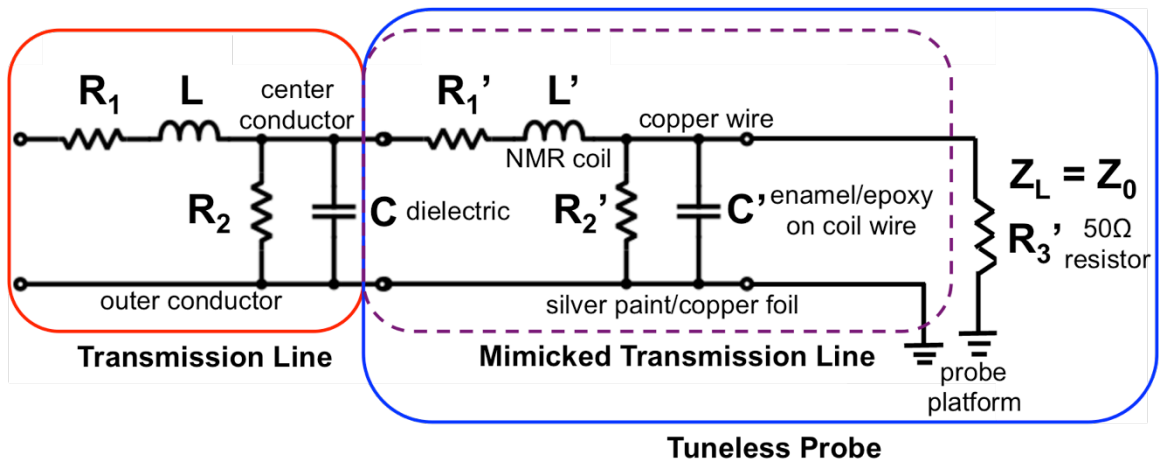


Figure 4 Circuit diagram for a transmission line and tuneless probe

### 2.2.1 Probe Construction

Figure 5 shows the homebuilt probe body and probe head used in this work <sup>1</sup>. The extended probe body is sized to place the probe head near the inflowing cryogen stream when top-loaded into the cryostat. The probe body consists of a 0.25" OD semi-rigid coaxial cable and two structurally supporting hollow aluminum tubes (0.25" OD, 0.18" ID) attached to supporting copper baffles by solder and epoxy, respectively. There is also a removable fiberglass rod linking the sample stage to an ex-situ goniometer mounted on the probe base.

The probe head is constructed from components listed in Table 2 following the procedures below.

### 2.2.1.1 Probe Head Construction Steps

#### Platform Construction

1. Solder platform to connector
2. Add temporary nuts and bolts to hold platform together while soldering additional components to platform
3. Cut copper strip from foil
4. Solder copper strip to platform
5. Solder resistor to platform

#### Coil Construction

6. Turn coil on form
7. Pull coil from both ends to make gap for optical access
8. Wrap coil in tape
9. Make epoxy by mixing equal parts by weight resin and curing agent
10. Coat coil with epoxy using toothpick
11. Remove excess epoxy by twisting clean NMR tube in coil
12. Dry overnight
13. Remove tape
14. Cut coil to desired height (most important for using goniometer platform)
15. Scrape enamel off coil ends using razor blade

#### Final Assembly

16. Solder coil to pin on SMA connector and to resistor tab
17. Attach copper strip to coil with silver paint
18. Continue adding silver paint until impedance is (relatively) constant 50 Ohms over frequency range of interest

Table 2 Components used in homebuilt tuneless probe construction

Probe Part	Component
SMA connector	Delta RF 1313-000-G051-500
Platform	Custom made (UCB CoC Machine Shop)
Enameled Coil Wire (22AWG)	Belden 8077
Epoxy	Equal parts Epon 828 Resin and Versamid 140 curing agent
Silver Paint	Electrodag 16040
Copper Foil	0.05 mm thick
Resistor	Component General Inc. CCT-375-1

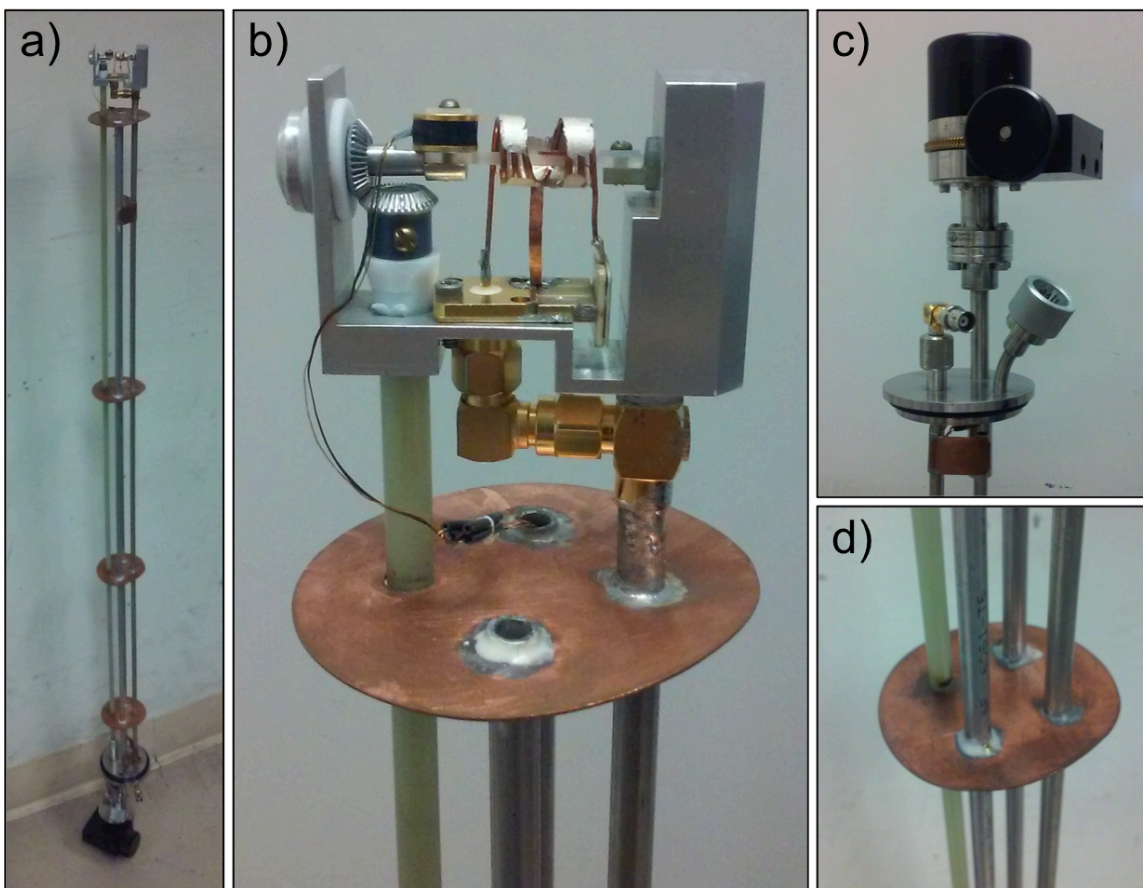


Figure 5 a) Full NMR probe body b) NMR probe head c) external goniometer adjustment, RF port, and temperature sensor port d) copper spacer showing soldering to coaxial cable and epoxy to aluminum rods

## 2.3 Temperature Control

A zirconium oxynitride temperature sensor (Lakeshore CX-1050-CU-HT) is fed through one of the aluminum tubes and mounted to the sample platform to measure the local temperature at the sample. A second temperature sensor is located on the inner wall of the cryostat vacuum jacket. The local sample temperature differs from that of the bulk volume when the laser illuminates the sample. Temperatures from both sensors are measured using two Oxford temperature controllers. Either temperature can be used to control the sample temperature through resistive heating in Kapton film heaters mounted to the inner wall of the vacuum jacket of the cryostat. In low temperature experiments, cryogen flow rate is adjusted manually using a needle valve in the cryogen transfer line. Flow rate is set to the minimum rate capable of stably maintaining the set temperature.

## 2.4 Lasers and Optics

Spin polarization is manipulated using a Viasho 532nm frequency-doubled Nd:YAG laser and a Coherent Innova 300 Ar+ laser (main line 488nm). Lasers are mounted

on an optics breadboard underneath the magnet. Mirrors guide the beam into the bore of the magnet. Alignment of the laser onto the sample is confirmed by observing red fluorescence coming off the illuminated diamond. Shuttering of the lasers is achieved through TTL switching within the laser driver itself (Viasho laser) or using a separate shutter (Coherent laser). These TTL switches are programmed directly into the NMR pulse sequence and controlled through the Tecmag spectrometer.

#### 2.4.1 Coherent Innova 300 Ar+ Laser Maintenance

The Coherent Innova 300 Ar+ laser was drastically underperforming at one point in this project. Maximum output power was 400mW, but the laser is rated to output as high as 5-6W. Maintenance was performed following directions in the manufacturer's manual, including: mirror alignment, mirror cleaning, Brewster window cleaning, and tube support adjustment. Figure 6 shows the laser output power as a function of current after maintenance in 2000, and before and after maintenance in 2015. Maintenance was able to restore laser output to 4W maximum power. Since this was sufficient for our needs, additional maintenance to achieve higher laser powers was not attempted.

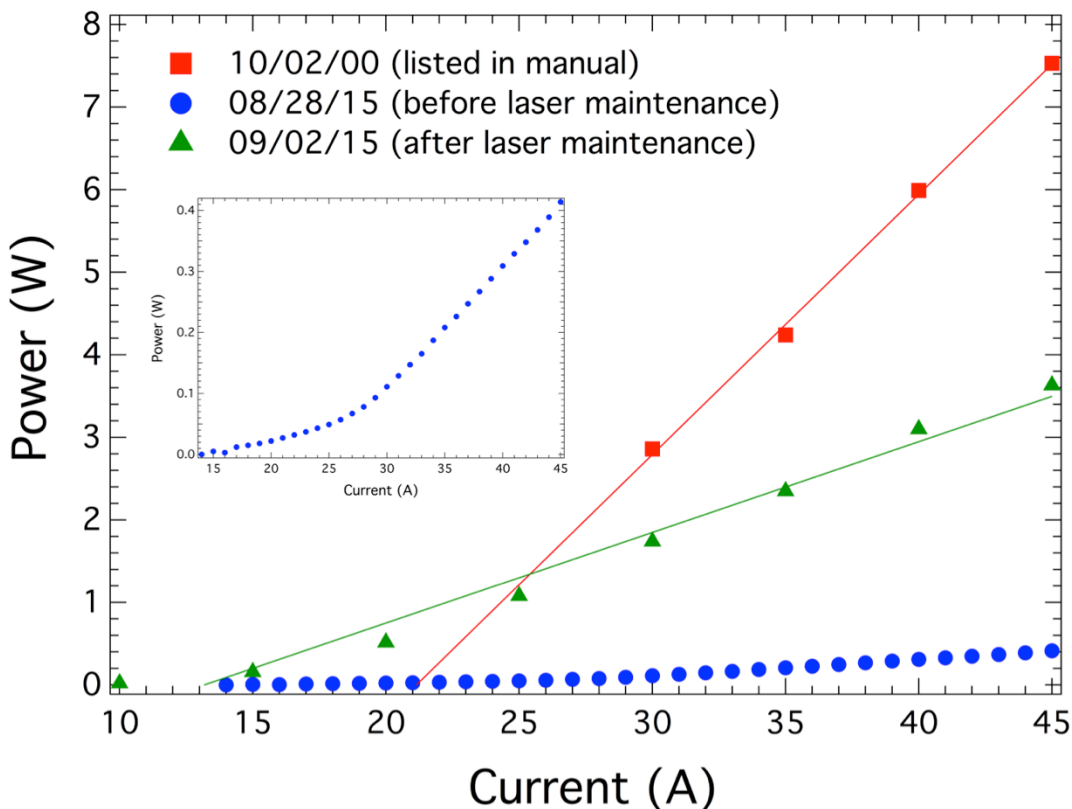


Figure 6 Ar+ laser output power after maintenance in 2000, and before and after maintenance in 2015. Inset is a blow up of the pre-maintenance power curve in 2015.

Figure 7 shows the Brewster windows after cleaning. The windows were cleaned using the hemostat and lens paper method described in the laser manual. Figure 8



shows the locations of the tube supports. Minor adjustments were performed, but did not have a significant effect on the output laser power. Figure 8 also shows the methods for defeating the safety interlocks so that the laser power could be tested during maintenance.

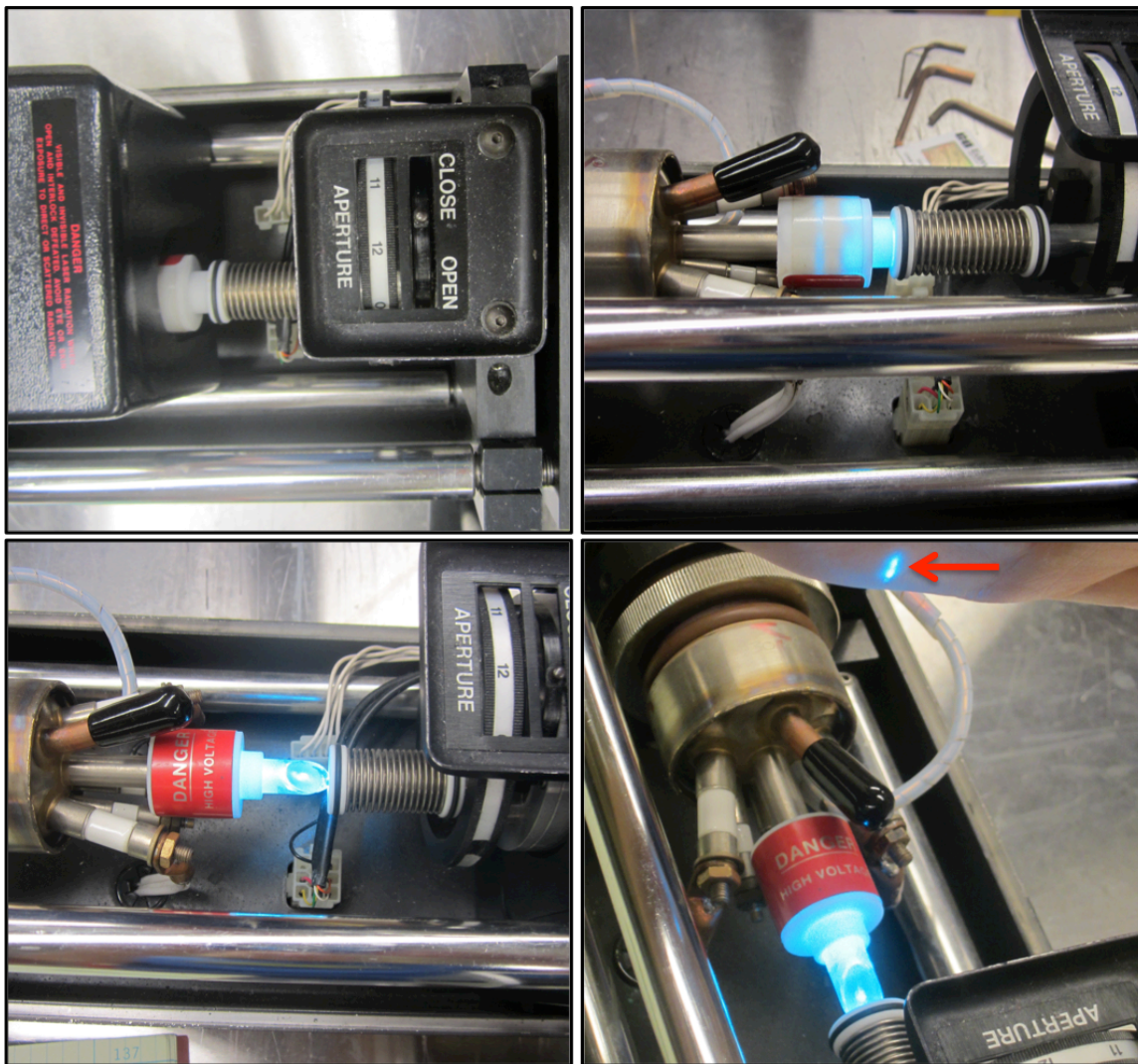


Figure 7: a) Laser head showing internal safety cover and closed bellows cover. b) Laser head without internal safety cover, laser on. c) Laser head with Brewster window exposed (bellows pulled back). d) Reflected beam spot from front Brewster window, emphasized by red arrow. Be vigilant of such reflections when working on the laser.

## 2.5 EPR Systems

EPR experiments in this work were performed on three instruments: an Active Spectrum X-band instrument in our lab, a Bruker X-band instrument in Songi Han's lab at UC Santa Barbara, and a 240GHz homebuilt instrument in the Institute for Terahertz Science and Technology (ITST) at UC Santa Barbara in collaboration with Mark Sherwin's lab.

## 2.6 Diamond Samples

Samples used in this work are synthetic high pressure, high temperature (HPHT) type Ib diamonds purchased from Element 6 and Sumitomo. All samples were irradiated with 1 MeV electrons at  $10^{18}$  cm<sup>-2</sup> fluence (Prism Gem LLC, Ionisos). Samples were annealed at 850°C for 2 hours, with the exception of Sample #1 which was annealed for 1 hour. Table 3 summarizes the vendors, dimensions, lattice orientations, and defect concentrations post-treatment. Defect concentrations were previously obtained using spin counting EPR <sup>2</sup>. Figure 9 shows photographs of the diamonds with labeled lattice orientations.

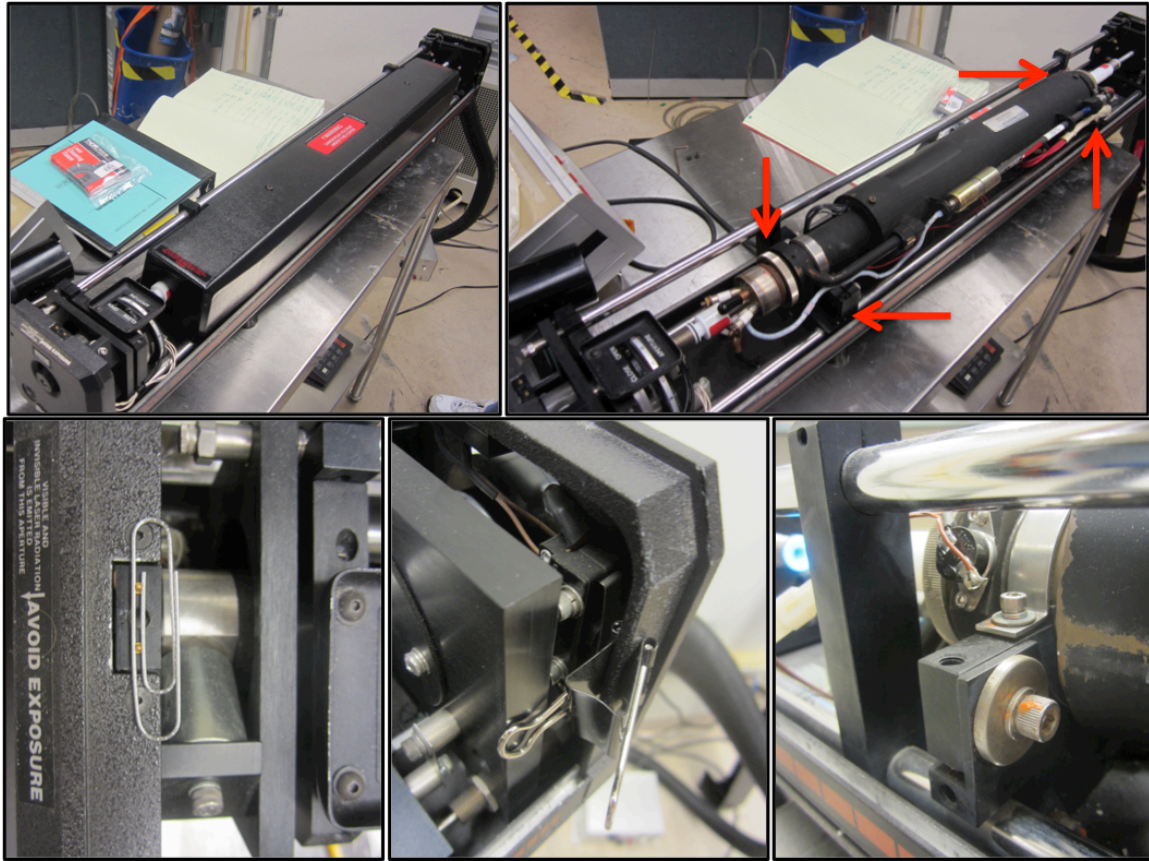


Figure 8: a) Laser with internal safety cover. b) Laser without safety cover, tube supports indicated by red arrows. c) Interlock defeat with a paperclip. d) Interlock defeat with a binder clip .e) Close-up of a tube support highlighted in b).

Table 3 Sample characteristics

Sample #	Vendor	Dimensions (mm)	Out of plane orientation	Edge orientation	Corner orientation	[NV-] (ppm)	[P1] (ppm)
1	Element 6	3.24 x 3.24 x 0.31	100	100	110	1.4 ± 0.2	17 ± 2
2	Element 6	3.23 x 3.24 x 0.31	100	110	100	1.9 ± 0.2	24 ± 3
3	Sumitomo	2.00 x 2.00 x 0.33	100	100	110	7.8 ± 1.0	71 ± 9
4	Sumitomo	2.01 x 2.02 x 0.35	100	100	110	6.9 ± 0.8	48 ± 6
5	Sumitomo	2.02 x 2.02 x 0.30	110	100, 110	-	7.3 ± 0.9	52 ± 6
6	Sumitomo	2.01 x 2.01 x 0.28	110	100, 110	-	8.7 ± 1.1	101 ± 12
7	Sumitomo	2.06 x 2.06 x 0.34	111	110, 112	-	4.2 ± 0.5	22 ± 3
8	Sumitomo	2.05 x 2.05 x 0.34	111	110, 112	-	6.7 ± 0.8	40 ± 5



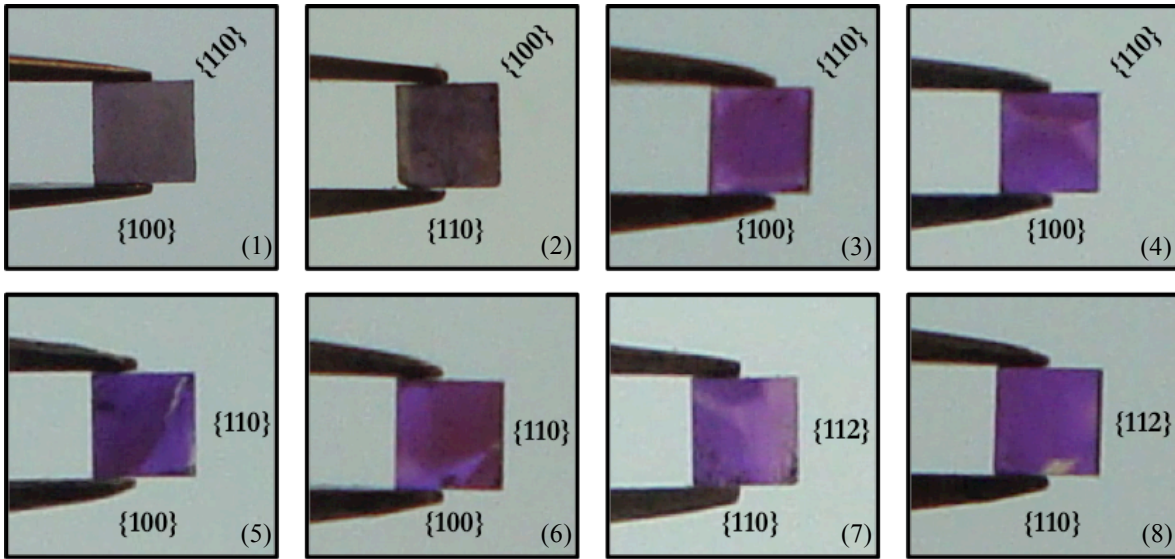


Figure 9 Photographs of diamond samples. Dimensions, orientations, and defect concentrations are listed in Table 3

## 2.7 Acknowledgements

Credit for the original design and construction of the probe goniometer goes to Dr. Eric Scott (former lab member) and Eric Granlund (College of Chemistry machine shop). I highly recommend reading Dr. Eric Scott's thesis for additional details on original probe designs and cryostat maintenance. Special thanks to Ralph Page for his help in performing the Ar+ laser maintenance described in Section 2.4.1 and for general discussions and guidance related to optics.

## 3 $^{13}\text{C}$ Polarization from Nitrogen Vacancy Centers at 9.4T

---

### 3.1 Abstract

Optically pumping NV- diamonds at high magnetic fields and low temperatures can generate  $^{13}\text{C}$  nuclear polarization without the assistance of microwaves. In certain diamonds,  $^{13}\text{C}$  polarization can be generated at room temperature as well. The sign and magnitude of the  $^{13}\text{C}$  polarization sensitively depends on the orientation of the diamond with respect to the directions of the applied magnetic field and laser polarization. The  $^{13}\text{C}$  polarization magnitude further depends on the defect concentrations, magnitude of the applied magnetic field, temperature, and the illumination conditions: wavelength, power, and exposure time.

### 3.2 Introduction

Nuclear spin polarization is a growing field aimed at increasing the capabilities of and applications for NMR and MRI. These nuclear spin based technologies are currently limited by their low sensitivity to thermal signals, especially for low-abundance nuclei such as  $^{13}\text{C}$ . In order to make a significant improvement in NMR sensitivity, the system must be put in a non-equilibrium state, also called a polarized or hyperpolarized state, with a non-Boltzmann distribution of spins.

As listed in Section 1.3 of Chapter 1, there are many methods for polarizing nuclear spins. Optical pumping NV- diamonds is a novel method of solid-state nuclear polarization that doesn't rely on angular momentum of light (as in traditional OPNMR), or microwaves (as in traditional DNP).

There have been many studies of nuclear polarization from NV- diamonds (Chapter 1, Section 1.4.5 and references therein), but the majority of these have focused on polarization at 1000G or 500G magnetic fields where a level anti-crossing occurs in the ground or excited state energy levels, respectively. These level anti-crossings lead to a well understood method of polarization transfer from the NV- defects to the  $^{13}\text{C}$  nuclei in the crystal lattice, but the relatively low magnetic fields cannot provide the superior resolution of high field NMR. Some groups have gotten around this issue by using complex shuttling systems to quickly transport the diamond from the stray field below a high field magnet (for polarization) up into the high field (for detection) <sup>1</sup>.

Here we present  $^{13}\text{C}$  polarization in diamonds generated and detected at 7.05T and 9.4T magnetic fields. We characterize the polarization dependence on defect concentration, field magnitude, and laser illumination wavelength, power, and exposure time. These findings provide important clues toward understanding the

underlying mechanism of  $^{13}\text{C}$  polarization, which is modeled in the following chapter.

### 3.3 Methods

NMR was used to measure  $^{13}\text{C}$  polarization in NV- imbedded diamonds at 9.4T and variable temperatures under laser illumination from a 532nm or Ar+ laser. In some experiments a 488nm filter was placed on the output of the Ar+ laser to isolate the effects of that wavelength. Variable temperature experiments were performed over a range of 10K to room temperature using an Oxford cryostat and liquid helium.

Figure 1 shows two NMR pulse sequences used in this work. The top row of the sequence represents the RF pulses applied, first a series of pulses to saturate any thermal signal, then a 90 degree pulse to put the magnetization into the plane of the NMR coil for detection. The signal is then acquired (indicated by the decaying oscillation). The bottom row of the sequence represents the timing of the laser illumination with respect to the NMR pulse sequence timing.

The sequence in Figure 1a was used to measure  $^{13}\text{C}$  NMR signal after a fixed laser illumination time,  $\tau_L$ . In polarization buildup experiments,  $\tau_L$  was varied over a series of measurements to track the timescale of  $^{13}\text{C}$  polarization buildup. The sequence shown in Figure 1b was used to measure the decay of  $^{13}\text{C}$  NMR signal after the laser illumination was turned off. In these experiments,  $\tau_L$  is set to a fixed time and  $\tau_D$  is varied over a series of measurements.

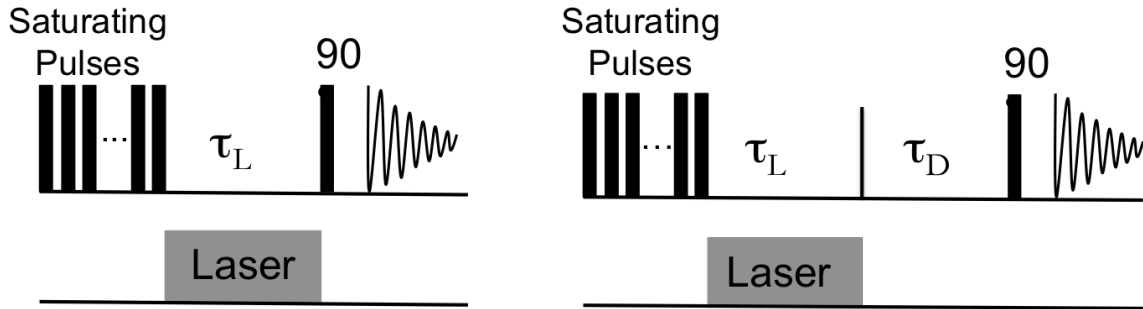


Figure 1 NMR pulse sequences for observing a) polarization buildup and b) polarization decay. Top line shows timing of RF pulses and acquisition. Bottom line shows timing of laser illumination.

The polarization buildup and decay data were fit to Equation 1 and 2, respectively, to extract the characteristic time for the dynamics,  $\tau$ .

$$S = M_Z \left(1 - e^{-\frac{t}{\tau}}\right) \quad (1)$$

$$S = M_Z \left(e^{-\frac{t}{\tau}}\right) \quad (2)$$

NMR signal is converted to a percent polarization by comparing the athermal  $^{13}\text{C}$  single crystal diamond signal with that of a thermal  $^{13}\text{C}$  signal from diamond powder. Ideally the single crystal diamond would serve as its own thermal signal comparison standard, but there are not enough spins in the samples to see thermal signal. Equation 3 is used to relate the thermal and athermal signals to determine percent polarization in the single crystals.

$$\% Pol_{crystal} = \frac{1}{2} \left( e^{-\frac{E_{-1/2}}{kT}} - e^{-\frac{E_{+1/2}}{kT}} \right) \frac{n_{powder} A_{crystal}}{n_{crystal} A_{powder}} 100\% \quad (3)$$

In Equation 3,  $n$  is the number of  $^{13}\text{C}$  spins in the measured sample,  $A$  is the integrated NMR peak area,  $k$  is Boltzmann's constant,  $T$  is temperature, and  $E_i$  is the energy for the  $i$  magnetic sublevel involved in the NMR transition of  $^{13}\text{C}$  in the diamond powder.  $E_i$  are defined in Equations 4 and 5, where  $\hbar$  is the reduced Planck's constant,  $\gamma$  is the gyromagnetic ratio for  $^{13}\text{C}$ , and  $B_0$  is the applied magnetic field strength.

$$E_{+1/2} = -\hbar\gamma B_0 \left( +\frac{1}{2} \right) \quad (4)$$

$$E_{-1/2} = -\hbar\gamma B_0 \left( -\frac{1}{2} \right) \quad (5)$$

The number of  $^{13}\text{C}$  spins in the diamond powder and in the single crystal were determined by measuring samples' weights and combining this information with the molecular weight of diamond and 1.1% natural abundance of  $^{13}\text{C}$ .

The diamond orientations were adjusted about two axes of rotation in orientation-dependence experiments. Changing the orientation of the diamond with respect to the applied magnetic field changes the orientation of the four NV defect directions as described in Appendix A. The two axes of rotation are 1) about the  $B_0$  field (z-axis), which is adjusted by mounting the diamonds with their edges at various angles with respect to the sapphire substrate edges, and 2) about the long-axis of the sapphire substrate (x-axis), which can be rotated in-situ using the goniometer described in Chapter 2.

### 3.4 Orientation Dependence

The sign and magnitude of  $^{13}\text{C}$  polarization was found to sensitively depend on crystal orientation with respect to the magnetic field and laser propagation axis <sup>2,3</sup>. Note that these axes are parallel in our NMR setup, so all effects shown here are convolutions of field-dependence and laser-dependence effects. Circularly polarized

light was used to minimize the laser-dependence effects, but polarization-dependent transmission prevents completely eliminating this effect (Appendix B).

Preliminary NMR experiments to isolate laser orientation effects are discussed in the Future Work section of Chapter 8. Orientation effects of the NV center's polarization with respect to a magnetic field were studied decoupled from the effects of laser orientation effects using X-band EPR (Chapter 7).

Figure 2 shows  $^{13}\text{C}$  polarization under 1W circularly polarized 532nm light at 20K and 7.05T and 9.4T in Sample #6 mounted at a 35 degree rotation about the z axis and tilted about the x-axis (see Appendix A for further description of rotations and tilts). From this figure, we see that 1) orientation dependence is independent of field strength and 2) that  $^{13}\text{C}$  polarization is larger at higher fields.

In certain orientations,  $^{13}\text{C}$  polarization inverts. Figure 3 shows data from Sample #2 at several orientations, the 25° tilt results in negative polarization. Extensive descriptions of further orientation-dependent experiments are published elsewhere <sup>2,3</sup>. Chapter 4 discusses a proposed model to explain this orientation dependence.

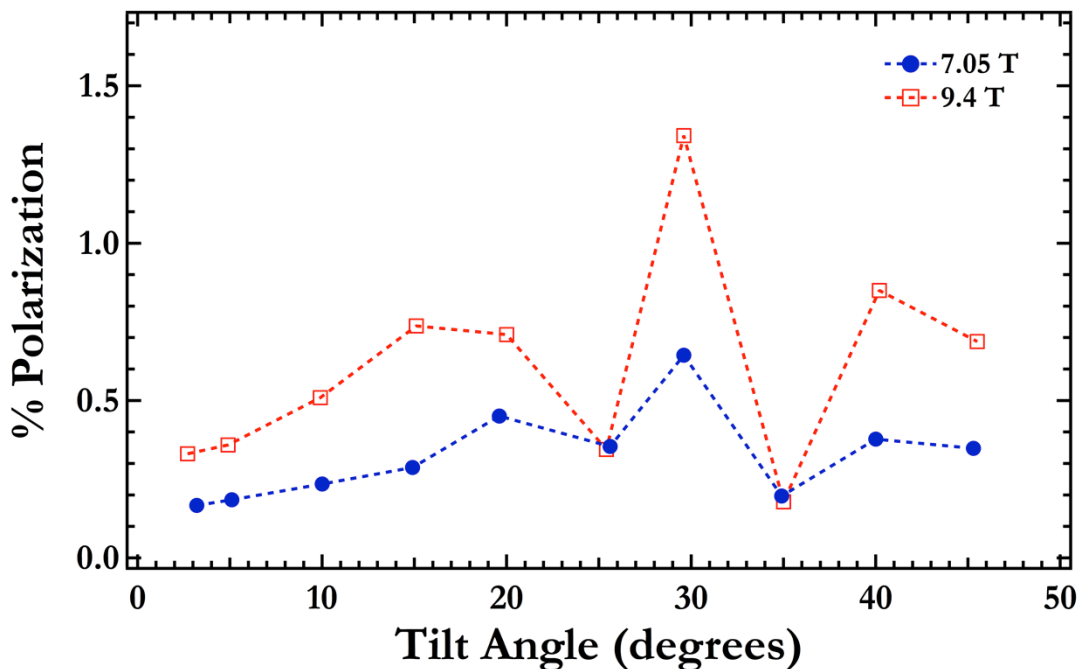


Figure 2  $^{13}\text{C}$  polarization in Sample #6 mounted at a 35° rotation taken under conditions of 20K and 7.05T (blue circles) and 9.4T (red open squares). 1W circularly polarized 532nm laser illumination.

### 3.5 Time Dependence

$^{13}\text{C}$  polarization builds up under laser illumination over a timescale of minutes depending on the laser power and sample concentration. This polarization also

decays exponentially after the laser has been turned off. The time constants defining this  $^{13}\text{C}$  buildup and decay are independent of the diamond orientation, even if that orientation changes the sign of the resulting polarization (Figure 3, Table 1).

**Table 1**  $^{13}\text{C}$  polarization buildup time constants for Sample #2 fits shown in Figure 3

Tilt Angle	Time Constant (min)
7.3°	20.2 ± 0.9
9.7°	19.5 ± 3.2
15.3°	17.1 ± 0.6
23.9°	18.1 ± 2.1
31.4°	22.3 ± 2.3

Buildup and decay times were measured at 20K and 1W 532nm laser illumination in all samples at 7.05T and 9.4T. Figure 4 shows the characteristic times as a function of defect concentration. Exact times and errors are listed in Table 2. Errors in 9.4T time constants are from repeat measurements (Figures 5 and 6) and fit errors. Errors in 7.05T time constants are from fit errors <sup>3</sup>. It is expected that polarization buildup will only depend on the source of polarization (NV-) and that polarization decay will depend on both NV- and P1 centers, as both act as paramagnetic sources for  $^{13}\text{C}$  relaxation when the laser is turned off.

We see no significant difference in time constants at 7T or 9.4T, except for Sample #1 and Sample #2. The  $^{13}\text{C}$  polarization buildup times are shorter and decay times longer at 7T than 9.4T for these samples. The origin of this difference being unique to Sample #1 and #2 is unknown. Future work should seek to understand any differences in diamond quality between the Element 6 (Sample # 1,2) and Sumitomo (Sample #3-8) vendors. Figures 5 and 6 show the individual buildup and decay curves and fits to Equation 1 and 2 from which the 9.4T time constants in Figure 4 were extracted. Curves and fits for the 7.05T data can be found elsewhere <sup>2,3</sup>.

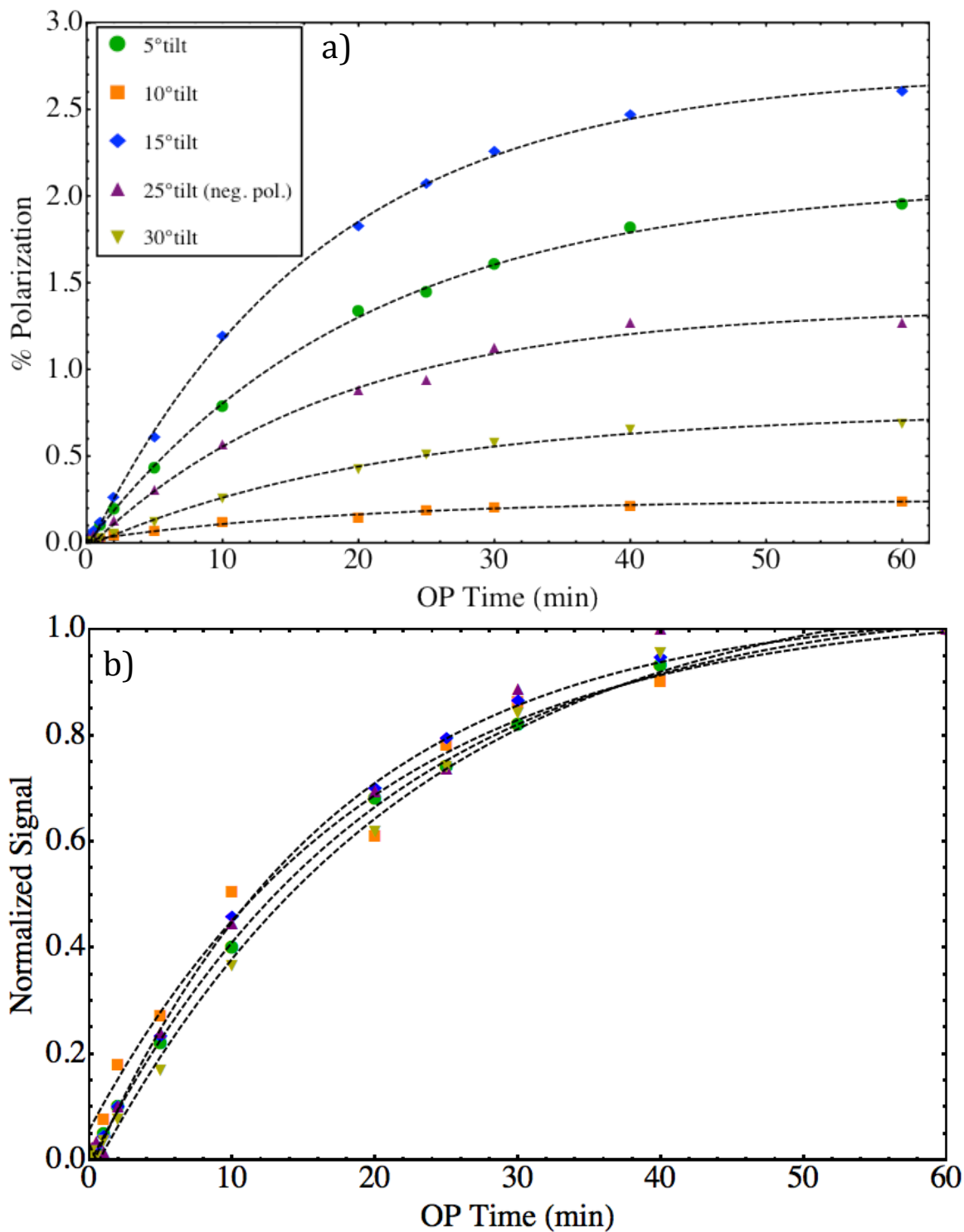


Figure 3  $^{13}\text{C}$  polarization buildup in Sample #2 at 9.4T, 20K, 1W 532nm light as a function of diamond tilt angle with respect to the applied magnetic field. a)  $^{13}\text{C}$  polarization b) normalized signal. 25° tilt data has negative polarization, but plotted positive for better visual comparison to other data.

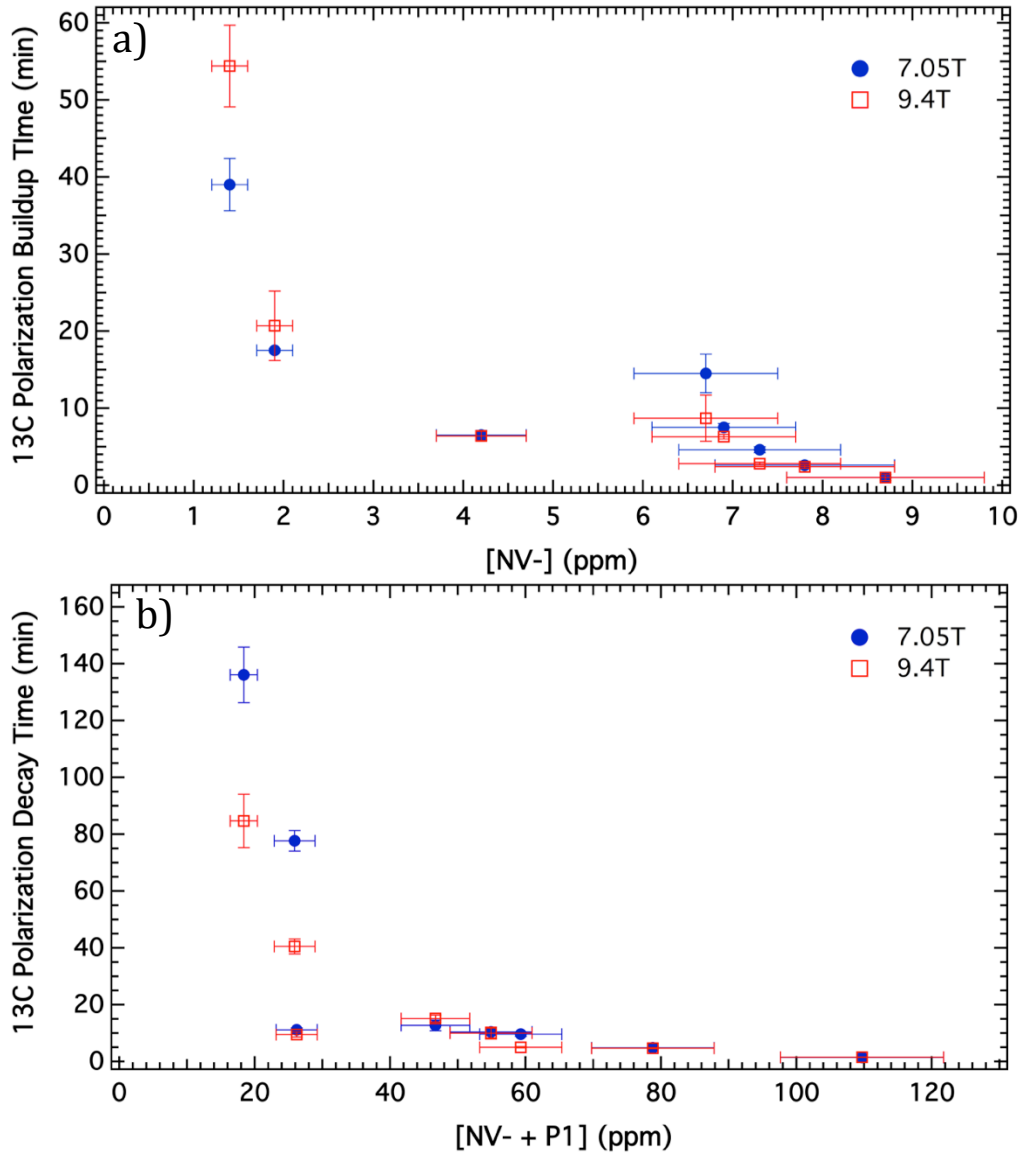


Figure 4 a)  $^{13}\text{C}$  polarization buildup time constants as a function of NV- concentration. b)  $^{13}\text{C}$  polarization decay time constant as a function of combined NV- and P1 concentration

Table 2  $^{13}\text{C}$  polarization buildup and decay time constants at 7.05T and 9.4T and defect concentrations

Sample	[NV-] (ppm)	[P1] (ppm)	7.05T		9.4T	
			Buildup time (min)	Decay time (min)	Buildup time (min)	Decay time (min)
1	$1.4 \pm 0.2$	$17 \pm 2$	$39.0 \pm 3.4$	$136.1 \pm 9.8$	$54.4 \pm 5.3$	$84.7 \pm 9.4$
2	$1.9 \pm 0.2$	$24 \pm 3$	$17.5 \pm 0.2$	$77.7 \pm 3.6$	$20.7 \pm 4.5$	$40.5 \pm 2.6$
3	$7.8 \pm 1.0$	$71 \pm 9$	$2.6 \pm 0.3$	$4.8 \pm 0.4$	$2.4 \pm 0.2$	$4.7 \pm 0.2$
4	$6.9 \pm 0.8$	$48 \pm 6$	$7.5 \pm 0.5$	$10.4 \pm 0.7$	$6.3 \pm 0.3$	$10.0 \pm 2.1$
5	$7.3 \pm 0.9$	$52 \pm 6$	$4.6 \pm 0.4$	$9.6 \pm 0.8$	$2.8 \pm 0.2$	$5.0 \pm 0.2$
6	$8.7 \pm 1.1$	$101 \pm 12$	$1.0 \pm 0.1$	$1.4 \pm 0.1$	$1.0 \pm 0.4$	$1.5 \pm 0.1$
7	$4.2 \pm 0.5$	$22 \pm 3$	$6.5 \pm 0.6$	$11.1 \pm 0.7$	$6.4 \pm 0.6$	$9.5 \pm 0.9$
8	$6.7 \pm 0.8$	$40 \pm 5$	$14.5 \pm 2.5$	$12.7 \pm 1.9$	$8.7 \pm 3.0$	$15.1 \pm 1.2$



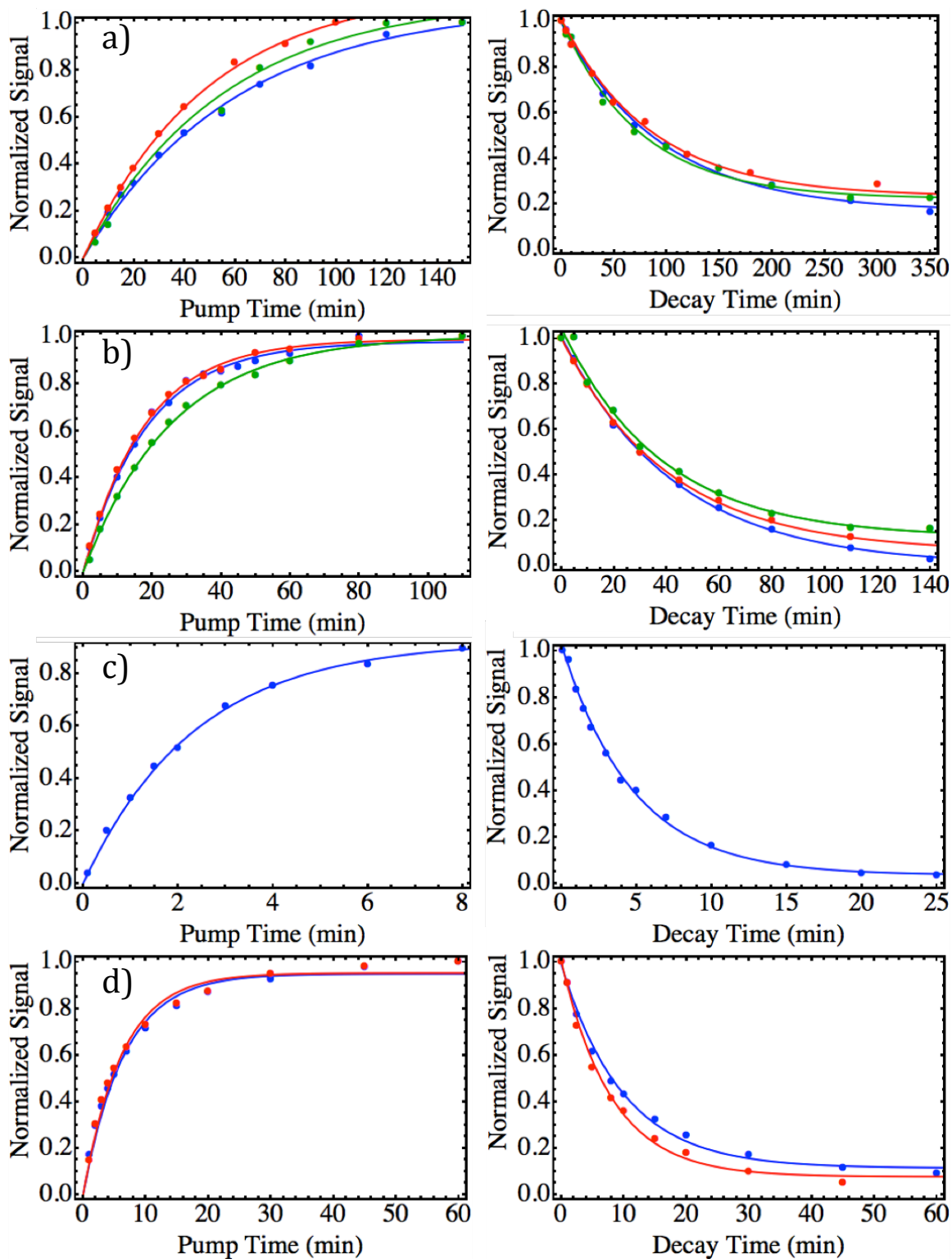


Figure 5 9.4T, 20K, 1W 532nm light  $^{13}\text{C}$  polarization buildup and decay data (dots) and fits to exponential functions (lines) for a) Sample #1, b) Sample #2, c) Sample #3, d) Sample #4. Repeat measurements shown for Samples #1, #2, and #4.

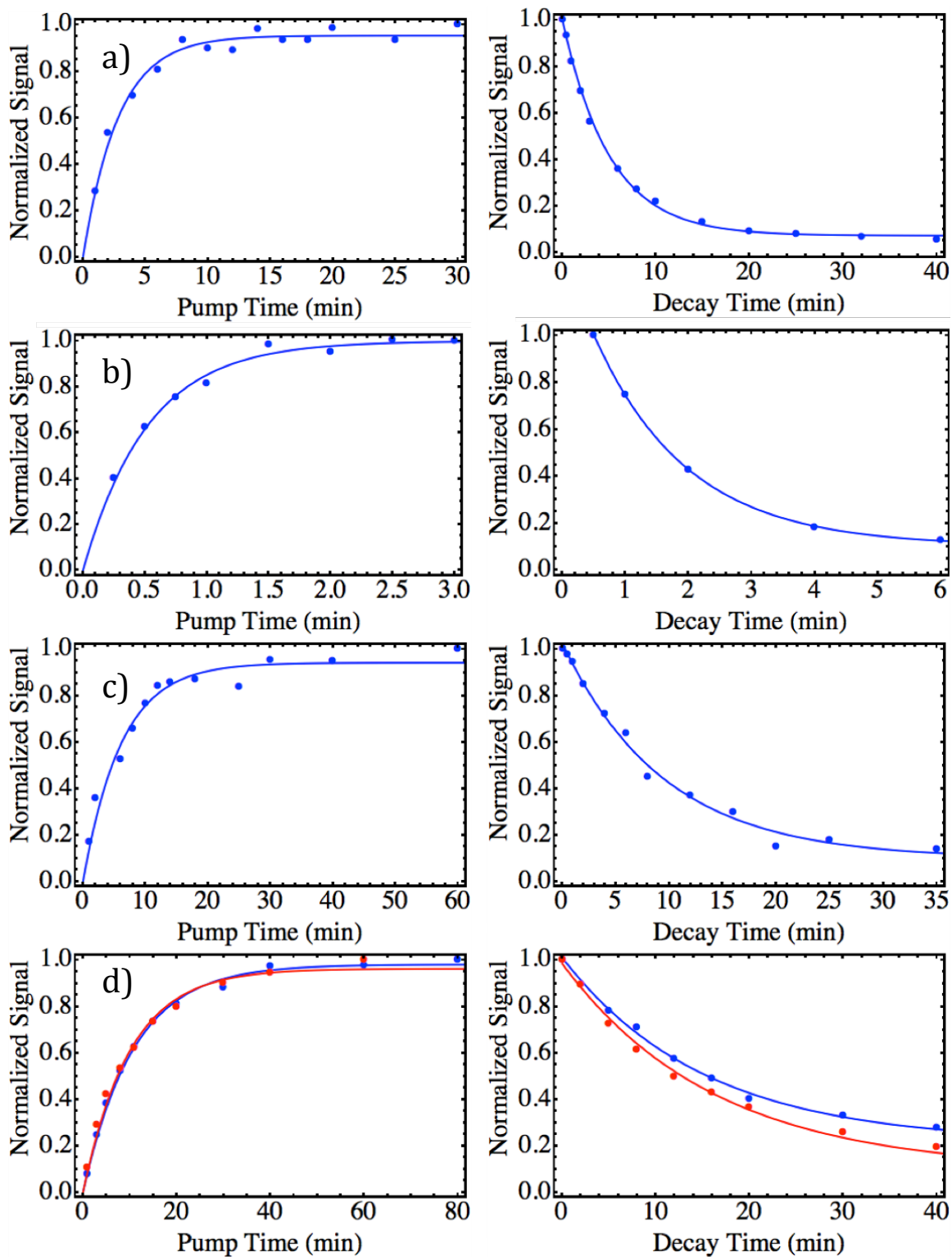


Figure 6 9.4T, 20K, 1W 532nm light  $^{13}\text{C}$  polarization buildup and decay data (dots) and fits to exponential functions (lines) for a) Sample #5, b) Sample #6, c) Sample #7, d) Sample #8. Repeat measurements shown for Sample #8.

### 3.6 Laser Wavelength Dependence

Laser wavelength has been shown to influence the NV- population <sup>4</sup>, with maximum populations roughly plateauing over a range of 490nm to 560nm. The influence of laser wavelength on <sup>13</sup>C polarization between 488nm, 532nm, and a full Ar+ laser spectral output (13 wavelengths 351.1 – 1092.3 nm) are shown in Figure 7 for Sample #2 at 175mW laser illumination, 9.4T, and 15K. The <sup>13</sup>C polarization buildup time constants are listed in Table 3. The buildup time constant varies on the order of 40% between 488nm and 532nm laser illumination experiments. Based on the literature, we expect a difference of about 4% in NV- population between 488nm and 532nm illuminations (estimated from 0.73 (488nm) and 0.76 (532nm) NV-populations in <sup>4</sup>). The origin of the significant difference in laser wavelength is unknown and warrants further study when additional laser wavelengths become available to the lab.

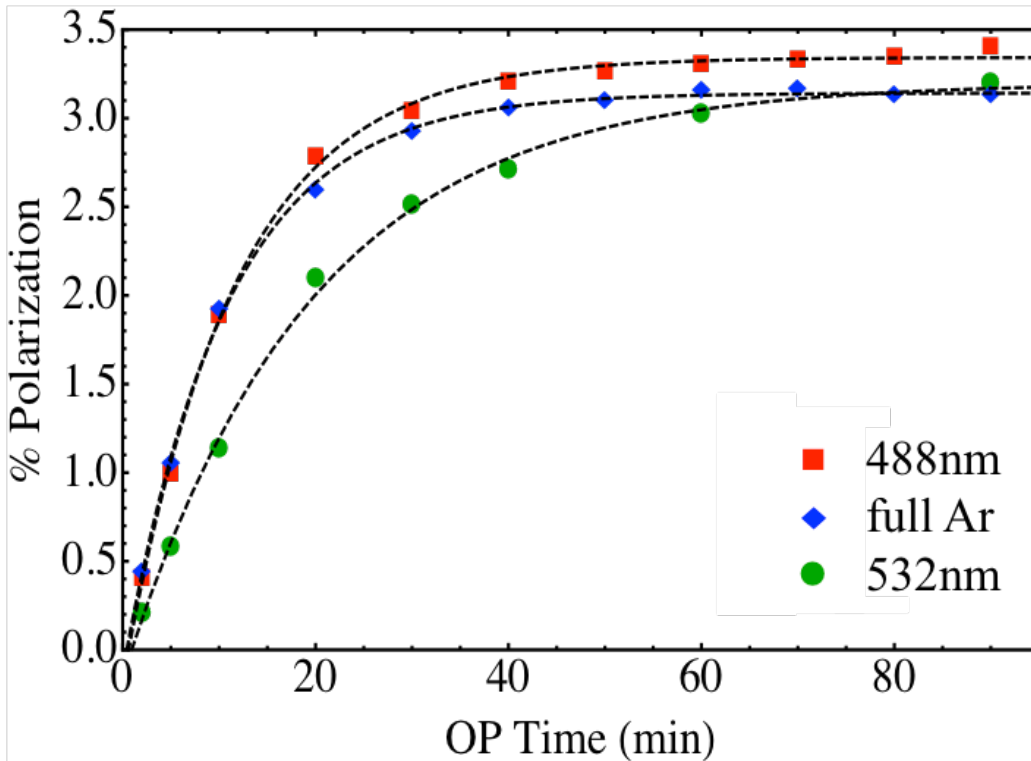


Figure 7 Wavelength dependence of <sup>13</sup>C polarization buildup curves in Sample #2. Measured at 9.4T, 15K, and 175mW of 488nm (red square), full Ar+ (blue diamond), and 532nm (green circle) laser illumination.

Table 3 <sup>13</sup>C polarization buildup time constants for Sample #2 at 9.4T, 15K, and 175mW laser power

Laser Wavelength	<sup>13</sup> C Polarization Buildup Time Constant (min)
532nm	19.4 ± 1.2
488 nm	11.5 ± 0.4
Full Ar+ laser spectrum	10.7 ± 0.3

### 3.7 Temperature Dependence

$^{13}\text{C}$  polarization increases exponentially with decreasing temperature <sup>3,5</sup>. Figure 8 shows  $^{13}\text{C}$  polarization in Sample #2 at 9.4T after 10 minutes of 532nm illumination at various cryogenic temperatures. Temperature dependence of polarization can be fit to Equation 6, where  $T$  is temperature in Kelvin.

$$Pol = 2.48e^{-.032T} \quad (6)$$

Samples #1 and #2 are able to sustain  $^{13}\text{C}$  polarization at 7.05 and 9.4T and room temperature <sup>2</sup>. In these experiments, room temperature has to be maintained with a low flow of cold nitrogen gas to prevent significant heating from the laser. Room temperature polarization in Sample #1 mounted at a 45 degree rotation and 27 degree tilt with 1W of 532nm laser illumination for 1 hour at 9.4T is 0.017%. Room temperature polarization at 7.05T has been extensively characterized elsewhere <sup>2</sup>.

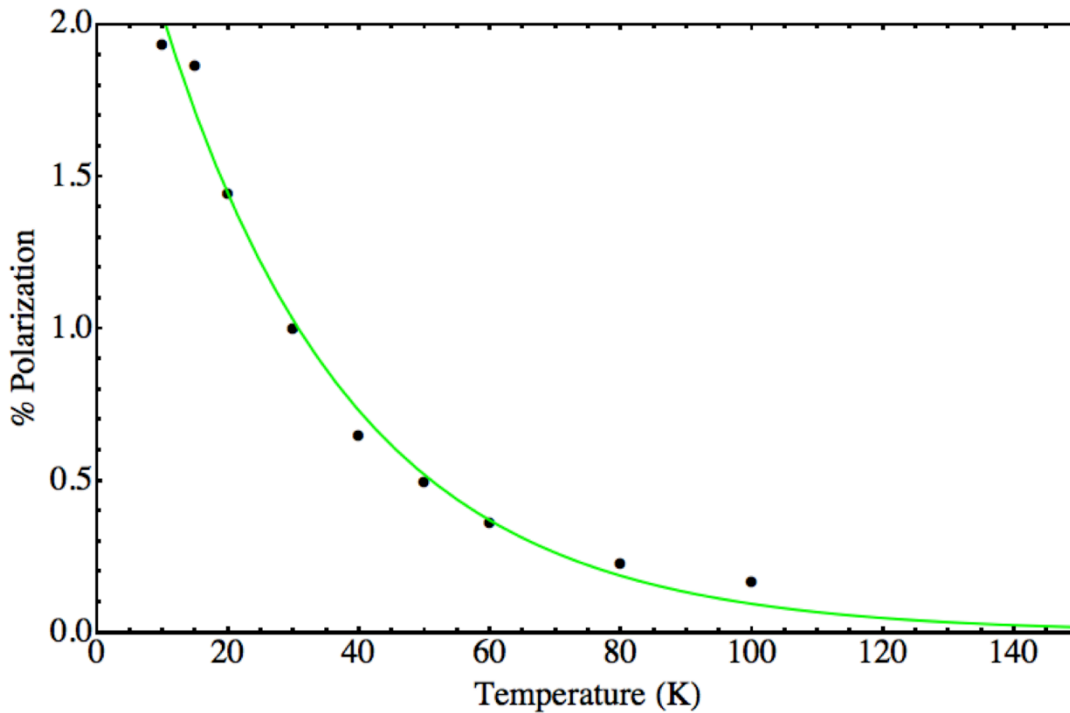


Figure 8  $^{13}\text{C}$  polarization in Sample #2 at 9.4T after 10 minutes of 250mW, 532nm laser illumination at various cryogenic temperatures (black dots) fit to an exponential decay (green line) given in Equation 6.

### 3.8 Conclusion

We have presented  $^{13}\text{C}$  polarization in NV- diamonds under laser illumination at 7.05T and 9.4T at various temperatures. Polarization builds up over a period of minutes at 20K with 1W of 532nm laser illumination, and persists for the same order of magnitude after the laser has been turned off. Polarization builds up faster in diamonds with higher NV- concentration, but also decays faster with higher total defect concentrations. Laser wavelength was also found to have a significant effect

on the polarization buildup time, with 488nm light generating  $^{13}\text{C}$  polarization faster than 532nm light. The sign and magnitude of  $^{13}\text{C}$  polarization is sensitively dependent on crystal orientation with respect to the field, and shows the same orientation dependence at 7.05T and 9.4T.  $^{13}\text{C}$  polarization is highest at low temperatures, but can persist to room temperature in samples with the lowest defect concentrations.

### **3.9 Acknowledgements**

Thank you to Dr. Eric Scott for his close collaboration on this work, and to Dr. Jonathan King for helpful discussions.

# 4 Orientation-Dependent Two-Spin Cross Relaxation Model of NV-Mediated $^{13}\text{C}$ Polarization in Diamond at High Magnetic Fields

---

## 4.1 Abstract

The mechanism for observed  $^{13}\text{C}$  polarization in NV-imbibed diamonds under laser illumination at high magnetic fields (7.05T, 9.4T) is unknown. Here we model the polarization of a NV-NV dipolar coupled reservoir at 7.05T under laser illumination and find that there are orientation-dependent energy matching conditions with  $^{13}\text{C}$  which could explain experimentally observed  $^{13}\text{C}$  polarization. The model qualitatively captures the existence of  $^{13}\text{C}$  polarization, its positive and negative sign changes with crystal orientation, and the acute nature of the orientation sensitivity. Quantitative agreement with experimental data requires further model refinement.

## 4.2 Introduction

Negatively charged nitrogen vacancy electronic defects in diamond are polarized through a known intersystem crossing mechanism upon irradiation by 532nm light <sup>1</sup>. We propose a nuclear polarization mechanism in diamond by which pairs of dipolar coupled, polarized NV- centers transfer polarization to a nearby  $^{13}\text{C}$  spin if the dipolar coupled NV- centers have energy level transitions that match those of the  $^{13}\text{C}$  spin <sup>2</sup>. Nuclear spin diffusion then spreads this local  $^{13}\text{C}$  polarization throughout the bulk of the crystal. NV- polarization, and therefore local  $^{13}\text{C}$  polarization, is replenished through continuous illumination by a laser.

## 4.3 Dipolar Coupled NV-NV Polarization Model

The Hamiltonian for a system of NV- electronic spins and  $^{13}\text{C}$  nuclear spins can be broken into three parts: NV-only interactions ( $H_S$ ),  $^{13}\text{C}$ -only interactions ( $H_I$ ), and electron-nuclear interactions ( $H_{IS}$ ).

$$H = H_S + H_{IS} + H_I \tag{1}$$

We model the NV-only interactions to probe the sign and magnitude of the resulting dipolar coupled spin reservoir as a function of orientation relative to a parallel magnetic field and laser propagation axis. The polarization of the dipolar coupled NV- spin reservoir serves as a proxy for the expected  $^{13}\text{C}$  polarization.

### 4.3.1 Hamiltonian

The dipolar coupled NV reservoir consisting of two spin-1 electrons has the following Hamiltonian:

$$H_S = \omega_S(S_{Z1} + S_{Z2}) + D_1 \left( S_Z^2 - \frac{S(S+1)}{3} \right) + D_2 \left( S_Z^2 - \frac{S(S+1)}{3} \right) + AS_{Z1}S_{Z2} - \frac{1}{4}A(S_{1+}S_{2-} + S_{1-}S_{2+}) + E_1(S_{1+}^2 + S_{1-}^2) + E_2(S_{2+}^2 + S_{2-}^2) \quad (2)$$

The Hamiltonian consists of a Zeeman ( $\omega_S$ ), Zero Field Splitting (D), and Strain (E) interaction for each of the NV- centers in the dipolar coupled pair, as well as a Dipolar Coupling term (A) describing their interaction. Subscripts 1 and 2 indicate the two NV defects in the pair. All terms must be represented in the same reference frame. We choose to put everything into the lab frame, which we define as having a z-axis parallel to the applied magnetic field  $B_0$ . The Zeeman term interaction, which is two orders of magnitude larger than the other terms, is therefore already in the correct frame. However, the zero field splitting and crystal strain terms are represented in the defect frame and need to be put into the lab frame.

We first represent the terms as spherical tensor operators ( $\hat{T}_\mu^{(\omega)}$ ), where  $\omega$  is the rank of the tensor. We then determine the Wigner Rotation ( $D_{q\mu}^{(\omega)}$ ) needed to transform the tensor into the new basis, which is defined by the relationship<sup>3,4</sup>:

$$R\hat{T}_\mu^{(\omega)}R^{-1} = \sum_{q=-\omega}^{\omega} D_{q\mu}^{(\omega)}T_q^{(\omega)} \quad (3)$$

We use the secular approximation that  $q=0$  because only  $T_0^{(2)}$  commutes with the Zeeman term. Both the zero field splitting and crystal strain terms are rank 2. Based on the change in angular momentum induced by the spin operators, it is easy to see that the zero field splitting and crystal strain terms belong to  $\mu=0$  and  $\mu=\pm 2$ , respectively.

$$D \left( S_Z^2 - \frac{S(S+1)}{3} \right) \rightarrow D \left( \hat{T}_0^{(2)} \right) \quad (4)$$

$$R\hat{T}_0^{(2)}R^{-1} = \sum_{q=-2}^2 D_{q0}^{(2)}T_q^{(2)} = D_{00}^{(2)}T_0^{(2)} = \left( \frac{3\cos^2\gamma-1}{2} \right) T_0^{(2)} \quad (5)$$

$$E(S_+^2 + S_-^2) \rightarrow E \left( \hat{T}_{\pm 2}^{(2)} \right) \quad (6)$$

$$R\hat{T}_{\pm 2}^{(2)}R^{-1} = \sum_{q=-2}^2 D_{q\pm 2}^{(2)}T_q^{(2)} = D_{0\pm 2}^{(2)}T_0^{(2)} = \left( \sqrt{\frac{3}{8}} \sin^2\gamma \right) T_0^{(2)} \quad (7)$$

The zero field splitting term in the lab frame is:

$$D \left( \frac{3\cos^2\gamma-1}{2} \right) \left( S_Z^2 - \frac{S(S+1)}{3} \right) \quad (8)$$

And the crystal strain term in the lab frame is:

$$E \left( \sqrt{\frac{3}{8}} \sin^2 \gamma \right) (S_+^2 + S_-^2) \quad (9)$$

The Hamiltonian is a function of each defect's orientation - within the applied magnetic field (in the case of the ZFS term and crystal strain term) and with respect to the position of its coupled partner (in the case of the Dipolar Coupling term). We keep only the dipolar coupling terms that commute with the Zeeman Hamiltonian ( $\Delta S=0$ ), meaning we ignore the crystal strain term and nonsecular dipolar coupling terms. This leaves us with two orientation-dependent terms:

$$D_i = 2870 \text{MHz} \frac{3 \cos^2 \gamma_i - 1}{2} \quad (10)$$

$$A = \frac{\mu_0}{4\pi} \hbar \gamma_{NV}^2 \frac{1}{r^3} \text{MHz} (1 - 3 \cos^2 \theta) \quad (11)$$

Here the subscript  $i$  indexes the paired NV- centers. Given that in a single crystal diamond there are four unique axes along which an NV- can be directed, there are 16 pairwise combinations of NV- defects which each have their own unique Hamiltonian for a given crystal orientation within the applied magnetic field.  $\gamma$  indicates the angle between an NV- defect axis and the applied magnetic field axis.  $r$  refers to the distance between a dipolar coupled pair of NV- centers, and  $\theta$  refers to the angle between a line connecting the two coupled NV- centers and the applied magnetic field (Figure 1). In our model, the dipolar coupling parameter  $A$  is left as a variable and not broken down to its dependence on  $r$  and  $\theta$ .

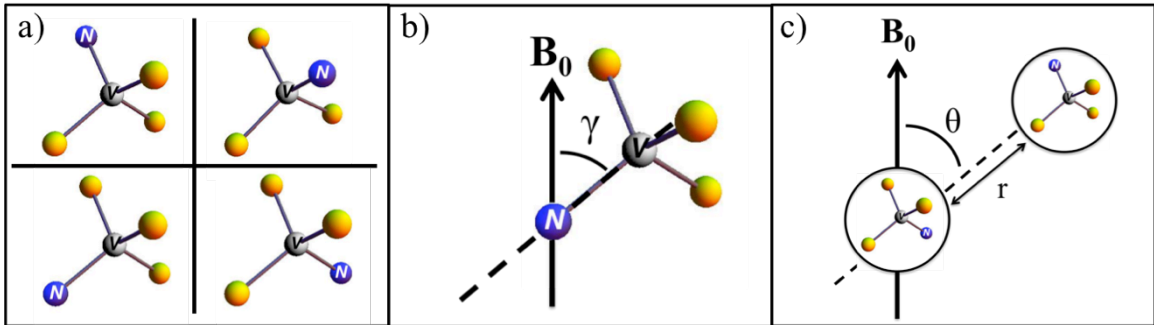


Figure 1 a) Illustration of the four reservoirs of NV center orientations present in diamonds with a large ensemble of defects. b) Definition of  $\gamma_j$ , where  $j$  indicates one of the four defect orientations represented in a), as the angle between a single NV center axis and the magnetic field. c)  $r$  and  $\theta$  are defined as the distance between two defects and the angle between the magnetic field and a vector connecting the two defects, respectively. The two dipolar coupled defects may each have any of the four orientations shown in a), leading to 16 pairwise combinations.

The nine dipolar-coupled NV- reservoir basis vectors for two spin-1 electrons in the Zeeman basis are listed in Table 1, where  $S_{Z1}$  and  $S_{Z2}$  refer to the spin of each individual NV center, and  $S_z$  represents the spin order of the pair.



$$S_Z = S_{Z1} + S_{Z2} \quad (12)$$

The Hamiltonian in Equation 2 can be represented as a 9x9 Hamiltonian matrix (Equation 14), with elements defined by the inner product with the basis states (Equation 13).

$$\langle S_{Z1}, S_{Z2} | H_S | S_{Z1}, S_{Z2} \rangle \quad (13)$$

**Table 1 9 Basis States for NV-NV Coupled System**

Total $S_z$	Basis Vector $ S_{Z1}, S_{Z2}\rangle$
+2	$ +1,+1\rangle$
+1	$ +1,0\rangle,  0,+1\rangle$
0	$ +1,-1\rangle,  0,0\rangle,  -1,+1\rangle$
-1	$ -1,0\rangle,  0,-1\rangle$
-2	$ -1,-1\rangle$

$$H_S = \begin{pmatrix} 2\omega_S + D_1 + D_2 + A & 0 & 0 & 0 & 0 & 0 & 0 & 0 & 0 \\ 0 & \omega_S + D_1 & -\frac{A}{2} & 0 & 0 & 0 & 0 & 0 & 0 \\ 0 & -\frac{A}{2} & \omega_S + D_2 & 0 & 0 & 0 & 0 & 0 & 0 \\ 0 & 0 & 0 & D_1 + D_2 - A & -\frac{A}{2} & 0 & 0 & 0 & 0 \\ 0 & 0 & 0 & -\frac{A}{2} & 0 & -\frac{A}{2} & 0 & 0 & 0 \\ 0 & 0 & 0 & 0 & -\frac{A}{2} & D_1 + D_2 - A & 0 & 0 & 0 \\ 0 & 0 & 0 & 0 & 0 & 0 & -\omega_S + D_1 & -\frac{A}{2} & 0 \\ 0 & 0 & 0 & 0 & 0 & 0 & -\frac{A}{2} & -\omega_S + D_2 & 0 \\ 0 & 0 & 0 & 0 & 0 & 0 & 0 & 0 & -2\omega_S + D_1 + D_2 + A \end{pmatrix} \quad (14)$$

### 4.3.2 Eigenstates

Diagonalizing  $H_S$  gives 9 energy levels for each of the 16 NV dipolar reservoirs, distinguished by their individual  $D_{ij}$  pairs. Within each 9-energy manifold, only transitions for which  $\Delta S_Z = 0$  may participate in nuclear spin transitions because the large Zeeman energy of an individual NV defect (198GHz at 7.05T) cannot induce a  $^{13}\text{C}$  spin transition (75MHz) at 7.05T. The eigenstates for this system are:

$$|1\rangle = \frac{1}{\sqrt{2}} ( -|+1,-1\rangle + |-1,+1\rangle ) \quad (15)$$

$$|2\rangle = \frac{1}{N_2} ( |+1,-1\rangle - \beta|0,0\rangle + |-1,+1\rangle ) \quad (16)$$

$$|3\rangle = \frac{1}{N_3} ( |+1,-1\rangle - \alpha|0,0\rangle + |-1,+1\rangle ) \quad (17)$$

$$|4\rangle = |-1,-1\rangle \quad (18)$$

$$|5\rangle = \frac{1}{N_4} (-\gamma|-1,0\rangle + |0,-1\rangle) \quad (19)$$

$$|6\rangle = \frac{1}{N_5} (-\delta|-1,0\rangle + |0,-1\rangle) \quad (20)$$

$$|7\rangle = |+1,+1\rangle \quad (21)$$

$$|8\rangle = \frac{1}{N_4} (-\gamma|+1,0\rangle + |0,+1\rangle) \quad (22)$$

$$|9\rangle = \frac{1}{N_5} (-\delta|+1,0\rangle + |0,+1\rangle) \quad (23)$$

where,

$$\alpha = \frac{A-D_1-D_2+\sqrt{2A^2+(D_1+D_2-A)^2}}{A} \quad (24)$$

$$\beta = \frac{A-D_1-D_2-\sqrt{2A^2+(D_1+D_2-A)^2}}{A} \quad (25)$$

$$\gamma = \frac{D_1-D_2-\sqrt{A^2+(D_1-D_2)^2}}{A} \quad (26)$$

$$\delta = \frac{D_1-D_2+\sqrt{A^2+(D_1-D_2)^2}}{A} \quad (27)$$

$$N_2 = \frac{1}{\sqrt{2+|\beta|^2}} \quad (28)$$

$$N_3 = \frac{1}{\sqrt{2+|\alpha|^2}} \quad (29)$$

$$N_4 = \frac{1}{\sqrt{2+|\gamma|^2}} \quad (30)$$

$$N_5 = \frac{1}{\sqrt{2+|\delta|^2}} \quad (31)$$

$\Delta S=0$  transitions occur between states within the  $S_z = 0$  manifolds (states  $|1\rangle$  through  $|3\rangle$ ) and between states within the  $S_z = \pm 1$  manifolds (states  $|5\rangle$ ,  $|6\rangle$  and  $|8\rangle$ ,  $|9\rangle$ ).

### 4.3.3 Eigenenergies

The energies corresponding to the above eigenstates are listed below. Our lab's previous model simplified the energy levels based on an order of magnitude argument that  $D_1+D_2 \gg A^2$ . While this held true for the crystal orientation studied in that paper, it cannot be generalized to other orientations and we must work with the full forms of all energy levels when studying orientation-dependence.

$$E_1 = -A + D_1 + D_2 \quad (32)$$

$$E_2 = \frac{1}{4} \left( -2A - \sqrt{8A^2 + (-2A + 2D_1 + 2D_2)^2} + 2D_1 + 2D_2 \right) \quad (33)$$

$$E_3 = \frac{1}{4} \left( -2A + \sqrt{8A^2 + (-2A + 2D_1 + 2D_2)^2} + 2D_1 + 2D_2 \right) \quad (34)$$

$$E_4 = A + D_1 + D_2 - 2\omega_{NV} \quad (35)$$

$$E_5 = \frac{1}{2} \left( D_1 + D_2 - \sqrt{A^2 + (D_1 - D_2)^2} \right) - 2\omega_{NV} \quad (36)$$

$$E_6 = \frac{1}{2} \left( 2D_1 + 2D_2 + \sqrt{A^2 + (D_1 - D_2)^2} \right) - 2\omega_{NV} \quad (37)$$

$$E_7 = A + D_1 + D_2 + 2\omega_{NV} \quad (38)$$

$$E_8 = \frac{1}{2} \left( 2D_1 + 2D_2 - \sqrt{A^2 + (D_1 - D_2)^2} \right) + 2\omega_{NV} \quad (39)$$

$$E_9 = \frac{1}{2} \left( 2D_1 + 2D_2 + \sqrt{A^2 + (D_1 - D_2)^2} \right) + 2\omega_{NV} \quad (40)$$

### 4.3.4 Populations

The model incorporates the defect-frame populations for individual NV centers, which can be measured by comparing dark and illuminated EPR spectra (Chapter 7). In Equation 41,  $\rho_{NV}$  is the density matrix for an NV- center aligned with  $B_0$  in the defect reference frame.  $P_0$  is the  $m_s=0$  population of the NV- center, as determined by the methods described in Chapter 7 ( $P_0 \sim 0.4-0.5$ ). The populations of  $m_s=\pm 1$  were found to be equal at all orientations <sup>5</sup>.

$$\rho_{NV} = \begin{pmatrix} \sqrt{\frac{1-P_0}{2}} & 0 & 0 \\ 0 & \sqrt{P_0} & 0 \\ 0 & 0 & \sqrt{\frac{1-P_0}{2}} \end{pmatrix} \quad (41)$$

The NV center density matrix is brought into the lab frame using the Wigner rotation matrix for a spin-1 system,  $D^1$  (Equation 51), as described in Appendix C <sup>4</sup>.

$$d_{1,1}^1 = \frac{1+\cos\gamma}{2} \quad (42)$$

$$d_{1,0}^1 = -\frac{\sin\gamma}{\sqrt{2}} \quad (43)$$

$$d_{1,-1}^1 = \frac{1-\cos\gamma}{2} \quad (44)$$

$$d_{0,1}^1 = \frac{\sin\gamma}{\sqrt{2}} \quad (45)$$

$$d_{0,0}^1 = \cos\gamma \quad (46)$$

$$d_{0,-1}^1 = -\frac{\sin\gamma}{\sqrt{2}} \quad (47)$$

$$d_{-1,1}^1 = \frac{1-\cos\gamma}{2} \quad (48)$$

$$d_{-1,0}^1 = \frac{\sin\gamma}{\sqrt{2}} \quad (49)$$

$$d_{-1,-1}^1 = \frac{1+\cos\gamma}{2} \quad (50)$$

$$D^1 = \begin{pmatrix} d_{1,1}^1 & d_{0,1}^1 & d_{-1,1}^1 \\ d_{1,0}^1 & d_{0,0}^1 & d_{-1,0}^1 \\ d_{1,-1}^1 & d_{0,-1}^1 & d_{-1,-1}^1 \end{pmatrix} \quad (51)$$

Here we rename  $\rho_{NV}$  as  $\rho_1^{\text{defect}}$ , the *1* index for future differentiation between two NV centers involved in a dipolar pair, and the *defect* index to denote reference frame. See Appendix C for a full derivation of the ensemble density matrix (shown here) from individual defects.

$$\rho_1^{lab} = D^1 \rho_1^{defect} (D^1)^T \quad (52)$$

The populations in the lab frame for individual NV centers are then described by Equations 53-55 and plotted as a function of  $P_0$  in Figure 3.

$$P_{+1}^{lab} = (d_{1,1}^1)^2 \left( \sqrt{\frac{1-P_0}{2}} \right)^2 + (d_{0,1}^1)^2 (\sqrt{P_0})^2 + (d_{-1,1}^1)^2 \left( \sqrt{\frac{1-P_0}{2}} \right)^2 \quad (53)$$

$$P_0^{lab} = (d_{1,0}^1)^2 \left( \sqrt{\frac{1-P_0}{2}} \right)^2 + (d_{0,0}^1)^2 (\sqrt{P_0})^2 + (d_{-1,0}^1)^2 \left( \sqrt{\frac{1-P_0}{2}} \right)^2 \quad (54)$$

$$P_{-1}^{lab} = (d_{1,-1}^1)^2 \left( \sqrt{\frac{1-P_0}{2}} \right)^2 + (d_{0,-1}^1)^2 (\sqrt{P_0})^2 + (d_{-1,-1}^1)^2 \left( \sqrt{\frac{1-P_0}{2}} \right)^2 \quad (55)$$

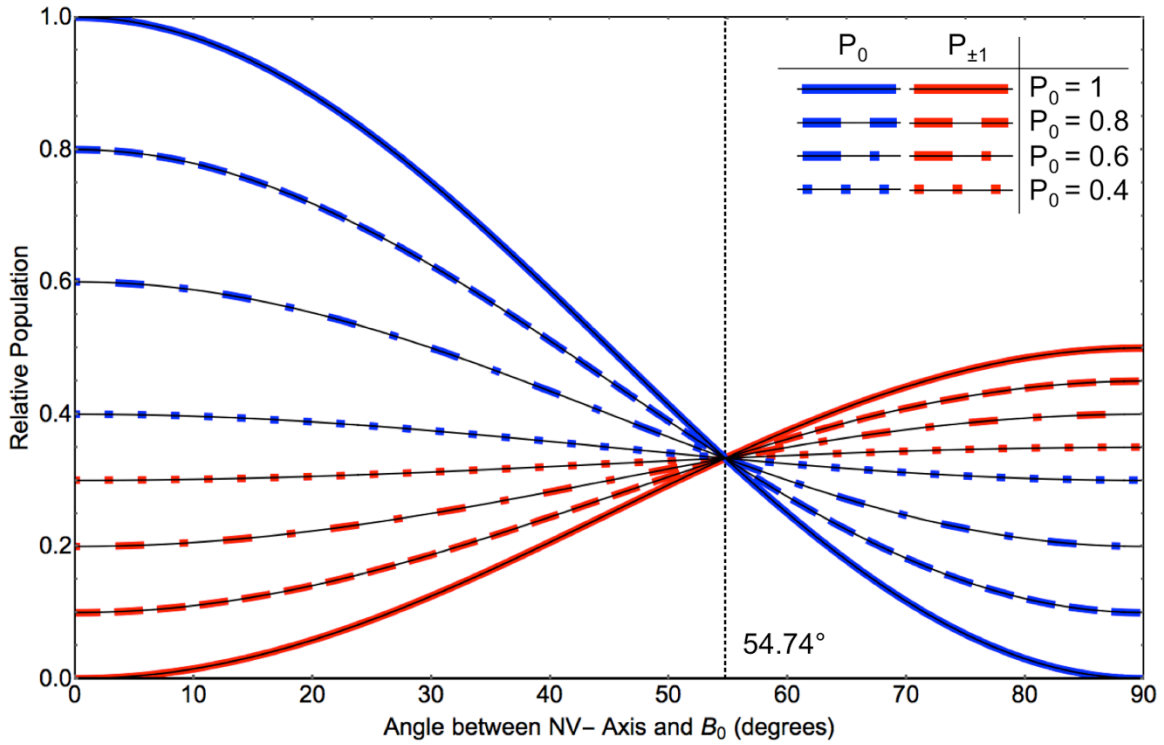


Figure 2 Modeled NV polarization as a function of defect angle with respect to  $B_0$ . Plotted for various  $P_0$  values. See Chapter 7 for experimental confirmation of the model.

Applying these Wigner rotations allots various amounts of defect frame polarization into the  $S_z = 0$  and  $S_z = \pm 1$  manifolds in the lab frame. Therefore, dipolar transitions which induce nuclear spin transitions can be between any pair of states within the  $S_z = 0$  manifold as well as transitions within the  $S_z = \pm 1$  manifolds. These latter transitions were not accounted for in the previous model, which assumed all polarization was propagated into the  $|S_{z,1}, S_{z,2}\rangle = |0,0\rangle$  lab-frame dipolar state <sup>2</sup>. The populations of each lab-frame state can be found by taking the

diagonals of the Kroenecker product of these lab-frame density matrices, where  $i$  in Equation 53 refers to one of the eigenstates listed above.

$$P_i = \langle i | \rho_1^{lab} \otimes \rho_2^{lab} | i \rangle \quad (53)$$

The populations will be orientation-dependent in accordance with the orientation dependence of the eigenstates and the Wigner rotation matrices.

#### 4.3.5 Nuclear Polarization

Transitions within the NV-NV dipolar reservoir will only lead to nuclear polarization if the difference between energy levels is energy conserving with nuclear spin transitions. The sign and magnitude of the nuclear polarization are assumed to track that of the NV-NV reservoir polarization when these energy-conserving conditions are met. We therefore seek to model the sign and magnitude of the NV-NV reservoir polarization as a function of sample orientation.

To do this, we solve for the dipolar coupling value,  $A$ , which gives an NV-NV reservoir energy capable of inducing  $^{13}\text{C}$  transitions at 7.05T ( $\pm 75\text{MHz}$ ). We then apply a Lorentzian distribution (Equation 54) with a width equal to the NV center X-band EPR line width ( $\delta \sim 15\text{MHz}$ ) to weight the  $A$  values based on the probability of that interaction strength existing in the system. We weight the NV-NV reservoir polarization by this Lorentzian distribution.

$$L(A_{\pm}) = \frac{\delta}{\pi(\delta^2 + A_{\pm}^2)} \quad (54)$$

We also weight the polarization by the relative light absorption for the dipolar NV pair,  $\alpha_k$ , taken as an average of the light absorption for each individual NV center based on its orientation relative to the laser propagation axis, parallel to  $B_0$ ). See Appendix B for a full description of  $\alpha$  under the circular polarization experimental conditions modeled here.

Finally, we sum over all 16 energy reservoirs distinguished by their  $D_{ij}$  pairs (Equation 55). The subscript of  $A$  denotes whether it satisfies a positive or negative energy difference ( $\Delta E(A_{\pm}) = \pm 75\text{MHz}$ ). The Kronecker delta function is solved when its argument equals 0, so  $\delta(\Delta E + 75)$  is solved when  $\Delta E = -75$ .

$$Pol_{NV-NV,weighted} = \sum_{k=1}^{16} L(A_{\mp}) \delta(\Delta E(A_{\mp}) \pm 75\text{MHz}) (\%Pol(A_{\mp})) \alpha_k \quad (55)$$

The polarization of the spin-conserving transitions within the  $S_z = 0$  and  $S_z = \pm 1$  manifolds are calculated using Equation 56, where the  $(i,j)$  indices correspond to the eigenstates in Equations 15-23. Figure 3 illustrates how the sign of polarization associated with  $A_{\pm}$  are determined. These manifest in the positive and negative coefficients in front of the two polarization terms in Equation 56.

$$\%Pol(A) = \sum_{(i,j)=(1,2),(1,3),(2,3),(4,5),(6,7)} \left( \frac{P_i(A_-) - P_j(A_-)}{P_i(A_-) + P_j(A_-)} \right) - \left( \frac{P_i(A_+) - P_j(A_+)}{P_i(A_+) + P_j(A_+)} \right) \quad (56)$$

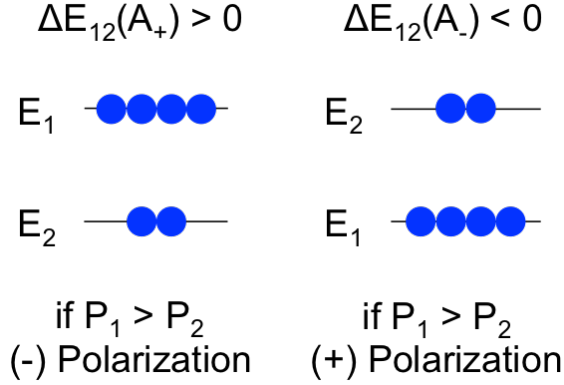


Figure 3 Illustration of the sign of dipolar coupled NV polarization depending on the sign of the energy difference that matches a nuclear transition ( $\Delta E_{ij}$ ) and the relative populations of the two levels involved in the transition ( $P_i, P_j$ ).

#### 4.4 Model Results

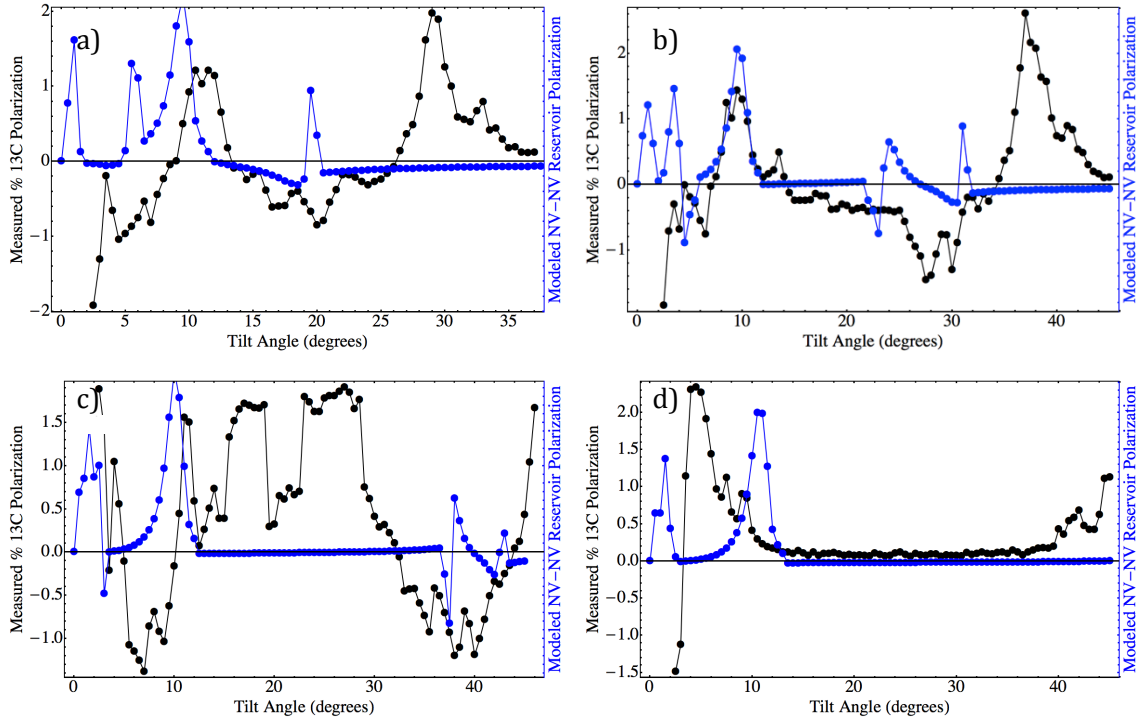
Figure 4 compares model results for weighted dipolar coupled NV-NV polarization under conditions of 75MHz transitions (Equation 55) to high-resolution ( $0.5^\circ$  tilt increments)  $^{13}\text{C}$  NMR polarization in Sample #2 taken at 7.05T and 20K after 25 minutes of 1W 532nm illumination. High-resolution data is available for mounted positions of  $5^\circ, 10^\circ, 15^\circ,$  and  $20^\circ$  rotations as defined in Appendix A <sup>6</sup>.

Model results qualitatively capture 1) the presence of NV-NV dipolar reservoir polarization with 75MHz transitions at 7.05T, 2) the ability to achieve both positive and negative polarization as a function of crystal orientation, and 3) the acuteness of the orientation sensitivity. However, as seen in Figure 4, the model results do not quantitatively match the  $^{13}\text{C}$  polarization profile as a function of crystal tilt angle.

Figures 5 and 6 shows the five energy transitions for each of the 16 pairwise combinations of NV defects for the  $10^\circ$  rotation results shown in Figure 4b. Transitions are labeled with subscripts matching the eigenstates listed in Equations 15 – 23. Figure 5 shows the transitions when the diamond is tilted  $1^\circ$  (resulting in positive polarization in Figure 4b). Figure 6 shows the transitions when the diamond is tilted  $15^\circ$  (resulting in zero polarization in Figure 4b). Dipolar coupling values for which an energy transition matches the  $\pm 75\text{MHz}$  condition (shown as a black dashed line in Figures 5 and 6) solve the Kronecker delta function in Equation 55.

Figure 5a and 6a show the Lorentzian distribution used to weight the likelihood of the dipolar coupling value existing between two NV defects in the sample. The blue

curves were used in the model results shown in Figure 4. The red, green, and yellow curves are discussed in the following section.

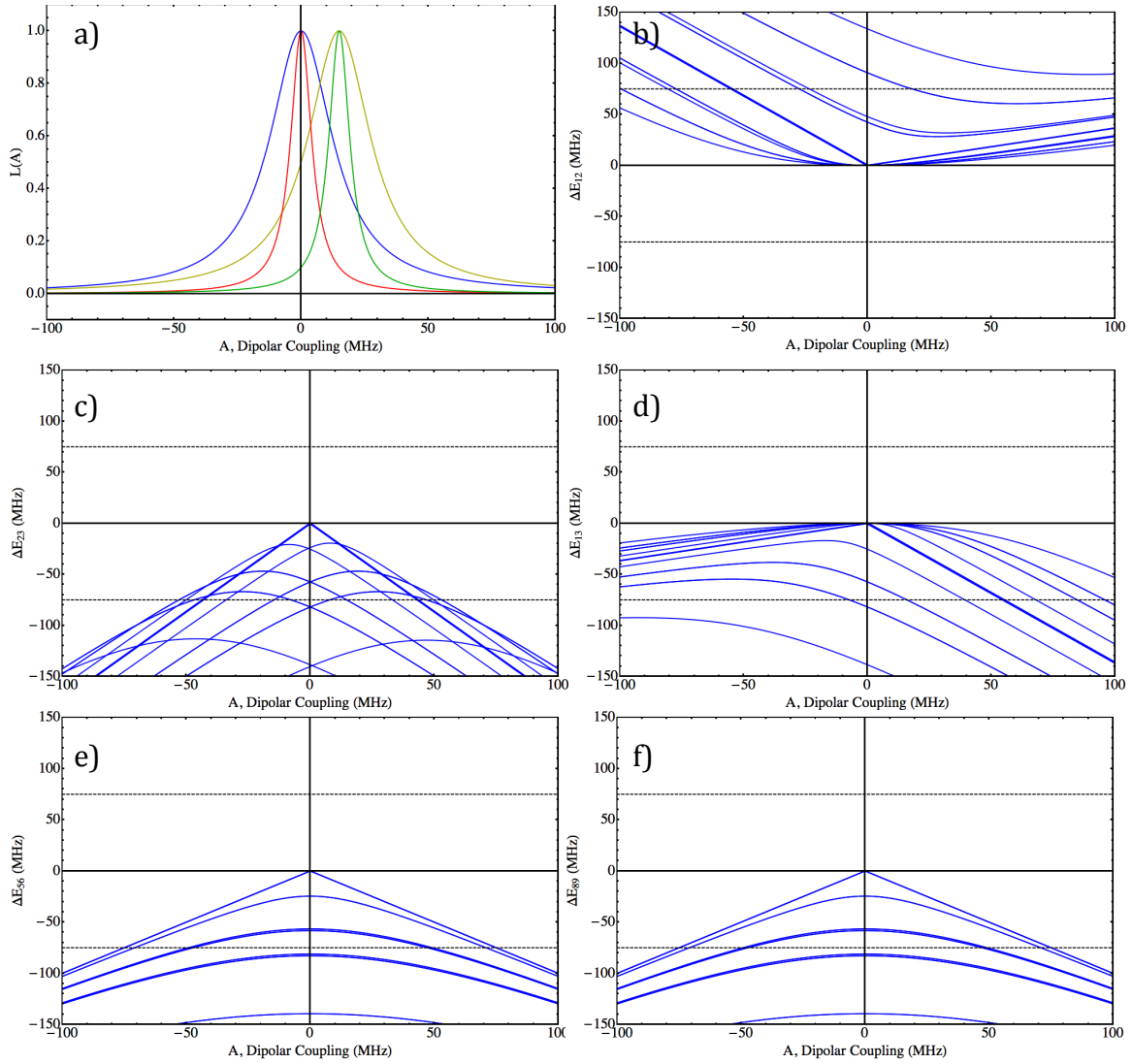


**Figure 4** Model results in arbitrary units (blue) overlaid with measured  $^{13}\text{C}$  polarization (black) for Sample #2 at 7.05T, 20K 1W 532nm illumination for 25 minutes mounted at a rotation of a)  $5^\circ$ , b)  $10^\circ$ , c)  $15^\circ$ , d)  $20^\circ$ . Model used 15 MHz dipolar coupling distribution width centered at 0MHz with a nuclear transition matching condition of 75MHz.

#### 4.4.1 Sensitivity to Model Parameters

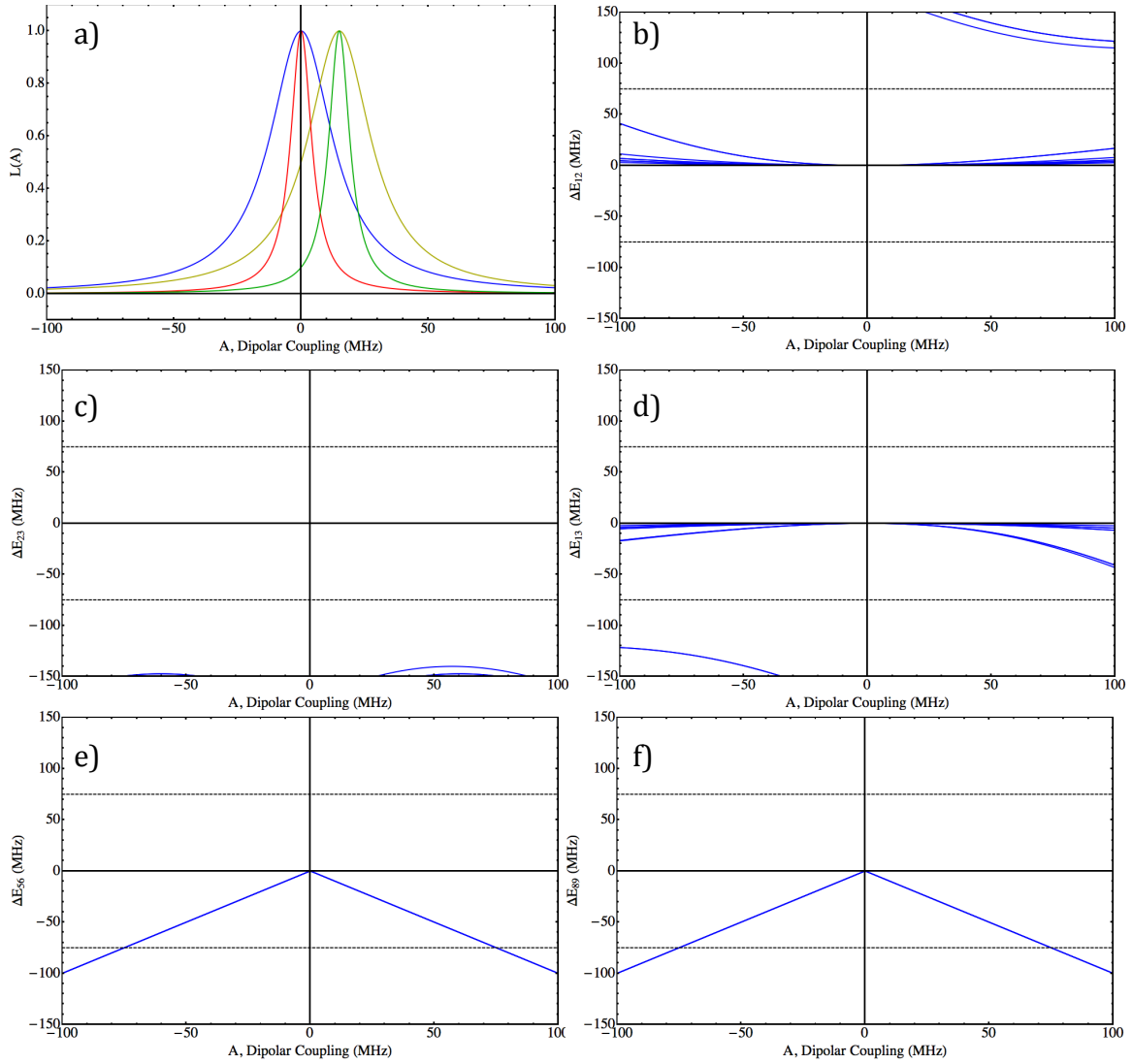
Figure 7 illustrates model's sensitivity to the Lorentzian distribution used to weight the dipolar coupling strengths. Figure 7 model results correspond to the like-colored Lorentzian distributions shown in Figures 5a and 6a. Figure 7a is the same  $10^\circ$  rotation model result shown in Figure 4b, which used a Lorentzian distribution centered at 0MHz with a width of 15MHz. The low tilt angles are extremely sensitive to the Lorentzian distribution, but higher tilt angles are less sensitive. In general, the Lorentzian distribution does not affect which tilt angle regions result in zero predicted polarizations.

Figure 8 illustrates the model's sensitivity to the energy transition matching frequency, showing model results for the  $10^\circ$  rotation case shown in Figure 4b solved for energy matching frequencies of 30MHz, 50MHz, 75MHz (same as Figure 4b), 90MHz, 110MHz, and 130MHz. Matching frequencies influence which tilt angles lead to predicted polarization, but over the 100MHz range of matching frequencies shown in Figure 8, none of them predict the polarization at the largest tilt angles seen in the experimental data.  $^{13}\text{C}$  near the NV are expected to have frequencies shifted from the bulk's 75MHz Zeeman interaction by their hyperfine coupling to the NV defect <sup>7</sup>.

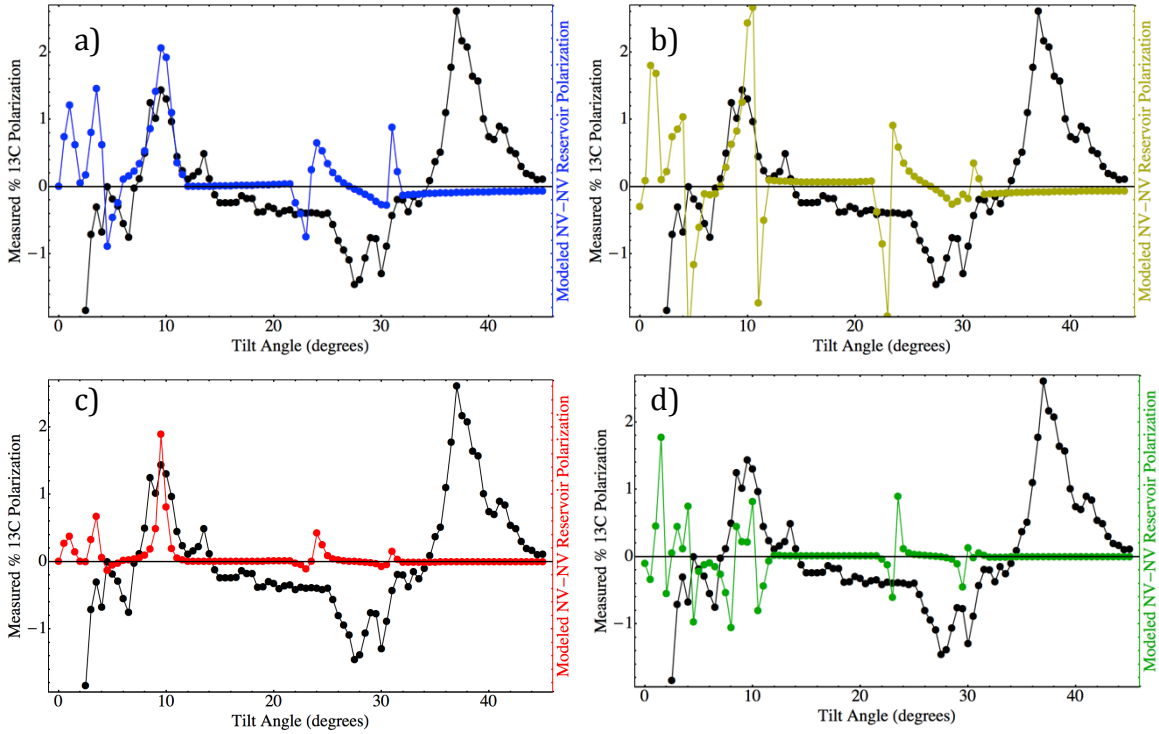


**Figure 5** a) Lorentzian distributions used in the model to weight the dipolar coupling strengths (MHz). Distributions are centered at 0MHz with a 15MHz width (blue), centered at 0MHz with a 5MHz width (red), centered at 15MHz with a 15MHz width (yellow), and centered at 15MHz with a 5MHz width (green). Colors correspond to model results plotted in Figure 7. b-f) Energy transitions (MHz) for 16 pairwise combinations of NV defects as a function of their dipolar coupling strength (MHz) modeled for Sample #2 mounted at rotation of  $10^\circ$  and tilted  $1^\circ$ . Nuclear transition matching condition of  $\pm 75$ MHz shown as dashed black lines.





**Figure 6** a) Lorentzian distributions used in the model to weight the dipolar coupling strengths (MHz). Distributions are centered at 0MHz with a 15MHz width (blue), centered at 0MHz with a 5MHz width (red), centered at 15MHz with a 15MHz width (yellow), and centered at 15MHz with a 5MHz width (green). Colors correspond to model results plotted in Figure 7. b-f) Energy transitions (MHz) for 16 pairwise combinations of NV defects as a function of their dipolar coupling strength (MHz) modeled for Sample #2 mounted at rotation of  $10^\circ$  and tilted  $15^\circ$ . Nuclear transition matching condition of  $\pm 75$ MHz shown as dashed black lines.



**Figure 7** Model results in arbitrary units (color) overlaid with measured  $^{13}\text{C}$  polarization (black) for Sample #2 at 7.05T, 20K 1W 532nm illumination for 25 minutes mounted at a rotation of  $10^\circ$ . Model used a nuclear transition matching condition of 75MHz and a dipolar coupling distribution a) centered at 0MHz with a width of 15 MHz, b) centered at 15MHz with a width of 15MHz, c) centered at 0 MHz with a width of 5MHz, d) centered at 15MHz with a width of 5MHz.

## 4.5 Additional Model Refinements

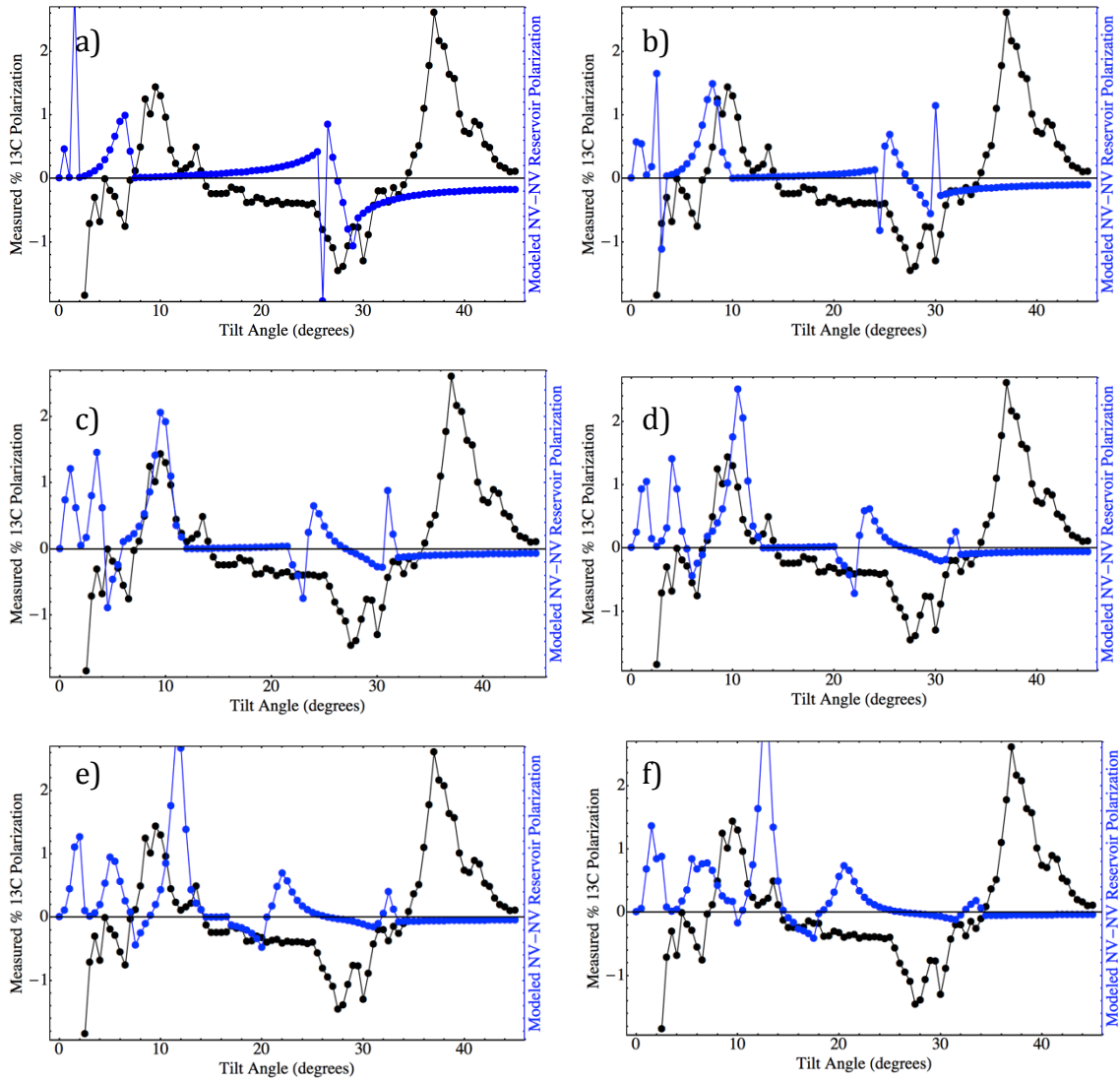
In addition to the core model described above, the model was also expanded to include considerations of  $^{14}\text{N}$  interactions and internal reflection of the laser. Neither of these refinements changes the resulting tilt angle polarization profiles.

### 4.5.1 $^{14}\text{N}$ Interactions

The model described above was further refined to include the  $^{14}\text{N}$  of the NV defect, including its Zeeman ( $\omega_I$ ), Quadrupolar (Q), and Hyperfine ( $A_{\parallel}$ ) interactions. The Hamiltonian including  $^{14}\text{N}$  is given in Equation 57.

$$H = \omega_S(S_{Z1} + S_{Z2}) + D_1 \left( S_Z^2 - \frac{S(S+1)}{3} \right) + D_2 \left( S_Z^2 - \frac{S(S+1)}{3} \right) + AS_{Z1}S_{Z2} - \frac{1}{4}A(S_{1+}S_{2-} + S_{1-}S_{2+}) + E_1(S_{1+}^2 + S_{1-}^2) + E_2(S_{2+}^2 + S_{2-}^2) + \omega_I(I_Z) + Q(I_Z) + A_{\parallel}(S_Z I_Z) \quad (57)$$

This expanded model now has 27 eigenstates and 15 spin transitions within the  $\Delta S_Z=0$  and  $\Delta S_Z=\pm 1$  manifolds for which  $\Delta I_Z=0$  as well, but the resulting tilt angle polarization profile is exactly the same.



**Figure 8** Model results in arbitrary units (blue) overlaid with measured  $^{13}\text{C}$  polarization (black) for Sample #2 at 7.05T, 20K 1W 532nm illumination for 25 minutes mounted at a rotation of  $10^\circ$ . Model used 15 MHz dipolar coupling distribution width centered at 0MHz with a nuclear transition matching condition of a) 30MHz, b) 50MHz, c) 75MHz, d) 90MHz, e) 110MHz, f) 130MHz.

#### 4.5.2 Internal Reflection

In addition to the photophysics included in the model as described in Appendix B, the model was further refined to include internal reflection of the laser from the back surface of the diamond. Figure 9 illustrates this contribution as well as the initial transmission as a function of sample tilt angle. The low amount of internal reflection is attributed with the lack of influence on the resulting modeled polarization.

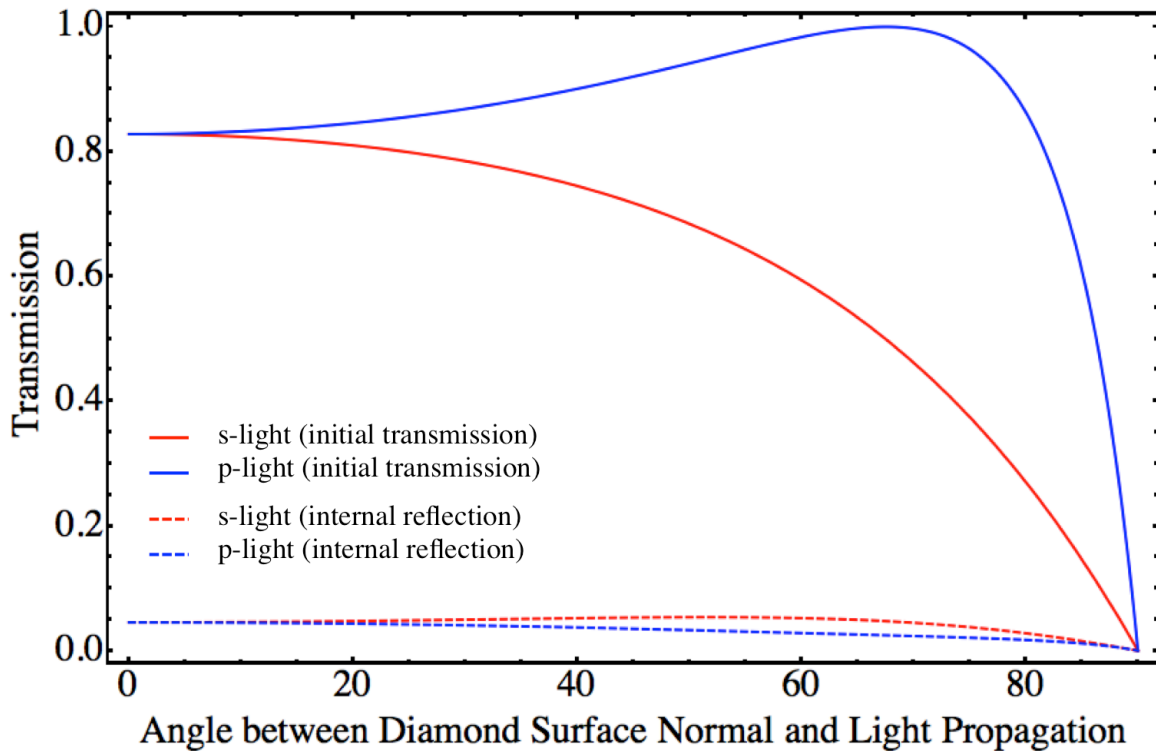


Figure 9 Normalized light transmission into the diamond (solid lines) and internal reflection off the back of the diamond (dashed lines) for given sample tilt angles relative to the laser propagation direction.

#### 4.6 Conclusions

We modeled a nuclear polarization mechanism in diamond by which pairs of dipolar coupled, polarized NV- centers transfer polarization to a nearby  $^{13}\text{C}$  spin if the dipolar coupled NV- centers have energy level transitions that match those of the  $^{13}\text{C}$  spin <sup>2</sup>. Model results qualitatively capture 1) the presence of NV-NV dipolar reservoir polarization with 75MHz transitions at 7.05T, 2) the ability to achieve both positive and negative polarization as a function of crystal orientation, and 3) the acuteness of the orientation sensitivity. Refining the model to include  $^{14}\text{N}$  interactions and internal reflection still do not provide quantitative matching to the  $^{13}\text{C}$  polarization profile as a function of crystal tilt angle. Future work should continue to refine the model to include hyperfine interactions with the  $^{13}\text{C}$ .

# 5 Double Electron-Electron Resonance Measurements

---

## 5.1 Abstract

Here we present Double Electron-Electron Resonance (DEER) measurements probing pairwise interactions of NV- and NV-, NV- and P1, and P1 and P1 pairs of defects. No oscillations characteristic of pairwise defect clustering were observed, indicating a homogeneous distribution of defects on the nanometer scale. The background decay in the DEER data was used to calculate defect concentrations, which were compared with those measured previously using spin counting EPR.

## 5.2 Introduction

Pairwise dipolar interactions between NV centers have been proposed as a source of nuclear polarization in optically illuminated diamonds at high magnetic fields <sup>1</sup>. These pairwise interactions are a function of the distance between interacting defects. In order to accurately model these or other pairwise mechanisms, it is therefore necessary to ascertain whether NV and P1 defects in diamond occur in spatial clusters or are homogeneously distributed on the nanometer length scale.

Double electron-electron resonance (DEER), also known as pulsed electron double resonance (PELDOR), is a method for measuring electron-electron dipolar coupling strengths between pairs of paramagnetic centers separated by 1 to 10nm. The measured coupling strength can be used to determine the separation distance between any pairwise coupled defects. The background signal decay further serves as an estimate of total defect concentration. DEER has been used previously to measure P1 concentrations in diamond <sup>2</sup>. Here we use DEER measurements to probe the existence of spatially paired NV-NV, NV-P1, or P1-P1 defects as well as obtain rough estimates of NV- and P1 defect concentrations.

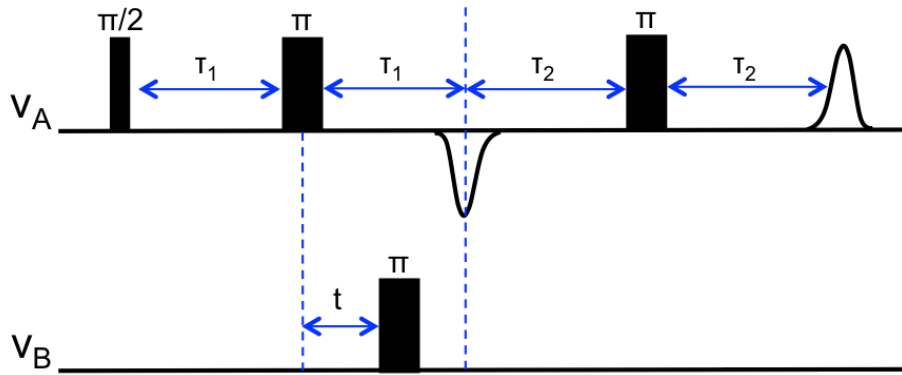
## 5.3 Methods

Figure 1 depicts the four-pulse DEER sequence used in this work. Coupling strength is measured between the detected 'spin A' and the probed 'spin B'. Microwave pulses are applied at frequencies resonant with each electron spin,  $\nu_A$  and  $\nu_B$ .

The four-pulse DEER sequence can be understood by first analyzing the time evolution of the pulsed excitation and electron spin response shown in Figure 1. 'A' spins are brought into the x-y plane with a  $\pi/2$  pulse, and then two  $\pi$  pulses refocus any coherence loss due to field inhomogeneities or dipolar couplings before the final acquisition. It is effectively an echo-detected "90-acquire" sequence. When we include the probe pulse at  $\nu_B$ , the 'B' spins are inverted, changing their dipolar

coupling influence on the 'A' spins. This changes the precession frequency of the 'A' spins by the frequency of the dipolar coupling and results in modulation of the echo intensity as the timing of the 'B' Pi pulse is changed. Oscillations in the integrated echo intensity occur at the dipolar interaction frequency between the 'A' and 'B' spins. These oscillations are superimposed on an exponential decay due to the greater spin bath of the detected 'A' spins. This decay, in turn, can be fit to determine the overall 'A' spin concentration.

Microwave pulses typically excite a much narrower bandwidth than the EPR line shape, so  $\nu_A$  and  $\nu_B$  can be very close without encountering overlap. In fact, the frequencies are required to be close in order to not move too far from the optimal tuning of the microwave cavity used in these experiments. The Bruker MD5 resonator used in this work has a maximally overcoupled Q-factor of about 50, giving a 200MHz bandwidth, and can be used to find coupling strengths between spins with a frequency difference ( $\nu_A - \nu_B$ ) of approximately 100MHz. Given the time resolution and response of the instrument, and the  $r^{-6}$  dependence of the dipolar interaction, the setup is capable of observing pairwise distances on the order of 2.5-10nm. Because the NV- EPR spectrum is orientation dependent, EasySpin simulations were performed before the experiments to find crystal mounting orientations that gave optimal separations between EPR lines. X-band, room temperature DEER measurements were performed for probe-detect combinations of NV- and NV-, NV- and P1, and P1 and P1 pairs of defects.



**Figure 1** Four-pulse DEER sequence on species A (detect spin) and B (probe spin). DEER is a two frequency experiment, with separate pulses applied at Larmor frequencies  $\nu_A$  and  $\nu_B$ . Rectangles indicate pulses labeled by tip angle. Curves indicate the appearance of echoes of species A. The final echo is acquired for varying pulse sequence times, and the resulting echo will vary with time according to the distance between A and B spins.

Before each DEER measurement, a field swept echo was performed to locate the EPR transition frequencies. This was particularly important for calibrating the EasySpin determined NV- transitions. These field swept echo spectra were also used to estimate the fraction of excited 'B' spins, which is needed to calculate total 'A' spin concentration.

## 5.4 Double Electron-Electron Resonance (DEER)

This section outlines the measured DEER decay curves, fits, and defect concentrations derived from the fits. The DEER-derived concentrations are compared to concentrations calculated from spin counting EPR<sup>3</sup>.

### 5.4.1 Raw Data and Fits

Figures 2 - 7 depict the DEER decay curves for each probe-detect pair of defects as well as the exponential fits used to calculate defect concentrations of the 'detect' spins from each experiment. DEER decays should be symmetric about time zero, defined as  $t=0$  in Figure 1.

Most data sets shown here include a non-physical artifact seen as an asymmetric sharp dip about time  $t=0$ . Measurements were repeated taking data at negative time points (applying a Pi pulse on the B spins before the initial Pi pulse on the A spins), and the same artifact was observed, confirming that the source of the artifact is in the experimental apparatus and not the result of any spin physics.

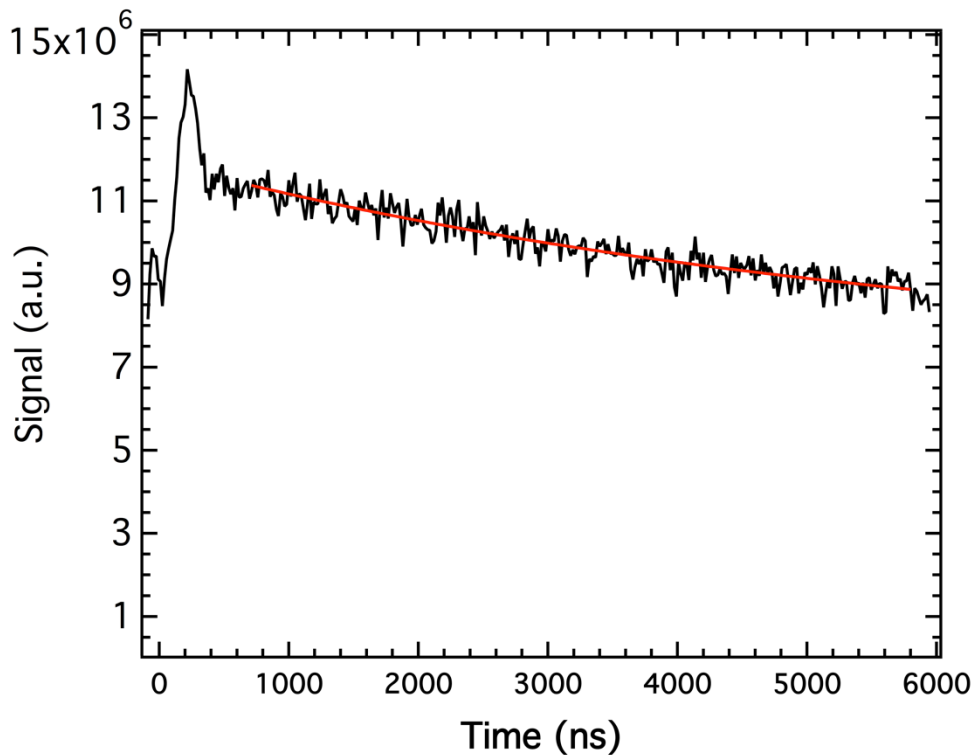


Figure 2 DEER data for probe-detect NV-NV in Sample #1

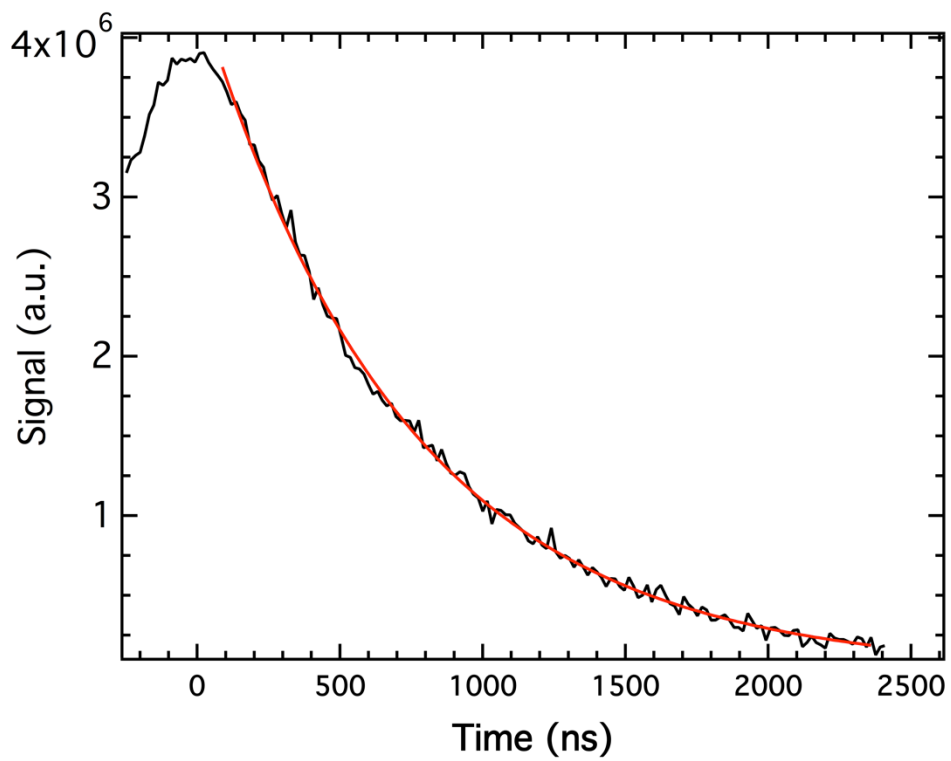
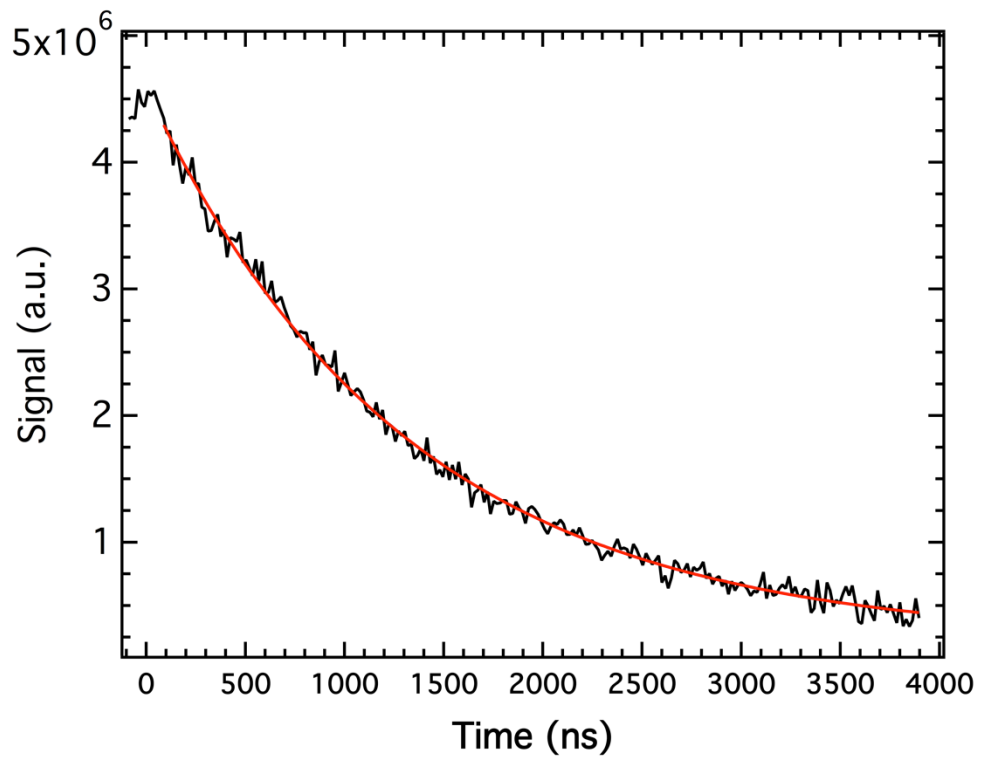


Figure 3 DEER data for probe-detect a) NV-P1 and b) P1-P1 in Sample #1



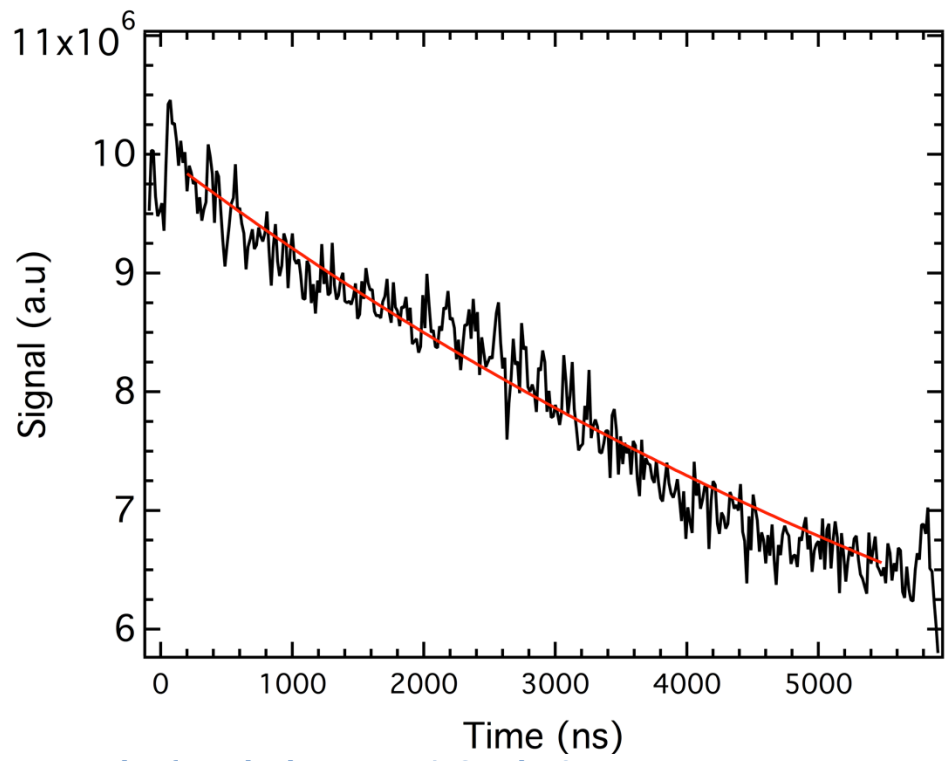


Figure 4 DEER data for probe-detect NV-NV in Sample #2

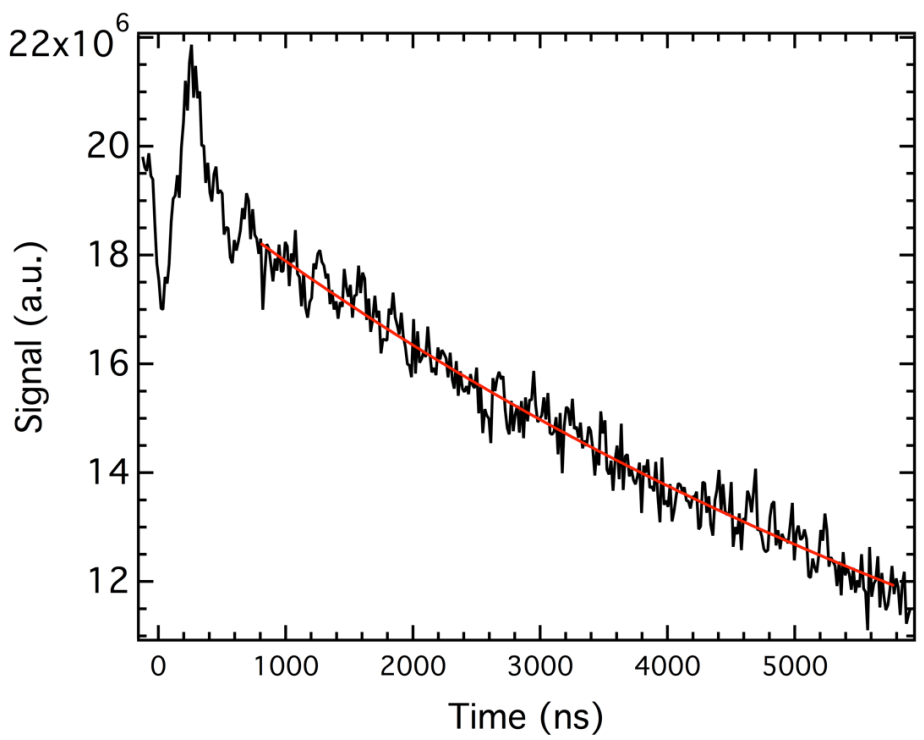


Figure 5 DEER data for probe-detect NV-NV in Sample #7

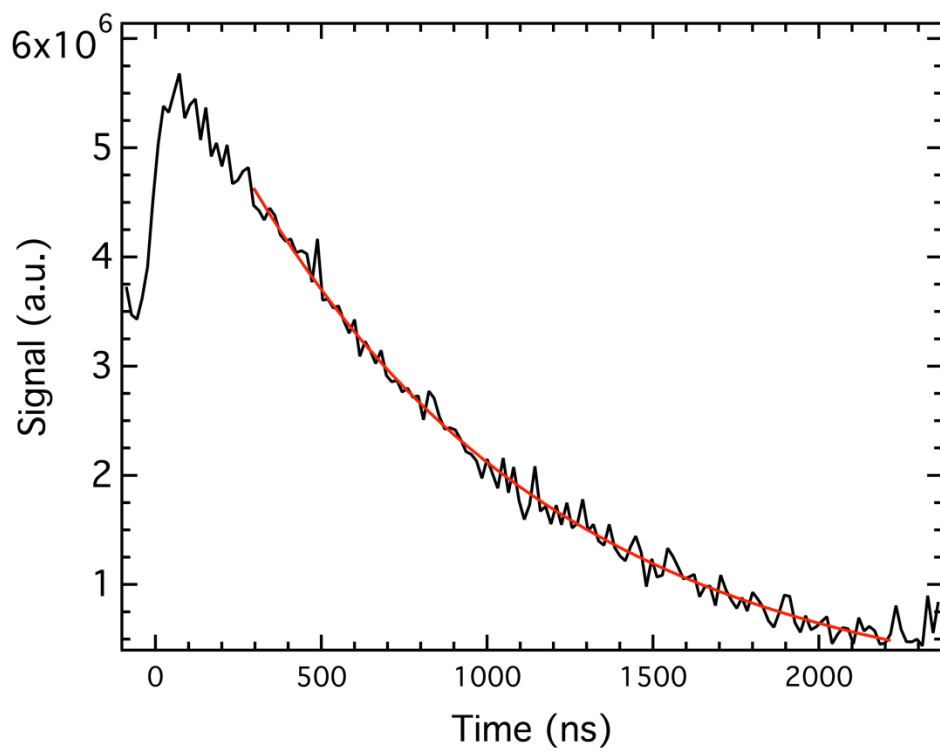
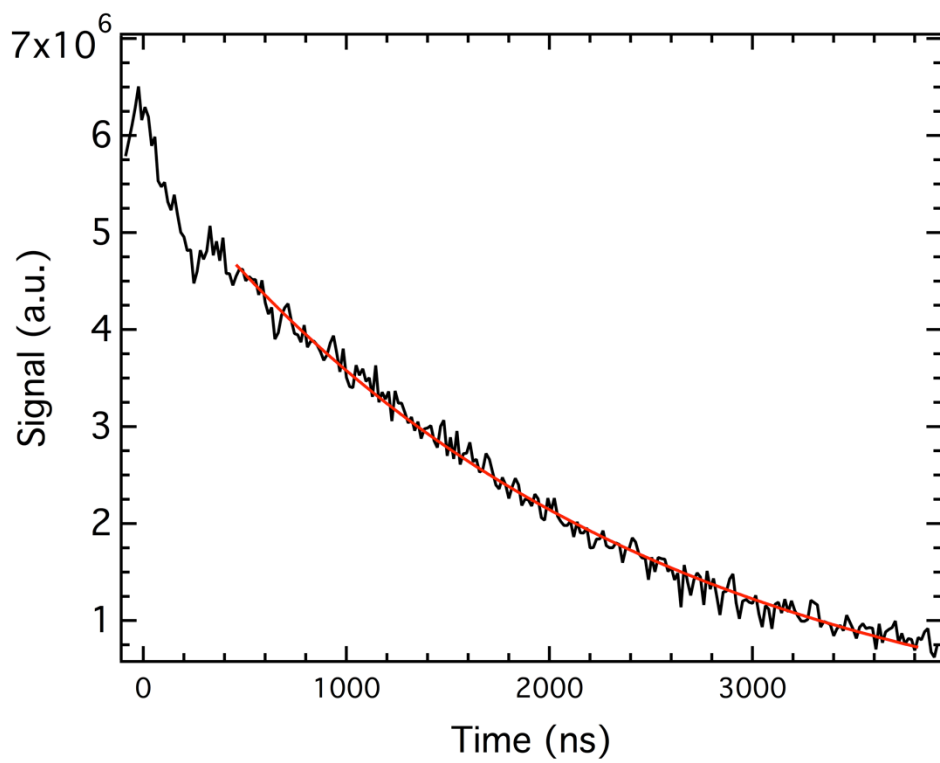


Figure 6 DEER data for probe-detect a) NV-P1 and b) P1-P1 in Sample #2

Oscillations in the NV-P1 DEER decay of Sample # 7 (Figure 7) are due to electron spin echo envelope modulation (ESEEM) <sup>4</sup>. ESEEM oscillations are the result of the microwave pulse flipping an electron spin and nuclear spin coupled to it. This nuclear spin prevents perfect refocusing of the echo and results in modulation at electron-nuclear double resonance (ENDOR) frequencies. ESEEM is typically seen when isotropic hyperfine coupling is weak and anisotropic hyperfine coupling is comparable to the nuclear Zeeman interaction or Quadrupolar couplings are present <sup>5</sup>.

The ESEEM oscillation frequencies in the DEER decay were found by taking Fourier Transforms of the data, shown in Figure 8. These ESEEM oscillations occur at 5 – 6 MHz, on the order of magnitude of the P1 <sup>14</sup>N nuclear interactions. The nuclear quadrupole coupling of the <sup>14</sup>N of the NV- center is -5.04 MHz <sup>6</sup>. <sup>14</sup>N hyperfine coupling to the NV- center is  $A_{\parallel} = -2.14$  MHz and  $A_{\perp} = -2.7$  MHz <sup>7</sup>.

The DEER results presented in Figures 2-7 do not exhibit any dipolar oscillations indicative of pairwise clustering of defects. We conclude that all defects are homogeneously distributed throughout the diamonds on a macroscopic scale.

#### 5.4.1 Fit Derivation

For a homogeneous distribution of electrons, the DEER decay is described by <sup>8</sup>,

$$V_{DEER}^{hom}(t) = \exp(-\tau t) \quad (1)$$

$$\tau = k C_A F_B \quad (2)$$

where  $C_A$  is the concentration of A spins and  $F_B$  is the fraction of B spins excited by the pump pulse.  $k$  is defined in Equation 3 <sup>8</sup>,

$$k = \frac{2\pi\mu_0\beta^2 g_A g_B}{9\sqrt{3}\hbar} \quad (3)$$

where  $\mu_0$ ,  $\beta$ , and  $\hbar$  are defined in Table 2.  $g_A$  and  $g_B$  are the g-factors for spins A and B. Table 1 lists the  $\tau$  values and errors extracted from fitting Equation #1 to the data.

$F_B$  is estimated from a model of the pulse excitation profile. Once  $\tau$  and  $F_B$  are known,  $C_A$  is calculated using Equation 2.

**Table 1 Exponential decay fits and error bars for probe-detect defect combinations listed in column 1**

	Sample #2		Sample #1		Sample #7	
	Tau (1/ms)	Tau Error (1/ms)	Tau (1/ms)	Tau Error (1/ms)	Tau (1/ms)	Tau Error (1/ms)
NV-NV	111.2	19.0	182.0	35.6	119.8	18.0
NV-P1	445.0	16.4	768.4	11.4	268.6	28.0
P1-P1	1065.5	37.9	1386.6	16.3	248.0	10.4

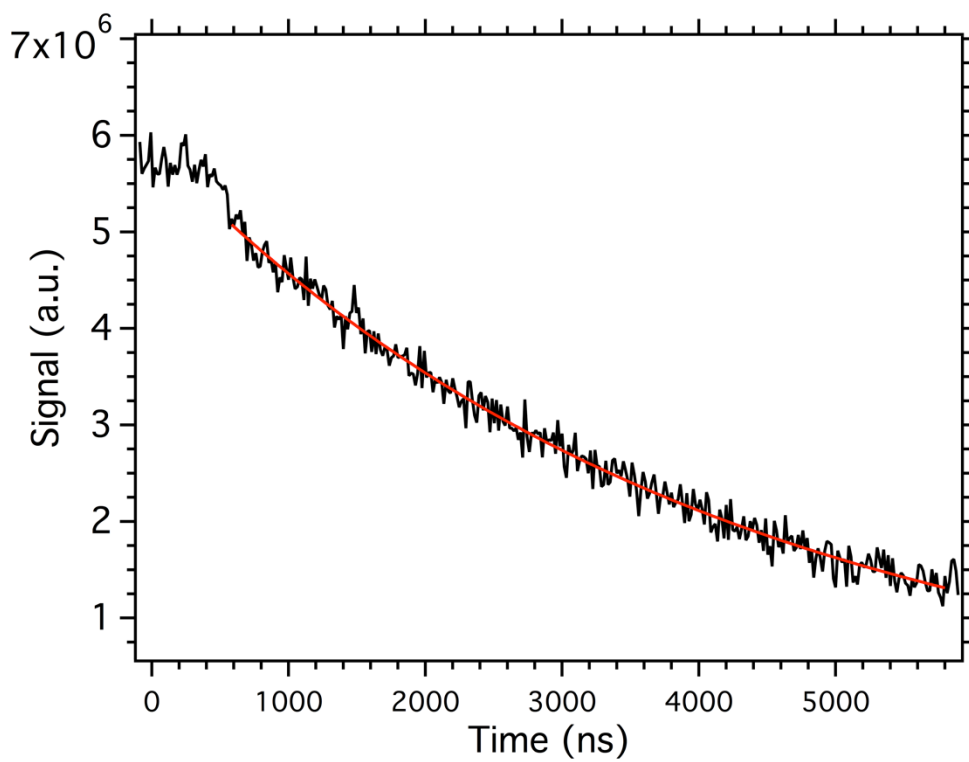
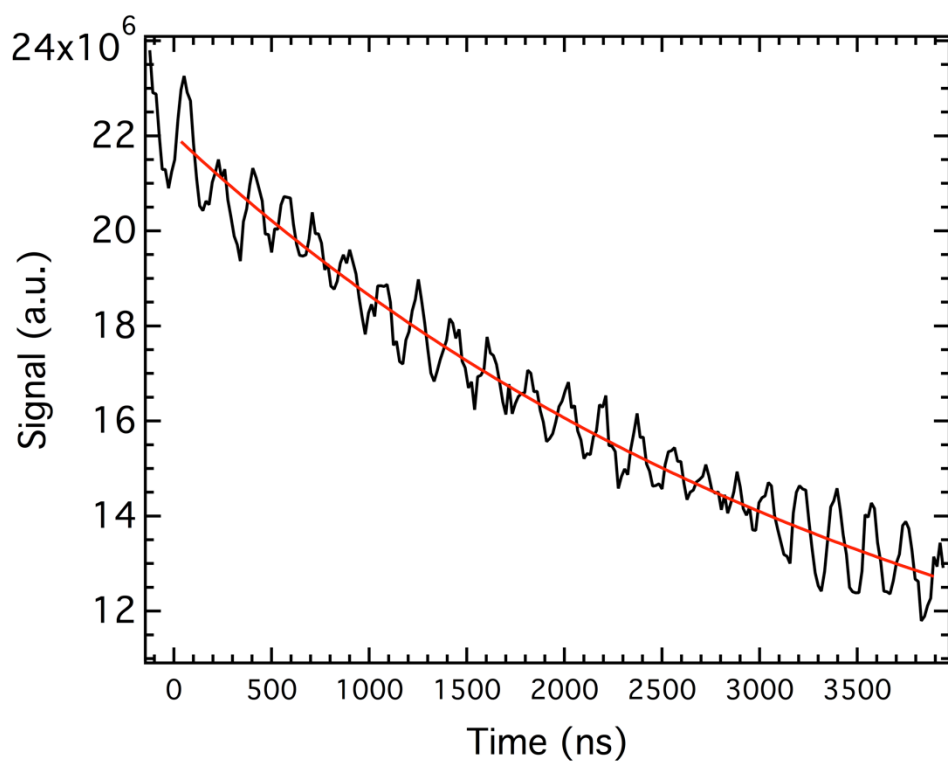


Figure 7 DEER data for probe-detect a) NV-P1 and b) P1-P1 in Sample #7

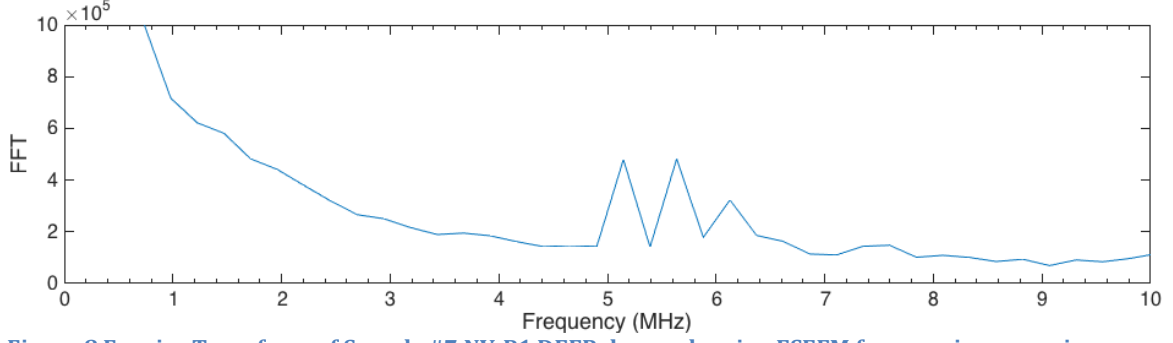


Figure 8 Fourier Transform of Sample #7 NV-P1 DEER decay, showing ESEEM frequencies occurring between 5 - 6 MHz

Table 2 Physical constants used in calculating spin concentration from DEER measurements

$\beta$	$9.274 \cdot 10^{-24}$	J/T	Bohr magneton
$\mu_0$	$1.2566 \cdot 10^{-6}$	$T^2/(J \cdot m^3)$	Permeability of vacuum
$\hbar$	$1.0546 \cdot 10^{-34}$	J·s	Reduced Planck's constant
$g_{NV}$	2.0028		NV g factor
$g_{P1}$	2.0024		P1 g factor

#### 5.4.1.1 Estimating $F_B$

The fraction of excited B spins,  $F_B$ , is estimated through modeling the excitation profile of the pulse given the pulse parameters used in the experiment and then comparing this profile to the measured EPR spectrum. Equations 4 - 12 outline this model.

Equation 4 defines the density matrix describing the initial state of B spins before the Pi pulse.

$$\rho(0) = 2I_z \quad (4)$$

Equation 5 is the Hamiltonian describing the influence of the  $\pi$  pulse on a spin system. This Hamiltonian gets inserted into a propagator (Equation 6) and applied to the initial spin state (Equation 7) to describe the time evolution of the B spins due to the applied pulse.  $\rho$  is the final spin state after applying the pulse for a time  $t_p$ .

$$H = 2\pi\omega_{offset}I_z + \omega_1I_y \quad (5)$$

$$P = e^{-iHt_p} \quad (6)$$

$$\rho = P\rho(0)P^\dagger \quad (7)$$

The magnetization profile of the B spins due to the pulse is calculated by taking the trace of the magnetization operator times the density matrix describing the post-

pulse state of the B spin system (Equation 8). This is depicted as the blue trace in Figure 9.

$$\langle I_Z \rangle = \text{Tr}(I_Z^\dagger \rho) \quad (8)$$

A Hadamard product of this magnetization profile and the measured EPR spectrum gives the spectrum for inverted B spins (Equation 9). The measured EPR spectrum is represented as *spectrum* in Equation 9 and plotted as the black trace in Figure 9. The spectrum of the modeled effect of the pulse, plotted as the red trace in Figure 9, looks like a 'hole' burned into the measured spectrum due to inversion of the spins.

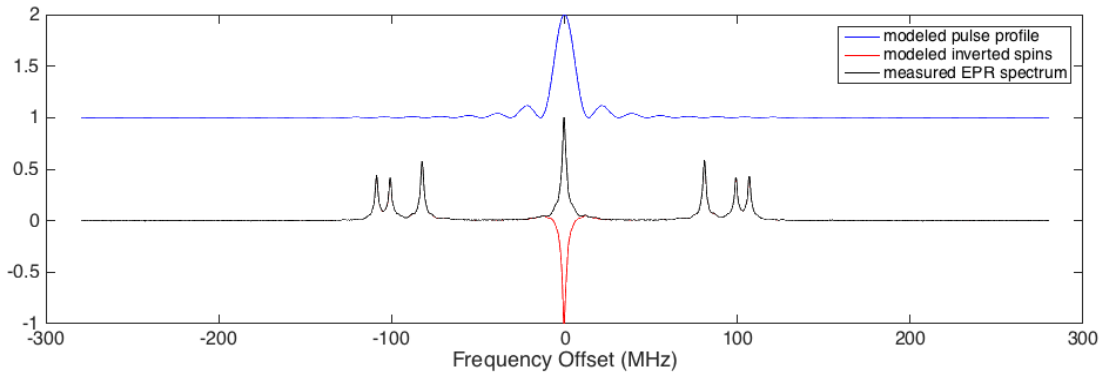
$$\text{hole} = \text{spectrum} \circ \langle I_Z \rangle \quad (9)$$

The relative number of electron spins in the measured (Equation 10) and modeled (Equation 11) spectra are proportional to the integrals of the spectra over frequency,  $f$ . The ratio of these spins can be used to calculate how many B spins were excited by the pulse (Equation 12).

$$\text{spins}_{\text{total}} = \int \text{spectrum} df \quad (10)$$

$$\text{spins}_{\text{hole}} = \int \text{hole} df \quad (11)$$

$$F_B = \frac{1}{2} \left( 1 - \frac{\text{spins}_{\text{hole}}}{\text{spins}_{\text{total}}} \right) \quad (12)$$



**Figure 9** Modeled excitation pulse profile (blue). Measured X-band EPR spectrum of P1 centers in Sample #1 (black). Modeled effect of inversion pulse on spins (red) determined by projecting the modeled pulse profile onto the measured EPR spectrum. The black and red spectra overlap everywhere the red is not separately visible.

### 5.4.2 Spin Counting

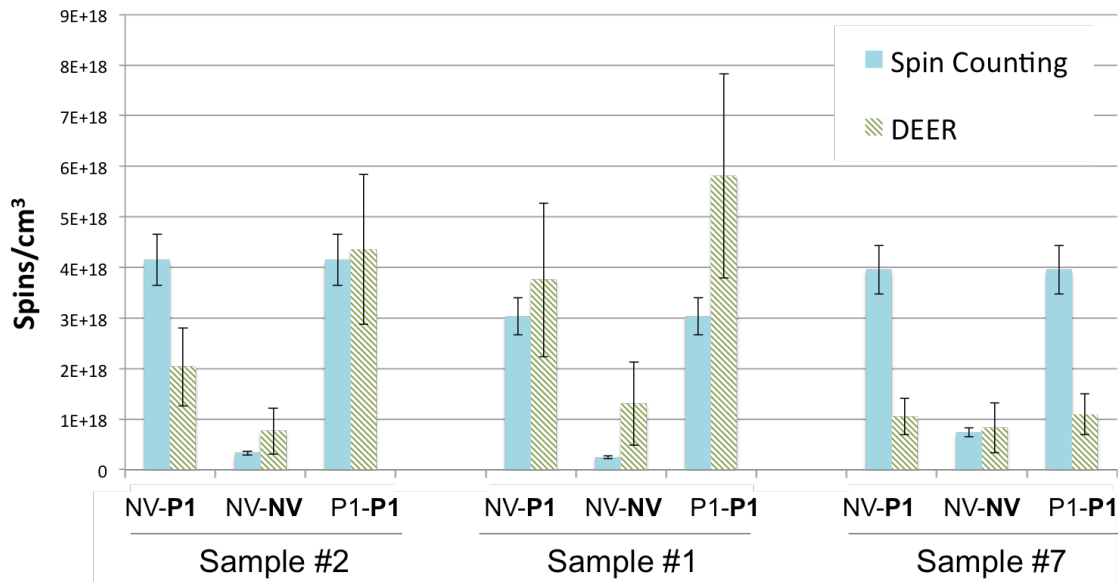
NV- and P1 defect concentrations in each sample were previously quantified by comparing double integrals of the X-band EPR spectrum of the diamond with that of a cupric sulfate pentahydrate standard<sup>3</sup>. Double electron-electron resonance (DEER) experiments were performed to assess homogeneity of defects, but also provide a

measure of defect concentration <sup>2</sup>. The defect concentrations calculated from these two techniques are compared in Figure 10 and Table 3.

Errors for DEER-measured concentrations listed in Table 3 were calculated by propagating the error in exponential fit to the DEER curve and a fixed 0.05 error in the calculated fraction of excited probe spins. Errors for concentrations measured via spin counting are standard deviations from multiple experiments. Note that there are large discrepancies between the P1 concentrations measured in the NV-P1 and P1-P1 probe-detect DEER experiments for both Sample #1 and Sample #2, suggesting even larger uncertainty than were calculated from the exponential fit errors and estimated  $F_B$  errors.

**Table 3 NV- and P1 concentrations as measured by EPR spin counting <sup>3</sup> and DEER**

Sample Number	Spin Counting [NV-] (ppm)	Spin Counting [P1] (ppm)	NV-NV DEER [NV-] (ppm)	NV-P1 DEER [P1] (ppm)	P1-P1 DEER [P1] (ppm)
1	1.4 ± 0.2	17 ± 2	4.3 ± 2.6	11.6 ± 4.4	24.7 ± 8.4
2	1.9 ± 0.2	24 ± 3	7.4 ± 4.7	21.3 ± 8.6	33.0 ± 11.5
7	4.2 ± 0.5	22 ± 3	4.7 ± 2.8	6.0 ± 2.1	6.2 ± 2.3



**Figure 10 Comparison of defect concentrations determined from DEER (green stripe) and EPR Spin Counting (blue) for three diamond samples. Labels indicate the probe-detect defect pair in the DEER experiment. The concentration is plotted for the ‘detect’ defect in each instance, highlighted in bold in each label. Error bars on DEER concentrations were calculated by propagating the error in exponential fit to the DEER curve and a fixed 0.05 error in the calculated fraction of excited probe spins. Error bars for spin counting are standard deviations from multiple experiments.**

## 5.5 Conclusion

We have presented DEER measurements of Samples #1, #2, and #7 that exhibit no characteristic pairwise spatial clustering of NV-NV, NV-P1, or P1-P1 defects. Un-

modulated exponential decays indicate homogeneous distributions of defects on the nanometer length scale.

Nuclear polarization mechanisms involving pairwise defect interactions must account for the distribution of pairwise interactions occurring in a randomly dispersed defect environment.

The background exponential decay in the DEER data were used to calculate defect concentrations, which were compared with those measured using spin counting EPR. Concentrations matched within an order of magnitude. Concentrations from DEER measurements had large errors due to poor signal-to-noise.

## **5.6 Acknowledgements**

X-band DEER measurements were taken in collaboration with Tim Keller and Songi Han at UC Santa Barbara. Special thanks to Tim Keller for sharing his MATLAB code for simulating the fraction of spins excited.



# 6 Nitrogen Vacancy and Substitutional Nitrogen Relaxation in Diamond

---

## 6.1 Abstract

This chapter presents  $T_1$  and  $T_2$  relaxation times for NV- and P1 defects measured in diamonds with total defect concentrations ranging between 10 - 110 ppm. Both  $T_1$  and  $T_2$  times were measured on a 240GHz pulsed EPR system.  $T_2$  times were also measured on a 9.6GHz (X-band) pulsed EPR system. NV- relaxation times were consistently longer than P1 relaxation times in the same sample. The data does not show a strong correlation between relaxation times and defect concentrations.

NV-  $T_1$  times at 240GHz ranged from 3.4-5.2 ms. P1  $T_1$  times at 240GHz ranged from 1.8-2.3 ms. NV-  $T_2$  times at 240GHz ranged from 1.7-13.9us. NV-  $T_2$  times at 9.6GHz ranged from 0.1-1.6us. P1  $T_2$  times at 9.6GHz ranged from 0.3-2.5 us. In Sample #7, which has visually observable defect concentration inhomogeneity, both NV- and P1 defect relaxation curves at X-band were best fit to double exponential functions. At 240GHz, both NV- and P1 defect relaxations in Sample #7 were best fit to stretched exponentials.

## 6.2 Introduction

NV- relaxation times are important for the defect's many proposed applications. Long  $T_2$  relaxation times are necessary for applications such as magnetometry <sup>1</sup>, quantum information <sup>2</sup>, and hyperpolarization transfer <sup>3-11</sup>. Much work has been done to engineer defects in diamond with long relaxation times near the surface <sup>12-14</sup>. Here we measure  $T_1$  and  $T_2$  relaxation times of bulk defects in our diamonds using pulsed X-band and 240GHz EPR.

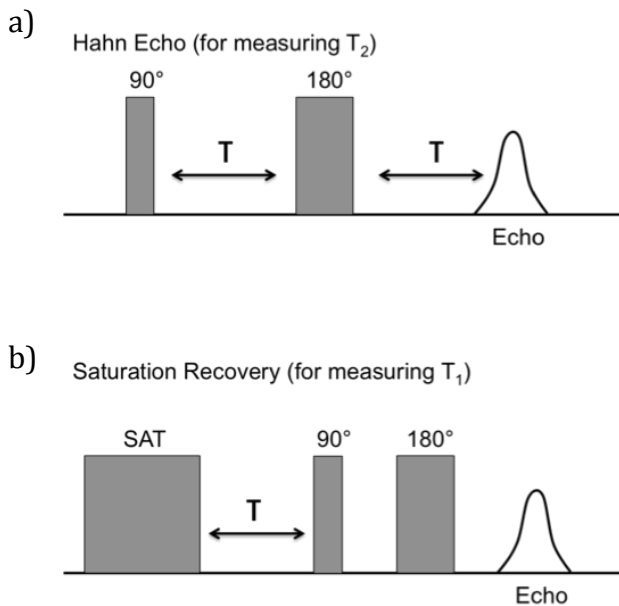
Previous diamond relaxation studies found correlations between  $T_2$  relaxation times and defect concentrations <sup>15-19</sup>. This study found no strong correlation over the 10 - 110 ppm defect concentration range represented among our samples.  $T_2$  values of P1 centers in our sample agree within an order of magnitude to measured and theoretically predicted values in the literature <sup>15,17,18</sup>. Direct comparison is complicated by the fact that literature  $T_2$  values for P1 centers are reported in diamonds without NV- centers.

## 6.3 Methods

Room temperature NV- and P1 relaxation time constants were measured using pulsed EPR at X-band (Bruker system in the lab of Songi Han at UCSB) and 240GHz (homebuilt system in the ITST at UCSB). Both  $T_1$  and  $T_2$  times were measured at 240GHz. Only  $T_2$  times were measured at X-band. Relaxation time constants were calculated from exponential fits to measured echo integrals of Saturation Recovery ( $T_1$ ) and Hahn Echo ( $T_2$ ) experiments. Pulse sequences are shown in Figure 1.

240GHz measurements had large errors in the exponential fits due to poor signal-to-noise ratio. Measured values also varied drastically between repeat measurements. One possible

explanation for the poor repeatability is that the time constants may be orientation-dependent <sup>20</sup>.



**Figure 1 a) Hahn Echo pulse sequence with time represented in the horizontal axis. b) Saturation Recovery pulse sequence. Sequences are repeated for a series of tau values and the integral of the resulting echo is plotted as a function of tau and fit to an exponential to extract the a)  $T_2$  value and b)  $T_1$  value.**

X-band Saturation Recovery data were fit to either a single exponential decay (Equation 1) or double exponential decay (Equation 2) which included a fit parameter for a shift in the initial time point ( $t_0$ ). The fit parameter  $T$  (or  $T_{short}$  and  $T_{long}$  for a double exponential fit) is the  $T_2$  relaxation time constant.

$$Echo = c + ae^{\frac{-(t-t_0)}{T}} \quad (1)$$

$$Echo = c + a_1e^{\frac{-(t-t_0)}{T_{short}}} + a_2e^{\frac{-(t-t_0)}{T_{long}}} \quad (2)$$

The 240GHz Saturation Recovery data and Hahn Echo data were fit to a similar expression, Equation 3, without allowing for a shift in the initial time point.

$$Echo = c + ae^{\frac{-t}{T}} \quad (3)$$

In several cases, data was compared to a stretched exponential fit, either including the exponential stretch,  $n$ , as a fitting parameter (Equation 4), or fixing it to a value of 3/2 (Equation 5). Spectral diffusion can cause  $T_2$  relaxation to occur in the form of a stretched exponential with  $n$  between 0.5 and 2 in paramagnetic centers in solids <sup>21</sup>. When this occurs, the relaxation time is called the phase memory time,  $T_M$ .

$$Echo = c + ae^{-\left(\frac{t}{T_1}\right)^n} \quad (4)$$

$$Echo = c + ae^{-\left(\frac{t}{T_1}\right)^{\frac{3}{2}}} \quad (5)$$

## 6.4 NV and P1 Relaxation Time Constants

### 4.6.1 240GHz T<sub>1</sub>

Figure 2 shows T<sub>1</sub> relaxation values measured using Saturation Recovery sequences on a 240GHz EPR system for NV<sup>-</sup> and P1 centers in four diamonds, plotted as a function of total defect concentration. Raw data and the exponential fits from which the T<sub>1</sub> relaxation values in Figure 2 were derived are shown in Figures 3 - 6. Due to the larger SNR from the more abundant P1 centers, their data is much less noisy and fit error thus much smaller than for the NV<sup>-</sup> centers. NV<sup>-</sup> centers had consistently longer T<sub>1</sub> values than the P1 centers by several milliseconds.

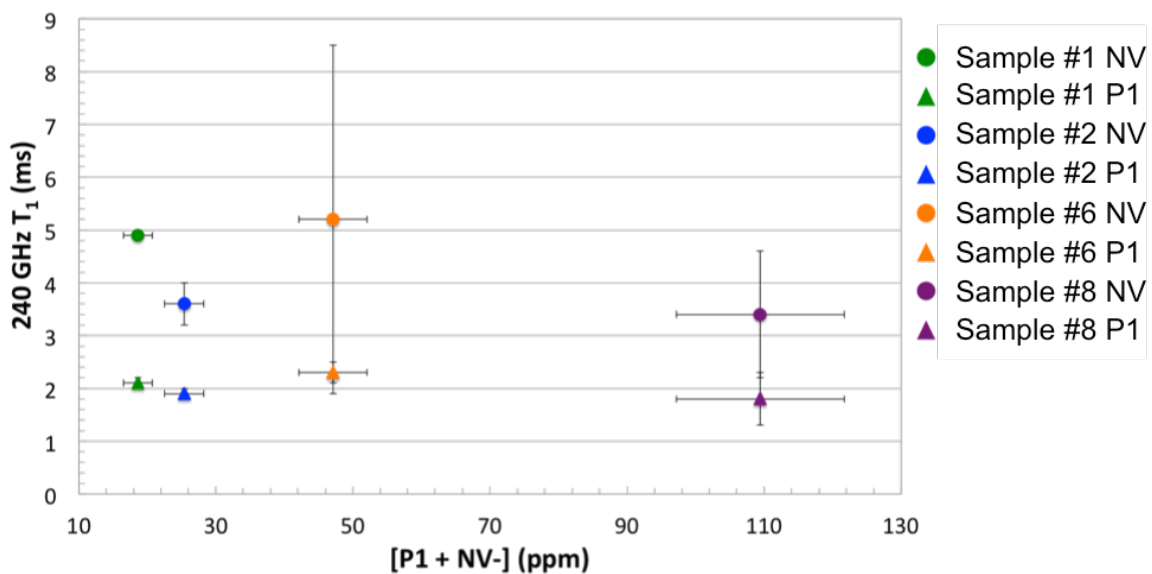


Figure 2 T<sub>1</sub> values at 240GHz for NV<sup>-</sup> and P1 centers in four different samples plotted as a function of total defect concentration. Error bars are from the error in exponential fits to the echo data.

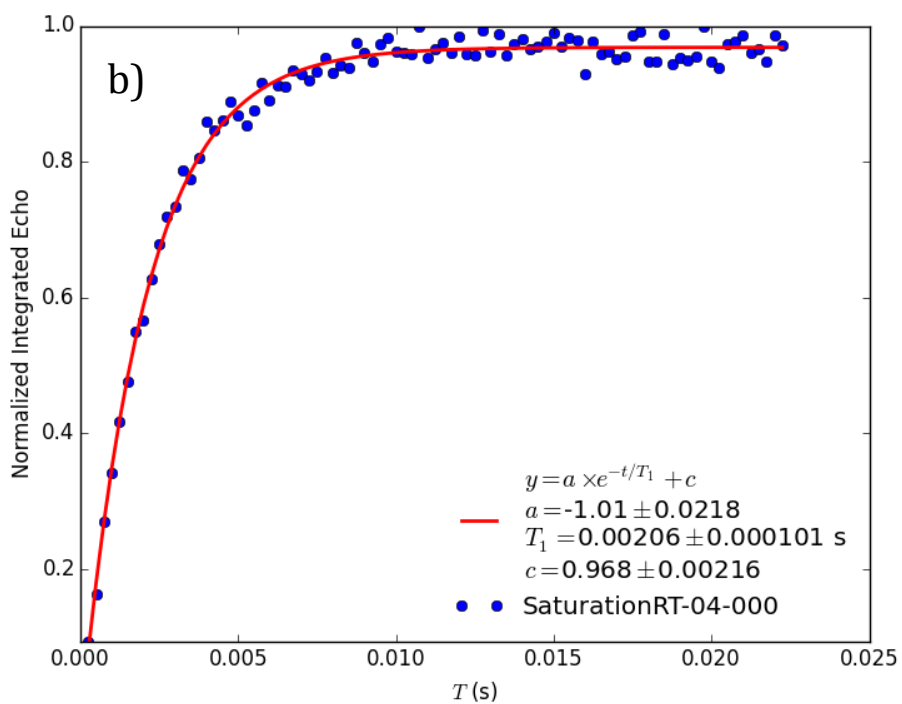
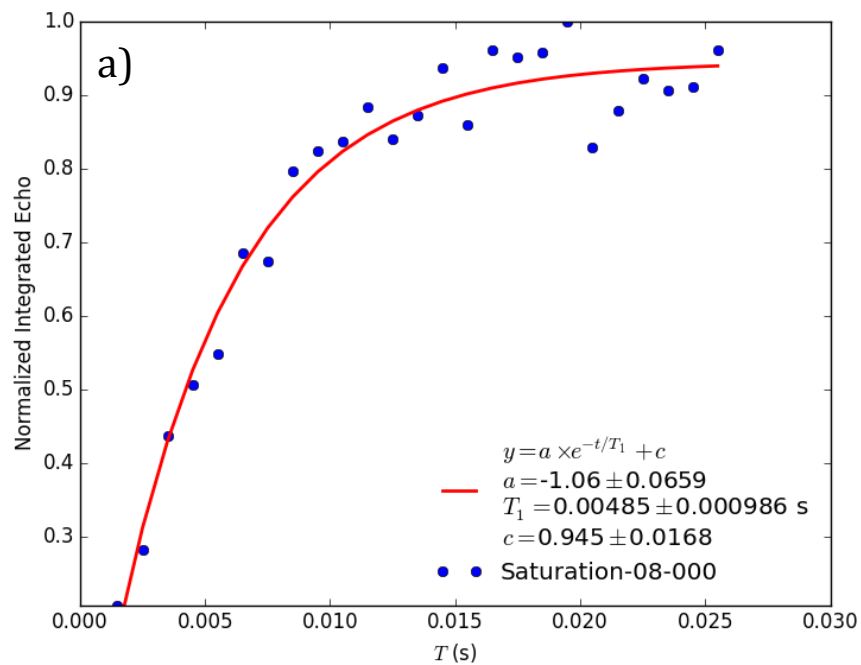


Figure 3 240GHz Saturation Recovery data for Sample #1 for a) NV and b) P1. Data is shown in blue circles and the exponential fit is shown as a red line. Fit parameters are listed in the inset.

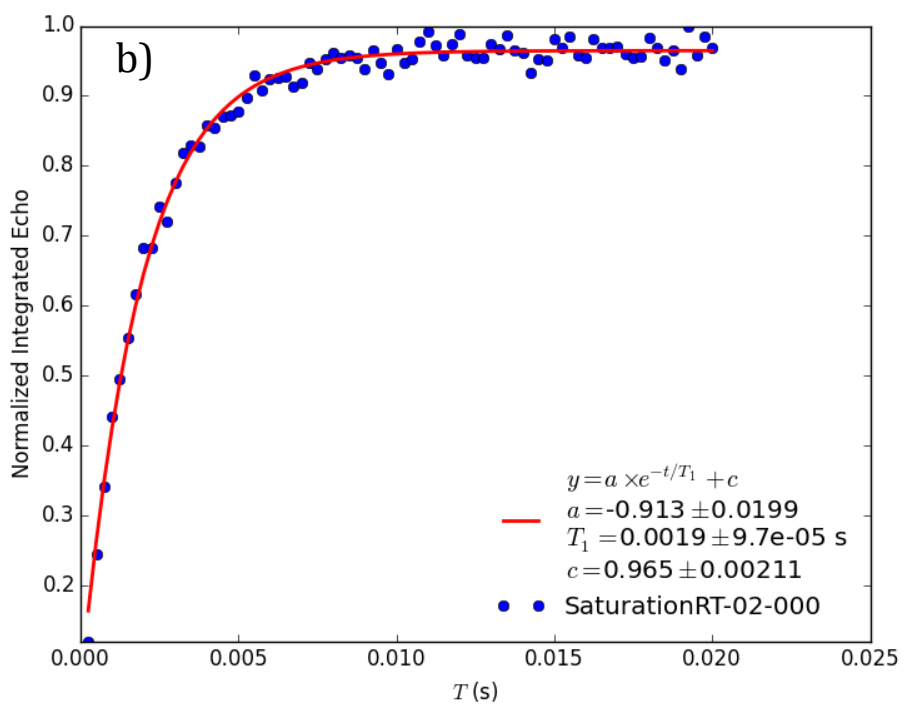
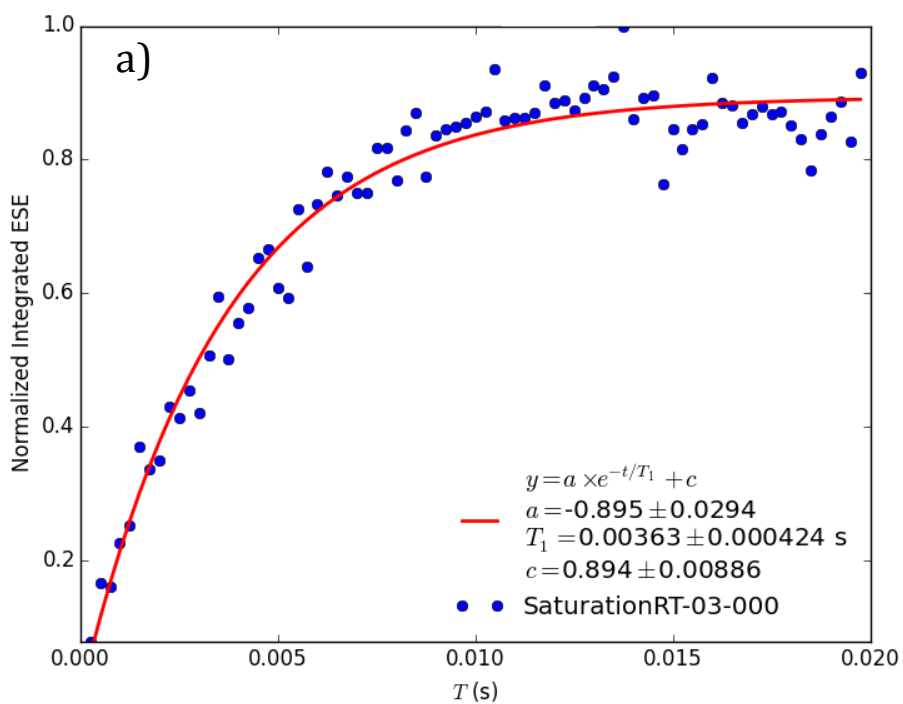


Figure 4 240GHz Saturation Recovery data for Sample #2 for a) NV and b) P1. Data is shown in blue circles and the exponential fit is shown as a red line. Fit parameters are listed in the inset.

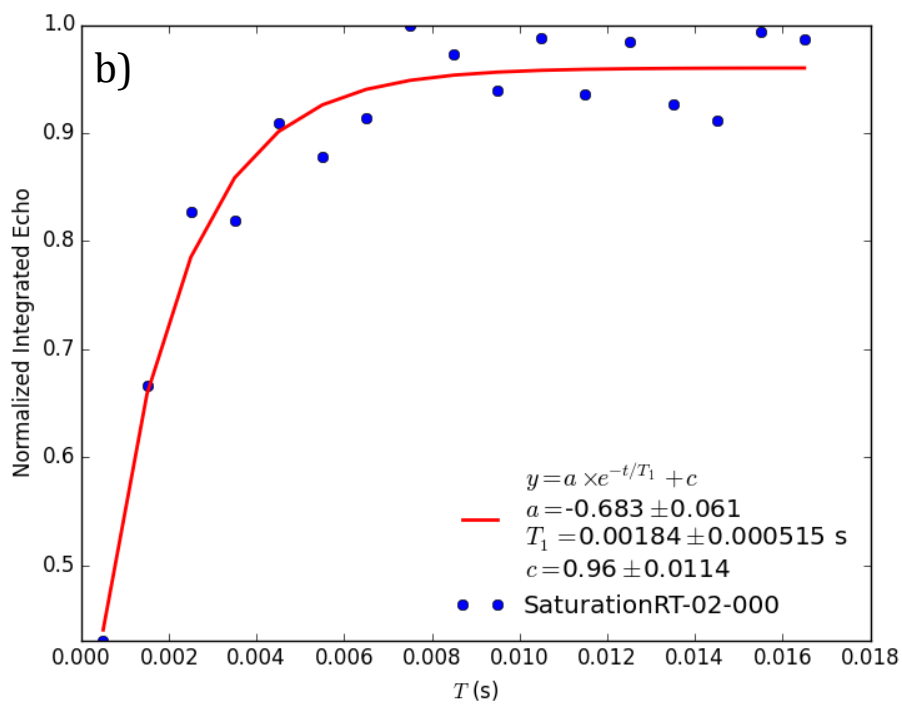
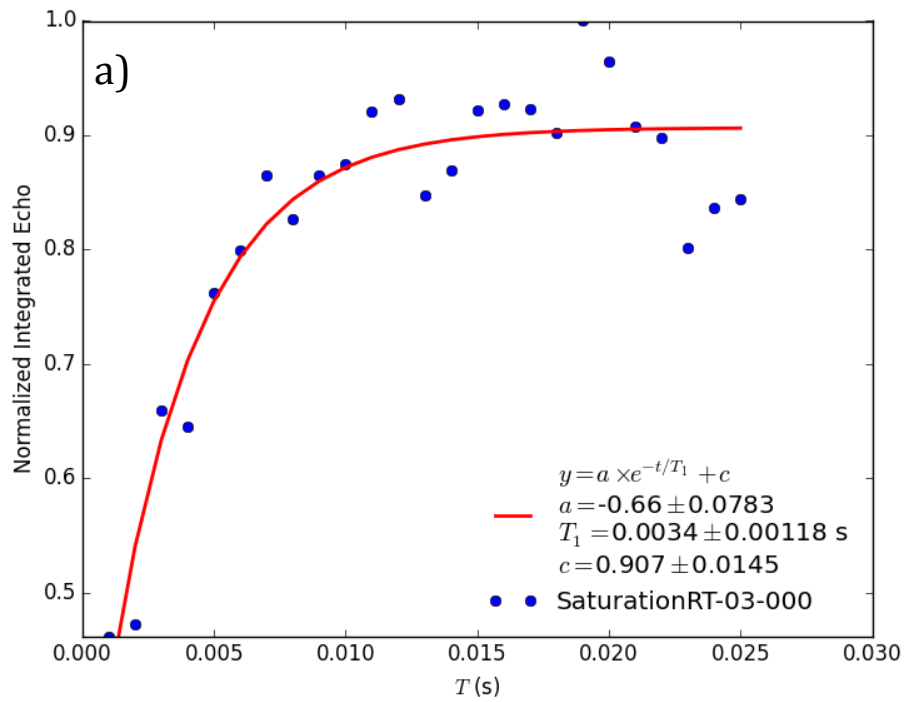


Figure 5 240GHz Saturation Recovery data for Sample 6 for a) NV and b) P1. Data is shown in blue circles and the exponential fit is shown as a red line. Fit parameters are listed in the inset.

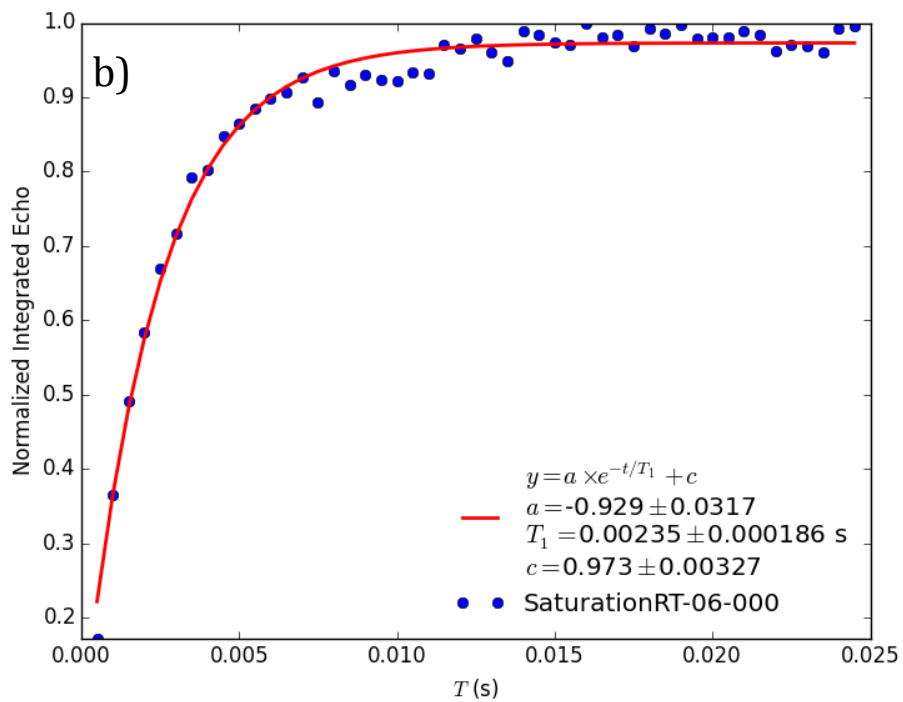
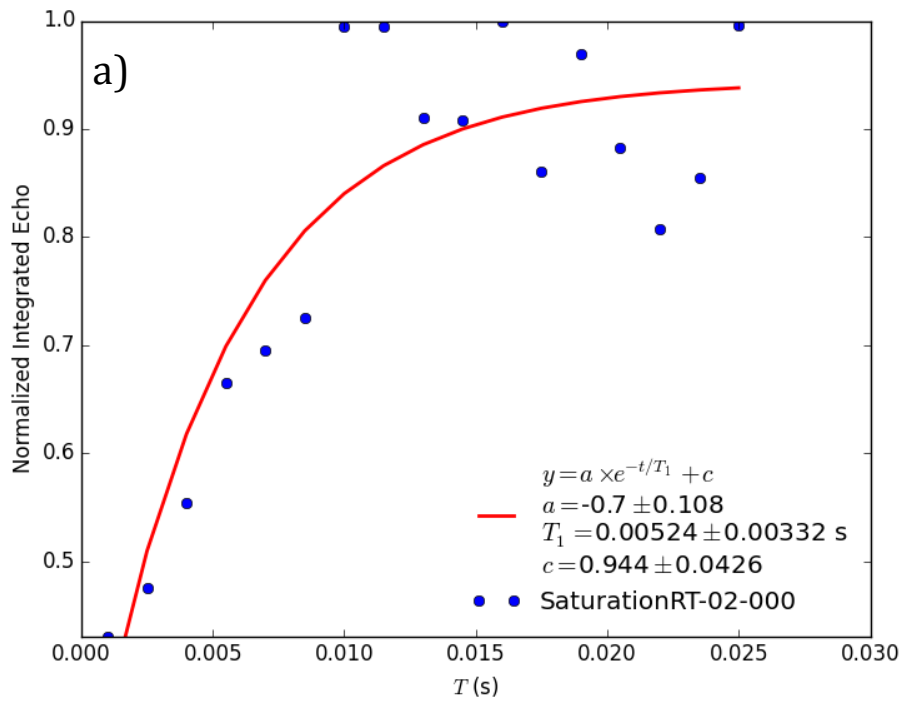


Figure 6 240GHz Saturation Recovery data for Sample #8 for a) NV and b) P1. Data is shown in blue circles and the exponential fit is shown as a red line. Fit parameters are listed in the inset.

### 4.6.1 240GHz T<sub>2</sub>

Figure 7 shows T<sub>2</sub> relaxation values measured using Hahn Echo sequences on a 240GHz EPR system for NV- and P1 centers in four diamonds, plotted as a function of total defect concentration. Raw data and the exponential fits from which the data in Figure 7 was derived are shown in Figures 8 – 14. Due to the larger SNR from the more abundant P1 centers, their data is much less noisy and fit error thus much smaller than for the NV-centers.

Hahn Echo decays were measured twice for NV- and P1 defects in Sample #1 and for P1 defects in Sample #8. The open shapes in Figure 7 indicate the second measurements. In Sample #1 the second measurement of NV- and P1 T<sub>2</sub> relaxation times fall outside of the error bars from the first measurements, indicating that the fit error is insufficient to fully capture the uncertainty in the measurements.

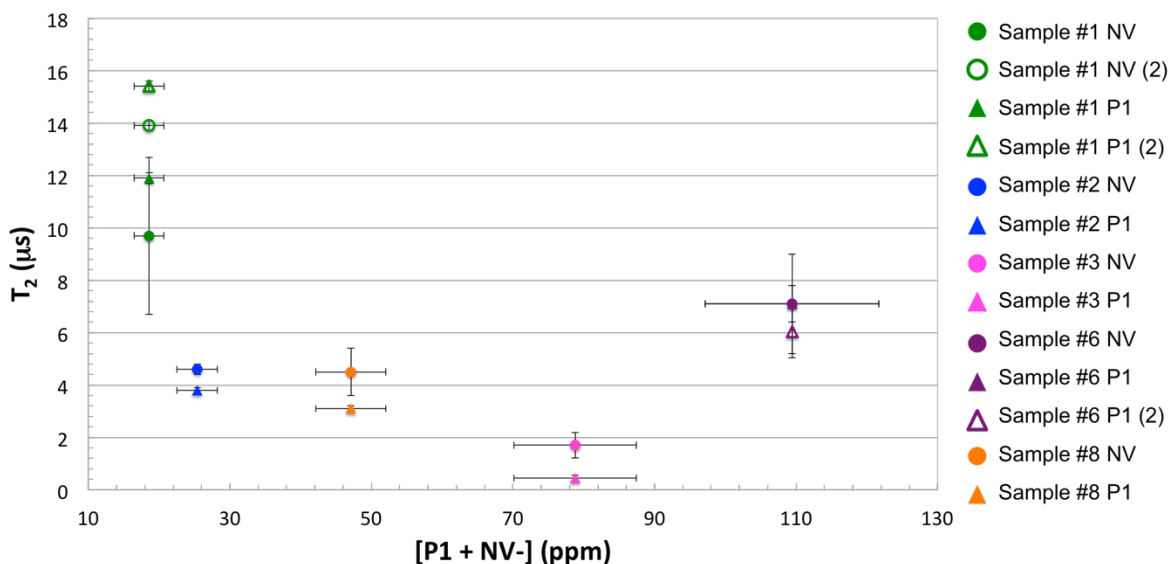


Figure 7 T<sub>2</sub> values at 240GHz for NV and P1 centers in five different samples plotted as a function of total defect concentration. Error bars are from the error in exponential fits to the echo data. T<sub>2</sub> values for NV and P1 in Sample #1 and P1 in Sample #8 were measured twice. These second measurements are marked with a (2) and represented by an open shape.

The T<sub>2</sub> measurement for P1 centers in Sample #1 was best fit to a stretched exponential with n=3/2, as seen in Figure 9. Spectral diffusion can cause T<sub>2</sub> relaxation to occur in the form of a stretched exponential with n between 0.5 and 2 in paramagnetic centers in solids<sup>21</sup>. When this occurs, the relaxation time is called the phase memory time, T<sub>M</sub>.



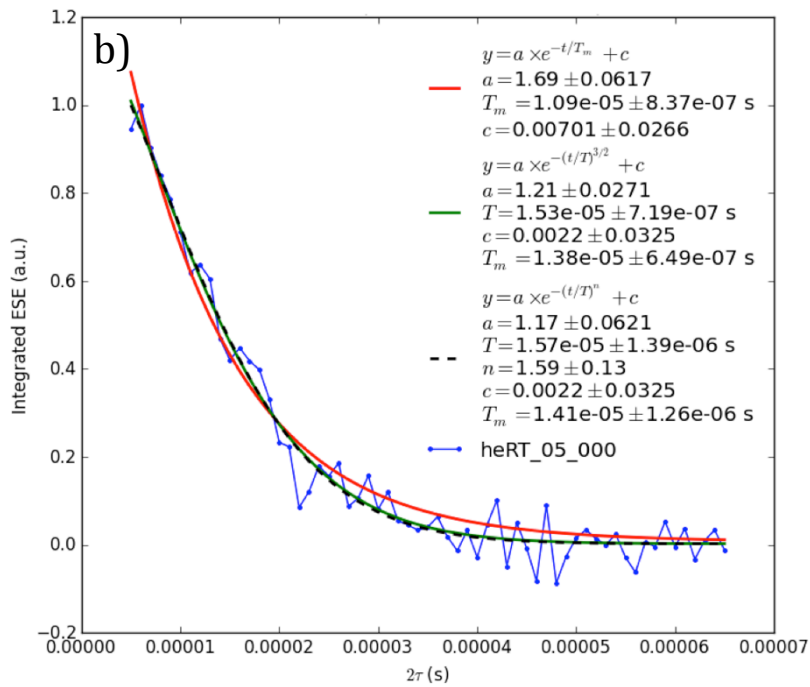
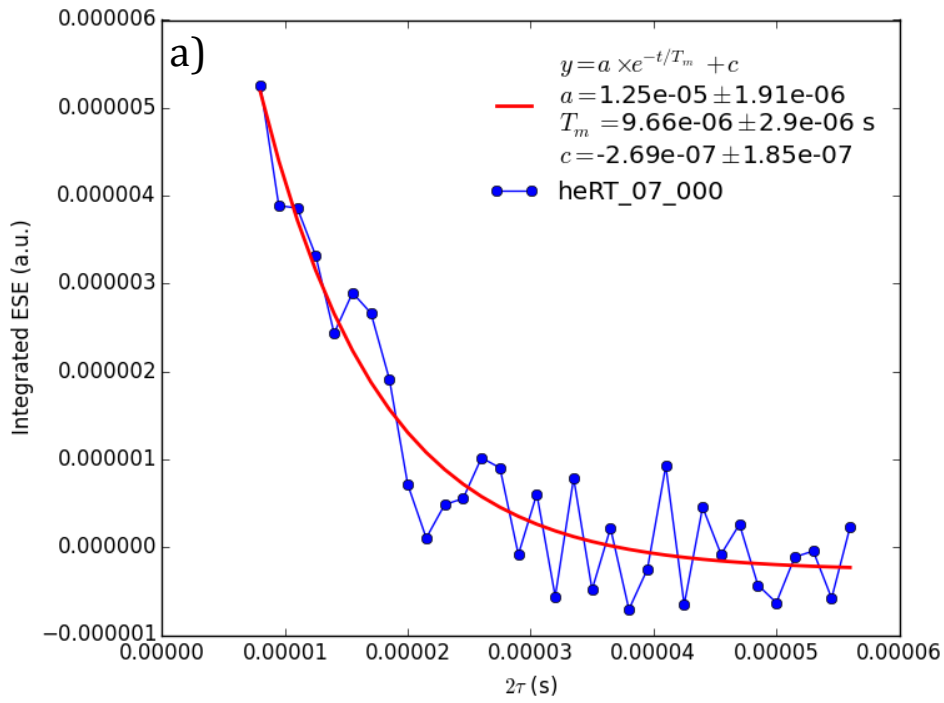


Figure 8 Hahn Echo data for NV in Sample #1. Taken on two separate dates. Data is shown in blue circles and the exponential fit is shown as a blue line. The second graph is also compared to a stretched exponential with a fixed stretch of 3/2 (green line) and a stretch left as a parameter (black dashed line). Due to the noise in the data, the non-stretched exponential (red) is taken as the best fit. All fit parameters are listed in the inset.

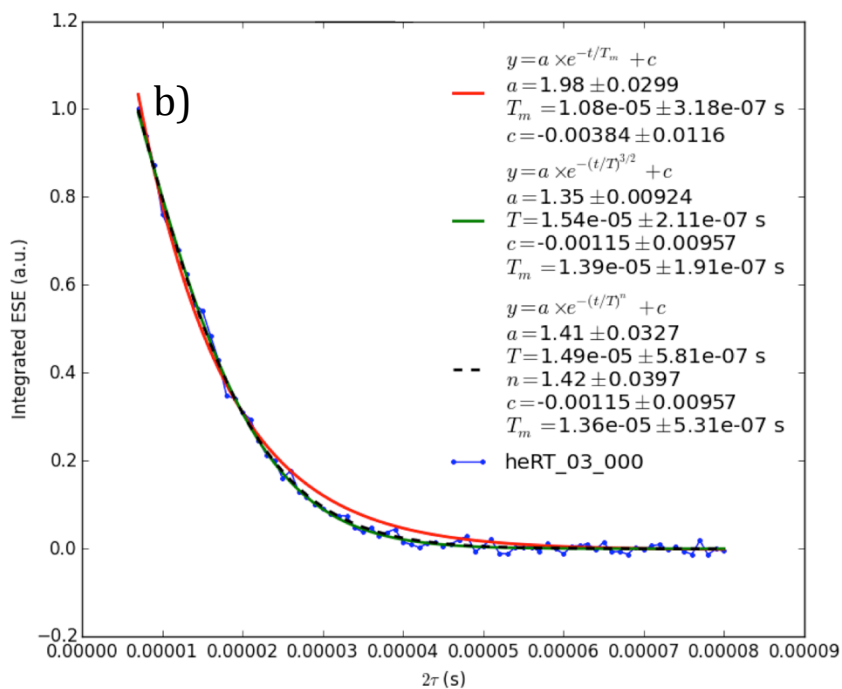
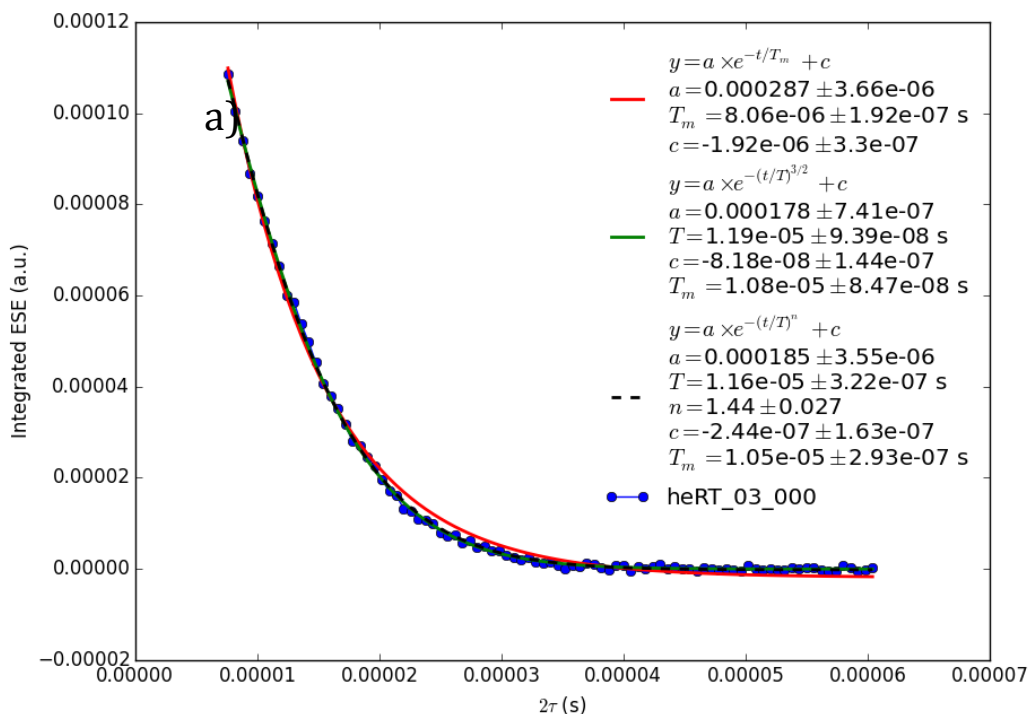


Figure 9 Hahn Echo data for P1 in Sample #1. Taken on two separate dates. Data is shown in blue circles and fits are shown for an exponential decay (red line), a stretched exponential with a fixed stretch of 3/2 (green line) and a stretch left as a parameter (black dashed line). All fit parameters are listed in the inset.

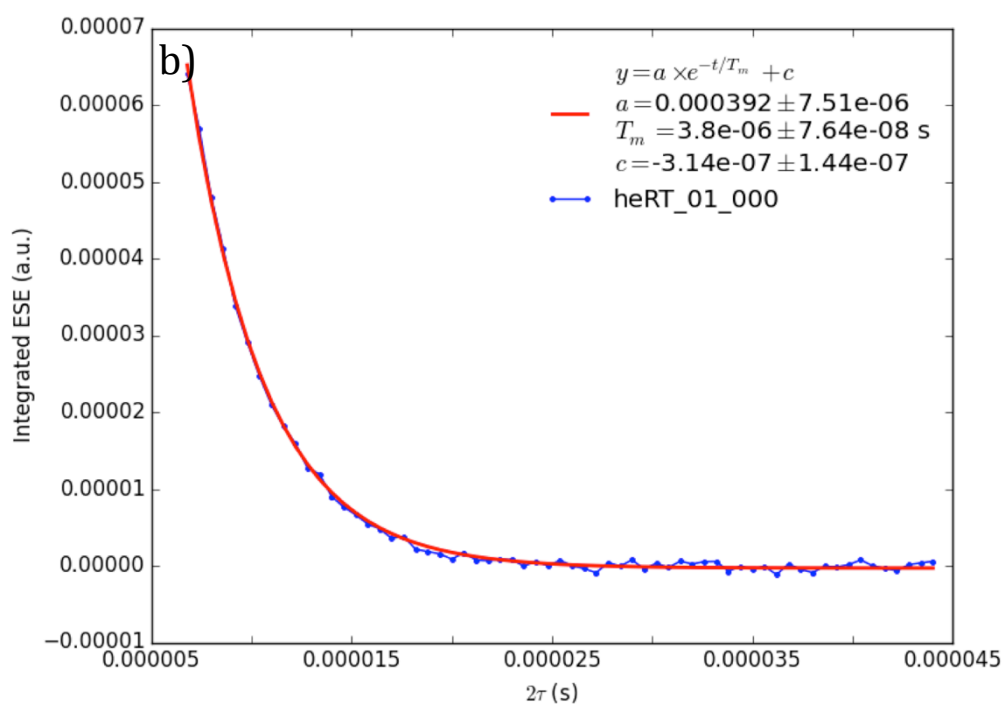
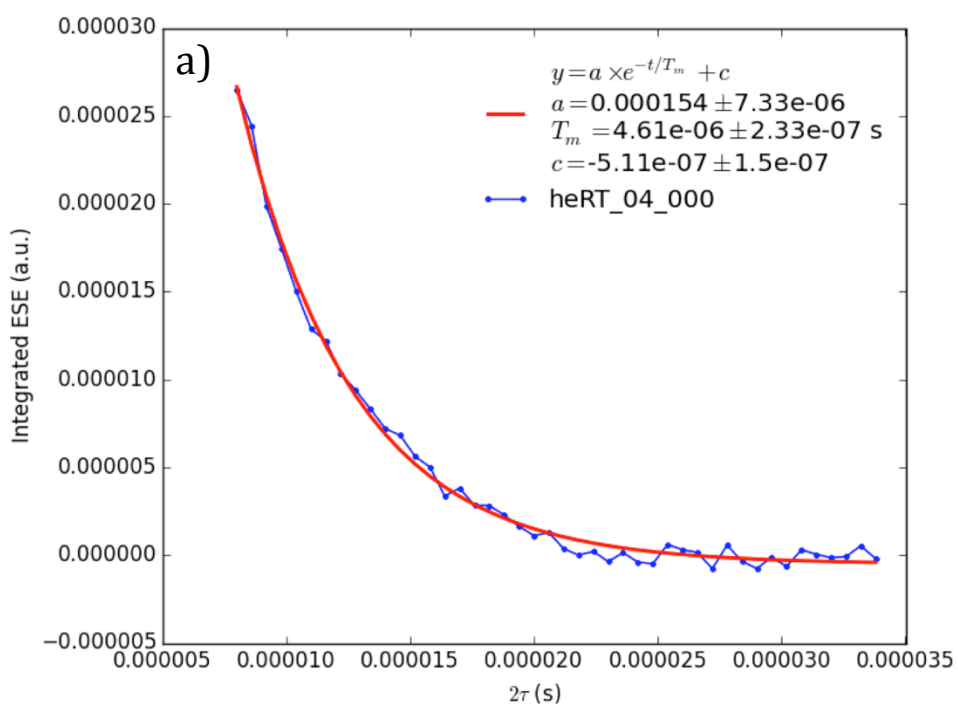


Figure 10 Hahn Echo data for a) NV and b) P1 in Sample #2. Data is shown in blue circles and the exponential fit is shown as a red line. Fit parameters are listed in the inset.

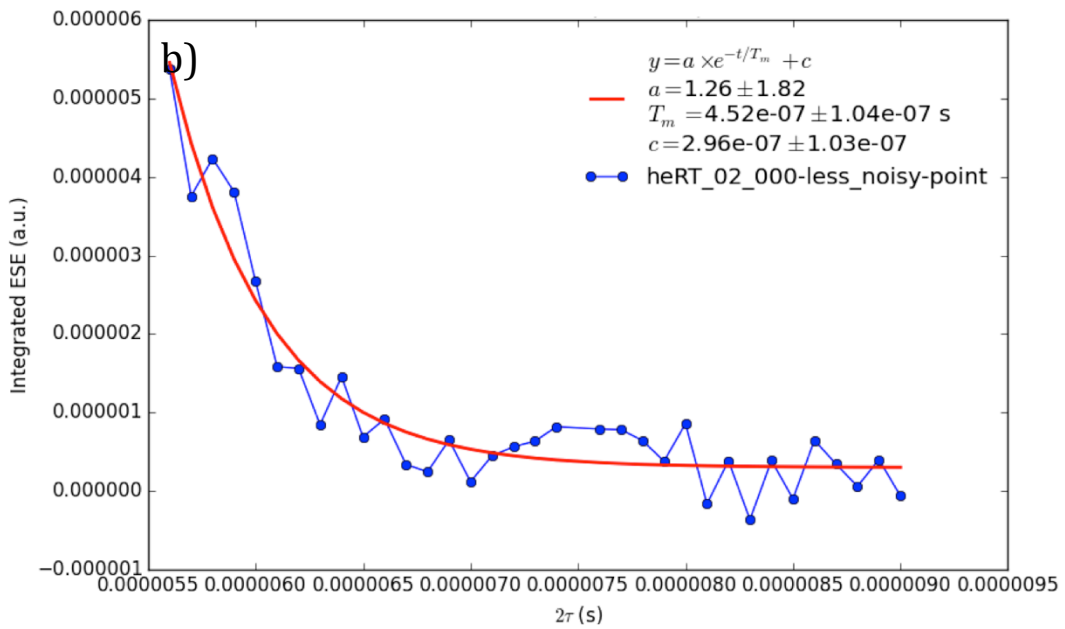
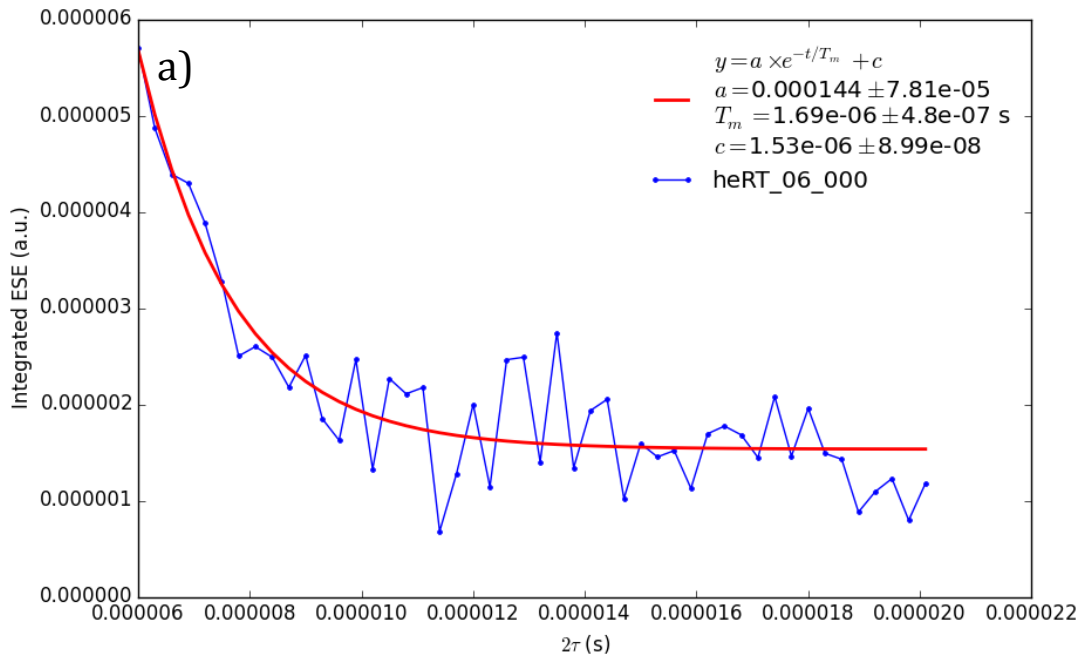


Figure 11 Hahn Echo data for a) NV and b) P1 in Sample #3. Data is shown in blue circles and the exponential fit is shown as a red line. Fit parameters are listed in the inset.

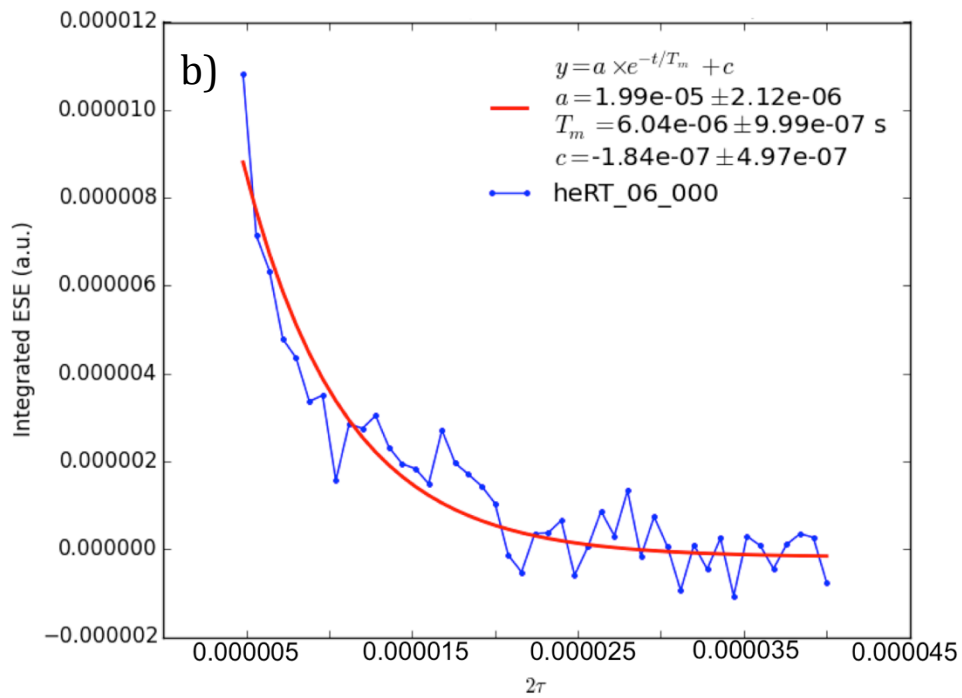
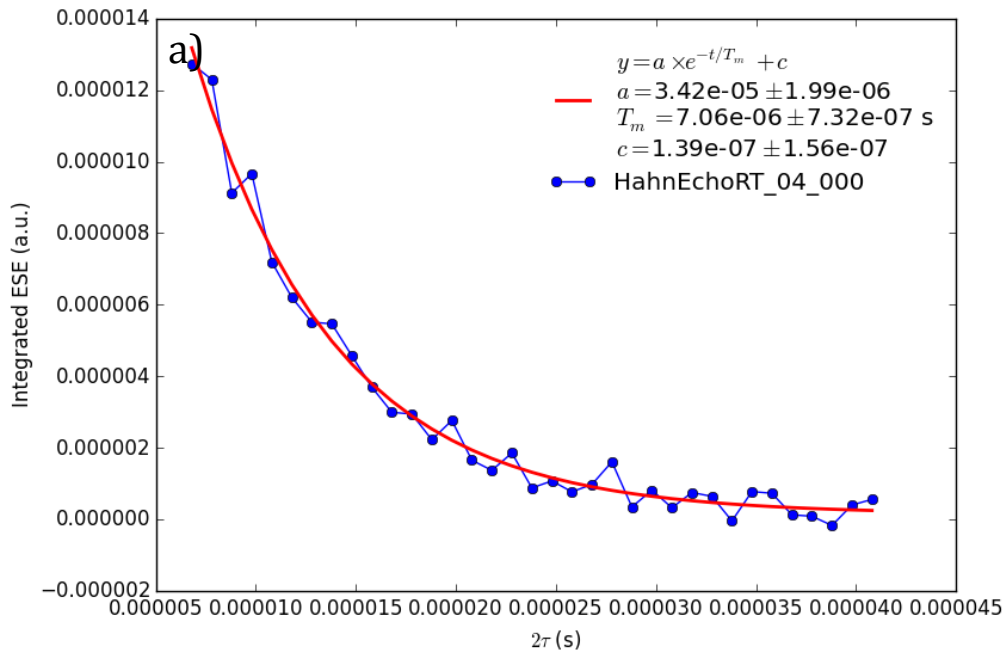


Figure 12 Hahn Echo data for P1 in Sample #6. Taken on two dates. Data is shown in blue circles and the exponential fit is shown as a red line. Fit parameters are listed in the inset.

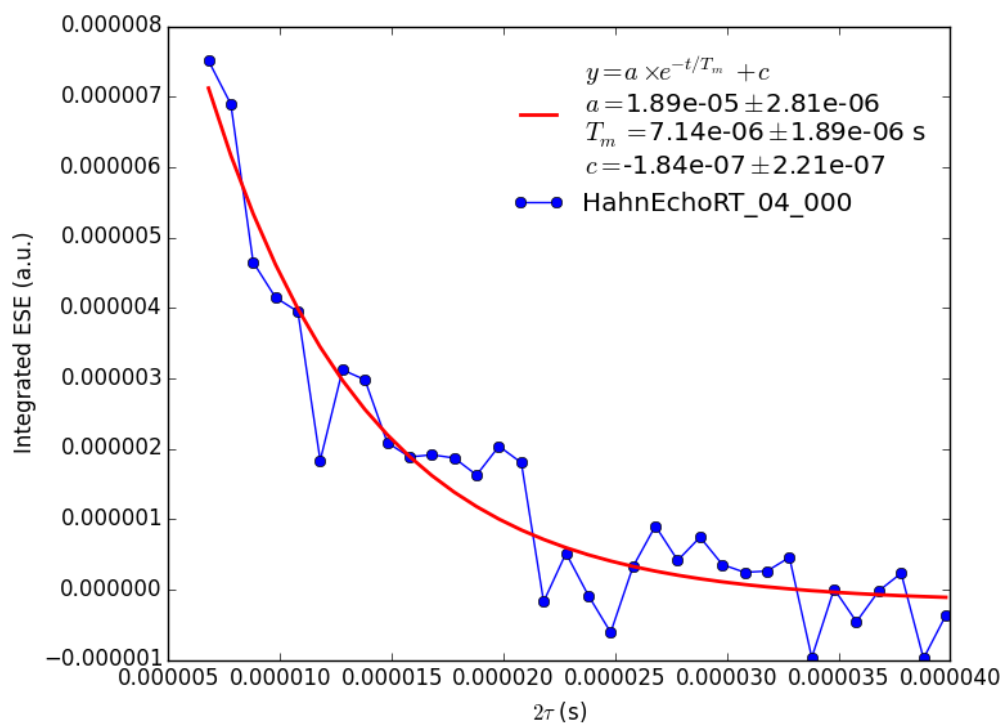


Figure 13 Hahn Echo data for NV in Sample #6. Data is shown in blue circles and the exponential fit is shown as a red line. Fit parameters are listed in the inset.

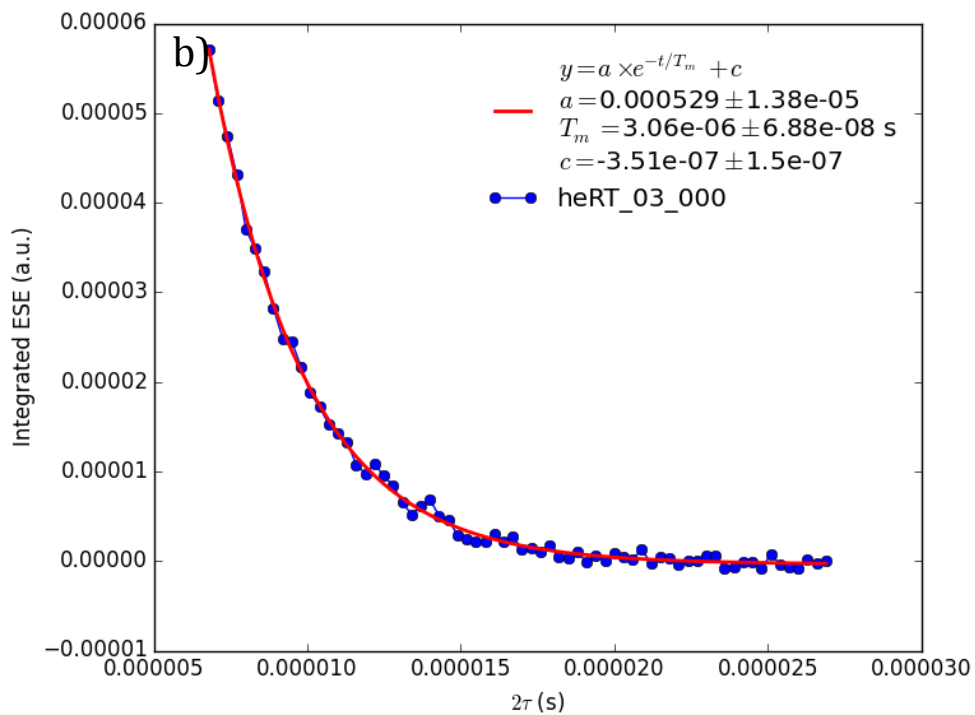
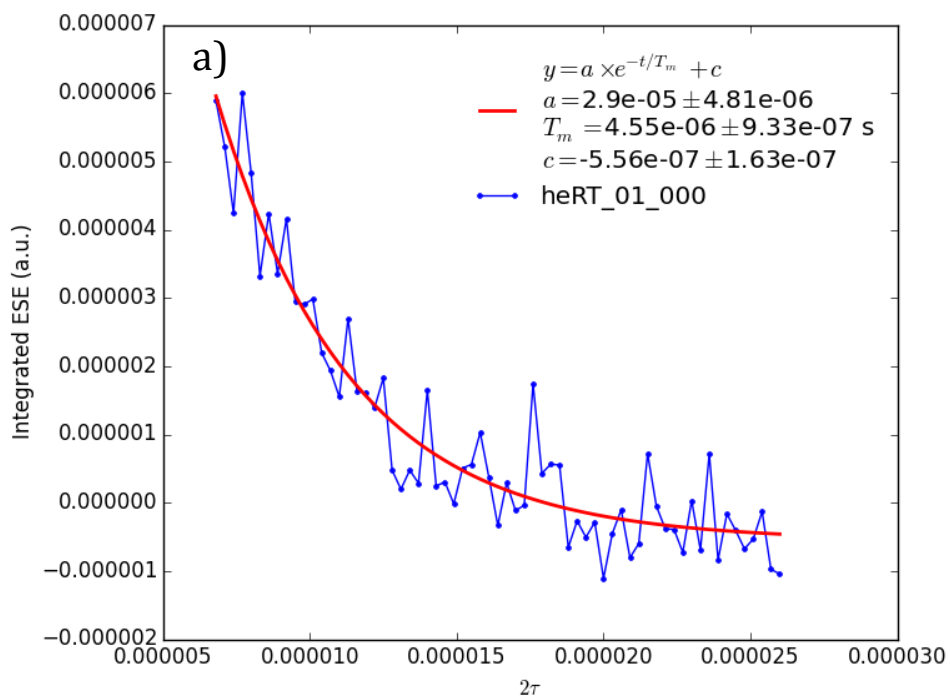


Figure 14 Hahn Echo data for a) NV and b) P1 in Sample #8. Data is shown in blue circles and the exponential fit is shown as a red line. Fit parameters are listed in the inset.

### 4.6.3 X-band T<sub>2</sub>

Figure 15 shows T<sub>2</sub> relaxation values measured using a Hahn Echo pulse sequence on a 9.6GHz (X-band) EPR system for NV- and P1 centers in three diamonds, plotted as a function of total defect concentration. Raw data and the exponential fits from which the data in Figure 15 was derived are shown in Figures 17 – 19.

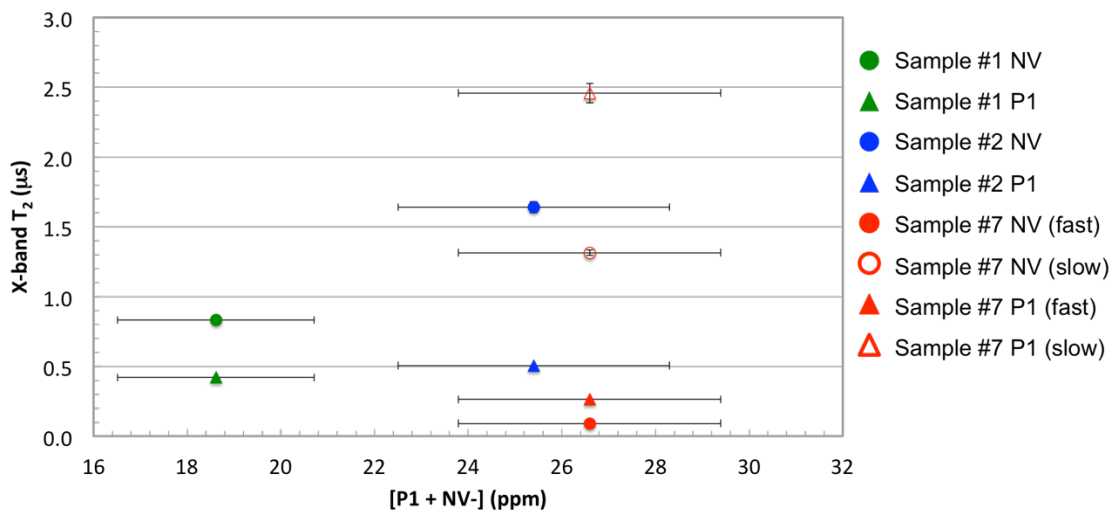


Figure 15 NV- and P1 center T<sub>2</sub> relaxation times measured using X-band EPR for three samples plotted as a function of total P1 and NV- concentration. Sample #7 was best fit to a double exponential. Both time constants are plotted. Error bars on T<sub>2</sub>, calculated from the error in the exponential fit parameter, are smaller than the marker for all but the slow P1 T<sub>2</sub> value in Sample #7.

As seen in Figure 19, Sample #7 X-band Hahn Echo data was best fit to a double exponential. This is likely due to two regions of different concentration within the sample. The inset to Figure 16 is a photograph of Sample #7. Two regions of distinct concentrations can clearly be identified by the difference in purple intensity. These regions could be the result of unique growth planes during crystal synthesis, which are known to incorporate nitrogen at different rates<sup>22</sup>. This would mean that the Sample #7 T<sub>2</sub> data in Figure 15 would better be plotted against the local concentration of each region. The fast relaxation times are attributed to a region of the diamond with a concentration greater than 26.5 ppm and the slow relaxation times are attributed to a region of the diamond with a concentration less than 26.5 ppm.

EPR spin counting on samples with masks limiting microwave absorption to local areas could provide local concentrations, but the low signal to noise precludes such experiments on these samples. Measuring the local strain using ODMR is another way to quantify the relative concentrations. These measurements were performed on Sample #7 with Claudia Avalos, and are shown in Figure 16. Strain is determined by the ODMR peak splitting. The light purple region had a strain of 2.38MHz and the dark purple region had a strain of 3.88MHz. The large strain difference (1.5MHz) confirms a difference in defect concentration between the two regions, but cannot confirm the exact concentrations without further calibration.



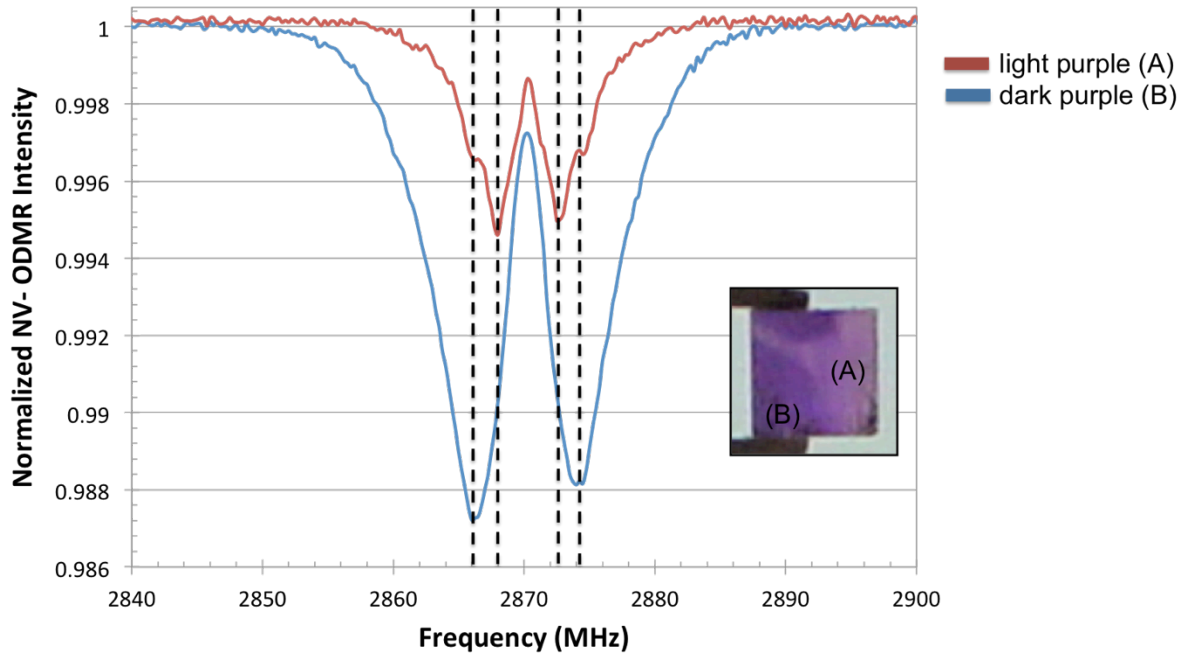


Figure 16 ODMR of NV- in Sample #7 taken in (A) light purple and (B) dark purple regions of sample. Inset is a photograph of Sample #7 with labeled regions.

Oscillations in the NV- X-band  $T_2$  decays are due to electron spin echo envelope modulation (ESEEM)<sup>21</sup>. ESEEM oscillations are the result of the microwave pulse flipping an electron spin and nuclear spin coupled to it. This nuclear spin prevents perfect refocusing of the echo modulated at electron-nuclear double resonance (ENDOR) frequencies. ESEEM is typically seen when isotropic hyperfine coupling is weak and anisotropic hyperfine coupling is comparable to the nuclear Zeeman interaction.

The ESEEM oscillation frequencies in the NV- X-band  $T_2$  decays were found by taking Fourier Transforms of the data, shown in Figure 20. These ESEEM oscillations occur at frequencies of about 3 MHz (Sample #1), 3MHz (Sample #2), and 5 MHz (Sample #7). These frequencies are on the order of magnitude of the NV-<sup>14</sup>N nuclear interactions. <sup>14</sup>N hyperfine coupling to the NV- center is  $A_{\text{parallel}} = -2.14$  MHz and  $A_{\text{perpendicular}} = -2.7$  MHz<sup>23</sup>. The nuclear quadrupole coupling of the <sup>14</sup>N of the NV- center is -5.04 MHz<sup>24</sup>.

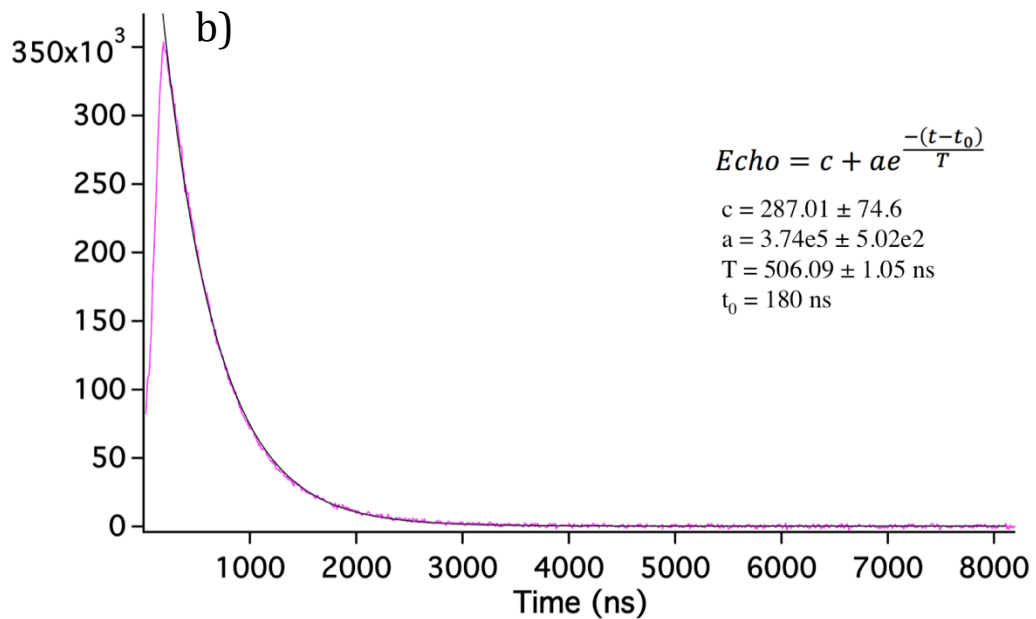
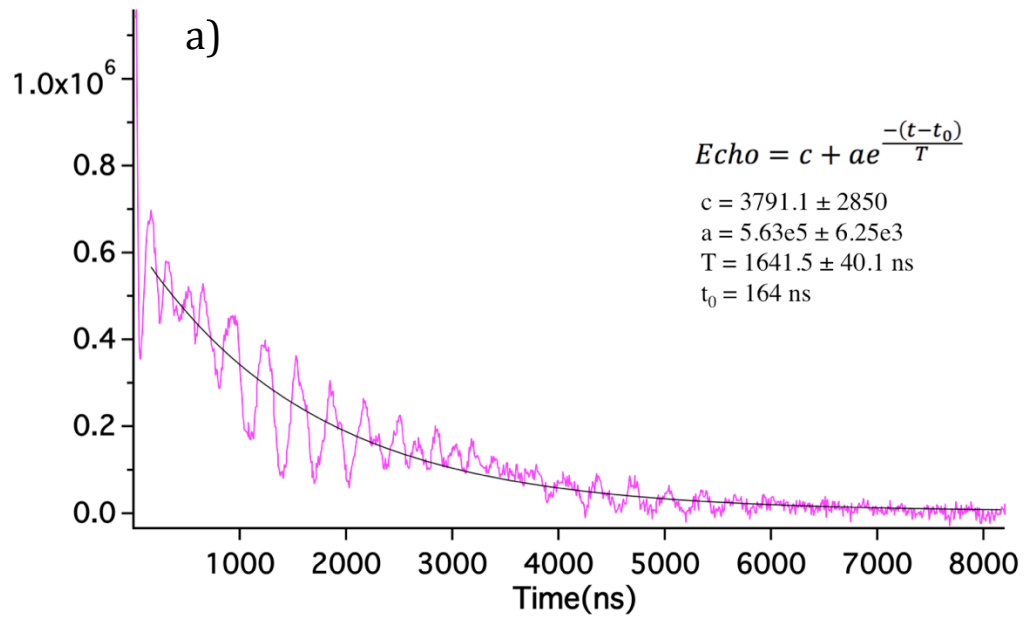


Figure 17 Hahn Echo data (pink) for Sample #2 probing the a) NV- and b) P1 centers. Modulation in a) is due to ESEEM mixing of hyperfine states. Fit parameters to Equation 1 are listed in the insets. Fits are plotted in black.

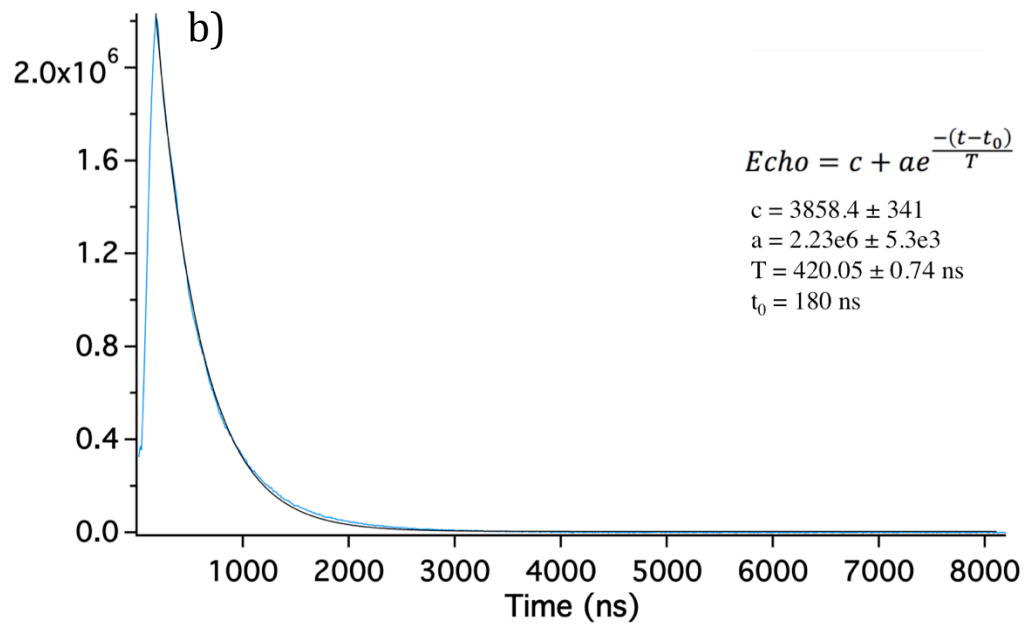
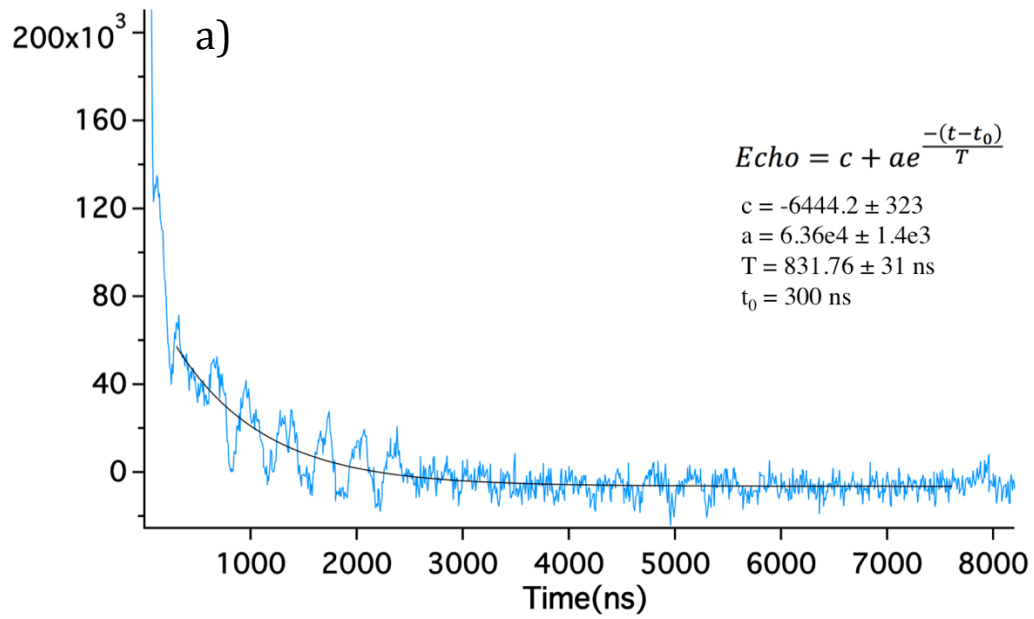


Figure 18 Hahn Echo data (blue) for Sample #1 probing the a) NV and b) P1 centers. Modulation in a) is due to ESEEM mixing of hyperfine states. Fit parameters to Equation 1 are listed in the insets. Fits are plotted in black.

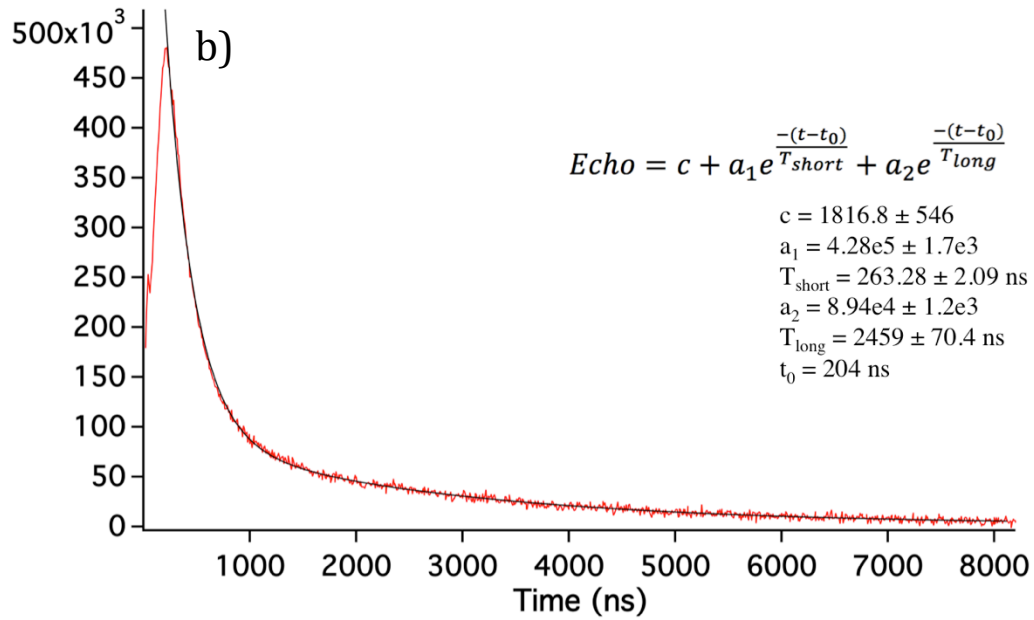
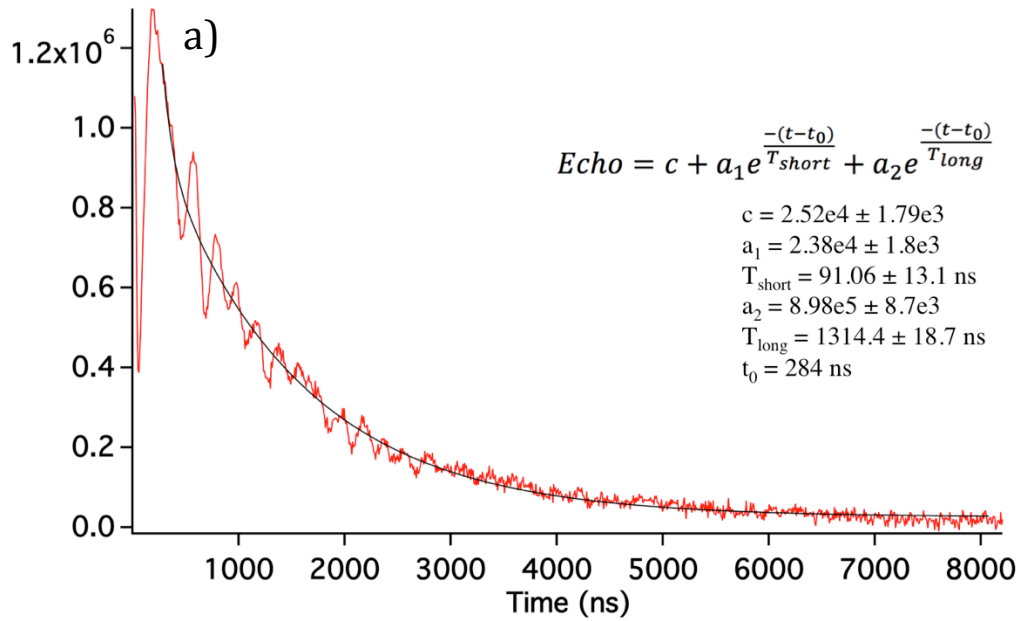


Figure 19 Hahn Echo data for Sample #7 probing the a) NV and b) P1 centers. Modulation in a) is due to ESEEM mixing of hyperfine states. Fit parameters to double exponentials, described by Equation 2, are listed in the insets. Fits are plotted in black.

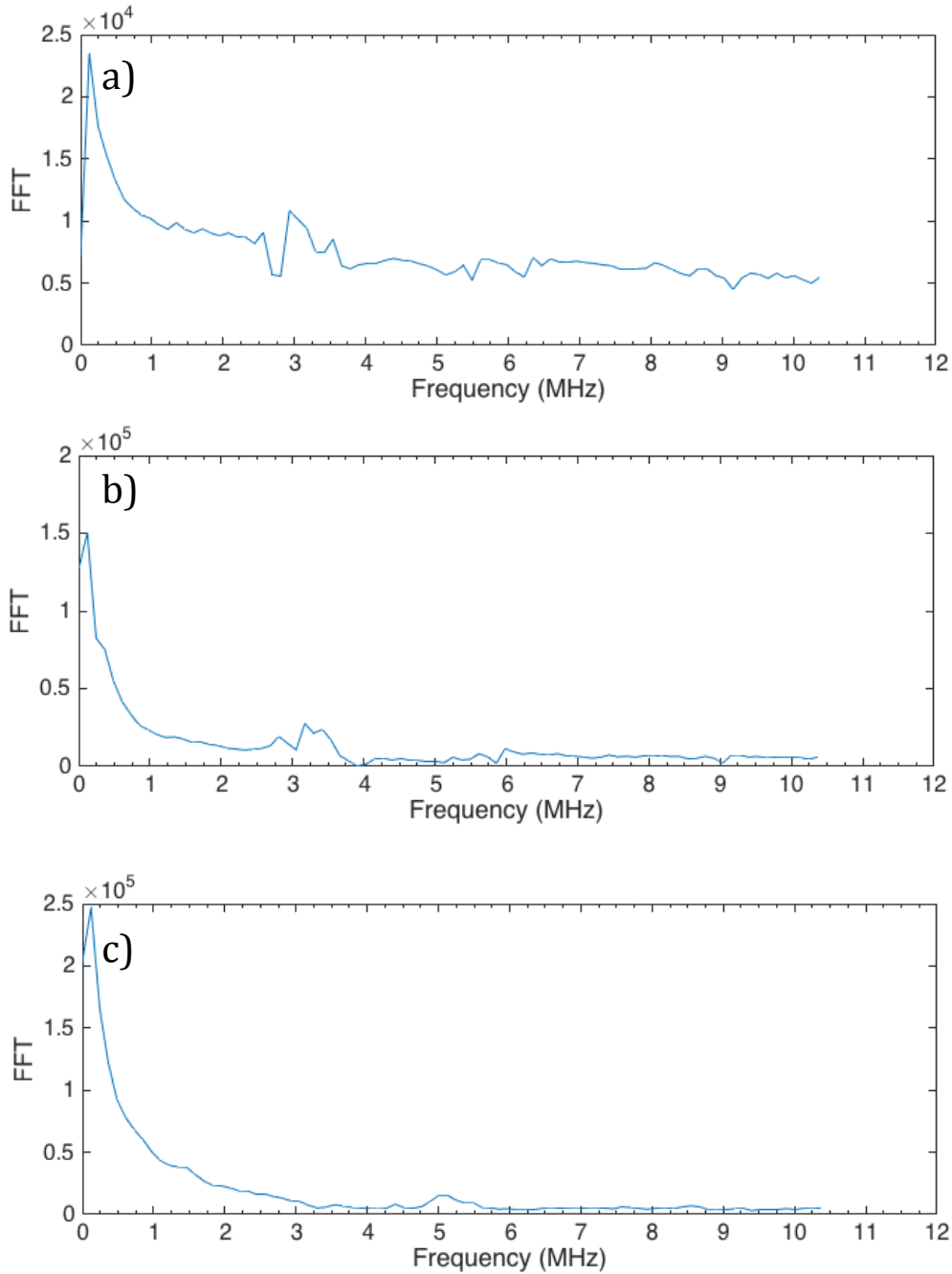


Figure 20 Fourier Transform of  $T_2$  Decays for a) Sample #1 b) Sample #2 and c) Sample #7. Peaks near 3 - 5 MHz appear at the frequencies of the ESEEM oscillations in the  $T_2$  decay curves

#### 4.6.4 Comparison of $T_2$ Measurements to Literature

Figure 21 summarizes the  $T_2$  relaxation times for P1 and NV- centers measured with X-band and 240GHz EPR and compares them to two fits and one simulation for concentration-dependent P1 relaxation times in the literature <sup>15,17,18</sup>. A direct

comparison is complicated by the fact that literature values are measured in diamonds without NV- defects.

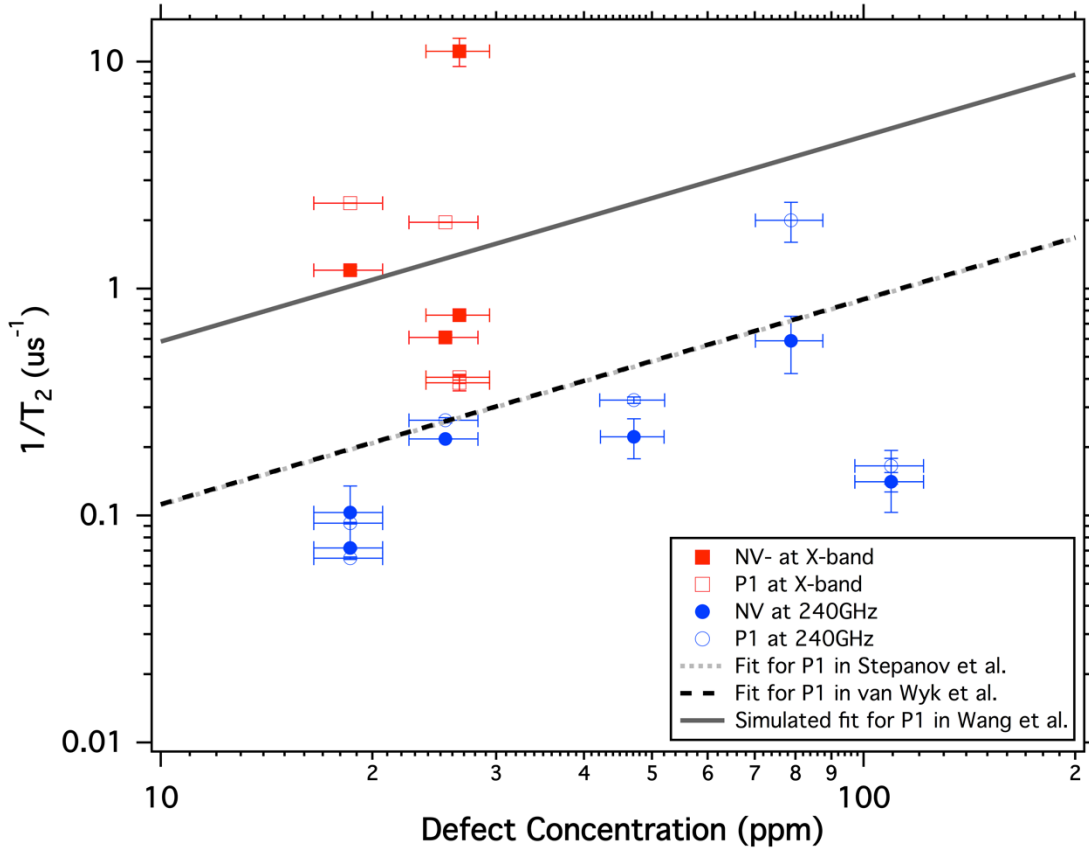


Figure 21  $T_2$  values for NV- and P1 defects at X-band (squares) and 240GHz (circles) as well as literature fits and simulations for  $T_2$  relaxation rates of P1 centers in 'yellow' (no NV-) diamonds <sup>15,17,18</sup>.

## 6.5 Conclusion

We have presented  $T_1$  and  $T_2$  relaxation times for NV- and P1 defects measured using X-band and 240GHz EPR in diamonds with total defect concentrations ranging between 10 - 110 ppm. NV- relaxation times were consistently longer than P1 relaxation times in the same sample.

NV-  $T_1$  times at 240GHz ranged from 3.4-5.2 ms. P1  $T_1$  times at 240GHz ranged from 1.8-2.3 ms. NV-  $T_2$  times at 240GHz ranged from 1.7-13.9us. NV-  $T_2$  times at 9.6GHz ranged from 0.1-1.6us. P1  $T_2$  times at 9.6GHz ranged from 0.3-2.5 us. In Sample #7, which has visually observable defect concentration inhomogeneity, both NV- and P1 defect relaxation curves at X-band were best fit to double exponential functions. At 240GHz, both NV- and P1 defect relaxations in Sample #7 were best fit to stretched exponentials.

Room temperature relaxation measurements for NV- and P1 defects in diamond are restricted by low defect concentrations and small sample sizes. Poor repeatability could be due to orientation dependence <sup>20</sup>. Future work should seek to improve signal-to-noise ratio

and repeatability, as well as understand why some  $T_2$  relaxation times are best fit by stretched exponentials.

## 6.6 Acknowledgements

240GHz relaxation time constants were measured in collaboration with Blake Wilson, Nick Agladze, and Mark Sherwin of the ITST facility at UC Santa Barbara. X-band  $T_2$  relaxation times were measured in collaboration with Tim Keller and Songi Han at UC Santa Barbara. Claudia Avalos measured the ODMR data in the lab of Alex Pines at UC Berkeley.

# 7 NV- Spin Polarization: Dependence on Orientation and P1 Concentration

---

## 7.1 Abstract

This chapter presents a quantitative, systematic study of the polarization of the Zeeman magnetic sublevels of the NV- defect in diamond as a function of magnetic field alignment relative to the NV- defect axis. The orientation dependence of NV- polarization in the lab frame is accounted for by a Wigner rotation of a constant defect frame polarization. We also find that the NV- defect polarizations vary with the P1 defect concentration, and that the polarization of the  $m_s=0$  state with optical pumping decreases from 46% to 36% in samples as P1 concentrations vary from 20ppm to 100ppm, respectively. This work was previously published <sup>1</sup>.

## 7.2 Introduction

While many applications utilize single defects aligned with an applied magnetic field, understanding orientation dependence of NV- polarization is important for applications involving ensembles of defects in single crystals as well as defects in nanodiamonds. For example, significant bulk <sup>13</sup>C nuclear polarization has been measured in NV-doped diamonds subject to optical pumping of the ensemble of NV- defects at large (7T) magnetic fields<sup>2,3</sup>. The quantum mechanical processes that yield this nuclear hyperpolarization remain unclear, and modeling the phenomena likely requires an understanding of each NV-defect polarization at a given orientation to the field. Previous work shows the maximum NV- polarization occurs when the NV- defect axis is aligned with an applied magnetic field and has been observed to decrease with misalignment through spin dependent photoluminescence <sup>4,5</sup> and defect-mediated nuclear polarization <sup>6</sup>.

Polarization into the  $m_s=0$  sublevel can be quantified through a comparison of dark and optically illuminated EPR spectra<sup>7,8</sup>. Here we use that method to study of the effect of magnetic field orientation on the polarization of the NV- Zeeman sub-levels. We further introduce a different method for calculating these polarizations that does not rely on assumptions about the relative magnitudes of  $m_s=\pm 1$  polarization <sup>7,8</sup>. The maximum NV-polarizations are compared across a number of samples with varying NV- and P1 defect concentrations.

## 7.3 Methods

### 7.3.1 Polarization of NV as a function of Field Alignment and P1 Concentration

The sample used for the orientation study is Sample #1 <sup>3</sup> with an NV- concentration of  $1.9 \pm 0.2$  ppm and a P1 concentration of  $24 \pm 3$  ppm. X-ray diffraction was used to determine the in-plane crystal orientation to be  $\langle 110 \rangle$  along the sample edges and  $\langle 100 \rangle$  along the corners. The samples used to probe polarization as a function of defect concentration have also been characterized previously as samples #1-8 (See Chapter 2) <sup>3</sup>.



X-band CW EPR experiments were performed at room temperature with a modified Active Spectrum extended range benchtop EPR system. Optical access to the sample was added perpendicular to the magnetic field direction by mounting a 45-degree mirror underneath an existing hole in the bottom of the microwave cavity. Samples were mounted on the end of a fiberglass rod cut at an angle that allowed one of the four NV- defect axes to be aligned with the field while exposing the large diamond face to the direction of laser propagation. The microwave power incident on the cavity was set to 0.00158 mW. Spectra were recorded with 100 data points per mT using a conversion time of 100 ms, a modulation frequency of 43 kHz, and amplitude of 0.2 mT. Defect alignment relative to the magnetic field was adjusted by rotating the sample mount about the laser propagation axis. Sample position relative to the field was determined by adjusting azimuthal and polar angles in an EasySpin simulation of the EPR spectrum until NV- peak positions matched those of the experimental spectrum <sup>9</sup>. A sample EPR spectrum and simulation overlay are depicted in Figure 1a. NV- parameters used in the EasySpin simulation are given in table 1. The symmetry of the diamond crystal dictates that for each orientation of a crystal axis in the magnetic field there will be four orientations of the NV- bond direction. Thus every EPR spectrum provides data for four unique defect orientations relative to the magnetic field. EasySpin simulations were also used to correctly assign the two transitions as  $m_s=0$  to  $m_s=+1$  or  $m_s=0$  to  $m_s=-1$ , which change sides of the spectrum under certain orientations.

Spectra were acquired with (1 scan) and without (30 scans) 600mW 532nm circularly polarized laser light at each sample orientation. Using circularly polarized light and rotating the sample about the laser propagation axis allowed field alignment to be adjusted without introducing differences in laser absorption. Spectra were fit to sums of first derivative Tsallian lineshapes <sup>10</sup>. To avoid baseline problems and for more accurate results <sup>11</sup>, double integration was carried out on line fits of the derivative spectra. An example EPR spectrum and fits are depicted in Figure 1b,c.

**Table 1 Defect parameters used in EasySpin simulations for calculating NV- orientation from EPR peak positions**

Parameter	Value	Reference
$g_{NV}$	2.0028	Loubser and van Wyk [12]
$g_{P1}$	2.0024	Smith et al. <sup>13</sup>
$D_{NV}$	2880 MHz	Loubser and van Wyk <sup>12</sup>
$A_{P1}^{14N}$	$A_{\perp} = 81$ MHz $A_{\parallel} = 115$ MHz	Smith et al. <sup>13</sup>
$A_{P1}^{13C}$	$A_{\perp} = 141.8$ MHz $A_{\parallel} = 340.8$ MHz	Cox et al. <sup>14</sup>

### 7.3.2 EPR Signal as a Function of Light Intensity

NV- EPR signal intensity was measured as a function of laser intensity for four samples. Samples all showed a maximum EPR intensity in the range of 10-30 mW/mm<sup>2</sup>. Furthermore, it is unintuitive why higher concentration samples would saturate at lower laser intensities. As discussed in Section 7.4.4, photo-ionization or increased relaxation from P1 centers may explain these results.

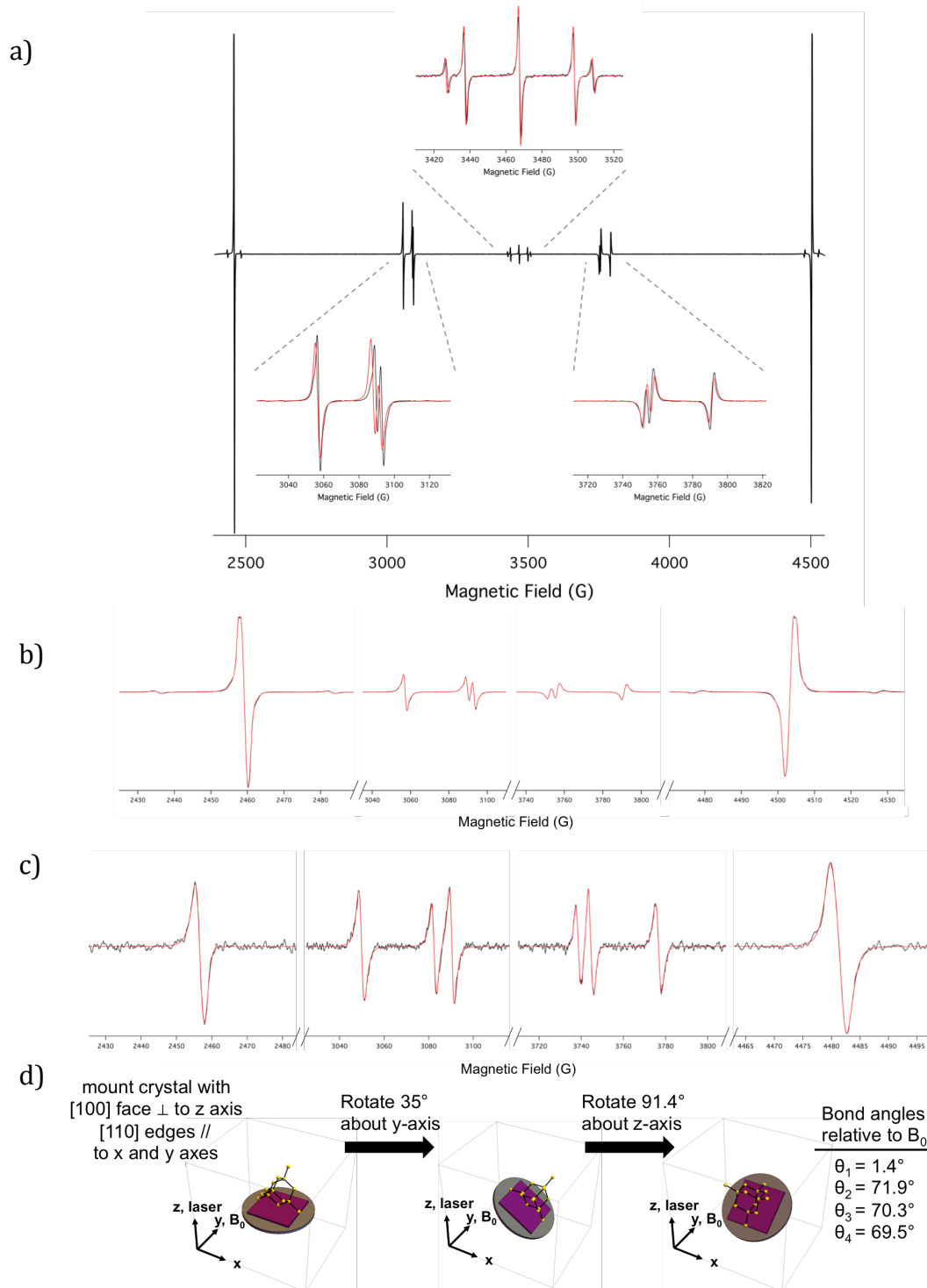


Figure 1 a) Single scan X-band CW EPR spectrum under  $30.6\text{mW/mm}^2$  of 532nm circularly polarized illumination (black) with insets of EasySpin simulation (red) using NV- angles relative to  $B_0$  field of  $1.4^\circ$ ,  $71.9^\circ$ ,  $70.3^\circ$ ,  $69.5^\circ$ . Central peaks are from P1 centers. b) NV- EPR peaks from a) (black) fit to sums of Tsallian curves (red). c) NV- EPR spectra (30 scans) without illumination (black) fit to sums of Tsallian curves (red). Spectra in b) and c) were acquired at the same orientation. Vertical axis in c) is scaled 340x greater than in b). d) Crystal mounting procedure and final orientation relative to  $B_0$  and the laser propagation axis for experimental data and corresponding simulations depicted in a). Ball and stick model represents diamond lattice relative to the faces and edges of the diamond crystal (purple square). Grey circle represents bottom of sample mount used in the EPR cavity.

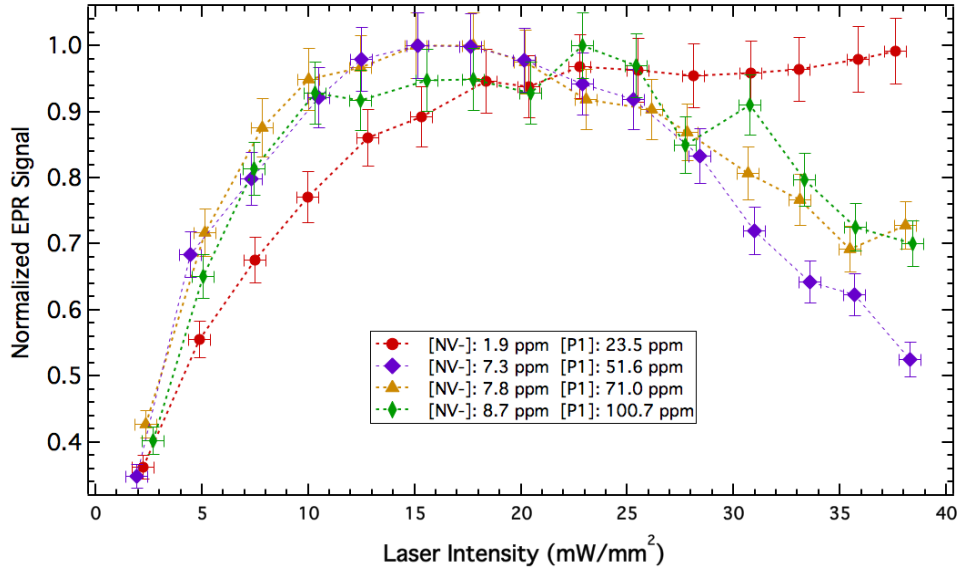


Figure 2 Normalized laser saturation curves for several diamonds via measured NV- EPR signals. Dashed lines are guides for the eye. Data acquired under illumination by a 532nm laser with 5mm beam diameter. Laser intensity was adjusted by increasing laser power from 50-750mW. Red circle data points are from the diamond used in the NV polarization as a function of field alignment study. Defect concentrations were found using spin counting EPR techniques in a previous study<sup>3</sup>.

## 7.4 Polarization of NV as a function of Field Alignment and P1 Concentration

### 7.4.1 Calculating Laser-illuminated Polarizations from Thermal Polarizations

Populations of the three NV- eigenstates under illumination were calculated using the following set of equations:

$$P_{+1,L} = P_{0,L} - (P_{0,D} - P_{+1,D}) \frac{A_{+,L}}{A_{+,D}} \quad (1)$$

$$P_{0,L} = \frac{1}{3} \left[ 1 + (P_{0,D} - P_{-1,D}) \frac{A_{-,L}}{A_{-,D}} + (P_{0,D} - P_{+1,D}) \frac{A_{+,L}}{A_{+,D}} \right] \quad (2)$$

$$P_{-1,L} = P_{0,L} - (P_{0,D} - P_{-1,D}) \frac{A_{-,L}}{A_{-,D}} \quad (3)$$

Subscripts L and D represent laser-on and dark experiments, respectively. The subscripts +1, 0, and -1 represent the corresponding NV- magnetic sublevel, and + and - represent the 0 to +1 and 0 to -1 NV- EPR transitions, respectively. P is the population of the energy level and A is the EPR double integral. Thermal populations in the dark were calculated from Boltzmann distributions using measured experimental temperatures and calculated energies at the experimental defect orientations.

Equations 1-3 are rearrangements of Equations 4-6. Given the experimental restriction of operating in the linear regime of the power saturation curve, the double integral of the dispersive EPR line shapes is proportional to the population difference of the states involved in the transition. Equations 4 and 5 relate the ratios of population differences to EPR signal area for each of the NV- transitions. Equation 6 states that the fractional populations must sum to unity.

$$\frac{P_{0,L}-P_{+1,L}}{A_{+,L}} = \frac{P_{0,D}-P_{+1,D}}{A_{+,D}} \quad (4)$$

$$\frac{P_{0,L}-P_{-1,L}}{A_{-,L}} = \frac{P_{0,D}-P_{-1,D}}{A_{-,D}} \quad (5)$$

$$P_{+1,L} + P_{0,L} + P_{-1,L} = 1 \quad (6)$$

#### 7.4.2 Rotating the Hamiltonian into the Lab Frame

The NV- center Hamiltonian is composed of three terms, representing the Zeeman interaction, the zero field splitting interaction, and crystal strain. Wigner rotations were used to put all interactions into the laboratory frame, which we define as having a z-axis parallel to the applied  $B_0$  field of the X-band EPR apparatus. The Zeeman interaction term ( $\gamma B_0 S_z$ ) is therefore already in the correct frame. However, the zero field splitting ( $D(S_z^2 - S(S+1)/3)$ ) and crystal strain ( $E(S_+^2 + S_-^2)$ ) terms are represented in the defect frame and need to be rotated into the laboratory frame.

We first represent the terms as a spherical tensor ( $\hat{T}_\mu^{(\omega)}$ ), where  $\omega$  is the rank of the tensor. We then determine the Wigner Rotation ( $D_{q\mu}^{(\omega)}$ ) needed to transform the tensor into the new basis, which is defined by the relationship:

$$R\hat{T}_\mu^{(\omega)}R^{-1} = \sum_{q=-\omega}^{\omega} D_{q\mu}^{(\omega)}T_q^{(\omega)} \quad (7)$$

We use the secular approximation that  $q=0$  because only  $T_0^{(2)}$  commutes with the Zeeman term. Both the zero field splitting and crystal strain terms are rank 2. Based on the change in angular momentum induced by the spin operators, it is easy to see that the zero field splitting and crystal strain terms belong to  $\mu=0$  and  $\mu=\pm 2$ , respectively.

$$D\left(S_z^2 - \frac{S(S+1)}{3}\right) \rightarrow D\left(\hat{T}_0^{(2)}\right) \quad (8)$$

$$R\hat{T}_0^{(2)}R^{-1} = \sum_{q=-2}^2 D_{q0}^{(2)}T_q^{(2)} = D_{00}^{(2)}T_0^{(2)} = \left(\frac{3\cos^2\theta-1}{2}\right)T_0^{(2)} \quad (9)$$

$$E(S_+^2 + S_-^2) \rightarrow E\left(\hat{T}_{\pm 2}^{(2)}\right) \quad (10)$$

$$R\hat{T}_{\pm 2}^{(2)}R^{-1} = \sum_{q=-2}^2 D_{q\pm 2}^{(2)}T_q^{(2)} = D_{0\pm 2}^{(2)}T_0^{(2)} = \left(\sqrt{\frac{3}{8}}\sin^2\theta\right)T_0^{(2)} \quad (11)$$

The NV- Hamiltonian in the lab frame is then:

$$H = \gamma B_0 S_Z + D \left( \frac{3\cos^2\theta - 1}{2} \right) \left( S_Z^2 - \frac{S(S+1)}{3} \right) + E \left( \sqrt{\frac{3}{8}} \sin^2\theta \right) (S_+^2 + S_-^2) \quad (12)$$

The following expressions relate the lab-frame populations ( $P_{+1}$ ,  $P_0$ ,  $P_{-1}$ ) to the defect-frame populations ( $P'_{+1}$ ,  $P'_0$ ,  $P'_{-1}$ ), through a Wigner Rotation. Figure 3 plots these populations as a function of defect angle with respect to the magnetic field. See Appendix C for the full derivation.

$$P_{+1} = d(\theta)_{11}^2 P'_{+1} + d(\theta)_{01}^2 P'_0 + d(\theta)_{-11}^2 P'_{-1} \quad (13)$$

$$P_0 = d(\theta)_{10}^2 P'_{+1} + d(\theta)_{00}^2 P'_0 + d(\theta)_{-10}^2 P'_{-1} \quad (14)$$

$$P_{-1} = d(\theta)_{1-1}^2 P'_{+1} + d(\theta)_{0-1}^2 P'_0 + d(\theta)_{-1-1}^2 P'_{-1} \quad (15)$$

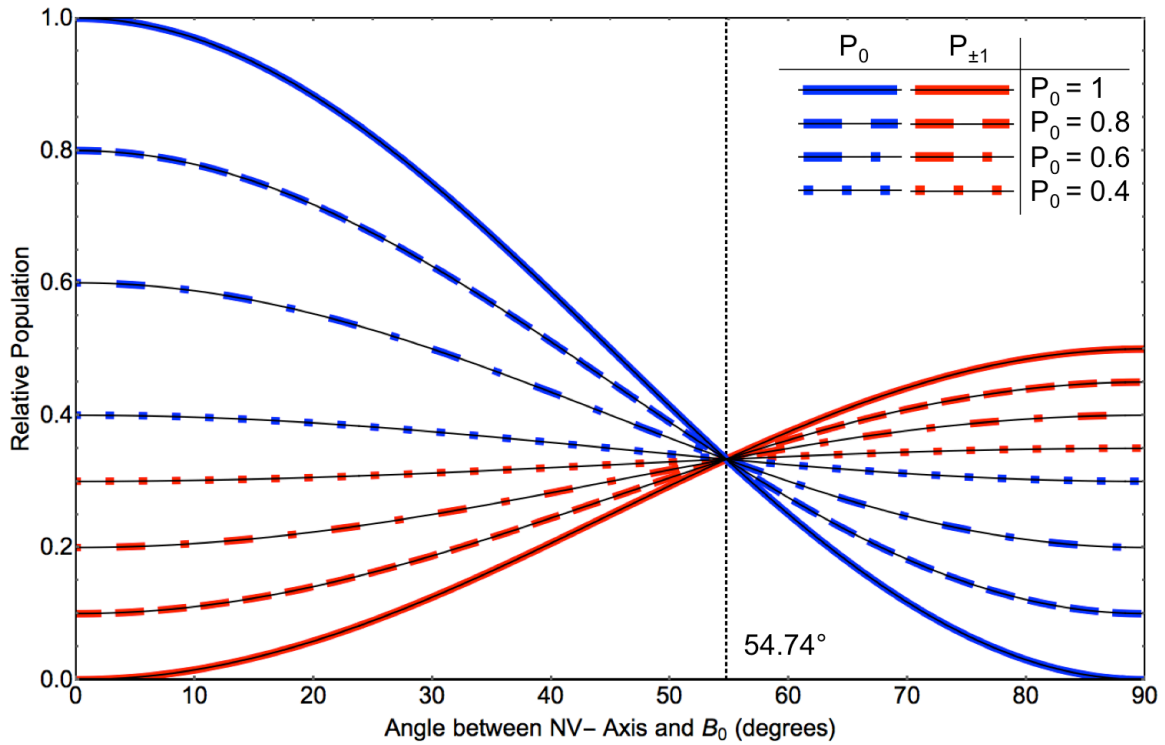
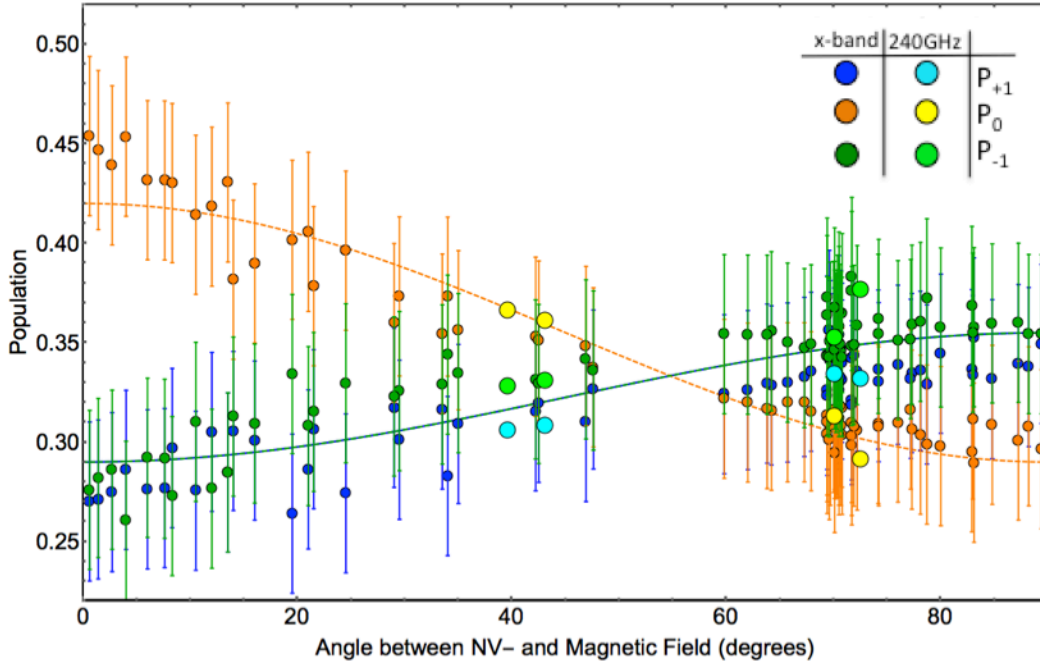


Figure 3 Graphical depiction of Equations 13-15 for given  $P_0'$  values, which are equivalent to  $P_0$  when a defect is aligned with the field (0 degree angle). If the data falls on any of these lines, it means the polarization is constant in the defect frame ( $P'_0$ ,  $P'_{+1}$ ,  $P'_{-1}$  are constant), and the orientation-dependence is fully accounted for by a Wigner rotation into the laboratory reference frame.

### 7.4.3 NV Polarization as a Function of Field Alignment

Figure 4 shows the calculated NV- populations as a function of NV- bond axis angle relative to the magnetic field. When the magnetic field is aligned parallel to the NV- defect axis the derived population of the  $m_s=0$  state is  $0.45 \pm 0.04$ , in agreement with room temperature X-band values reported previously in the literature ( $0.42 \pm 0.04$ )<sup>7</sup>. The populations of  $m_s = \pm 1$  were confirmed to be equal within experimental error. Our error in the calculated NV-bond axis angle relative to the field is estimated to be within 0.5 degrees based on multiple EasySpin fits to the same spectrum. Thus the error is approximately equal to the marker

size in Figure 4. To determine error in the calculated populations ( $\pm 0.02$ ), multiple spectra were acquired at the same orientation, separately fit, and integrated. This error is perhaps better assessed from the spread in populations around  $70^\circ$  misalignment (Figure 3). While the orientations were never exactly reproduced, we find a variation of approximately ( $\pm 0.04$ ) in the clustering of data points, which was used in plotting the error bars.



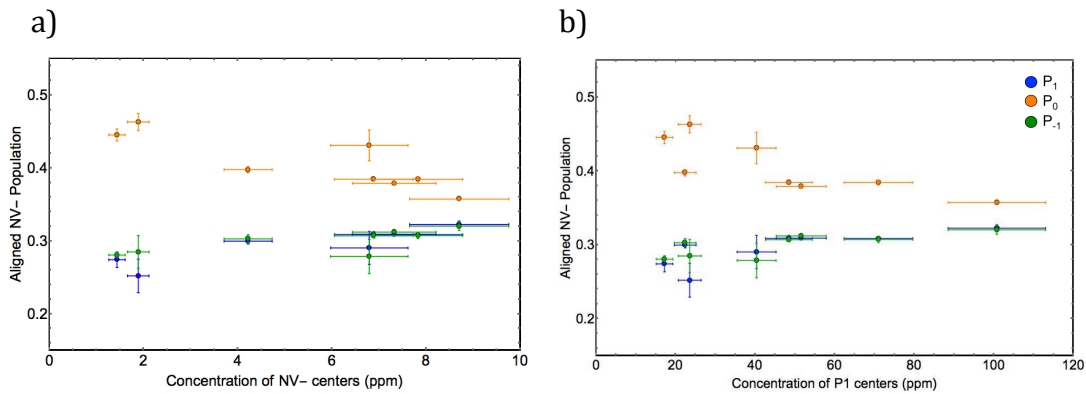
**Figure 4 Polarization of NV- Zeeman eigenstates under  $30.6\text{mW}/\text{mm}^2$  of circularly polarized  $532\text{nm}$  illumination as determined from equations (1)-(3) and the X-band spectra (dark blue, orange, green) and select  $240\text{GHz}$  spectra (cyan, yellow, light green). The lines represent calculated populations using Wigner rotations of the NV- bond-aligned polarizations into the lab frame.  $240\text{GHz}$  data was taken at the ITST at UC Santa Barbara.**

Under perfect alignment of the NV- bond axis with the magnetic field, the lab frame and defect frame are identical and the Zeeman eigenstates are quantized along the defect axis. A Wigner rotation can be applied to this defect frame population to predict the lab frame population at a different orientation assuming the defect-frame population is independent of alignment (see Figure 3). The curves in Figure 4 represent a fit to the data of a Wigner rotation of  $0.42(0.29)$  aligned population for the  $m_s=0(\pm 1)$  states into the laboratory frame at various orientations. The reasonable fit to the data indicates that the defect-frame NV-polarization is constant as a function of defect misalignment with the field. The similar difference between the  $\pm 1$  states at X-band and  $240\text{GHz}$  indicates that there is not a population difference due to thermal equilibrium competing with polarization (in which case the  $240\text{GHz}$  spectra would have a much greater difference in  $\pm 1$  populations).

#### 7.4.4 NV- Polarization as a Function of Defect Concentration

NV- polarizations of defects aligned with their bond axis parallel with magnetic field were measured for eight Type 1b HPHT diamonds with varying NV- and P1 concentrations (Samples #1-8). Polarization was found to decrease with increasing NV- concentration as well as increasing P1 concentration, as seen in Figure 5, but did not trend with the ratio of

NV- to P1 concentrations (Figure 6). Polarization into the  $m_s=+1$  and  $m_s=-1$  states were equal in all samples. The experiments were all performed at  $30.56\text{mW}/\text{mm}^2$  laser intensity, which falls on a different region of each sample's laser saturation curve as shown in Figure 2. The samples with  $>7\text{ppm}$  NV- were all past saturation at this intensity and would be expected to have larger polarizations at lower laser intensities based on Figure 2. Increased concentrations of P1 centers may decrease NV- polarization through increasing relaxation<sup>15</sup> or through facilitating NV- to NV<sup>0</sup> photo-ionization<sup>16-18</sup>. Photo-ionization increases with laser intensity<sup>16-18</sup>, and may explain the observed laser saturation trends. Additional studies of the influence of laser intensity on NV- polarization using a larger sample pool with greater variation in defect concentrations are needed to further understand these observed trends.



**Figure 5 NV- polarizations as a function of a) NV- concentration and b) P1 concentration in Type 1b HPHT synthetic diamonds.**

The significant increase in NV- polarization with decreasing P1 concentration is consistent with previously observed optically pumped nuclear polarizations in these samples at high magnetic fields [7]. Only samples with approximately 20 ppm P1 centers had observable <sup>13</sup>C polarization at room temperature and 7T and 9.4T fields.

Figure 6 shows the same NV- population data from Figure 5 plotted as a function of the ratio of NV- to P1 concentrations. One might expect that the NV- polarization would be greater as the ratio of  $[\text{NV-}]/[\text{P1}]$  is increased due to greater distances between NV- and P1 and therefore decreased interactions leading to relaxation and photoionization, but that was not observed.

## 7.5 Conclusion

We have presented a systematic study of NV- polarization as a function of magnetic field orientation relative to the NV- bond axis and defect concentration. NV- polarizations were found to be constant in the defect frame at X-band EPR field strengths. The experimentally observed orientation dependence was fully accounted for by a Wigner rotation of the NV-bond axis frame into the laboratory frame. NV- polarization of the  $m_s=+1$  and  $m_s=-1$  states were confirmed to be equal using a straightforward method for separately calculating their polarizations. NV- polarization of aligned defects was found to trend with NV- and P1 concentrations, but not their ratio. Polarization into  $m_s=0$  varied from 46% to 36% in

samples where P1 concentrations varied from 20ppm to 100ppm, respectively, and NV- concentrations varied from 1.4ppm – 9ppm,

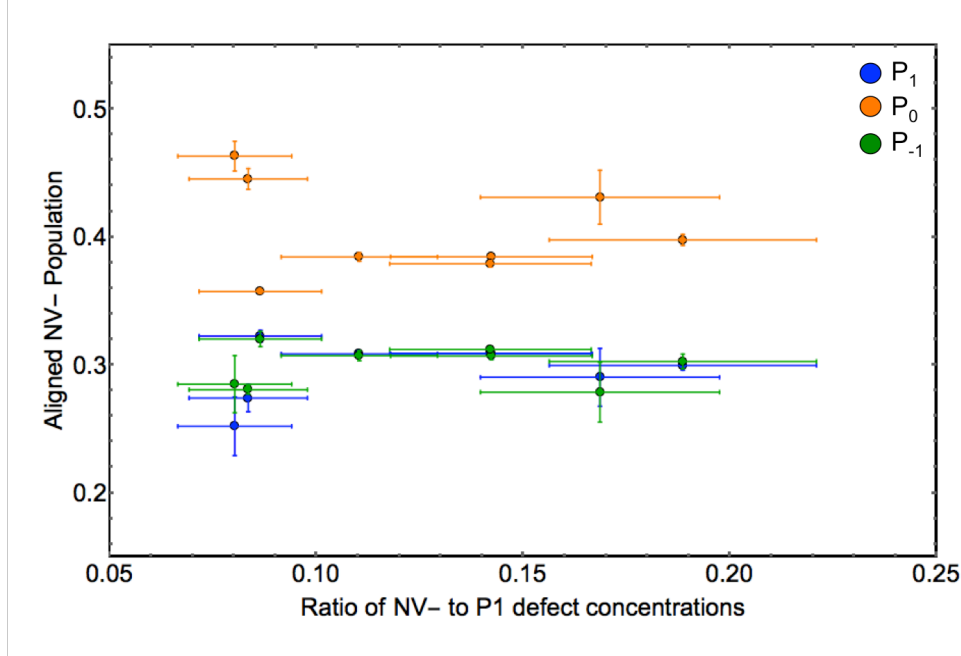


Figure 6 NV- polarizations as a function of the ratio of NV- to P1 concentrations in Type 1b HPHT synthetic diamonds.

These results affirm the use of constant Zeeman level polarizations in the defect frame for all orientations of the NV- defect relative to the magnetic field. This magnetic field orientation independence is an important consideration for applications utilizing ensembles of defects in single crystals and defects in nanodiamonds. Further, the significant increase in NV- polarization in diamonds with lower P1 concentrations provides a design metric for future sample optimization for applied spin technologies.

## 7.6 Acknowledgements

The 240GHz EPR data shown in Figure 4 was acquired at the Institute for Terahertz Science and Technology (ITST) at UCSB with the help of Nick Agladze and Mark Sherwin. The X-band EPR data was made possible with the help of Active Spectrum retrofitting our instrument with optical access.



## 8 Conclusions and Suggested Future Work

---

### 8.1 Conclusions

Optically pumping NV- diamonds at high magnetic fields and low temperatures can generate  $^{13}\text{C}$  nuclear polarization without the assistance of microwaves necessary in traditional DNP experiments. In certain diamonds,  $^{13}\text{C}$  polarization can be generated at room temperature as well.

The sign and magnitude of the  $^{13}\text{C}$  polarization sensitively depends on the orientation of the diamond with respect to the directions of the applied magnetic field and laser polarization. The polarization magnitude further depends on the defect concentrations, magnitude of the applied magnetic field, temperature, and the illumination conditions: wavelength, power, and exposure time.

To better understand the source of polarization, the NV defects were characterized with EPR to determine relaxation times, concentrations, and homogeneity. EPR was also used to determine the orientation dependence of NV polarization. The NV polarization is constant in the defect frame, which, when rotated into the laboratory frame, results in highest polarization when aligned with the field, yields zero polarization at 54 degrees, and inverted polarization at higher angles. These EPR insights into the NV physics were incorporated into models for  $^{13}\text{C}$  polarization mechanisms.

Dipolar coupled pairs of NV centers were proposed as the source for  $^{13}\text{C}$  polarization in NV- diamonds at high magnetic fields. Modeling pairwise combinations of NV centers shows that these dipolar-coupled manifolds have transitions matching the frequency of the  $^{13}\text{C}$  nuclei, making them a feasible source of spontaneous polarization transfer. The model also qualitatively captures the polarization sign changes as a function of crystal orientation. However, the model cannot reproduce the exact trends of the orientation dependence observed in experiments. Further modeling work is needed to fully understand and explain these polarization phenomena.

### 8.2 Future Work

Additional work in this field could focus on three areas: 1) Using linearly polarized light to isolate contributions of separate NV- orientations toward nuclear polarization, 2) Transferring nuclear polarization across the diamond interface, and 3) Expanding ISC-OPNMR at high fields to new materials. The following subsections outline preliminary work and considerations in these areas.

### 8.2.1 Linear Polarized Light Experiments to Isolate NV- Orientations Contributing to Nuclear Polarization

Studying nuclear polarization generated by ensembles of NV centers in diamond is complicated by the fact that NMR cannot distinguish the contribution from each of the four NV orientations in single crystals.

One way of isolating the contribution of different NV orientations is to cleverly weight their polarizations using linearly polarized light. The electric dipole transitions of the NV center are allowed in the plane perpendicular to the defect axis<sup>1,2</sup>. Appendix B describes the process for modeling NV light absorption as a function of defect orientation and crystal surface orientation relative to the direction of light propagation. The relative light absorption of circularly polarized light for each of the four NV orientations are different from each, but the differences become exaggerated when using linearly polarized light.

Figure 1 models the degree of linearly polarized light absorption for NV defects as a function of their angle with respect to the light polarization vector. Each defect has an angle-dependent absorption, but the sum of all absorption is constant with angle (black circles in Figure 1). If each defect orientation is contributing equally to the nuclear polarization, you would expect the NMR signal to follow this angle-independent cumulative absorption black circle trace. However, if some defect orientations contribute positive polarization and others contribute negative polarizations, the NMR signal would start to trend as weighted sums and differences of the respective angle-dependent color traces.

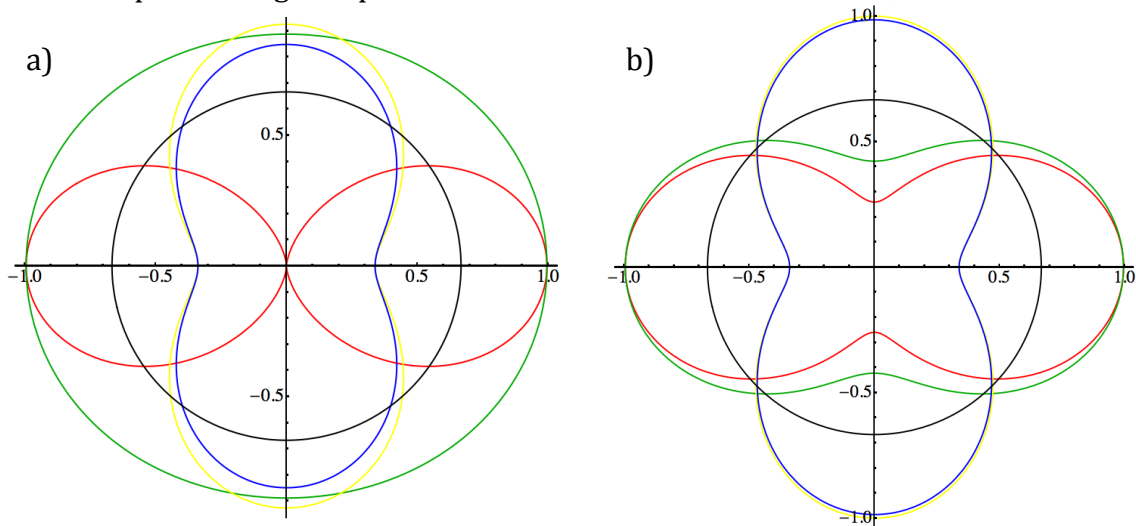


Figure 1 Polar plot of relative linearly polarized light absorption as a function of the angle between the light polarization vector and the tilt axis (x-axis) for a 100 sample with 100-edges and 110-corners a) rotated with one edge 5° from the tilt axis and tilted 35° degrees b) rotated with one edge 5° from the tilt axis and tilted 5° degrees. Each color curve (red, yellow, green blue) represents a separate NV orientation within the diamond. Black curve is an average of all four. It can be seen in a) that certain combinations of crystal orientation and linear light orientation lead to zero absorption by one of the defects (red curve)

Rotating a half-wave plate optic in the beam path can experimentally generate such curves. A half-wave plate transmits linearly polarized light at a phase angle dependent on the rotation of the plate. Figure 2 shows preliminary results using this technique. Figure 2 shows  $^{13}\text{C}$  polarization in Sample #2 taken in 10 degree half-wave rotation increments compared to modeled absorption. Note that effects of changing transmission amounts described by Fresnel Equations (see Appendix B) are not included in these models. The absolute reference between polar axes of the data and model are also arbitrary.

Future work using this technique would require calibrating the absolute orientation of the NMR probe and diamond with respect to the polarization vector of the linearly polarized light.

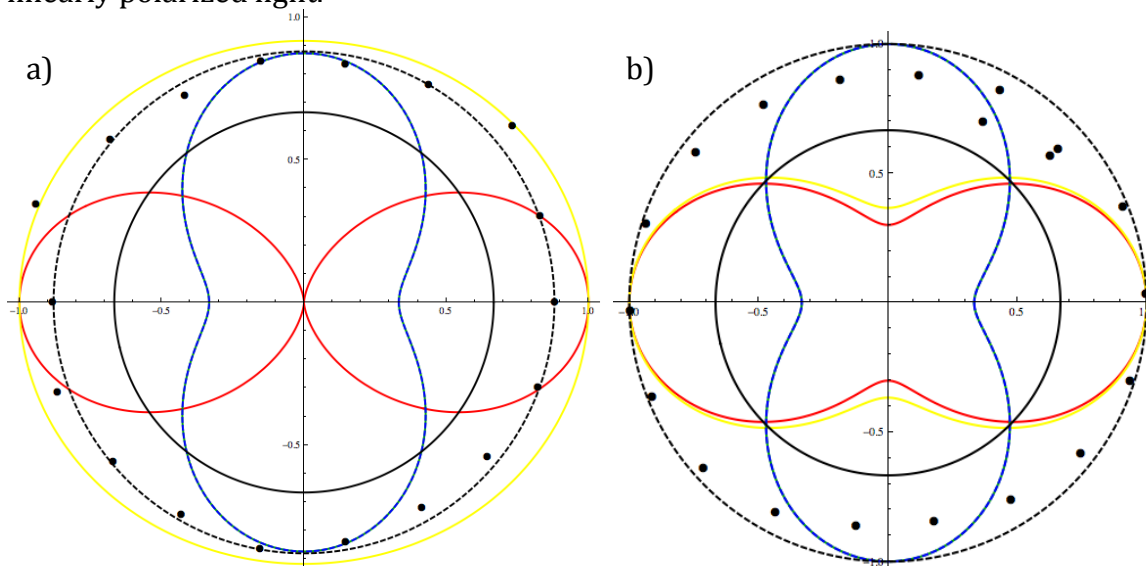


Figure 2 Polar plot of relative linearly polarized light absorption (lines) and measured (20K, 9.4T)  $^{13}\text{C}$  polarization in Sample #2 (points) as a function of the angle between the light polarization vector and the tilt axis (x-axis) for a 100 sample with 100-edges and 110-corners a) rotated with one edge  $0^\circ$  from the tilt axis and tilted  $38^\circ$  degrees b) rotated with one edge  $0^\circ$  from the tilt axis and tilted  $2^\circ$  degrees. Each color curve (red, yellow, green blue) represents a separate NV orientation within the diamond. Black solid curve is an average of all four. Black dashed curve is a scaled version of the solid black curve to aid in visualizing asymmetry in the  $^{13}\text{C}$  data. b) shows clear asymmetry in the  $^{13}\text{C}$  data. Note there is no absolute reference between the rotation of the data and model in the plot because the relative orientation of the linear polarized light vector and sample edge was not calibrated for these preliminary measurements.

### 8.2.2 Polarization Transfer across Diamond Interface

One highly anticipated application of the NV defect is nuclear polarization of bulk solutions without the use of cryogenics or microwaves. This requires transferring polarization across the diamond interface. Theoretical work has simulated conditions necessary for polarization transfer <sup>3</sup>, but as yet the closest achievement has been polarization of adsorbed species on nanodiamonds using traditional microwave-driven DNP <sup>4</sup>.

Figure 3 summarizes the many pathways by which spin polarization can transfer from within a diamond to external nuclei. Ongoing collaborations with the Pines and

Meriles labs are already working on actualizing several methods of polarization transfer outside of single crystal-, nanostructured single crystal-, and nano-diamonds. Future work will continue these efforts.

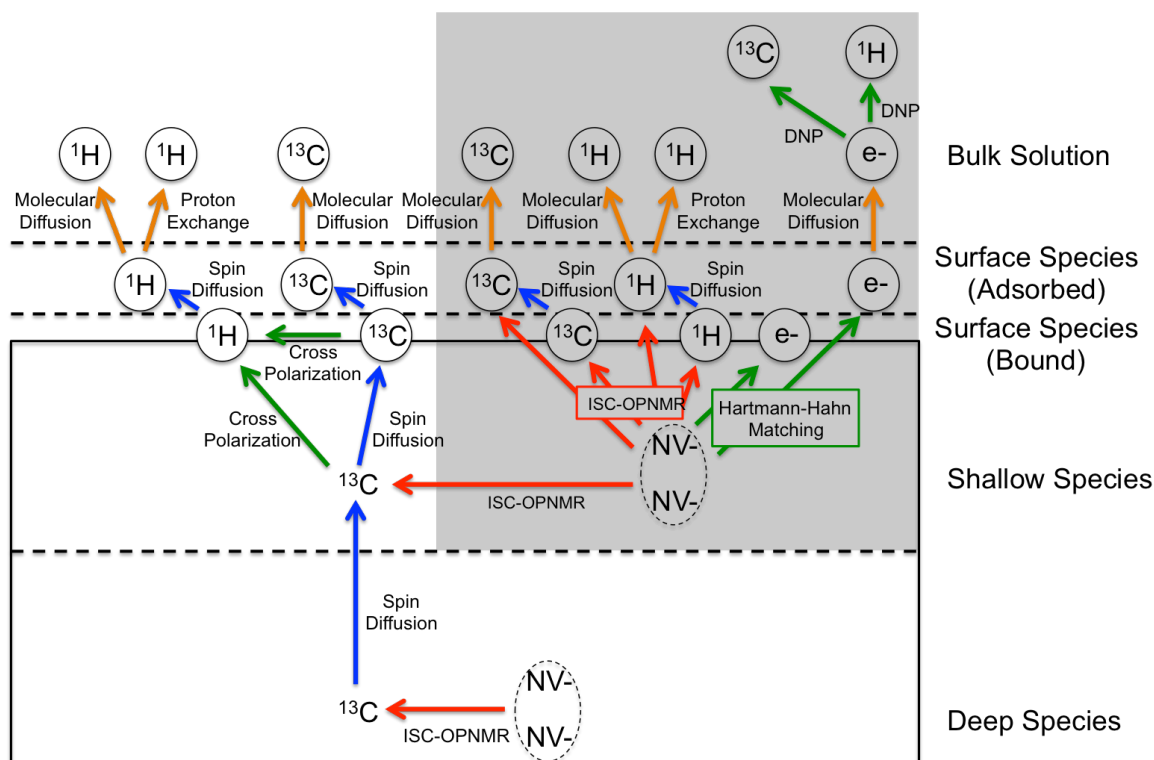


Figure 3 Pathways for transferring polarization from NV pairs in diamonds to nuclei in bulk solution. Pathways include steps of: Intersystem Crossing Optically Pumped NMR (ISC-OPNMR) polarization transfer to nuclei (red arrows), spin diffusion (blue arrows), RF or microwave-driven transfer between heteronuclei or electrons (green arrows), and molecular diffusion or proton exchange (orange arrows). The gray box represents unlikely pathways due to the decreased probability of NV- polarization near the surface of diamonds. The ISC-OPNMR steps could be replaced by traditional DNP steps to overcome this, but would not have the advantage of the athermal NV- polarization available in the bulk of the diamond.

The orientation dependence of the NV centers presents difficulties in using nanodiamonds or powdered diamonds as a polarization source. As opposed to single crystals, in which only four orientations of defects are present, a packed bed of nanodiamonds will have each crystal uniquely oriented, creating a distribution of NV centers over every possible orientation. Ongoing collaborative work using nanodiamonds seeks to employ the Integrated Solid Effect to overcome this <sup>5,6</sup>.

Figure 4 shows EasySpin <sup>7</sup> simulations for the EPR spectra of NV nanodiamonds. Figure 5 shows an X-band EPR spectrum of nanodiamonds purchased from Adamas Nanotechnology. The P1 signature agrees well with simulation. No NV centers were observed.

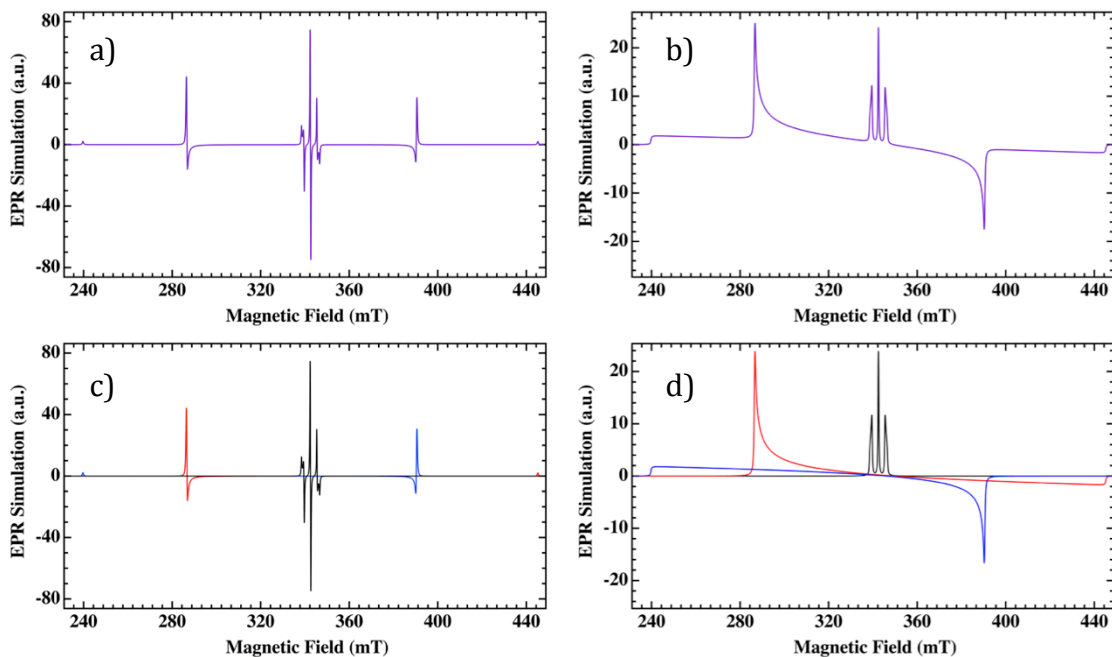


Figure 4 EasySpin X-band EPR simulations of NV- and P1 centers in nanodiamonds. a) Dispersive EPR line shapes. b) Absorptive EPR line shapes as would be probed using the Integrated Solid Effect (ISE). c) Simulation from a) highlighting the NV- contributions from the +1 to 0 (red), -1 to 0 (blue) transitions, and the P1 transitions (black). d) Simulation from b) highlighting the NV- contributions from the +1 to 0 (red), -1 to 0 (blue) transitions, and the P1 transitions (black).

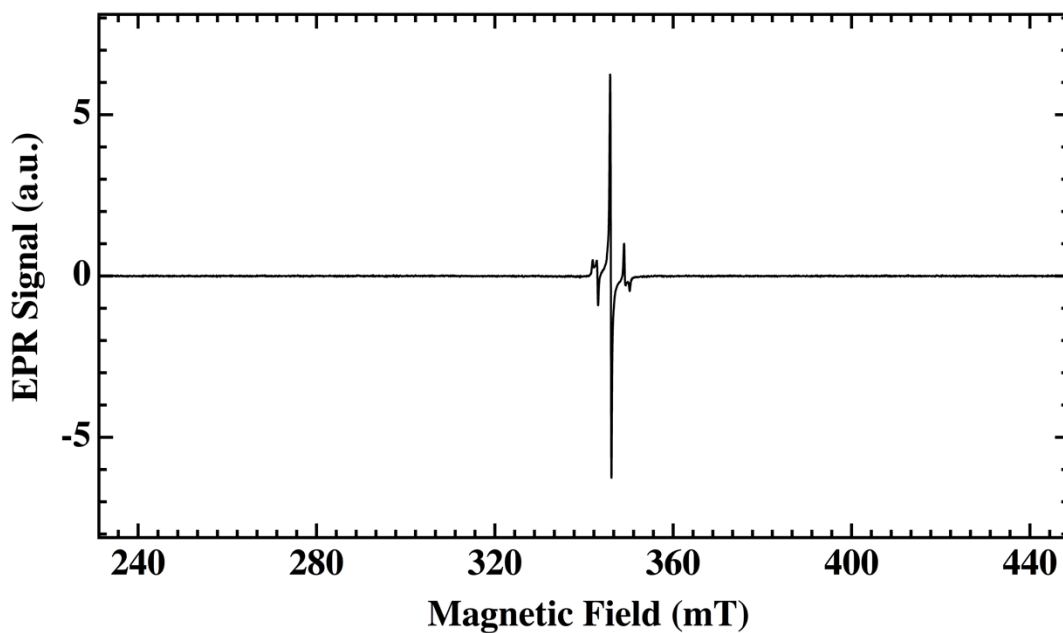


Figure 5 X-band EPR spectrum of NV-imbibed nanodiamonds with average particle size of 100nm and carboxylated surfaces (purchased from Adamas Nanotechnology). Only P1 centers appear in the spectrum.

### 8.2.3 Alternative ISC-OPNMR Materials

The NV- defect in diamond is not unique in its ISC-OPNMR nuclear polarization mechanism. Defects with analogous energy level structures and excitation/decay pathways have been theoretically proposed in Silicon Carbide (SiC), cubic Boron Nitride (c-BN), and Zinc Oxide (ZnO) <sup>8-13</sup>. Defects in SiC have already been shown to polarize nuclei at level anticrossing magnetic fields<sup>8</sup>. Future work should seek to generate nuclear spin polarization in these materials at high magnetic fields such as those used in the NV- studies discussed in Chapter 3.

#### 8.2.3.1 $V_{Si}V_C$ and PL6 defects in Silicon Carbide

The  $V_{Si}V_C$  and PL6 defects in Silicon Carbide (SiC) have already generated <sup>29</sup>Si polarization through an ISC-OPNMR mechanism at level anticrossing magnetic fields <sup>8,9</sup>.

SiC provides an interesting platform for nuclear polarization in comparison to diamond. Additional physics can be probed in SiC due to 1) the presence of heteronuclei, 2) the increased abundance of <sup>29</sup>Si, 3) the presence of multiple polarization-inducing defects, and 4) the multitude of SiC polytypes available. Table 1 outlines the NMR-active nuclei present in SiC.

Table 1 NMR-active nuclei in SiC

Isotope	Natural Abundance	Spin
<sup>13</sup> C	1.1%	1/2
<sup>29</sup> Si	4.7%	1/2

#### 8.2.3.2 Oxygen-Boron Vacancy defect in cubic Boron Nitride

The Oxygen-Boron Vacancy ( $O_N-V_B$ ) defect in cubic Boron Nitride (c-BN) has an analogous energy level structure to NV- in diamond, but has yet to generate nuclear polarization <sup>10</sup>.

Table 2 outlines the NMR-active nuclei present in c-BN. The cubic environment of c-BN will prevent NMR peak broadening from the Quadrupolar nuclei.

Table 2 NMR-active nuclei in c-BN

Isotope	Natural Abundance	Spin
<sup>10</sup> B	19.6%	3
<sup>11</sup> B	80.4%	3/2
<sup>14</sup> N	99.6%	1
<sup>15</sup> N	0.4%	1/2

#### 8.2.3.3 Zinc Vacancies in ZnO

Zinc Vacancies ( $V_{Zn}^{\cdot-}$ ) and other vacancy-related defects in ZnO demonstrate similar photophysics to NV-, but have not yet been studied in the context of spin

polarization <sup>11-13</sup>. Table 3 outlines the NMR-active nuclei present in ZnO. ZnO occurs in hexagonal wurtzite and cubic zincblende polytypes. Unlike the NV- and the analogous defects in SiC and c-BN, the V<sub>Zn</sub>- defect in ZnO only involves a single lattice point. The symmetry of the defect would preclude orientation-dependence.

**Table 3 NMR-active nuclei in ZnO**

Isotope	Natural Abundance	Spin
<sup>67</sup> Zn	4.11%	5/2
<sup>17</sup> O	0.037%	5/2

# References

---

## Chapter 1

1. Levitt, M. H. *Spin dynamics: Basics of nuclear magnetic resonance, 2nd edition*. (Wiley, 2009). doi:10.1002/cmra.20130
2. Eaton, G. R., Eaton, S. S., Barr, D. P. & Weber, R. T. *Quantitative EPR*. (Springer-Verlag/Wien, 2010).
3. Weil, J. A. & Bolton, J. R. *Electron Paramagnetic Resonance: Elemental Theory and Practical Applications*. (John Wiley & Sons, Inc., 2007).
4. Happer, W. & van Wijngaarden, W. A. An Optical Pumping Primer. *Hyperfine Interact.* **38**, 435–470 (1987).
5. Hayes, S. E., Mui, S. & Ramaswamy, K. Optically pumped nuclear magnetic resonance of semiconductors. *J. Chem. Phys.* **128**, 52203 (2008).
6. Happer, W. Optical Pumping. *Rev. Mod. Phys.* **44**, 169–249 (1972).
7. Tycko, R. & Reimer, J. A. Optical Pumping in Solid State Nuclear Magnetic Resonance. **3654**, 13240–13250 (1996).
8. Jacques, V. *et al.* Dynamic Polarization of Single Nuclear Spins by Optical Pumping of Nitrogen-Vacancy Color Centers in Diamond at Room Temperature. *Phys. Rev. Lett.* **102**, 57403 (2009).
9. King, J. P., Coles, P. J. & Reimer, J. A. Optical polarization of  $^{13}\text{C}$  nuclei in diamond through nitrogen vacancy centers. *Phys. Rev. B* **81**, 1–4 (2010).
10. Wang, H.-J. *et al.* Sensitive magnetic control of ensemble nuclear spin hyperpolarization in diamond. *Nat. Commun.* **4**, 1940 (2013).
11. Fischer, R. *et al.* Bulk Nuclear Polarization Enhanced at Room Temperature by Optical Pumping. *Phys. Rev. Lett.* **111**, 57601 (2013).
12. Álvarez, G. A. *et al.* Local and bulk  $^{13}\text{C}$  hyperpolarization in nitrogen-vacancy-centred diamonds at variable fields and orientations. *Nat. Commun.* **6**, 8456 (2015).
13. Fischer, R., Jarmola, A., Kehayias, P. & Budker, D. Optical polarization of nuclear ensembles in diamond. *Phys. Rev. B* **87**, 125207 (2013).
14. King, J. P. *et al.* Room-Temperature in situ Nuclear Spin Hyperpolarization from Optically-Pumped Nitrogen Vacancy Centers in Diamond. *Nat. Commun.* **6**, 8965 (2015).
15. Smeltzer, B., McIntyre, J. & Childress, L. Robust control of individual nuclear spins in diamond. *Phys. Rev. A* **80**, 50302 (2009).
16. Pagliero, D., Laraoui, A., Henshaw, J. D. & Meriles, C. A. Recursive polarization of nuclear spins in diamond at arbitrary magnetic fields. **242402**, 0–5 (2014).
17. Kuprov, I. Chemically Induced Dynamic Nuclear Polarization of  $^{19}\text{F}$  Nuclei. *Thesis* (2005).
18. Tateishi, K. *et al.* Room temperature hyperpolarization of nuclear spins in bulk. *Proc. Natl. Acad. Sci. U. S. A.* **111**, 7527–30 (2014).
19. Henstra, A., Lin, T.-S., Schmidt, J. & Wenckebach, W. T. High dynamic nuclear polarization at room temperature. *Chem. Phys. Lett.* **165**, 6–10 (1990).



20. Sosnovsky, D. V., Jeschke, G., Matysik, J., Vieth, H. M. & Ivanov, K. L. Level crossing analysis of chemically induced dynamic nuclear polarization: Towards a common description of liquid-state and solid-state cases. *J. Chem. Phys.* **144**, (2016).
21. Abragam, A. & Goldman, M. Principles of dynamic nuclear polarisation. *Reports Prog. Phys.* **41**, (1978).
22. Hovav, Y., Feintuch, A. & Vega, S. Theoretical aspects of dynamic nuclear polarization in the solid state - The solid effect. *J. Magn. Reson.* **207**, 176–189 (2010).
23. Corzilius, B., Smith, A. A. & Griffin, R. G. Solid effect in magic angle spinning dynamic nuclear polarization. *J. Chem. Phys.* **137**, 54201 (2012).
24. Smith, A. A., Corzilius, B., Barnes, A. B., Maly, T. & Griffin, R. G. Solid effect dynamic nuclear polarization and polarization pathways. *J. Chem. Phys.* **136**, (2012).
25. Wollan, D. S. Dynamic nuclear polarization with an inhomogeneously broadened ESR line. II. Experiment. *Phys. Rev. B* **13**, 3686–3696 (1976).
26. Wollan, D. S. Dynamic nuclear polarization with an inhomogeneously broadened ESR line. I. Theory. *Phys. Rev. B* **13**, 3671–3685 (1976).
27. Henstra, A., Dirksen, P. & Wenckebach, W. Enhanced dynamic nuclear polarization by the integrated solid effect. *Phys. Lett. A* **134**, 134–136 (1988).
28. Hovav, Y., Feintuch, A. & Vega, S. Theoretical aspects of dynamic nuclear polarization in the solid state - The cross effect. *J. Magn. Reson.* **214**, 29–41 (2012).
29. Hwang, C. F. & Hill, D. A. New Effect in Dynamic Polarization. *Phys. Rev. Lett.* **18**, 110–112 (1967).
30. Overhauser, A. W. Polarization of Nuclei in Metals. *Phys. Rev.* **92**, 411–415 (1953).
31. Carver, T. R. & Slichter, C. P. Experimental verification of the overhauser nuclear polarization effect. *Phys. Rev.* **102**, 975–980 (1956).
32. Hovav, Y., Feintuch, A. & Vega, S. Theoretical aspects of dynamic nuclear polarization in the solid state - spin temperature and thermal mixing. *Phys. Chem. Chem. Phys.* **15**, 29–41 (2013).
33. Bowers, C. R. & Weitekamp, D. P. Parahydrogen and synthesis allow dramatically enhanced nuclear alignment. *J. Am. Chem. Soc.* **109**, 5541–5542 (1987).
34. Bowers, C. R. & Weitekamp, D. P. Transformation of Symmetrization Order to Nuclear-Spin Magnetization by Chemical Reaction and Nuclear Magnetic Resonance. *Phys. Rev. Lett.* **57**, 2645 (1986).
35. Pravica, M. G. & Weitekamp, D. P. Net NMR alignment by adiabatic transport of parahydrogen addition products to high magnetic field. *Chem. Phys. Lett.* **145**, 255–258 (1988).
36. Green, R. A. *et al.* The theory and practice of hyperpolarization in magnetic resonance using parahydrogen. *Prog. Nucl. Magn. Reson. Spectrosc.* **67**, 1–48 (2012).
37. Adams, R. W., Duckett, S. B., Green, R. A., Williamson, D. C. & Green, G. G. R. A theoretical basis for spontaneous polarization transfer in non-hydrogenative

- parahydrogen-induced polarization. *J. Chem. Phys.* **131**, (2009).
38. Adams, R. W. *et al.* Reversible Interactions with para-Hydrogen Enhance NMR Sensitivity by Polarization Transfer. *Science (80-. )*. **323**, 1708–1711 (2009).
  39. Scott, E. A Phenomenological Study of High-Field Optically Pumped <sup>13</sup>C NMR in Diamond. (University of California, Berkeley, 2015).  
doi:10.1017/CBO9781107415324.004
  40. Loubser, J. H. N. & van Wyk, J. A. Electron spin resonance in the study of diamond. *Reports Prog. Phys.* **41**, 1201–1248 (1978).
  41. Lawson, S. C., Fisher, D., Hunt, D. C. & Newton, M. E. On the existence of positively charged single-substitutional nitrogen in diamond. *J. Phys. Condens. Matter* **10**, 6171–6180 (1998).
  42. Gali, A., Fyta, M. & Kaxiras, E. Ab initio supercell calculations on nitrogen-vacancy center in diamond: Electronic structure and hyperfine tensors. *Phys. Rev. B* **77**, 155206 (2008).
  43. Doherty, M. W., Manson, N. B., Delaney, P. & Hollenberg, L. C. L. The negatively charged nitrogen-vacancy centre in diamond: the electronic solution. *New J. Phys.* **13**, 25019 (2011).
  44. Deák, P., Aradi, B., Kaviani, M., Frauenheim, T. & Gali, A. Formation of NV centers in diamond: A theoretical study based on calculated transitions and migration of nitrogen and vacancy related defects. *Phys. Rev. B* **89**, 75203 (2014).
  45. Waldermann, F. C. *et al.* Creating diamond color centers for quantum optical applications. *Diam. Relat. Mater.* **16**, 1887–1895 (2007).
  46. Mainwood, A. Nitrogen and nitrogen-vacancy complexes and their formation in diamond. *Phys. Rev. B* **49**, 7934 (1994).
  47. Collins, A. T. & Kiflawi, I. The annealing of radiation damage in type Ia diamond. *J. Phys. Condens. Matter* **21**, 364209 (2009).
  48. Rabeau, J. R. *et al.* Implantation of labelled single nitrogen vacancy centers in diamond using <sup>15</sup>N. J. R. Rabeau \*, P. Reichart. *arXiv* 1–14
  49. Pezzagna, S., Naydenov, B., Jelezko, F., Wrachtrup, J. & Meijer, J. Creation efficiency of nitrogen-vacancy centres in diamond. *New J. Phys.* **12**, (2010).
  50. Orwa, J. O. *et al.* Engineering of nitrogen-vacancy color centers in high purity diamond by ion implantation and annealing. *J. Appl. Phys.* **109**, 83530 (2011).
  51. Acosta, V. M. *et al.* Diamonds with a high density of nitrogen-vacancy centers for magnetometry applications. *Phys. Rev. B* **80**, 1–15 (2009).
  52. Edmonds, a. *et al.* Production of oriented nitrogen-vacancy color centers in synthetic diamond. *Phys. Rev. B* **86**, 35201 (2012).
  53. Doherty, M. W. *et al.* The nitrogen-vacancy colour centre in diamond. *Phys. Rep.* **528**, 1–45 (2013).
  54. Tetienne, J.-P. *et al.* Magnetic-field-dependent photodynamics of single NV defects in diamond: an application to qualitative all-optical magnetic imaging. *New J. Phys.* **14**, 103033 (2012).
  55. Aslam, N., Waldherr, G., Neumann, P., Jelezko, F. & Wrachtrup, J. Photo-induced ionization dynamics of the nitrogen vacancy defect in diamond investigated by single-shot charge state detection. *New J. Phys.* **15**, 13064 (2013).

56. Manson, N. B. & Harrison, J. P. Photo-ionization of the nitrogen-vacancy center in diamond. *Diam. Relat. Mater.* **14**, 1705–1710 (2005).
57. Gaebel, T. *et al.* Photochromism in single nitrogen-vacancy defect in diamond. *Appl. Phys. B* **82**, 243–246 (2005).
58. Scott, E., Drake, M. & Reimer, J. A. The phenomenology of optically pumped <sup>13</sup>C NMR in diamond at 7.05 T: Room temperature polarization, orientation dependence, and the effect of defect concentration on polarization dynamics. *J. Magn. Reson.* **264**, 154–162 (2016).

## Chapter 2

1. Scott, E. A Phenomenological Study of High-Field Optically Pumped <sup>13</sup>C NMR in Diamond. (University of California, Berkeley, 2015).  
doi:10.1017/CBO9781107415324.004
2. Scott, E., Drake, M. & Reimer, J. A. The phenomenology of optically pumped <sup>13</sup>C NMR in diamond at 7.05 T: Room temperature polarization, orientation dependence, and the effect of defect concentration on polarization dynamics. *J. Magn. Reson.* **264**, 154–162 (2016).

## Chapter 3

1. Fischer, R. *et al.* Bulk Nuclear Polarization Enhanced at Room Temperature by Optical Pumping. *Phys. Rev. Lett.* **111**, 57601 (2013).
2. Scott, E., Drake, M. & Reimer, J. A. The phenomenology of optically pumped <sup>13</sup>C NMR in diamond at 7.05 T: Room temperature polarization, orientation dependence, and the effect of defect concentration on polarization dynamics. *J. Magn. Reson.* **264**, 154–162 (2016).
3. Scott, E. A Phenomenological Study of High-Field Optically Pumped <sup>13</sup>C NMR in Diamond. (University of California, Berkeley, 2015).  
doi:10.1017/CBO9781107415324.004
4. Aslam, N., Waldherr, G., Neumann, P., Jelezko, F. & Wrachtrup, J. Photo-induced ionization dynamics of the nitrogen vacancy defect in diamond investigated by single-shot charge state detection. *New J. Phys.* **15**, 13064 (2013).
5. King, J. P., Coles, P. J. & Reimer, J. A. Optical polarization of <sup>13</sup>C nuclei in diamond through nitrogen vacancy centers. *Phys. Rev. B* **81**, 1–4 (2010).

## Chapter 4

1. Tetienne, J.-P. *et al.* Magnetic-field-dependent photodynamics of single NV defects in diamond: an application to qualitative all-optical magnetic imaging.

- New J. Phys.* **14**, 103033 (2012).
2. King, J. P., Coles, P. J. & Reimer, J. A. Optical polarization of  $^{13}\text{C}$  nuclei in diamond through nitrogen vacancy centers. *Phys. Rev. B* **81**, 1–4 (2010).
  3. Chandra Shekar, S. & Jerschow, A. Tensors in NMR. *Encycl. Magn. Reson.* 10–14 (2008). doi:10.1002/9780470034590.emrstm1050
  4. Morrison, M. a. & Parker, G. a. A Guide to Rotations in Quantum Mechanics. *Aust. J. Phys.* **40**, 465 (1987).
  5. Drake, M., Scott, E. & Reimer, J. A. Influence of magnetic field alignment and defect concentration on nitrogen-vacancy polarization in diamond. *New J. Phys.* **18**, (2016).
  6. Scott, E., Drake, M. & Reimer, J. A. The phenomenology of optically pumped  $^{13}\text{C}$  NMR in diamond at 7.05 T: Room temperature polarization, orientation dependence, and the effect of defect concentration on polarization dynamics. *J. Magn. Reson.* **264**, 154–162 (2016).
  7. Smeltzer, B., Childress, L. & Gali, A.  $^{13}\text{C}$  hyperfine interactions in the nitrogen-vacancy centre in diamond. *New J. Phys.* **13**, 25021 (2011).

## Chapter 5

1. King, J. P., Coles, P. J. & Reimer, J. A. Optical polarization of  $^{13}\text{C}$  nuclei in diamond through nitrogen vacancy centers. *Phys. Rev. B* **81**, 1–4 (2010).
2. Stepanov, V. & Takahashi, S. Determination of nitrogen spin concentration in diamond using double electron-electron resonance. *Phys. Rev. B - Condens. Matter Mater. Phys.* **94**, 1–9 (2016).
3. Scott, E., Drake, M. & Reimer, J. A. The phenomenology of optically pumped  $^{13}\text{C}$  NMR in diamond at 7.05 T: Room temperature polarization, orientation dependence, and the effect of defect concentration on polarization dynamics. *J. Magn. Reson.* **264**, 154–162 (2016).
4. *Electron paramagnetic resonance: a practitioner's toolkit.* (Wiley, 2009).
5. Dikanov, S. A. & Tsvetkov, Y. D. *Electron Spin Echo Modulation Spectroscopy.* (CRC Press, 1992).
6. He, X., Manson, N. B. & Fisk, P. T. H. Paramagnetic resonance of photoexcited NV defects in diamond. II. Hyperfine interaction with the  $^{14}\text{N}$  nucleus. *Phys. Rev. B* **47**, 8816–8822 (1993).
7. Felton, S. *et al.* Hyperfine interaction in the ground state of the negatively charged nitrogen vacancy center in diamond. *Phys. Rev. B* **79**, 75203 (2009).
8. Schweiger, A. & Jeschke, G. *Principles of Pulse Electron Paramagnetic Resonance.* (Oxford University Press, 2001).

## Chapter 6

1. Rondin, L. *et al.* Magnetometry with nitrogen-vacancy defects in diamond. *Rep Prog Phys* **77**, 56503 (2014).
2. Criger, B., Passante, G., Park, D. & Laflamme, R. Recent advances in nuclear magnetic resonance quantum information processing. *Philos. Trans. A. Math. Phys. Eng. Sci.* **370**, 4620–35 (2012).
3. Jacques, V. *et al.* Dynamic Polarization of Single Nuclear Spins by Optical Pumping of Nitrogen-Vacancy Color Centers in Diamond at Room Temperature. *Phys. Rev. Lett.* **102**, 57403 (2009).
4. King, J. P., Coles, P. J. & Reimer, J. A. Optical polarization of  $^{13}\text{C}$  nuclei in diamond through nitrogen vacancy centers. *Phys. Rev. B* **81**, 1–4 (2010).
5. Wang, H.-J. *et al.* Sensitive magnetic control of ensemble nuclear spin hyperpolarization in diamond. *Nat. Commun.* **4**, 1940 (2013).
6. Fischer, R. *et al.* Bulk Nuclear Polarization Enhanced at Room Temperature by Optical Pumping. *Phys. Rev. Lett.* **111**, 57601 (2013).
7. Álvarez, G. A. *et al.* Local and bulk  $^{13}\text{C}$  hyperpolarization in nitrogen-vacancy-centred diamonds at variable fields and orientations. *Nat. Commun.* **6**, 8456 (2015).
8. Fischer, R., Jarmola, A., Kehayias, P. & Budker, D. Optical polarization of nuclear ensembles in diamond. *Phys. Rev. B* **87**, 125207 (2013).
9. King, J. P. *et al.* Room-Temperature in situ Nuclear Spin Hyperpolarization from Optically-Pumped Nitrogen Vacancy Centers in Diamond. *Nat. Commun.* **6**, 8965 (2015).
10. Smeltzer, B., McIntyre, J. & Childress, L. Robust control of individual nuclear spins in diamond. *Phys. Rev. A* **80**, 50302 (2009).
11. Pagliero, D., Laraoui, A., Henshaw, J. D. & Meriles, C. A. Recursive polarization of nuclear spins in diamond at arbitrary magnetic fields. **242402**, 0–5 (2014).
12. Wrachtrup, J., Jelezko, F., Grotz, B. & McGuinness, L. Nitrogen-vacancy centers close to surfaces. *MRS Bull.* **38**, 149–154 (2013).
13. Ishikawa, T. *et al.* Optical and spin coherence properties of nitrogen-vacancy centers placed in a 100 nm thick isotopically purified diamond layer Sample information Distribution of NV center depths measured through confocal measurements Pulsed ODMR spectroscopy. 1–6 (2012).
14. Staudacher, T. *et al.* Enhancing the spin properties of shallow implanted nitrogen vacancy centers in diamond by epitaxial overgrowth. *Appl. Phys. Lett.* **101**, (2012).
15. Stepanov, V. & Takahashi, S. Determination of nitrogen spin concentration in diamond using double electron-electron resonance. *Phys. Rev. B - Condens. Matter Mater. Phys.* **94**, 1–9 (2016).
16. Takahashi, S., Hanson, R., van Tol, J., Sherwin, M. & Awschalom, D. Quenching Spin Decoherence in Diamond through Spin Bath Polarization. *Phys. Rev. Lett.* **101**, 47601 (2008).
17. Van Wyk, J. A., Reynhardt, E. C., High, G. L. & Kiflawi, I. The dependences of ESR line widths and spin - spin relaxation times of single nitrogen defects on the concentration of nitrogen defects in diamond. *J. Phys. D. Appl. Phys.* **30**, 1790–

- 1793 (1997).
18. Wang, Z. H. & Takahashi, S. Spin decoherence and electron spin bath noise of a nitrogen-vacancy center in diamond. *Phys. Rev. B - Condens. Matter Mater. Phys.* **87**, 1–6 (2013).
  19. Jensen, K., Acosta, V., Jarmola, a. & Budker, D. Light narrowing of magnetic resonances in ensembles of nitrogen-vacancy centers in diamond. *Phys. Rev. B* **87**, 14115 (2013).
  20. Mrózek, M. *et al.* Longitudinal spin relaxation in nitrogen-vacancy ensembles in diamond. *EPJ Quantum Technol.* **2**, 22 (2015).
  21. *Electron paramagnetic resonance: a practitioner's toolkit.* (Wiley, 2009).
  22. Burns, R. C. *et al.* Growth-Sector Dependence of Optical Features in Large Synthetic Diamonds. **104**, 257–279 (1990).
  23. Felton, S. *et al.* Hyperfine interaction in the ground state of the negatively charged nitrogen vacancy center in diamond. *Phys. Rev. B* **79**, 75203 (2009).
  24. He, X., Manson, N. B. & Fisk, P. T. H. Paramagnetic resonance of photoexcited NV defects in diamond. II. Hyperfine interaction with the  $^{14}\text{N}$  nucleus. *Phys. Rev. B* **47**, 8816–8822 (1993).

## Chapter 7

1. Drake, M., Scott, E. & Reimer, J. A. Influence of magnetic field alignment and defect concentration on nitrogen-vacancy polarization in diamond. *New J. Phys.* **18**, 13011 (2016).
2. King, J. P., Coles, P. J. & Reimer, J. A. Optical polarization of  $^{13}\text{C}$  nuclei in diamond through nitrogen vacancy centers. *Phys. Rev. B* **81**, 1–4 (2010).
3. Scott, E., Drake, M. & Reimer, J. A. The phenomenology of optically pumped  $^{13}\text{C}$  NMR in diamond at 7.05 T: Room temperature polarization, orientation dependence, and the effect of defect concentration on polarization dynamics. *J. Magn. Reson.* **264**, 154–162 (2016).
4. Tetienne, J.-P. *et al.* Magnetic-field-dependent photodynamics of single NV defects in diamond: an application to qualitative all-optical magnetic imaging. *New J. Phys.* **14**, 103033 (2012).
5. Epstein, R. J., Mendoza, F. M., Kato, Y. K. & Awschalom, D. D. Anisotropic interactions of a single spin and dark-spin spectroscopy in diamond. *Nat. Phys.* **1**, 94–98 (2005).
6. Jacques, V. *et al.* Dynamic Polarization of Single Nuclear Spins by Optical Pumping of Nitrogen-Vacancy Color Centers in Diamond at Room Temperature. *Phys. Rev. Lett.* **102**, 57403 (2009).
7. Felton, S. *et al.* Hyperfine interaction in the ground state of the negatively charged nitrogen vacancy center in diamond. *Phys. Rev. B* **79**, 75203 (2009).
8. Harrison, J., Sellars, M. J. & Manson, N. B. Measurement of the optically induced spin polarisation of N-V centres in diamond. *Diam. Relat. Mater.* **15**, 586–588 (2006).
9. Stoll, S. & Schweiger, A. EasySpin, a comprehensive software package for spectral simulation and analysis in EPR. *J. Magn. Reson.* **178**, 42–55 (2006).
10. Howarth, D. F., Weil, J. a. & Zimpel, Z. Generalization of the lineshape useful in magnetic resonance spectroscopy. *J. Magn. Reson.* **161**, 215–221 (2003).
11. Tseitlin, M., Eaton, S. S. & Eaton, G. R. Uncertainty Analysis for Absorption and First-Derivative Electron Paramagnetic Resonance Spectra. *Concepts Magn. Reson. Part A*

- 40A**, 295–305 (2012).
12. Loubser, J. H. N. & van Wyk, J. A. Electron spin resonance in the study of diamond. *Reports Prog. Phys.* **41**, 1201–1248 (1978).
  13. Smith, W. V., Sorokin, P. P., Gelles, I. L. & Lasher, G. J. Electron-Spin Resonance of Nitrogen Donors in Diamond. *Phys. Rev.* **115**, 1546–1553 (1959).
  14. Cox, A., Newton, M. E. & Baker, J. M. <sup>13</sup>C, <sup>14</sup>N and <sup>15</sup>N ENDOR measurements on the single substitutional nitrogen centre (P1) in diamond. *J. Phys. Condens. Matter* **6**, 551–563 (1994).
  15. Takahashi, S., Hanson, R., van Tol, J., Sherwin, M. & Awschalom, D. Quenching Spin Decoherence in Diamond through Spin Bath Polarization. *Phys. Rev. Lett.* **101**, 47601 (2008).
  16. Aslam, N., Waldherr, G., Neumann, P., Jelezko, F. & Wrachtrup, J. Photo-induced ionization dynamics of the nitrogen vacancy defect in diamond investigated by single-shot charge state detection. *New J. Phys.* **15**, 13064 (2013).
  17. Manson, N. B. & Harrison, J. P. Photo-ionization of the nitrogen-vacancy center in diamond. *Diam. Relat. Mater.* **14**, 1705–1710 (2005).
  18. Gaebel, T. *et al.* Photochromism in single nitrogen-vacancy defect in diamond. *Appl. Phys. B* **82**, 243–246 (2005).

## Chapter 8

1. Epstein, R. J., Mendoza, F. M., Kato, Y. K. & Awschalom, D. D. Anisotropic interactions of a single spin and dark-spin spectroscopy in diamond. *Nat. Phys.* **1**, 94–98 (2005).
2. Davies, G. & Hamer, M. F. Optical Studies of the 1.945 eV Vibronic Band in Diamond. *Proc. R. Soc. A Math. Phys. Eng. Sci.* **348**, 285–298 (1976).
3. Abrams, D., Trusheim, M. E., Englund, D., Shattuck, M. D. & Meriles, C. A. Dynamic Nuclear Spin Polarization of Liquids and Gases in Contact with Nanostructured Diamond. *Nano Lett.* (2014). doi:10.1021/nl500147b
4. Rej, E., Gaebel, T., Waddington, D. E. J. & Reilly, D. J. Hyperpolarized Nanodiamond Surfaces. *arXiv* **1606.06822**, 1–19 (2016).
5. Henstra, A., Dirksen, P. & Wenckebach, W. Enhanced dynamic nuclear polarization by the integrated solid effect. *Phys. Lett. A* **134**, 134–136 (1988).
6. Henstra, a. & Wenckebach, W. T. Dynamic nuclear polarisation via the integrated solid effect I: theory. *Mol. Phys.* 1–12 (2013). doi:10.1080/00268976.2013.861936
7. Stoll, S. & Schweiger, A. EasySpin, a comprehensive software package for spectral simulation and analysis in EPR. *J. Magn. Reson.* **178**, 42–55 (2006).
8. Falk, A. L. *et al.* Optical Polarization of Nuclear Spins in Silicon Carbide. *Phys. Rev. Lett.* **114**, 247603 (2015).
9. Ivady, V. *et al.* Theoretical model of dynamic spin polarization of nuclei coupled to paramagnetic point defects in diamond and silicon carbide. *Phys. Rev. B - Condens. Matter Mater. Phys.* **92**, 1–18 (2015).
10. Abtew, T. a. *et al.* Theory of Oxygen-Boron Vacancy Defect in Cubic Boron Nitride: A Diamond NV- Isoelectronic Center. *Phys. Rev. Lett.* **113**, 136401 (2014).



11. Wang, X. J., Vlasenko, L. S., Pearton, S. J., Chen, W. M. & Buyanova, I. a. Oxygen and zinc vacancies in as-grown ZnO single crystals. *J. Phys. D. Appl. Phys.* **42**, 175411 (2009).
12. Morfa, A. J. *et al.* Single-Photon Emission and Quantum Characterization of Zinc Oxide Defects. *Nano Lett.* **12**, 949 (2012).
13. Jungwirth, N. R. *et al.* A single-molecule approach to ZnO defect studies: Single photons and single defects. *J. Appl. Phys.* **116**, 43509 (2014).

## Appendix A

None

## Appendix B

1. Griffiths, D. J. *Introduction to Quantum Mechanics*. (Pearson Education, Inc., 2005).
2. Epstein, R. J., Mendoza, F. M., Kato, Y. K. & Awschalom, D. D. Anisotropic interactions of a single spin and dark-spin spectroscopy in diamond. *Nat. Phys.* **1**, 94–98 (2005).
3. Davies, G. & Hamer, M. F. Optical Studies of the 1.945 eV Vibronic Band in Diamond. *Proc. R. Soc. A Math. Phys. Eng. Sci.* **348**, 285–298 (1976).
4. Taylor, P., Lvovsky, A. I. & Lvovsky, A. I. Encyclopedia of Optical Engineering Fresnel Equations Fresnel Equations. 37–41 (2013). doi:10.1081/E-EOE-120047133

## Appendix C

1. Levitt, M. H. *Spin dynamics: Basics of nuclear magnetic resonance, 2nd edition*. (Wiley, 2009). doi:10.1002/cmr.a.20130
2. Drake, M., Scott, E. & Reimer, J. A. Influence of magnetic field alignment and defect concentration on nitrogen-vacancy polarization in diamond. *New J. Phys.* **18**, (2016).
3. Morrison, M. a. & Parker, G. a. A Guide to Rotations in Quantum Mechanics. *Aust. J. Phys.* **40**, 465 (1987).
4. King, J. P., Coles, P. J. & Reimer, J. A. Optical polarization of <sup>13</sup>C nuclei in diamond through nitrogen vacancy centers. *Phys. Rev. B* **81**, 1–4 (2010).



## Appendix D

1. Stoll, S. & Schweiger, A. EasySpin, a comprehensive software package for spectral simulation and analysis in EPR. *J. Magn. Reson.* **178**, 42–55 (2006).

## Appendix E

None

# Appendix A      Calculating NV Orientation Relative to Magnetic Field

---

Knowing the in-plane and out-of-plane crystal orientations of our samples allows us to calculate the angle between each of the four NV- defect axes and the applied magnetic field  $B_0$  at any given sample orientation in the field.

We model the sample orientation as a series of two rotations from a fixed starting orientation. The first rotation is about the z-axis, parallel to  $B_0$ . The second rotation is about the “tilt axis” (x-axis), which is the long-axis of the sapphire substrate about which the goniometer rotates the sample.

The starting orientation is physically related to how the diamond is mounted on the sapphire substrate, with respect to the tilt axis. For Samples #1-4, the starting orientation corresponds to any edge lined up square with the sapphire substrate, with the 100 edge aligned with the long-axis of the sapphire. For Samples #5-8, there are two edge orientations (see Table 1), and so care must be taken as to which edge is aligned with the long-axis of the sapphire. The model described below uses a starting position with the 110 axes of the Sample #5-8 diamonds pointed along the long-axis of the sapphire.

Table 1 depicts the in-plane orientations for each diamond and what the normalized starting vectors of the four NV- axes are relative to  $B_0$  for a diamond mounted flat in the starting orientation described above. Rotations are then applied to these starting vectors to determine the final angle of the NV- axes relative to  $B_0$  at other sample orientations.

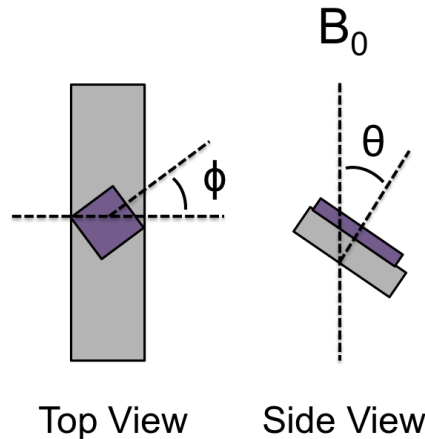


Figure 1 Schematic of diamond (purple square) on sapphire substrate (gray rectangle) illustrating definitions of the two rotations described in the main text.  $\phi$  and  $\theta$  are  $0^\circ$  when the edge and surface normal are respectively aligned with the long dashed lines.  $\phi$  and  $\theta$  are  $45^\circ$  when the edge and surface normal are respectively aligned with the shorter dashed lines, as they are illustrated in the figure.

The lab-frame axes are described by three unit vectors  $v_x$ ,  $v_y$ , and  $v_z$  shown below. The  $v_z$  vector is defined to point along the  $B_0$  axis. The  $v_x$  vector is defined along the long-axis of the sapphire mount, which is the axis about which the sample is tilted.


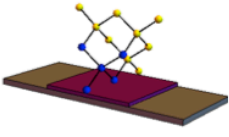

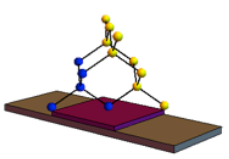

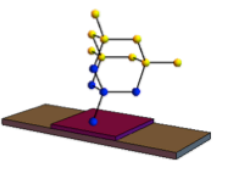

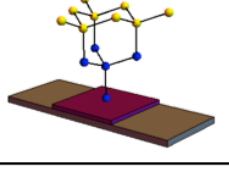
$$v_x = [100] \quad v_y = [010] \quad v_z = [001] \quad (\text{C.1})$$

The following rotation matrices are applied (from right to left) to the starting orientation vectors listed in Table 1. Angles of rotation ( $\theta$  and  $\phi$ ) are defined in Figure 1.

$$R(\theta, \phi) = \begin{pmatrix} 1 & 0 & 0 \\ 0 & \cos(\theta) & \sin(\theta) \\ 0 & -\sin(\theta) & \cos(\theta) \end{pmatrix} \begin{pmatrix} \cos(\phi) & -\sin(\phi) & 0 \\ \sin(\phi) & \cos(\phi) & 0 \\ 0 & 0 & 1 \end{pmatrix} \quad (\text{C.2})$$

The right matrix rotates the NV- starting vectors ( $v_{i,\text{flat}}$  listed in Table 1) about the  $v_z$  axis by angle  $\phi$ , and then the left matrix rotates about the  $v_x$  axis by angle  $\theta$ . This physically corresponds to first mounting the sample on the sapphire at a given angle between the diamond edge and the sapphire edge for a flat sapphire (normal to  $B_0$ ), then using the goniometer to tilt the plane of the sapphire and diamond by some angle  $\theta$  from normal.

**Table 1 Lattice Orientation of Diamonds and Vectors for NV Defect Orientations before Rotations**

Sample and Out-of-plane Orientation	In-plane Orientation	Lattice Illustration	$V_{1,\text{flat}}$	$V_{2,\text{flat}}$	$V_{3,\text{flat}}$	$V_{4,\text{flat}}$
Sample #2 100			$\begin{pmatrix} 0 \\ -0.81650 \\ -0.57735 \end{pmatrix}$	$\begin{pmatrix} 0 \\ 0.81650 \\ -0.57735 \end{pmatrix}$	$\begin{pmatrix} -0.81650 \\ 0 \\ 0.57735 \end{pmatrix}$	$\begin{pmatrix} 0.81650 \\ 0 \\ 0.57735 \end{pmatrix}$
Sample #1 Sample #3 Sample #4 100			$\begin{pmatrix} -0.57735 \\ -0.57735 \\ -0.57735 \end{pmatrix}$	$\begin{pmatrix} 0.57735 \\ 0.57735 \\ -0.57735 \end{pmatrix}$	$\begin{pmatrix} -0.57735 \\ 0.57735 \\ 0.57735 \end{pmatrix}$	$\begin{pmatrix} 0.57735 \\ -0.57735 \\ 0.57735 \end{pmatrix}$
Sample #5 Sample #6 110			$\begin{pmatrix} 0 \\ -0.57735 \\ -0.81650 \end{pmatrix}$	$\begin{pmatrix} 0.81650 \\ 0.57735 \\ 0 \end{pmatrix}$	$\begin{pmatrix} -0.81650 \\ 0.57735 \\ 0 \end{pmatrix}$	$\begin{pmatrix} 0 \\ -0.57735 \\ 0.81650 \end{pmatrix}$
Sample #7 Sample #8 111			$\begin{pmatrix} 0 \\ 0 \\ -1 \end{pmatrix}$	$\begin{pmatrix} 0.81650 \\ 0.47141 \\ 0.33333 \end{pmatrix}$	$\begin{pmatrix} -0.81650 \\ 0.47141 \\ 0.33333 \end{pmatrix}$	$\begin{pmatrix} 0 \\ -0.94281 \\ 0.33333 \end{pmatrix}$

The angle  $\gamma$  between the rotated NV- axes and the  $B_0$  field is found by taking the dot product of the rotated vectors,  $v_{i,\text{angled}}$ , with the  $v_z$  axis. The magnitude of the

coefficient in front of the cosine in Equation C.4 is 1 because we used normalized starting vectors and unit vectors.

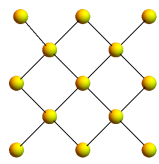
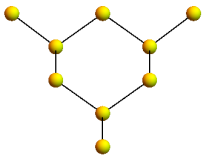
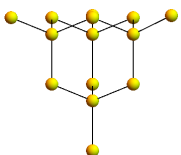
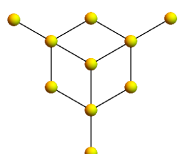
$$v_{i,angled}(\theta, \phi) = R(\theta, \phi)v_{i,flat} \quad (C.3)$$

$$v_{i,angled}(\theta, \phi) \cdot v_z = |1| \cos(\gamma) \quad (C.4)$$

$$\gamma = \cos^{-1}(v_{i,angled}(\theta, \phi) \cdot v_z) \quad (C.5)$$

Table 2 describes ways of identifying the diamond crystallographic directions mentioned above and in Table 1.

**Table 2 Descriptions and Illustrations for Several Crystallographic Directions in Diamond**

Crystal Direction	Description Looking along Crystal Direction	Illustration
100	Along backbone	
110	Through ring	
112	Through ring to bond	
111	Through ring to atom	

## Appendix B Modeling NV Light Absorption

This appendix outlines the mathematical model describing light absorption by ensembles of NV defects in single crystal diamonds.

First, we use Gram-Schmidt orthogonalization to determine a pair of orthonormal vectors in a plane normal to the defect axis<sup>1</sup>. The NV- center absorbs light along electric dipoles located perpendicular to the defect axis<sup>2,3</sup>.

We then sum the square of the dot product between these vectors, representing the dipole transitions, and vectors representing the s- and p-polarized components of the incident light to determine the light absorption by each NV- defect. Snell's law and the Fresnel Equations are used to determine the direction of propagation for the transmitted light and the relative intensity of the s- and p-polarized light components. These are found as a function of the crystal orientation relative to the incident light propagation axis (parallel to  $B_0$ ).

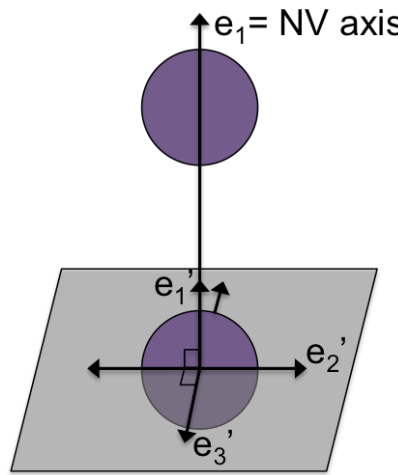


Figure 1 Illustration of orthonormal vectors  $e_1$ ,  $e_2'$ , and  $e_3'$ , where  $e_2'$  and  $e_3'$  represent the electric dipoles for the NV center (purple circles) located in the plane perpendicular to the defect axis.

### B.1 Gram-Schmidt Orthogonalization

For vectors in real space, Gram-Schmidt orthogonalization<sup>1</sup> begins with three linearly independent, non-orthonormal vectors. To find a pair of orthonormal vectors in a plane normal to the NV- defect axis, set one of the initial vectors as the defect axis.

$$|e_1\rangle = |NV\ axis\rangle, |e_2\rangle, |e_3\rangle \quad (B.1)$$

Then normalize the defect axis vector:

$$|e_1'\rangle = \frac{|e_1\rangle}{\| |e_1\rangle \|} \quad (B.2)$$

Find the projection of the second vector ( $e_2$ ) along the normalized first vector ( $e_1'$ ), subtract it from the second vector, and normalize the resulting vector to get a normalized vector orthogonal to the defect axis.

$$|e_2'\rangle = \frac{|e_2\rangle - \langle e_1'|e_2\rangle|e_1'\rangle}{\| |e_2\rangle - \langle e_1'|e_2\rangle|e_1'\rangle \|} \quad (\text{B.3})$$

Finally, find the projections of the third vector ( $e_3$ ) along the first two orthonormal vectors ( $e_1'$  and  $e_2'$ ), subtract them from the third vector, and normalize. The resulting vector is normalized and orthogonal to both  $e_1'$  and  $e_2'$ .

$$|e_3'\rangle = \frac{|e_3\rangle - \langle e_1'|e_3\rangle|e_1'\rangle - \langle e_2'|e_3\rangle|e_2'\rangle}{\| |e_3\rangle - \langle e_1'|e_3\rangle|e_1'\rangle - \langle e_2'|e_3\rangle|e_2'\rangle \|} \quad (\text{B.4})$$

The vectors  $e_2'$  and  $e_3'$  will depend on the initial choice of  $e_2$  and  $e_3$ , but this will not affect the calculated light absorption. Because the  $e_2'$  and  $e_3'$  are basis vectors spanning the plane perpendicular to the defect axis, summing the squares of their dot products with the perpendicular s- and p-polarized components of the transmitted light will result in the same absorption regardless of which orthonormal vectors in that plane are used to represent the defect's dipolar transitions.

## B.2 Snell's Law

Snell's Law is used to find the angle of transmitted light propagation relative to the surface normal vector ( $\theta_t$ ) in a system where the index of refraction of the initial ( $n_1$ ) and final ( $n_2$ ) materials and the angle of incident light ( $\theta_i$ ) are known. Figure 2a depicts such a system.

$$n_1 \sin \theta_i = n_2 \sin \theta_t \quad (\text{B.5})$$

$$\theta_t = \sin^{-1} \left( \frac{n_1}{n_2} \sin \theta_i \right) \quad (\text{B.6})$$

$$\theta_i = \theta_{\text{tilt}} \quad (\text{B.7})$$

The angle for the transmitted light with respect to the magnetic field ( $\theta_{t'}$ ) is given by Equation B.8.

$$\theta_{t'} = \theta_{\text{tilt}} - \theta_t \quad (\text{B.8})$$

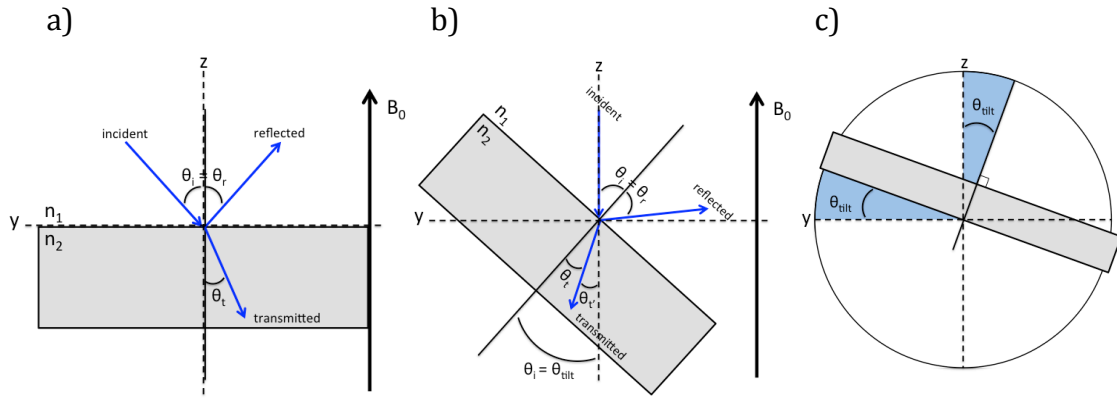


Figure 2 a) Side-view of diamond crystal (gray rectangle) and light vectors (blue) with labeled components involved in Snell's Law. b) Diamond and light vectors from a) tilted about the x-axis (into the page) by angle  $\theta_i$  such that the incident light is parallel to the magnetic field vector ( $B_0$ ). c) Simplified depiction of a tilted diamond highlighting the geometric relationship equating  $\theta_{\text{tilt}}$  to  $\theta_i$ .

### B.3 Fresnel Equations

Reflectance for s- and p-polarized light incident on a surface at an angle  $\theta_i$  and transmitted at  $\theta_t$  are described by the Fresnel Equations <sup>4</sup>.  $\theta_t$  is found using Snell's Law.

$$R_s = \left| \frac{n_1 \cos \theta_i - n_2 \cos \theta_t}{n_1 \cos \theta_i + n_2 \cos \theta_t} \right|^2 \quad (\text{B.9})$$

$$R_p = \left| \frac{n_1 \cos \theta_t - n_2 \cos \theta_i}{n_1 \cos \theta_t + n_2 \cos \theta_i} \right|^2 \quad (\text{B.10})$$

Transmittances for s- and p-polarized light can be found from the conservation of energy, which requires all incident light to be either reflected or transmitted.

$$T_s = 1 - R_s \quad (\text{B.11})$$

$$T_p = 1 - R_p \quad (\text{B.12})$$

Figure 3 shows the s- and p-polarized light transmission as a function of the angle between the diamond surface normal and the direction of light propagation,  $\theta_i$ .

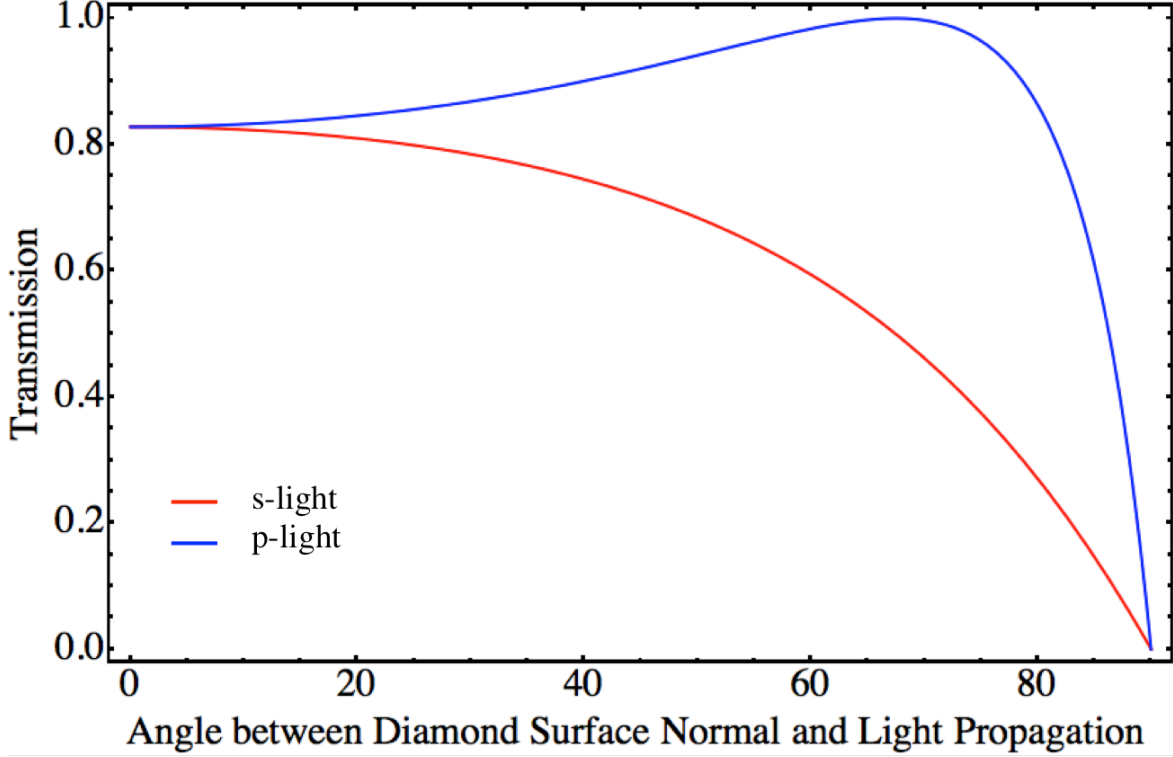


Figure 3 Normalized light transmission into the diamond for given sample tilt angles relative to the laser propagation direction.

S-polarized light is defined as parallel to the tilt axis of the diamond and sapphire substrate, which we call the x-axis throughout this text. P-polarized light is in the plane that holds the incident, transmitted, and reflected vectors (the plane of this page in Figure 2a,b). The transmitted light vectors are weighted by their relative transmissions calculated from the Fresnel Equations and oriented as calculated from Snell's Law.

$$|s_{light}\rangle = T_s \begin{pmatrix} 1 \\ 0 \\ 0 \end{pmatrix} \quad (\text{B.13})$$

$$|p_{light}\rangle = T_p \begin{pmatrix} 0 \\ \cos\theta_{tr} \\ \sin\theta_{tr} \end{pmatrix} \quad (\text{B.14})$$

#### B.4 NV- Light Absorption

The light absorption for each NV defect orientation is then found by squaring the dot product of each transition dipole with the transmitted s- and p-polarized light vectors.

$$\alpha_i = (|e_2'\rangle_i \cdot |s_{light}\rangle|^2 + |e_2'\rangle_i \cdot |p_{light}\rangle|^2 + |e_3'\rangle_i \cdot |s_{light}\rangle|^2 + |e_3'\rangle_i \cdot |p_{light}\rangle|^2) / 2 \quad (\text{B.15})$$

$i$  indicates each of the four defect orientations in a single crystal. The expression is divided by 2 to normalize the maximum absorption.



Figure 4 depicts NV absorption for circularly polarized light (s- and p-polarized light magnitudes are equal), ignoring the effects of surface reflection. This effect is combined with that of the reflection due to angle of the diamond surface in order to calculate the total light absorption as a function of crystal orientation.

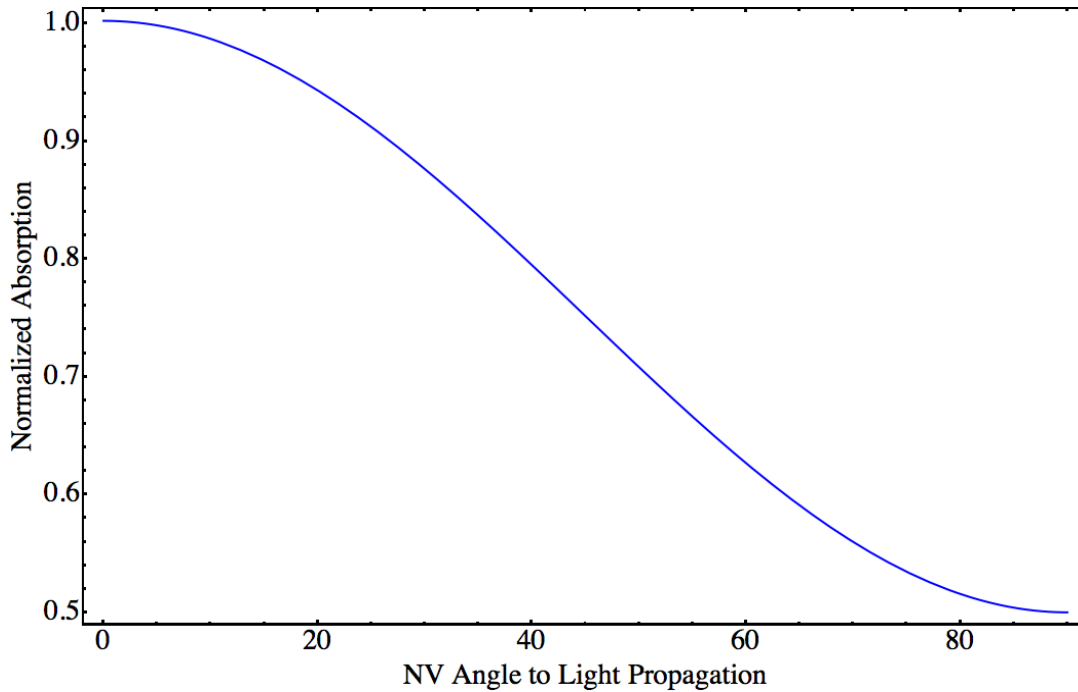


Figure 4 Normalized circularly polarized light absorption by an NV- defect as a function of the angle between NV- defect axis and the propagation of light. Does not take into account effects of reflection at the diamond surface.

Figure 5 is an example of the NV absorption accounting for both the defect orientation and the surface normal orientation effects. Unlike Figures 3 and 4 which describe trends generalized for any sample, the absorption trends in Figure 5 only apply to a diamond with a 100-surface orientation with 100-edges and 110-corners mounted with one edge rotated 50 degrees from the tilt axis.

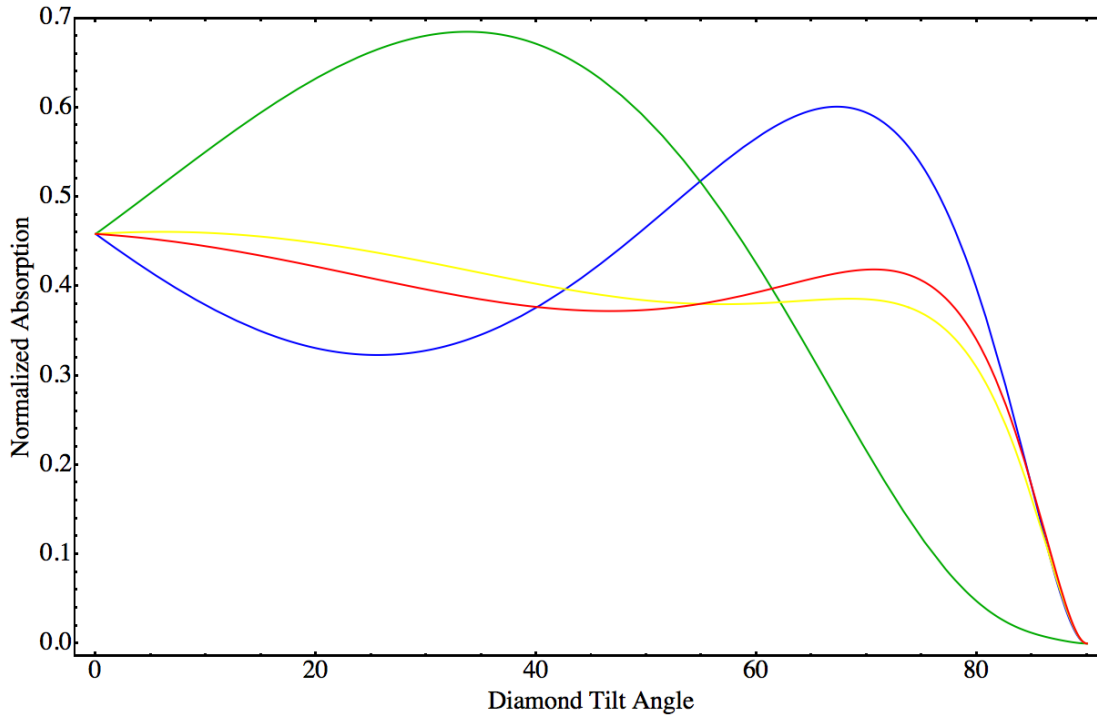


Figure 5 Relative absorption of four NV- defects (red, yellow, green, blue) in a 100-surface oriented diamond with 100-edges and 110-corners mounted with one edge rotated 50 degrees from the tilt axis.

These absorption relationships were incorporated into the model for nuclear polarization described in Chapter 4, and were modeled for bond and crystal orientations matching those of experiments when compared to data.

## B.5 Mathematica Code

### Defect Angles and Absorption By Rotation/Tilt

```

In[504]:= lattice = {{0, 0, 0}, {89.25, 89.25, 89.25}, {178.5, 178.5, 0}, {0, 178.5, 178.5}, {178.5, 0, 178.5}, {267.75, 267.75, 89.25},
  {357, 357, 0}, {178.5, 357, 178.5}, {357, 178.5, 178.5}, {89.25, 267.75, 267.75}, {11.156, 357, 357}, {178.5, 178.5, 357},
  {267.75, 89.25, 267.75}, {357, 11.156, 357}};

lattice2 = Table[y[[j]], {j, 1, Length[lattice]};

norm = Sqrt[89.25^2 + 89.25^2 + 89.25^2];

(*shifts lattice so one atoms is located at (0,0,0)*)
For[i = 1, i < Length[lattice], i++,
  lattice2[[i]] = lattice[[i]] + {-lattice[[2, 1]], -lattice[[2, 2]], -lattice[[2, 3]]}
];

v1 = Normalize[lattice2[[1]];
v2 = Normalize[lattice2[[3]];
v3 = Normalize[lattice2[[4]];
v4 = Normalize[lattice2[[5]];

R[phi_] := RotationMatrix[-phi*(Pi/180), {1, 0, 0}].RotationMatrix[phi*(Pi/180), {0, 0, 1}];

```

```

v1Lab[θ_] := R[θ].v1;
v2Lab[θ_] := R[θ].v2;
v3Lab[θ_] := R[θ].v3;
v4Lab[θ_] := R[θ].v4;

vx = {1, 0, 0};
vy = {0, 1, 0};
vz = {0, 0, 1};

(*use Gram-Schmidt procedure to find perpendicular basis to NV axis, with axis being one of the basis vectors → to use e2,
e3 as the dipolar transition vectors*)
(*dummy vectors (random) to use in finding perpendicular basis vectors*)
v2gs = {1, 1, 1};
v3gs = {1, 2, 0};

(*Gram-Schmidt basis vectors*)
e1Lab1[θ_] := v1Lab[θ]/Norm[v1Lab[θ]]; (*defect axis*)
e1Lab2[θ_] := (v2gs - e1Lab1[θ].v2gs + e1Lab1[θ])/Norm[(v2gs - e1Lab1[θ].v2gs + e1Lab1[θ])]; (*perpendicular to defect axis*)
e1Lab3[θ_] := (v3gs - e1Lab1[θ].v3gs + e1Lab1[θ] - e1Lab2[θ].v3gs + e1Lab2[θ])/
Norm[(v3gs - e1Lab1[θ].v3gs + e1Lab1[θ] - e1Lab2[θ].v3gs + e1Lab2[θ])]; (*perpendicular to defect axis*)

e2Lab1[θ_] := v2Lab[θ]/Norm[v2Lab[θ]]; (*defect axis*)
e2Lab2[θ_] := (v2gs - e2Lab1[θ].v2gs + e2Lab1[θ])/Norm[(v2gs - e2Lab1[θ].v2gs + e2Lab1[θ])]; (*perpendicular to defect axis*)
e2Lab3[θ_] := (v3gs - e2Lab1[θ].v3gs + e2Lab1[θ] - e2Lab2[θ].v3gs + e2Lab2[θ])/
Norm[(v3gs - e2Lab1[θ].v3gs + e2Lab1[θ] - e2Lab2[θ].v3gs + e2Lab2[θ])]; (*perpendicular to defect axis*)

e3Lab1[θ_] := v3Lab[θ]/Norm[v3Lab[θ]]; (*defect axis*)
e3Lab2[θ_] := (v2gs - e3Lab1[θ].v2gs + e3Lab1[θ])/Norm[(v2gs - e3Lab1[θ].v2gs + e3Lab1[θ])]; (*perpendicular to defect axis*)
e3Lab3[θ_] := (v3gs - e3Lab1[θ].v3gs + e3Lab1[θ] - e3Lab2[θ].v3gs + e3Lab2[θ])/
Norm[(v3gs - e3Lab1[θ].v3gs + e3Lab1[θ] - e3Lab2[θ].v3gs + e3Lab2[θ])]; (*perpendicular to defect axis*)

e4Lab1[θ_] := v4Lab[θ]/Norm[v4Lab[θ]]; (*defect axis*)
e4Lab2[θ_] := (v2gs - e4Lab1[θ].v2gs + e4Lab1[θ])/Norm[(v2gs - e4Lab1[θ].v2gs + e4Lab1[θ])]; (*perpendicular to defect axis*)
e4Lab3[θ_] := (v3gs - e4Lab1[θ].v3gs + e4Lab1[θ] - e4Lab2[θ].v3gs + e4Lab2[θ])/
Norm[(v3gs - e4Lab1[θ].v3gs + e4Lab1[θ] - e4Lab2[θ].v3gs + e4Lab2[θ])]; (*perpendicular to defect axis*)

θ1 = Table[ArcCos[v1Lab[(k-1)*Res].vz]*180/Pi, {k, 1, maxAng/Res + 1}];
θ2 = Table[ArcCos[v2Lab[(k-1)*Res].vz]*180/Pi, {k, 1, maxAng/Res + 1}];
θ3 = Table[ArcCos[v3Lab[(k-1)*Res].vz]*180./Pi, {k, 1, maxAng/Res + 1}];
θ4 = Table[ArcCos[v4Lab[(k-1)*Res].vz]*180/Pi, {k, 1, maxAng/Res + 1}];
tilts = Table[(k-1)*Res, {k, 1, maxAng/Res + 1}];

In[539]:= θt[θ_] := ArcSin[n1/n2*Sin[θ*Pi/180]]; (*rad - transmission angle into diamond relative to surface normal*)
θt2[θ_] := θ*Pi/180 - θt[θ]; (*rad - angle of transmitted light into diamond relative to z*)
θt3[θ_] := ArcSin[n2/n3*Sin[θt[θ]]]; (*rad - transmission angle out back of diamond relative to surface normal*)
θt4[θ_] := θt2[θ] + 2*θt[θ]; (*rad - internal reflection angle relative to z*)

Ts[θ_] := 1 - Abs[(n1*Cos[θ*Pi/180] - n2*Cos[θt[θ]])/(n1*Cos[θ*Pi/180] + n2*Cos[θt[θ]])]^2;
(*transmission of s-polarized component, θi=θ (sample tilt angle)*)
Tp[θ_] := 1 - Abs[(n1*Cos[θt[θ]] - n2*Cos[θ*Pi/180])/(n1*Cos[θt[θ]] + n2*Cos[θ*Pi/180])]^2;
(*transmission of p-polarized component*)

RsInt[θ_] := Ts[θ]*Abs[(n2*Cos[θt[θ]] - n3*Cos[θt3[θ]])/(n2*Cos[θt[θ]] + n3*Cos[θt3[θ]])]^2;
RpInt[θ_] := Tp[θ]*Abs[(n2*Cos[θt3[θ]] - n3*Cos[θt[θ]])/(n2*Cos[θt3[θ]] + n3*Cos[θt[θ]])]^2;

Slight[θ_] := Ts[θ]*Normalize[{1, 0, 0}]; (*S-pol light in transmission*)
Plight[θ_] := Tp[θ]*Normalize[{0, Cos[θt2[θ]], Sin[θt2[θ]]}]; (*P-pol light in transmission*)

SlightInt[θ_] := RsInt[θ]*Normalize[{1, 0, 0}]; (*S-pol light in internal reflection*)
PlightInt[θ_] := RpInt[θ]*Normalize[{0, Cos[θt4[θ]], Sin[θt4[θ]]}]; (*P-pol light in internal reflection*)

In[552]:= (*absorption efficiency - projecting defect axis direction onto laser propagation direction*)
(*defects only absorb perpendicular polarization (so max absorption when propagation is parallel to axis)*)
Alphaθ1[θ_] := (Abs[e1Lab2[θ].Slight[θ]]^2 + Abs[e1Lab2[θ].Plight[θ]]^2 + Abs[e1Lab3[θ].Slight[θ]]^2 + Abs[e1Lab3[θ].Plight[θ]]^2)/
2 +
(Abs[e1Lab2[θ].SlightInt[θ]]^2 + Abs[e1Lab2[θ].PlightInt[θ]]^2 + Abs[e1Lab3[θ].SlightInt[θ]]^2 + Abs[e1Lab3[θ].PlightInt[θ]]^2)/
2;
Alphaθ2[θ_] := (Abs[e2Lab2[θ].Slight[θ]]^2 + Abs[e2Lab2[θ].Plight[θ]]^2 + Abs[e2Lab3[θ].Slight[θ]]^2 + Abs[e2Lab3[θ].Plight[θ]]^2)/
2 +
(Abs[e2Lab2[θ].SlightInt[θ]]^2 + Abs[e2Lab2[θ].PlightInt[θ]]^2 + Abs[e2Lab3[θ].SlightInt[θ]]^2 + Abs[e2Lab3[θ].PlightInt[θ]]^2)/
2;
Alphaθ3[θ_] := (Abs[e3Lab2[θ].Slight[θ]]^2 + Abs[e3Lab2[θ].Plight[θ]]^2 + Abs[e3Lab3[θ].Slight[θ]]^2 + Abs[e3Lab3[θ].Plight[θ]]^2)/
2 +
(Abs[e3Lab2[θ].SlightInt[θ]]^2 + Abs[e3Lab2[θ].PlightInt[θ]]^2 + Abs[e3Lab3[θ].SlightInt[θ]]^2 + Abs[e3Lab3[θ].PlightInt[θ]]^2)/
2;
Alphaθ4[θ_] := (Abs[e4Lab2[θ].Slight[θ]]^2 + Abs[e4Lab2[θ].Plight[θ]]^2 + Abs[e4Lab3[θ].Slight[θ]]^2 + Abs[e4Lab3[θ].Plight[θ]]^2)/
2 +
(Abs[e4Lab2[θ].SlightInt[θ]]^2 + Abs[e4Lab2[θ].PlightInt[θ]]^2 + Abs[e4Lab3[θ].SlightInt[θ]]^2 + Abs[e4Lab3[θ].PlightInt[θ]]^2)/
2;

In[562]:= y = 0.5; (*aligned ms=0 population*)
Alpha1 = Map[Alphaθ1, tilts] * (y - 1/3) + 1/3
(* weights y by alpha such that its population value is meaningful relative to saturation (1/3)*)
Alpha2 = Map[Alphaθ2, tilts] * (y - 1/3) + 1/3
Alpha3 = Map[Alphaθ3, tilts] * (y - 1/3) + 1/3
Alpha4 = Map[Alphaθ4, tilts] * (y - 1/3) + 1/3

In[566]:= phi12 = {90 - Abs[90 - θ1], 90 - Abs[90 - θ2], 90 - Abs[90 - θ3], 90 - Abs[90 - θ4]};
NVangles = Tuples[{phi12, phi12}] * Pi/180;
Alpha = {Alpha1, Alpha2, Alpha3, Alpha4};
AlphaPairs = Tuples[{Alpha, Alpha}];

```

# Appendix C Derivation of NV Ensemble Density Matrix from that of Individual Defects

---

## C.1 Derivation

The density matrix ( $\rho$ ) for a single NV- center can be represented by an outer product of its eigenstates <sup>1</sup>. In Equation C.1, the superscript *defect* indicates we are operating in a reference frame pointed along the defect axis, and the subscript *NV* indicates we are considering a single NV defect. These labels will respectively be replaced by *lab*, indicating the laboratory frame, and *ensemble*, indicating an ensemble of NV defects, as we transform this density matrix into one representing an ensemble of defects in the laboratory reference frame, pointed along a large applied magnetic field.

$$\rho_{NV}^{defect} = |\psi\rangle^{defect}\langle\psi|^{defect} \quad (C.1)$$

A generalized form of the NV spin state is a linear combination of the basis states for a spin-1 system,  $| -1 \rangle$ ,  $| 0 \rangle$ , and  $| +1 \rangle$ . The square of the coefficients of these states represent the probability of measuring that basis state if you were to measure the system  $|\psi\rangle$  <sup>1</sup>. Equation C.2 indicates the relative phase of each component by  $e^{i\phi}$ . Equation C.3 combines this into a single coefficient represented by a prime mark.

$$|\psi\rangle^{defect} = ae^{i\phi_1}| +1 \rangle + be^{i\phi_2}| 0 \rangle + ce^{i\phi_3}| -1 \rangle \quad (C.2)$$

$$= a'| +1 \rangle + b'| 0 \rangle + c'| -1 \rangle \quad (C.3)$$

The outer product of the eigenstates leads to a matrix of these coefficients multiplied by their complex conjugates.

$$\rho_{NV}^{defect} = \begin{pmatrix} a' \\ b' \\ c' \end{pmatrix} (a'^* \ b'^* \ c'^*) \quad (C.4)$$

$$= \begin{pmatrix} (a')^2 & a'b'^* & a'c'^* \\ b'a'^* & (b')^2 & b'c'^* \\ c'a'^* & c'b'^* & (c')^2 \end{pmatrix} \quad (C.5)$$

As shown in Equation C.6, the phase component of the diagonal elements will multiply to unity. This simplifies Equation C.5 to give Equation C.7.

$$(a')^2 = (ae^{+i\phi_1})(ae^{-i\phi_1}) = a^2e^{+i\phi_1-i\phi_1} = a^2 \quad (C.6)$$

$$\rho_{NV}^{defect} = \begin{pmatrix} a^2 & abe^{i(\phi_1-\phi_2)} & ace^{i(\phi_1-\phi_3)} \\ bae^{i(\phi_2-\phi_1)} & b^2 & bce^{i(\phi_2-\phi_3)} \\ cae^{i(\phi_3-\phi_1)} & cbe^{i(\phi_3-\phi_2)} & c^2 \end{pmatrix} \quad (C.7)$$

We then average all NV- centers in our sample to create a density matrix representing this ensemble system, as indicated now by the new subscript *ensemble* in Equation C.8. Applying this to Equation C.7 gives Equation C.9.

$$\rho_{ensemble}^{defect} = \frac{1}{N} \sum_{j=1}^N \rho_j \quad (C.8)$$

$$\rho_{ensemble}^{defect} = \frac{1}{N} \begin{pmatrix} Na^2 & \sum_j abe^{i(\phi_{1,j}-\phi_{2,j})} & \sum_j ace^{i(\phi_{1,j}-\phi_{3,j})} \\ \sum_j bae^{i(\phi_{2,j}-\phi_{1,j})} & Nb^2 & \sum_j bce^{i(\phi_{2,j}-\phi_{3,j})} \\ \sum_j cae^{i(\phi_{3,j}-\phi_{1,j})} & \sum_j cbe^{i(\phi_{3,j}-\phi_{2,j})} & Nc^2 \end{pmatrix} \quad (C.9)$$

From Chapter 7, we know that a, b, and c are the same for all N number of spins in the ensemble in the defect frame of reference <sup>2</sup>. We can therefore pull these coefficients out from the summations. As each individual defect will have a different, uncorrelated phase, the sum over N exponentials of the difference between phases will average to zero, as represented in Equation C.10.

$$\sum_{j=1}^N abe^{i(\phi_{1,j}-\phi_{2,j})} = ab \sum_{j=1}^N e^{i(\phi_{1,j}-\phi_{2,j})} = ab(0) = 0 \quad (C.10)$$

We are left with a diagonal density matrix for an ensemble of defects in the defect reference frame (Equation C.11).

$$\rho_{ensemble}^{defect} = \begin{pmatrix} a^2 & 0 & 0 \\ 0 & b^2 & 0 \\ 0 & 0 & c^2 \end{pmatrix} \quad (C.11)$$

We apply a Wigner Rotation matrix for a spin-1 system,  $D^1$ , and its transpose  $(D^1)^T$  on either side of the defect-frame density matrix to transform it into the laboratory reference frame <sup>3</sup>.

$$\rho_{ensemble}^{lab} = D^1 \rho_{ensemble}^{defect} (D^1)^T \quad (C.12)$$

$$= \begin{pmatrix} (d_{1,1}^1)^2 a^2 + (d_{0,1}^1)^2 b^2 + (d_{-1,1}^1)^2 c^2 & (d_{1,1}^1)(d_{1,0}^1)a^2 + (d_{0,1}^1)(d_{0,0}^1)b^2 + (d_{-1,1}^1)(d_{-1,0}^1)c^2 & (d_{1,1}^1)(d_{1,-1}^1)a^2 + (d_{0,1}^1)(d_{0,-1}^1)b^2 + (d_{-1,1}^1)(d_{-1,-1}^1)c^2 \\ (d_{1,0}^1)(d_{1,1}^1)a^2 + (d_{0,0}^1)(d_{0,1}^1)b^2 + (d_{-1,0}^1)(d_{-1,1}^1)c^2 & (d_{1,0}^1)^2 a^2 + (d_{0,0}^1)^2 b^2 + (d_{-1,0}^1)^2 c^2 & (d_{1,0}^1)(d_{1,-1}^1)a^2 + (d_{0,0}^1)(d_{0,-1}^1)b^2 + (d_{-1,0}^1)(d_{-1,-1}^1)c^2 \\ (d_{1,-1}^1)(d_{1,1}^1)a^2 + (d_{0,-1}^1)(d_{0,1}^1)b^2 + (d_{-1,-1}^1)(d_{-1,1}^1)c^2 & (d_{1,-1}^1)(d_{1,0}^1)a^2 + (d_{0,-1}^1)(d_{0,0}^1)b^2 + (d_{-1,-1}^1)(d_{-1,0}^1)c^2 & (d_{1,-1}^1)^2 a^2 + (d_{0,-1}^1)^2 b^2 + (d_{-1,-1}^1)^2 c^2 \end{pmatrix}$$

The elements of the Wigner Rotation matrix  $d_{ij}$  are functions of the angle between the initial and final rotated reference frame. Their subscripts describe the states in the final and initial frames. Equations C.13-C.21 outline the Wigner Rotation matrix elements. Equation C.22 combines them into the Wigner Rotation matrix.

$$d_{1,1}^1 = \frac{1+\cos\gamma}{2} \quad (\text{C.13})$$

$$d_{1,0}^1 = -\frac{\sin\gamma}{\sqrt{2}} \quad (\text{C.14})$$

$$d_{1,-1}^1 = \frac{1-\cos\gamma}{2} \quad (\text{C.15})$$

$$d_{0,1}^1 = \frac{\sin\gamma}{\sqrt{2}} \quad (\text{C.16})$$

$$d_{0,0}^1 = \cos\gamma \quad (\text{C.17})$$

$$d_{0,-1}^1 = -\frac{\sin\gamma}{\sqrt{2}} \quad (\text{C.18})$$

$$d_{-1,1}^1 = \frac{1-\cos\gamma}{2} \quad (\text{C.19})$$

$$d_{-1,0}^1 = \frac{\sin\gamma}{\sqrt{2}} \quad (\text{C.20})$$

$$d_{-1,-1}^1 = \frac{1+\cos\gamma}{2} \quad (\text{C.21})$$

$$D^1 = \begin{pmatrix} d_{1,1}^1 & d_{0,1}^1 & d_{-1,1}^1 \\ d_{1,0}^1 & d_{0,0}^1 & d_{-1,0}^1 \\ d_{1,-1}^1 & d_{0,-1}^1 & d_{-1,-1}^1 \end{pmatrix} \quad (\text{C.22})$$

Assuming off-diagonal elements, which represent coherences, decay within the NV defect's  $T_2$  time (found to be several  $\mu\text{s}$  in Chapter 6) <sup>1</sup>, we are left with Equation C.23.

$$\rho_{ensemble}^{lab} = \begin{pmatrix} (d_{1,1}^1)^2(a)^2 + (d_{0,1}^1)^2(b)^2 + (d_{-1,1}^1)^2(c)^2 & 0 & 0 \\ 0 & (d_{1,0}^1)^2(a)^2 + (d_{0,0}^1)^2(b)^2 + (d_{-1,0}^1)^2(c)^2 & 0 \\ 0 & 0 & (d_{1,-1}^1)^2(a)^2 + (d_{0,-1}^1)^2(b)^2 + (d_{-1,-1}^1)^2(c)^2 \end{pmatrix} \quad (\text{C.23})$$

The diagonal elements are the populations of the NV eigenstates in a laboratory reference frame. This collapses to the previous model's density matrix (Equation C.24) under the assumption of 100% efficiency of pumping into  $m_s=0$  ( $a=c=0$ )<sup>4</sup>.

$$\rho_{ensemble,100\%ms=0}^{defect} = \begin{pmatrix} (d_{0,1}^1)^2 & 0 & 0 \\ 0 & (d_{0,0}^1)^2 & 0 \\ 0 & 0 & (d_{0,-1}^1)^2 \end{pmatrix} \quad (\text{C.24})$$



```

SysP1.lw=[0.06 0.11];
SysP1.Nucs='14N,(12,13)C,(12,13)C,(12,13)C,(12,13)C,(12,13)C,(12,13)C,(12,13)C,(12,13)C,(12,13)C,(12,13)C';
SysP1.Abund={1.0,[0.99 0.01],[0.99 0.01],[0.99 0.01],[0.99 0.01],[0.99 0.01],[0.99 0.01],[0.99 0.01],[0.99 0.01]};
SysP1.A=[81 81 115;141.8 141.8 340.8;32.1 32.1 41.3;32.1 32.1 41.3;26.8 26.8 23.3;26.8 26.8 23.3;26.8 26.8 23.3;11.2 11.2 14.5;11.2 11.2 14.5;11.2 11.2 14.5];
SysP1.AFrame=[-135 -54.7356 -180;-135 -54.7356 -180;-135 -54.7356 -180;-135 -54.7356 -180;-135 -54.7356 -180;-135 -54.7356 -180;-225 -54.7356 -180;-225 -54.7356 -180;-225 -54.7356 -180;-225 -54.7356 -180];
SysP1.weight=12.4;

ExpNV.mwFreq=9.73607;
ExpNV.Range=[240 455];
ExpNV.nPoints=21500;
ExpNV.CrystalSymmetry=227;
ExpNV.CrystalOrientation=Orientation;
ExpNV.ModAmp=0.2;
ExpNV.Temperature=293;
%Population_ms0=0.34;
%ExpNV.Temperature=[Population_ms0 (1-Population_ms0)/2 (1-Population_ms0)/2];

ExpP1.mwFreq=ExpNV.mwFreq;
ExpP1.Range=ExpNV.Range;
ExpP1.nPoints=ExpNV.nPoints;
ExpP1.CrystalSymmetry=ExpNV.CrystalSymmetry;
ExpP1.CrystalOrientation=ExpNV.CrystalOrientation;
ExpP1.ModAmp=ExpNV.ModAmp;
ExpP1.Temperature=293;

[Field,NV]=pepper(SysNV,ExpNV);
[Field2,P1]=pepper(SysP1,ExpP1);
Sim=NV+P1;
%Sim=rescale(Sim,'maxabs');
Sim=transpose(Sim);
Field=transpose(Field);
plot(Field,Sim)

```

## D.2 Simulating the Combined NV- and P1 X-band Spectrum in Diamond Powder, Coloring NV Transitions Red and Blue

```

clear

SysNV.S=1;
SysNV.g=2.0028;
SysNV.lwpp=[0.25 0.25];
SysNV.D=[2880 1.36];
SysNV.DFrame=[-135 -54.7356 -180]*(pi/180);
SysNV.weight=1;

SysP1.S=1/2;
SysP1.g=2.0024;
SysP1.lwpp=[0.18 0.18];
SysP1.Nucs='14N,(12,13)C';
SysP1.Abund={1.0,[0.99 0.01]};
SysP1.A=[81 81 115;141.8 141.8 340.8];
SysP1.AFrame=[-135 -54.7356 -180;-135 -54.7356 -180]*(pi/180);
SysP1.weight=100;

ExpNV.mwFreq=9.6;
ExpNV.Range=[220 460];
ExpNV.nPoints=21500;

```



```

ExpNV.CrystalSymmetry=227;
ExpNV.Harmonic=1;%absorptive lineshape when =0, deriv. when =1
(default)
ExpNV.Temperature=[.7 .15 .15];

ExpP1.mwFreq=ExpNV.mwFreq;
ExpP1.Range=ExpNV.Range;
ExpP1.nPoints=ExpNV.nPoints;
ExpP1.CrystalSymmetry=ExpNV.CrystalSymmetry;
ExpP1.Harmonic=1; %absorptive lineshape when =0, deriv. when =1
(default)
ExpP1.Temperature=293;

Opt.nKnots=181;

%Plots (0)<->(-1) RED
%Plots (0)<->( +1) BLUE
Opt.Transitions=[1 2];%(0)<->(-1)
Opt.Output='separate';
Opt.nKnots=181;
Opt2.Transitions=[2 3];%(0)<->( +1)
Opt2.Output='separate';
Opt2.nKnots=181;
[Field,NV1]=pepper(SysNV,ExpNV,Opt);
[Field2,NV2]=pepper(SysNV,ExpNV,Opt2);
[Field3,P1]=pepper(SysP1,ExpP1);

% plot all
plot(Field,NV1,'r',Field2,NV2,'b',Field3,P1,'k')

```

## D.3 Stackplot of Combined NV- and P1 X-band Spectrum Over 90 Degree Tilt Range, Coloring NV- Transitions Red and Blue

```

clear

StartOrientation=[1 1 1];

phi=0;
theta1=(0:5:90);
theta2=0;

[alpha,beta]=vec2ang(StartOrientation);gamma=0;
xyzL0=erot([alpha,beta,gamma]);
TiltAxis1=[1 tan(phi*(pi/180)) 0];
TiltAxis2=[tan(phi*(pi/180)) 1 0];
for k=1:numel(theta1)
    R1=rotaxi2mat(TiltAxis1,(theta1(k)*(pi/180)));
    R2=rotaxi2mat(TiltAxis2,theta2*(pi/180));
    xyzL=R2*R1*xyzL0;
    zL=xyzL(3,:);
end

```

```

    Orientation(:,k)=vec2ang(zL);
end

SysNV.S=1;
SysNV.g=2.0028;
SysNV.lwpp=[0.25 0.25];
SysNV.D=[2880 1.36];
SysNV.DFrame=[-135 -54.7356 -180]*(pi/180);
SysNV.weight=1;

SysP1.S=1/2;
SysP1.g=2.0024;
SysP1.lwpp=[0.18 0.18];
SysP1.Nucs='14N,(12,13)C';
SysP1.Abund={1.0,[0.99 0.01]};
SysP1.A=[81 81 115;141.8 141.8 340.8];
SysP1.AFrame=[-135 -54.7356 -180;-135 -54.7356 -180]*(pi/180);
SysP1.weight=6;

ExpNV.mwFreq=9.6;
ExpNV.Range=[220 460];
ExpNV.nPoints=21500;
ExpNV.CrystalSymmetry=227;
ExpNV.CrystalOrientation=Orientation.';
ExpNV.Temperature=[.45 .225 .225]; %polarization of zero field levels
in increasing energy order (so 0, +1/-1)

ExpP1.mwFreq=ExpNV.mwFreq;
ExpP1.Range=ExpNV.Range;
ExpP1.nPoints=ExpNV.nPoints;
ExpP1.CrystalSymmetry=ExpNV.CrystalSymmetry;
ExpP1.CrystalOrientation=ExpNV.CrystalOrientation;
ExpP1.Temperature=293;

Opt.Output='separate';

%Plots (0)<->(-1) RED
%Plots (0)<->(1) BLUE
Opt.Transitions=[1 2];%(0)<->(-1)
Opt.Output='separate';
Opt2.Transitions=[2 3];%(0)<->(1)
Opt2.Output='separate';
[Field,NV1]=pepper(SysNV,ExpNV,Opt);
[Field2,NV2]=pepper(SysNV,ExpNV,Opt2);
[Field3,P1]=pepper(SysP1,ExpP1);

% generate an offset matrix
% 2*max(max(NV1)) - estimates the amount that you need to shift spectra
by to avoid overlap
% repmat([1:size(NV1,1)]', 1, size(NV1,2)) - makes a vector 1 to number
of transitions and repeats that for the number of field points
a = 2 * max( max( NV1 ) ) * repmat([1:size(NV1,1)]', 1, size(NV1,2));
% then we just plot
plot(Field,a+NV1,'r',Field2,a+NV2,'b')

%add P1 peaks
hold on

```

```
plot(Field3,a(1)+P1, 'k',Field3,a(2)+P1, 'k',Field3,a(3)+P1, 'k',Field3,a(
4)+P1, 'k',Field3,a(5)+P1, 'k',Field3,a(6)+P1, 'k',Field3,a(7)+P1, 'k',Fiel
d3,a(8)+P1, 'k',Field3,a(9)+P1, 'k',Field3,a(10)+P1, 'k',Field3,a(11)+P1, '
k',Field3,a(12)+P1, 'k',Field3,a(13)+P1, 'k',Field3,a(14)+P1, 'k',Field3,a
(15)+P1, 'k',Field3,a(16)+P1, 'k',Field3,a(17)+P1, 'k',Field3,a(18)+P1, 'k'
,Field3,a(19)+P1, 'k')
```

# Appendix E      Mathematica Code of Orientation-Dependent Model of Dipolar Coupled NV Polarization

---

## Experimental Parameters and Constants

```
ClearAll["Global`*"] (*clears all variables*)

Experimental Parameters;
 $\phi = 25$ ; (*rotation of sample on sapphire holder*)
maxAng = 45; (*max tilt angle, usually 45*)
Res = .5; (*resolution, increments of tilt angle*)

ppmNV = 2; (*concentration of NV defects in ppm*)

B0 = 7.05; (*Tesla*)

Physical Constants;
n1 = 1; (*index of refraction air*)
n2 = 2.417; (*index of refraction diamond*)
n3 = 1.5; (*index of refraction of mount - 1.3 is n for ice, from wikipedia*)

u = 9.274 * 10-24; (* J/T bohr magneton*)
h = 6.626 * 10-34; (* J*s *)
g = 2.0028; (*g value of NV*)
hbar = h / (2  $\pi$ ); (*Joules*Seconds*)
 $\gamma$ NV = u * g / h; (*Hz/T*)
 $\gamma$ 13C = 10.705 * 106; (*Hz/T from Wikipedia*)
 $\omega$ I =  $\gamma$ 13C * B0 * 10-6; (*MHz*)
 $\omega$ NV =  $\gamma$ NV * B0 * 10-6; (*MHz*)
 $\mu$ 0 = 1.2566 * 10-6; (*T*m/A from wikipedia*)

dataRot50 = Import[
"/Users/melaniedrake/Google Drive/research/mathematica/DATA/compiled orientation
dependence/E6HC100HighRes_5rot.dat", "Data"];
dataRot55 = Import["/Users/melaniedrake/Google Drive/research/mathematica/DATA/compiled
orientation dependence/E6HC100HighRes_10rot.dat", "Data"];
dataRot60 = Import["/Users/melaniedrake/Google Drive/research/mathematica/DATA/compiled
orientation dependence/E6HC100HighRes_15rot.dat", "Data"];
dataRot65 = Import["/Users/melaniedrake/Google Drive/research/mathematica/DATA/compiled
orientation dependence/E6HC100HighRes_20rot.dat", "Data"];
dataS111Rot0 = Import["/Users/melaniedrake/Google
Drive/research/mathematica/DATA/compiled orientation
dependence/S111HighRes_0rot.dat", "Data"];
```

## Calculate Inter-defect distance

```
unitCellSide = 3.57; (*nm - length of side of diamond unit cell*)
unitCellAtoms = 8; (*number of atoms in a diamond unit cell*)

unitCellVol = (unitCellSide)3; (*nm3*)
CarbonAtomDensity = unitCellAtoms / unitCellVol; (*Carbon/nm3*)
FractionNV = ppmNV * (1 / 1000000); (*convert ppm to fraction*)
NVdensity = CarbonAtomDensity * FractionNV; (*NV/nm3*)
sphereNV = 1 / NVdensity; (*each NV in sphere of this volume nm3*)
(*for sphereNV nm3 volume = 4/3*pi*r3 *)
r = (sphereNV * 3 / 4 / Pi)(1 / 3); (*radius of sphereNV nm3 sphere,
equals half the distance between NV centers in nm*)
```

## Hamiltonian, Eigenvectors, Eigenvalues

```

      Ahf + D1 + D2 + 2 Z   0   0   0   0   0   0   0   0   0
      0   D1 + Z   -2 * Ahf / 4   0   0   0   0   0   0
      0   -2 * Ahf / 4   D2 + Z   0   0   0   0   0   0
      0   0   0   -Ahf + D1 + D2   -2 * Ahf / 4   0   0   0   0
      0   0   0   -2 * Ahf / 4   0   -2 * Ahf / 4   0   0   0
      0   0   0   0   -2 * Ahf / 4   -Ahf + D1 + D2   0   0   0
      0   0   0   0   0   0   D2 - Z   -2 * Ahf / 4   0
      0   0   0   0   0   0   -2 * Ahf / 4   D1 - Z   0
      0   0   0   0   0   0   0   0   Ahf + D1 + D2 - 2 Z
  H =
  )

(*eigenvectors*)
Evect = Normalize /@ Eigenvectors[H];
% // MatrixForm;

(*eigenvalues*)
Evals = Eigenvalues[H];
% // MatrixForm;

```

## Density Matrix and Wigner Rotation

```

(*budker.berkeley.edu/ADM/AtomicDensityMatrix/tutorial/ADMTutorial-
QuantumMechanicalRotations.html*)

Dwignera = { { d11a d01a dn11a },
             { d10a d00a dn10a },
             { dn11a dn01a dn11a } }; (*Wigner D matrix - defects w/ phi1 angle*)

Dwignerb = { { d11b d01b dn11b },
             { d10b d00b dn10b },
             { dn11b dn01b dn11b } }; (*Wigner D matrix - defects w/ phi2 angle*)

DwignerStara = ConjugateTranspose[Dwignera]; (*calculate conjugate transpose*)
DwignerStarb = ConjugateTranspose[Dwignerb];

rhoNVa = Dwignera . { a1^2 0 0
                     0 b1^2 0
                     0 0 c1^2 } . DwignerStara;

(*Wigner rotated density matrix, defects w/ phi1 angle*)

rhoNVb = Dwignerb . { a2^2 0 0
                     0 b2^2 0
                     0 0 c2^2 } . DwignerStarb;

(*Wigner rotated density matrix, defects w/ phi2 angle*)

rho2 = ArrayFlatten[Outer[Times, rhoNVa, rhoNVb]];
(*combine to 9x9 matrix for pairs of defects*)
(*KroneckerProduct[rhoNVa, rhoNVb]????*)
rho2 // MatrixForm;

d11[_] := (1 + Cos[-_]) / 2;
d10[_] := Sin[-_] / Sqrt[2];
dn11[_] := (1 - Cos[-_]) / 2;
d01[_] := -Sin[-_] / Sqrt[2];
d00[_] := Cos[-_];
dn01[_] := Sin[-_] / Sqrt[2];
dn11[_] := (1 - Cos[-_]) / 2;
dn10[_] := -Sin[-_] / Sqrt[2];
dn11[_] := (1 + Cos[-_]) / 2;
(*sign on 10 combos was wrong? 6/1/16*)

(*y=.5;*) (*population of ms=0*)
(*split into different NV polarizations →
y will be a function of light polarization/absorption*)
a[pol_] := Sqrt[(1 - pol) / 2];
b[pol_] := Sqrt[pol];
c[pol_] := Sqrt[(1 + pol) / 2];

(*A[theta_]=μ0/(4*Pi)*h*γNV^2*1/((r*10^-9)^3)*(1-3*Cos[theta]^2)*10^-6; (*MHz*)*)
Dzfs1[phi1_] := 2.87 * 10^3 * 0.5 * (3 * Cos[phi1]^2 - 1); (*MHz*)
Dzfs2[phi2_] := 2.87 * 10^3 * 0.5 * (3 * Cos[phi2]^2 - 1); (*MHz*)

a1 = a[pol1x]; b1 = b[pol1x]; c1 = c[pol1x];
a2 = a[pol2x]; b2 = b[pol2x]; c2 = c[pol2x];
D1 = Dzfs1[phi1x]; D2 = Dzfs2[phi2x];
Z = ωNV;

```

```

d11a = d11[phi1x]; d01a = d01[phi1x]; dn11a = dn11[phi1x];
d10a = d10[phi1x]; d00a = d00[phi1x]; dn10a = dn10[phi1x];
d1n1a = d1n1[phi1x]; d0n1a = d0n1[phi1x]; dn1n1a = dn1n1[phi1x];

d11b = d11[phi2x]; d01b = d01[phi2x]; dn11b = dn11[phi2x];
d10b = d10[phi2x]; d00b = d00[phi2x]; dn10b = dn10[phi2x];
d1n1b = d1n1[phi2x]; d0n1b = d0n1[phi2x]; dn1n1b = dn1n1[phi2x];

P1a = Conjugate[Evect[[1]].rho2.Evect[[1]];
P2a = Conjugate[Evect[[2]].rho2.Evect[[2]];
P3a = Conjugate[Evect[[3]].rho2.Evect[[3]];
P4a = Conjugate[Evect[[4]].rho2.Evect[[4]];
P5a = Conjugate[Evect[[5]].rho2.Evect[[5]];
P6a = Conjugate[Evect[[6]].rho2.Evect[[6]];
P7a = Conjugate[Evect[[7]].rho2.Evect[[7]];
P8a = Conjugate[Evect[[8]].rho2.Evect[[8]];
P9a = Conjugate[Evect[[9]].rho2.Evect[[9]];

totalpolarization = P1a + P2a + P3a + P4a + P5a + P6a + P7a + P8a + P9a;

```

---

## Defect Angles and Absorption By Rotation/Tilt

```

lattice = {{0, 0, 0}, {89.25, 89.25, 89.25}, {178.5, 178.5, 0}, {0, 178.5, 178.5},
{178.5, 0, 178.5}, {267.75, 267.75, 89.25}, {357, 357, 0}, {178.5, 357, 178.5},
{357, 178.5, 178.5}, {89.25, 267.75, 267.75}, {11.156, 357, 357},
{178.5, 178.5, 357}, {267.75, 89.25, 267.75}, {357, 11.156, 357}};

lattice2 = Table[y[j], {j, 1, Length[lattice]}];

norm = Sqrt[89.25^2 + 89.25^2 + 89.25^2];

(*shifts lattice so one atoms is located at (0,0,0)*)

For[i = 1, i <= Length[lattice], i++,
  lattice2[[i]] = lattice[[i]] + {-lattice[[2, 1]], -lattice[[2, 2]], -lattice[[2, 3]]}
];

v1 = Normalize[lattice2[[1]]];
v2 = Normalize[lattice2[[3]]];
v3 = Normalize[lattice2[[4]]];
v4 = Normalize[lattice2[[5]]];

R[theta_] := RotationMatrix[-theta * (Pi / 180), {1, 0, 0}].RotationMatrix[theta * (Pi / 180), {0, 0, 1}];

v1Lab[theta_] := R[theta].v1;
v2Lab[theta_] := R[theta].v2;
v3Lab[theta_] := R[theta].v3;
v4Lab[theta_] := R[theta].v4;

vx = {1, 0, 0};
vy = {0, 1, 0};
vz = {0, 0, 1};

(*use Gram-Schmidt procedure to find perpendicular basis to NV axis,
with axis being one of the basis vectors -> to use e2,
e3 as the dipolar transition vectors*)
(*dummy vectors (random) to use in finding perpendicular basis vectors*)
v2gs = {1, 1, 1};
v3gs = {1, 2, 0};

(*Gram-Schmidt basis vectors*)
e1Lab1[theta_] := v1Lab[theta] / Norm[v1Lab[theta]]; (*defect axis*)
e1Lab2[theta_] :=
(v2gs - e1Lab1[theta].v2gs + e1Lab1[theta]) / Norm[(v2gs - e1Lab1[theta].v2gs + e1Lab1[theta])];
(*perpendicular to defect axis*)
e1Lab3[theta_] := (v3gs - e1Lab1[theta].v3gs + e1Lab1[theta] - e1Lab2[theta].v3gs + e1Lab2[theta]) /
Norm[(v3gs - e1Lab1[theta].v3gs + e1Lab1[theta] - e1Lab2[theta].v3gs + e1Lab2[theta])];
(*perpendicular to defect axis*)

e2Lab1[theta_] := v2Lab[theta] / Norm[v2Lab[theta]]; (*defect axis*)
e2Lab2[theta_] :=
(v2gs - e2Lab1[theta].v2gs + e2Lab1[theta]) / Norm[(v2gs - e2Lab1[theta].v2gs + e2Lab1[theta])];
(*perpendicular to defect axis*)
e2Lab3[theta_] := (v3gs - e2Lab1[theta].v3gs + e2Lab1[theta] - e2Lab2[theta].v3gs + e2Lab2[theta]) /
Norm[(v3gs - e2Lab1[theta].v3gs + e2Lab1[theta] - e2Lab2[theta].v3gs + e2Lab2[theta])];
(*perpendicular to defect axis*)

e3Lab1[theta_] := v3Lab[theta] / Norm[v3Lab[theta]]; (*defect axis*)
e3Lab2[theta_] :=
(v2gs - e3Lab1[theta].v2gs + e3Lab1[theta]) / Norm[(v2gs - e3Lab1[theta].v2gs + e3Lab1[theta])];
(*perpendicular to defect axis*)
e3Lab3[theta_] := (v3gs - e3Lab1[theta].v3gs + e3Lab1[theta] - e3Lab2[theta].v3gs + e3Lab2[theta]) /
Norm[(v3gs - e3Lab1[theta].v3gs + e3Lab1[theta] - e3Lab2[theta].v3gs + e3Lab2[theta])];
(*perpendicular to defect axis*)

```

```

e4Lab1[θ_] := v4Lab[θ] / Norm[v4Lab[θ]]; (*defect axis*)
e4Lab2[θ_] :=
  (v2gs - e4Lab1[θ].v2gs + e4Lab1[θ]) / Norm[(v2gs - e4Lab1[θ].v2gs + e4Lab1[θ])];
(*perpendicular to defect axis*)
e4Lab3[θ_] := (v3gs - e4Lab1[θ].v3gs + e4Lab1[θ] - e4Lab2[θ].v3gs + e4Lab2[θ]) /
  Norm[(v3gs - e4Lab1[θ].v3gs + e4Lab1[θ] - e4Lab2[θ].v3gs + e4Lab2[θ])];
(*perpendicular to defect axis*)

θ1 = Table[ArcCos[v1Lab[(k - 1) * Res].vz] * 180 / Pi, {k, 1, maxAng / Res + 1}];
θ2 = Table[ArcCos[v2Lab[(k - 1) * Res].vz] * 180 / Pi, {k, 1, maxAng / Res + 1}];
θ3 = Table[ArcCos[v3Lab[(k - 1) * Res].vz] * 180. / Pi, {k, 1, maxAng / Res + 1}];
θ4 = Table[ArcCos[v4Lab[(k - 1) * Res].vz] * 180 / Pi, {k, 1, maxAng / Res + 1}];
tilts = Table[(k - 1) * Res, {k, 1, maxAng / Res + 1}]

θt[θ_] := ArcSin[n1 / n2 * Sin[θ * Pi / 180]];
(*rad - transmission angle into diamond relative to surface normal*)
θ2[θ_] := θ * Pi / 180 - θt[θ];
(*rad - angle of transmitted light into diamond relative to z*)
θ3[θ_] := ArcSin[n2 / n3 * Sin[θt[θ]]];
(*rad - transmission angle out back of diamond relative to surface normal*)
θ4[θ_] := θ2[θ] + 2 * θt[θ]; (*rad - internal reflection angle relative to z*)

Ts[θ_] :=
  1 - Abs[(n1 * Cos[θ * Pi / 180] - n2 * Cos[θt[θ]]) / (n1 * Cos[θ * Pi / 180] + n2 * Cos[θt[θ]])]^2;
(*transmission of s-polarized component, θi=θ (sample tilt angle)*)
Tp[θ_] :=
  1 - Abs[(n1 * Cos[θt[θ]] - n2 * Cos[θ * Pi / 180]) / (n1 * Cos[θt[θ]] + n2 * Cos[θ * Pi / 180])]^2;
(*transmission of p-polarized component*)

RsInt[θ_] :=
  Ts[θ] * Abs[(n2 * Cos[θt[θ]] - n3 * Cos[θ3[θ]]) / (n2 * Cos[θt[θ]] + n3 * Cos[θ3[θ]])]^2;
RpInt[θ_] := Tp[θ] *
  Abs[(n2 * Cos[θ3[θ]] - n3 * Cos[θt[θ]]) / (n2 * Cos[θ3[θ]] + n3 * Cos[θt[θ]])]^2;

Slight[θ_] := Ts[θ] * Normalize[{1, 0, 0}]; (*S-pol light in transmission*)
Plight[θ_] := Tp[θ] * Normalize[{0, Cos[θ2[θ]], Sin[θ2[θ]]}];
(*P-pol light in transmission*)

SlightInt[θ_] := RsInt[θ] * Normalize[{1, 0, 0}]; (*S-pol light in internal reflection*)
PlightInt[θ_] := RpInt[θ] * Normalize[{0, Cos[θ4[θ]], Sin[θ4[θ]]}];
(*P-pol light in internal reflection*)

(*Plot[{Norm[Slight[x]], Norm[Plight[x]], Norm[SlightInt[x]], Norm[PlightInt[x]]},
{x, 0, 90}, PlotStyle->{Red, Blue, Directive[Red, Dashed], Directive[Blue, Dashed]},
Frame->True, FrameStyle->Thick,
FrameLabel->{"Tilt", "Transmission (Ts=red, Tp=blue)", LabelStyle->28}*)
(*Plot[{Norm[Ts[x]], Norm[Tp[x]]}, {x, 0, 45}, PlotStyle->{Red, Blue}]*

(*absorption efficiency -
projecting defect axis direction onto laser propagation direction*)
(*defects only absorb perpendicular polarization
(so max absorption when propagation is parallel to axis)*)
Alphaθ1[θ_] := (Abs[e1Lab2[θ].Slight[θ]]^2 + Abs[e1Lab2[θ].Plight[θ]]^2 +
  Abs[e1Lab3[θ].Slight[θ]]^2 + Abs[e1Lab3[θ].Plight[θ]]^2) / 2 +
  (Abs[e1Lab2[θ].SlightInt[θ]]^2 + Abs[e1Lab2[θ].PlightInt[θ]]^2 +
  Abs[e1Lab3[θ].SlightInt[θ]]^2 + Abs[e1Lab3[θ].PlightInt[θ]]^2) / 2;
Alphaθ2[θ_] := (Abs[e2Lab2[θ].Slight[θ]]^2 + Abs[e2Lab2[θ].Plight[θ]]^2 +
  Abs[e2Lab3[θ].Slight[θ]]^2 + Abs[e2Lab3[θ].Plight[θ]]^2) / 2 +
  (Abs[e2Lab2[θ].SlightInt[θ]]^2 + Abs[e2Lab2[θ].PlightInt[θ]]^2 +
  Abs[e2Lab3[θ].SlightInt[θ]]^2 + Abs[e2Lab3[θ].PlightInt[θ]]^2) / 2;
Alphaθ3[θ_] := (Abs[e3Lab2[θ].Slight[θ]]^2 + Abs[e3Lab2[θ].Plight[θ]]^2 +
  Abs[e3Lab3[θ].Slight[θ]]^2 + Abs[e3Lab3[θ].Plight[θ]]^2) / 2 +
  (Abs[e3Lab2[θ].SlightInt[θ]]^2 + Abs[e3Lab2[θ].PlightInt[θ]]^2 +
  Abs[e3Lab3[θ].SlightInt[θ]]^2 + Abs[e3Lab3[θ].PlightInt[θ]]^2) / 2;
Alphaθ4[θ_] := (Abs[e4Lab2[θ].Slight[θ]]^2 + Abs[e4Lab2[θ].Plight[θ]]^2 +
  Abs[e4Lab3[θ].Slight[θ]]^2 + Abs[e4Lab3[θ].Plight[θ]]^2) / 2 +
  (Abs[e4Lab2[θ].SlightInt[θ]]^2 + Abs[e4Lab2[θ].PlightInt[θ]]^2 +
  Abs[e4Lab3[θ].SlightInt[θ]]^2 + Abs[e4Lab3[θ].PlightInt[θ]]^2) / 2;

```

```

y = 0.5; (*aligned ms=0 population*)
Alpha1 = Map[Alpha01, tilts] * (y - 1/3) + 1/3 (* weights y by alpha such
that its population value is meaningful relative to saturation (1/3)*)
Alpha2 = Map[Alpha02, tilts] * (y - 1/3) + 1/3
Alpha3 = Map[Alpha03, tilts] * (y - 1/3) + 1/3
Alpha4 = Map[Alpha04, tilts] * (y - 1/3) + 1/3
phi12 = {90 - Abs[90 - e1], 90 - Abs[90 - e2], 90 - Abs[90 - e3], 90 - Abs[90 - e4]};
NVangles = Tuples[{phi12, phi12}] * Pi / 180;
Alpha = {Alpha1, Alpha2, Alpha3, Alpha4};
AlphaPairs = Tuples[{Alpha, Alpha}];

Ptotal = Table[0, {x, 1, Length[tilts]}];
P1P2 = Table[0, {x, 1, Length[tilts]}];
P1P3 = Table[0, {x, 1, Length[tilts]}];
P2P3 = Table[0, {x, 1, Length[tilts]}];
P5P6 = Table[0, {x, 1, Length[tilts]}];
P8P9 = Table[0, {x, 1, Length[tilts]}];
E1E2plot = Table[0, {x, 1, Length[tilts]}];
E2E3plot = Table[0, {x, 1, Length[tilts]}];
E1E3plot = Table[0, {x, 1, Length[tilts]}];
E5E6plot = Table[0, {x, 1, Length[tilts]}];
E8E9plot = Table[0, {x, 1, Length[tilts]}];

(*For[freq=10, freq<=500, freq+=10, *)_

For[k = 1, k <= (maxAng + Res) / Res, k++, (*index of tilts*)

  phi1x = NVangles[[;;, 1, k]];
  phi2x = NVangles[[;;, 2, k]];
  pol1x = AlphaPairs[[;;, 1, k]];
  pol2x = AlphaPairs[[;;, 2, k]];

  (*Plot[totalpolarization, {Ahf, -10, 10},
  PlotRange->{{-10, 10}, {.9999999999, 1.0000000001}}]*)
  (*Plot[{P1a, P2a, P3a, P4a, P5a, P6a, P7a, P8a, P9a}, {Ahf, -5, 5}]*)

  E1E2 = Evals[[1, ;;]] - Evals[[2, ;;]]; (*energy transition for each of 16 j pairs*)
  E2E3 = Evals[[2, ;;]] - Evals[[3, ;;]]; (*energy transition for each of 16 j pairs*)
  E1E3 = Evals[[1, ;;]] - Evals[[3, ;;]]; (*energy transition for each of 16 j pairs*)
  E5E6 = Evals[[5, ;;]] - Evals[[6, ;;]]; (*energy transition for each of 16 j pairs*)
  E8E9 = Evals[[8, ;;]] - Evals[[9, ;;]]; (*energy transition for each of 16 j pairs*)

  E1E2plot[[k]] = E1E2;
  E1E3plot[[k]] = E1E3;
  E2E3plot[[k]] = E2E3;
  E5E6plot[[k]] = E5E6;
  E8E9plot[[k]] = E8E9;

  (*find Ahf2 values that match nuclear polarization*)
  (*13C = 75MHz, 14N=22MHz*)
  freq = 75.;
  DeltaPlus[x_] := NSolve[x == freq, Ahf, Reals];
  DeltaMinus[x_] := NSolve[x == -freq, Ahf, Reals];

  (*find Ahf values that match nuclear polarization*)
  Ahf12Plus = Ahf /. Map[DeltaPlus, E1E2] /. Ahf -> {Indeterminate};
  Ahf12Minus = Ahf /. Map[DeltaMinus, E1E2] /. Ahf -> {Indeterminate};

  Ahf23Plus = Ahf /. Map[DeltaPlus, E2E3] /. Ahf -> {Indeterminate};
  Ahf23Minus = Ahf /. Map[DeltaMinus, E2E3] /. Ahf -> {Indeterminate} /.
  {Indeterminate} -> {Indeterminate, Indeterminate};

```





```

(*solve polarizations for each j pair using Ahf solutions for each j pair*)
P9b89transisionAPlus = Table[P9a[[j]] /. Ahf -> Ahf89Plus[[j]], {j, 1, 16}] /.
  {Indeterminate} -> {Indeterminate, Indeterminate};
(*solve polarizations for each j pair using Ahf solutions for each j pair*)
P8b89transisionAMinus = Table[P8a[[j]] /. Ahf -> Ahf89Minus[[j]], {j, 1, 16}] /.
  {Indeterminate} -> {Indeterminate, Indeterminate};
(*solve polarizations for each j pair using Ahf solutions for each j pair*)
P9b89transisionAMinus = Table[P9a[[j]] /. Ahf -> Ahf89Minus[[j]], {j, 1, 16}] /.
  {Indeterminate} -> {Indeterminate, Indeterminate};
(*solve polarizations for each j pair using Ahf solutions for each j pair*)

Pol12Plus = (P1b12transisionAPlus - P2b12transisionAPlus) /
  (P1b12transisionAPlus + P2b12transisionAPlus) /. Indeterminate -> 0;
(*take difference in populations for each j and set indeterminates to zero*)
Pol12Minus = (P1b12transisionAMinus - P2b12transisionAMinus) /
  (P1b12transisionAMinus + P2b12transisionAMinus) /. Indeterminate -> 0;
(*take difference in populations for each j and set indeterminates to zero*)

Pol13Plus = (P1b13transisionAPlus - P3b13transisionAPlus) /
  (P1b13transisionAPlus + P3b13transisionAPlus) /. Indeterminate -> 0;
(*take difference in populations for each j and set indeterminates to zero*)
Pol13Minus = (P1b13transisionAMinus - P3b13transisionAMinus) /
  (P1b13transisionAMinus + P3b13transisionAMinus) /. Indeterminate -> 0;
(*take difference in populations for each j and set indeterminates to zero*)

Pol23Plus = (P2b23transisionAPlus - P3b23transisionAPlus) /
  (P2b23transisionAPlus + P3b23transisionAPlus) /. Indeterminate -> 0;
(*take difference in populations for each j and set indeterminates to zero*)
Pol23Minus = (P2b23transisionAMinus - P3b23transisionAMinus) /
  (P2b23transisionAMinus + P3b23transisionAMinus) /. Indeterminate -> 0;
(*take difference in populations for each j and set indeterminates to zero*)

Pol56Plus = (P5b56transisionAPlus - P6b56transisionAPlus) /
  (P5b56transisionAPlus + P6b56transisionAPlus) /. Indeterminate -> 0;
(*take difference in populations for each j and set indeterminates to zero*)
Pol56Minus = (P5b56transisionAMinus - P6b56transisionAMinus) /
  (P5b56transisionAMinus + P6b56transisionAMinus) /. Indeterminate -> 0;
(*take difference in populations for each j and set indeterminates to zero*)

Pol89Plus = (P8b89transisionAPlus - P9b89transisionAPlus) /
  (P8b89transisionAPlus + P9b89transisionAPlus) /. Indeterminate -> 0;
(*take difference in populations for each j and set indeterminates to zero*)
Pol89Minus = (P8b89transisionAMinus - P9b89transisionAMinus) /
  (P8b89transisionAMinus + P9b89transisionAMinus) /. Indeterminate -> 0;
(*take difference in populations for each j and set indeterminates to zero*)

(*Lorentzian weighting of A values*)
Ashift = 0; -
(*A[theta_]=mu0/(4*Pi)*h*gamma^2*1/((r*10^-9)^3)*(1-3*Cos[theta]^2)*10^-6; (*MHz*)*)
delta = 15; (*MHz - from 8.5T EPR spectrum*)
LorNormArea[Ahf_] := delta / (Pi * (delta^2 + (Ahf)^2));
LorNormHeight[Ahf_] := (1/LorNormArea[0]) * delta / (Pi * (delta^2 + (Ahf - Ashift)^2));

(*Plot[LorNormHeight[Ahf], {Ahf, -100, 100}, PlotRange -> {{-100, 100}, {0, 1}}];*)

weight12plus = LorNormHeight[Ahf12Plus] /.
  {Indeterminate} -> {Indeterminate, Indeterminate} /. Indeterminate -> 0;
weight13plus = LorNormHeight[Ahf13Plus] /. {Indeterminate} ->
  {Indeterminate, Indeterminate} /. Indeterminate -> 0;
weight23plus = LorNormHeight[Ahf23Plus] /. {Indeterminate} ->
  {Indeterminate, Indeterminate} /. Indeterminate -> 0;
weight56plus = LorNormHeight[Ahf56Plus] /. {Indeterminate} ->
  {Indeterminate, Indeterminate} /. Indeterminate -> 0;

```

```

weight89plus = LorNormHeight[Ahf89Plus] /. {Indeterminate} ->
  {Indeterminate, Indeterminate} /. Indeterminate -> 0;

weight12minus = LorNormHeight[Ahf12Minus] /.
  {Indeterminate} -> {Indeterminate, Indeterminate} /. Indeterminate -> 0;
weight13minus = LorNormHeight[Ahf13Minus] /.
  {Indeterminate} -> {Indeterminate, Indeterminate} /. Indeterminate -> 0;
weight23minus = LorNormHeight[Ahf23Minus] /.
  {Indeterminate} -> {Indeterminate, Indeterminate} /. Indeterminate -> 0;
weight56minus = LorNormHeight[Ahf56Minus] /.
  {Indeterminate} -> {Indeterminate, Indeterminate} /. Indeterminate -> 0;
weight89minus = LorNormHeight[Ahf89Minus] /.
  {Indeterminate} -> {Indeterminate, Indeterminate} /. Indeterminate -> 0;

P1P2plus = Map[Total, Map[Total, Pol12Plus * weight12plus, {1}], {0}];
P1P2minus = Map[Total, Map[Total, Pol12Minus * weight12minus, {1}], {0}];
P1P2Final = -P1P2plus + P1P2minus;

P1P3plus = Map[Total, Map[Total, Pol13Plus * weight13plus, {1}], {0}];
P1P3minus = Map[Total, Map[Total, Pol13Minus * weight13minus, {1}], {0}];
P1P3Final = -P1P3plus + P1P3minus;

P2P3plus = Map[Total, Map[Total, Pol23Plus * weight23plus, {1}], {0}];
P2P3minus = Map[Total, Map[Total, Pol23Minus * weight23minus, {1}], {0}];
P2P3Final = -P2P3plus + P2P3minus;

P5P6plus = Map[Total, Map[Total, Pol56Plus * weight56plus, {1}], {0}];
P5P6minus = Map[Total, Map[Total, Pol56Minus * weight56minus, {1}], {0}];
P5P6Final = -P5P6plus + P5P6minus;

P8P9plus = Map[Total, Map[Total, Pol89Plus * weight89plus, {1}], {0}];
P8P9minus = Map[Total, Map[Total, Pol89Minus * weight89minus, {1}], {0}];
P8P9Final = -P8P9plus + P8P9minus;

Ptotal[[k]] = P1P2Final + P1P3Final + P2P3Final + P5P6Final + P8P9Final;
P1P2[[k]] = P1P2Final;
P1P3[[k]] = P1P3Final;
P2P3[[k]] = P2P3Final;
P5P6[[k]] = P5P6Final;
P8P9[[k]] = P8P9Final;

]

Modeltot = Transpose[{tilts, Ptotal * 50}];
Model12 = Transpose[{tilts, P1P2 * 10}];
Model13 = Transpose[{tilts, P1P3 * 10}];
Model23 = Transpose[{tilts, P2P3 * 10}];
Model56 = Transpose[{tilts, P5P6 * 10}];
Model89 = Transpose[{tilts, P8P9 * 10}];

dataplot = {dataRot50, dataRot55, dataRot60, dataRot65};
dataplot[[{phi/5} - 9]]; (*automatically plots correct data for given phi rotation*)

partsplot = Show[
  ListLinePlot[dataplot[[{phi/5} - 9]], PlotRange -> Full, AxesOrigin -> {0, 0},
    PlotStyle -> {Thick, Black}, Frame -> True, FrameStyle -> {Directive[Thick, Black],
      Directive[Thick, Black], Directive[Thick, Black], Directive[Thick, Blue]},
    FrameLabel -> {"Tilt Angle (degrees)", "Measured % 13C Polarization", ,
      "Modeled NV-NV Reservoir Polarization"}, LabelStyle -> 36, ImageSize -> 1200],
  ListPlot[dataplot[[{phi/5} - 9]], PlotStyle -> Black, PlotMarkers -> {Automatic, Large}],
  ListLinePlot[Modeltot, PlotStyle -> Blue, PlotRange -> Full],
  ListPlot[Modeltot, PlotStyle -> Directive[Blue, PointSize[Large]], PlotRange -> Full],

```

```

ListLinePlot[Model12, PlotStyle → Red, PlotRange → Full],
ListPlot[Model12, PlotStyle → Directive[Red, PointSize[Large]], PlotRange → Full],

ListLinePlot[Model13, PlotStyle → Orange, PlotRange → Full],
ListPlot[Model13, PlotStyle → Directive[Orange, PointSize[Large]], PlotRange → Full],

ListLinePlot[Model23, PlotStyle → Yellow, PlotRange → Full],
ListPlot[Model23, PlotStyle → Directive[Yellow, PointSize[Large]], PlotRange → Full],

ListLinePlot[Model56, PlotStyle → Green, PlotRange → Full],
ListPlot[Model56, PlotStyle → Directive[Green, PointSize[Large]], PlotRange → Full],

ListLinePlot[Model89, PlotStyle → Purple, PlotRange → Full],
ListPlot[Model89, PlotStyle → Directive[Purple, PointSize[Large]], PlotRange → Full]
];

sumplot = Show[
ListLinePlot[dataplot[[( $\phi$  / 5) - 9]],
PlotRange → Full, AxesOrigin → {0, 0}, PlotStyle → {Thick, Black},
AxesStyle → Thick, Frame → True, FrameStyle → {Directive[Thick, Black],
Directive[Thick, Black], Directive[Thick, Blue]},
FrameLabel → {"Tilt Angle (degrees)", "Measured % 13C Polarization",
"Modeled NV-NV Reservoir Polarization"}, LabelStyle → 36, ImageSize → 1200],
ListPlot[dataplot[[( $\phi$  / 5) - 9]], PlotStyle → Black, PlotMarkers → {Automatic, Large}],
ListLinePlot[Modeltot, PlotStyle → {Thick, Red}, PlotRange → Full],
ListPlot[Modeltot, PlotStyle → Red, PlotMarkers → {Automatic, Large}]
]

Export["/Users/melaniedrake/Desktop/simulations/switch Ds in Hamiltonian/" <>
ToString[ $\phi$ ] <> "rot " <> ToString[Res] <> "res " <> ToString[freq] <>
"MHz " <> ToString[y] <> "pol Populations " <> ToString[n3] <>
" n for mount E6HC tot switchD shiftA0 15width.txt", Modeltot, "Table"]
Export["/Users/melaniedrake/Desktop/simulations/switch Ds in Hamiltonian/" <>
ToString[ $\phi$ ] <> "rot " <> ToString[Res] <> "res " <> ToString[freq] <>
"MHz " <> ToString[y] <> "pol Populations " <> ToString[n3] <>
" n for mount E6HC P1P2 switchD shiftA0 15width.txt", Model12, "Table"]
Export["/Users/melaniedrake/Desktop/simulations/switch Ds in Hamiltonian/" <>
ToString[ $\phi$ ] <> "rot " <> ToString[Res] <> "res " <> ToString[freq] <>
"MHz " <> ToString[y] <> "pol Populations " <> ToString[n3] <>
" n for mount E6HC P1P3 switchD shiftA0.txt", Model13, "Table"]
Export["/Users/melaniedrake/Desktop/simulations/switch Ds in Hamiltonian/" <>
ToString[ $\phi$ ] <> "rot " <> ToString[Res] <> "res " <> ToString[freq] <>
"MHz " <> ToString[y] <> "pol Populations " <> ToString[n3] <>
" n for mount E6HC P2P3 switchD shiftA0 15width.txt", Model23, "Table"]
Export["/Users/melaniedrake/Desktop/simulations/switch Ds in Hamiltonian/" <>
ToString[ $\phi$ ] <> "rot " <> ToString[Res] <> "res " <> ToString[freq] <>
"MHz " <> ToString[y] <> "pol Populations " <> ToString[n3] <>
" n for mount E6HC P5P6 switchD shiftA0 15width.txt", Model56, "Table"]
Export["/Users/melaniedrake/Desktop/simulations/switch Ds in Hamiltonian/" <>
ToString[ $\phi$ ] <> "rot " <> ToString[Res] <> "res " <> ToString[freq] <>
"MHz " <> ToString[y] <> "pol Populations " <> ToString[n3] <>
" n for mount E6HC P8P9 switchD shiftA0 15width.txt", Model89, "Table"]
Export["/Users/melaniedrake/Desktop/simulations/switch Ds in Hamiltonian/" <>
ToString[ $\phi$ ] <> "rot " <> ToString[Res] <> "res " <> ToString[freq] <>
"MHz " <> ToString[y] <> "pol Populations " <> ToString[n3] <>
" n for mount E6HC sum switchD shiftA0 15width.png", sumplot]
Export["/Users/melaniedrake/Desktop/simulations/switch Ds in Hamiltonian/" <>
ToString[ $\phi$ ] <> "rot " <> ToString[Res] <> "res " <> ToString[freq] <>
"MHz " <> ToString[y] <> "pol Populations " <> ToString[n3] <>
" n for mount E6HC parts switchD shiftA0 15width.png", partsplot]

(*]*)

```